

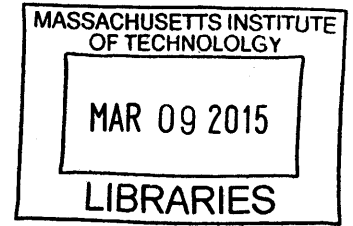
Bayesian-based Simulation Model Validation for Spacecraft Thermal Systems

ARCHIVES

by

Kevin Dale Stout

B.S., The University of Texas at Austin (2011)
S.M., Massachusetts Institute of Technology (2013)



Submitted to the Department of Aeronautics and Astronautics
in partial fulfillment of the requirements for the degree of

Doctor of Philosophy

at the

MASSACHUSETTS INSTITUTE OF TECHNOLOGY

February 2015

This material is declared a work of the United States Government and is not subject to copyright protection in the United States.

Signature redacted

Author Department of Aeronautics and Astronautics

Signature redacted

January 29, 2015

Certified by David W. Miller

Signature redacted

Professor of Aeronautics and Astronautics

Certified by Karen E. Willcox

Signature redacted

Professor of Aeronautics and Astronautics

Certified by Sheila E. Widnall

Signature redacted

Professor of Aeronautics and Astronautics

Certified by Rebecca A. Masterson

Signature redacted

Research Engineer

Accepted by Paulo Lozano

Chairman, Department Graduate Committee

Disclaimer: The views expressed in this thesis are those of the author and do not reflect the official policy or position of the United States Air Force, the United States Department of Defense, or the United States Government.

Bayesian-based Simulation Model Validation for Spacecraft Thermal Systems

by

Kevin Dale Stout

Submitted to the Department of Aeronautics and Astronautics
on January 29, 2015, in partial fulfillment of the
requirements for the degree of
Doctor of Philosophy

Abstract

Over the last several decades of space flight, spacecraft thermal system modeling software has advanced significantly, but the *model validation process*, in general, has changed very little. Although most thermal systems are successful, there is evidence of some model inaccuracy and thermal system overdesign due to the conservatism of the current (i.e., conventional) validation process. A significant improvement to the model validation process can result in the reduction of resource-related (e.g., mass, volume, or power) or process-related (e.g., design, verification and validation, operations) mission costs.

This thesis proposes a Bayesian-based Model Validation (BMV) methodology as a tailored framework that combines the state of the art model validation methods within the fields of Uncertainty Quantification (UQ) and Design of Experiments (DOE) to improve the thermal model validation process. In BMV, model uncertainties are rigorously quantified *upstream* of the model and propagated through the model to determine their influence on the quantities of interest (QoIs). Critical system parameters that most significantly create variance in the QoIs are identified. Optimal parameter inference experiments, implemented prior to system-level model validation experiments, target the critical system parameters to learn more about the system earlier in the project lifecycle. Finally, given experimental data, Bayesian inference methods are utilized to systematically update the model. BMV is model-based and takes advantages of system-specific information. Furthermore, the validation process is iterative, and the outcome of each step informs the validation procedures for the subsequent step.

The first of two case studies is a passive spacecraft radiator. The radiator is a simple, notional system, and the primary objective of the case study is to demonstrate the basic aspects of the BMV methodology. Synthetic data are generated for the radiator case study. It is shown through BMV that analyses, test conditions, and decision-making during the validation process can differ from a conventional validation approach because more information is available to the engineer. By identifying and reducing uncertainty in the critical system parameter (the radiator's emissivity) early in the lifecycle, the case study shows that the final radiator's mass and volume could be lower than a conventional approach.

The second case study of the thesis is the REgolith X-ray Imaging Spectrometer (REXIS)

Solar X-ray monitor (SXM). In the SXM case study, the driving thermal system parameter, the maximum interface temperature with the spacecraft, T_{O-REx} , is relaxed to determine the maximum value to which T_{O-REx} could have been set using BMV. Of the three operational SXM requirements, uncertainty analysis reveals that the detector temperature is the driving QoI. Global sensitivity analysis reveals that the uncertainty in a conductance parameter most significantly creates uncertainty in the detector temperature. Both an optimized parameter inference experiment to reduce the conductance's uncertainty and a model validation experiment are implemented in a thermal vacuum chamber. A model calibration procedure, utilizing a Markov Chain Monte Carlo (MCMC) method, is used to systematically update the model parameters. Finally, once the model parameters are updated, a model discrepancy term is added to the model output to account for the persisting model inadequacy. The validated SXM model is used predictively to show that the maximum value of T_{O-REx} could have been set up to 10 °C warmer than the original upper limit.

The primary innovation of BMV is the improvement to the thermal model validation *process*. BMV is a rigorous, systematic validation methodology that can identify and reduce important model uncertainties in a spacecraft thermal system. BMV can increase knowledge of the system early in the project lifecycle when important design decisions are made by focusing research and testing efforts on critical system sensitivities. Because model uncertainties are better understood, margin, if needed, can be applied in a system-specific manner to address particular system or environmental uncertainties.

Thesis Supervisor: David W. Miller
Title: Professor of Aeronautics and Astronautics

Thesis Supervisor: Karen E. Willcox
Title: Professor of Aeronautics and Astronautics

Thesis Supervisor: Sheila E. Widnall
Title: Professor of Aeronautics and Astronautics

Thesis Supervisor: Rebecca A. Masterson
Title: Research Engineer

Acknowledgments

Beginning my Air Force career by completing a PhD in the MIT AeroAstro department was a dream, made a reality, by the UT Austin ROTC detachment. The Detachment 825 cadre spent countless hours making this opportunity possible. I am grateful for their mentorship and will draw from their leadership lessons for the rest of my career. “Be a leader, all the time...”

I would like to express my gratitude to the Air Force for my education at both the undergraduate and graduate levels—my Air Force training has enhanced my academic experience and makes me a more effective leader. I am excited to pay it forward. Thank you to AFIT and the MIT AFROTC unit for their support during the PhD program.

Thank you to my extraordinary thesis committee: Prof David Miller, Prof Karen Willcox, Prof Sheila Widnall, Dr. Rebecca Masterson, Prof Youssef Marzouk, and Mr. Ed Powers, for their guidance and commitment to this research. Prof Miller and Dr. Masterson welcomed me to the Space Systems Laboratory and personally guided me through the Masters and PhD programs. Thank you for believing that this was possible in three short years.

During my time at MIT, I worked on the REXIS project as a thermal engineer. Over the years, we have experienced the full set of emotions of a flight project, most importantly the extreme high of testing a system that you helped designed and seeing it work (mostly) as intended. I am indebted to Dr. Rebecca Masterson (REXIS Program Manager) and all of my fellow graduate student REXIS-ians (REXonians?). On such a small team, no individual system can be successful without the entire team—this was particularly true for the thermal system. Thank you for the opportunity to work on this project, which developed my thermal skills and the experience necessary to complete this thesis. Also, thank you to Mr. Ed Powers and Mr. Michael Choi who spent many hours working with the REXIS project and educating me on the thermal engineering process.

There were many student peers who both helped me navigate the PhD program and assisted in many technical problems in this thesis. Thank you to Farah Alibay for your mentorship, time looking over slides, talking about research, and working on class work. Thank you to Ryan Xun Huan for your assistance in formulating the Optimal Bayesian

Experimental Design problems and to Alex Gorodetsky for your advice in Gaussian Process modeling.

To my wife Andrea, I love you more than I can express through words. You have endless patience and kindness. Thank you for supporting me in all things.

To God Be The Glory

“But grow in the grace and knowledge of our Lord and Savior Jesus Christ. To Him be the glory both now and forever! Amen.” 2 Peter 3:18

Contents

List of Figures	13
List of Tables	17
1 Introduction	23
1.1 Thesis Primer	23
1.2 Background	24
1.2.1 Thermal System Engineering	25
1.2.2 Thermal Simulation Models	26
1.2.3 Traditional Treatment of Model Uncertainty	29
1.2.4 Model Validation	30
1.3 Motivation	32
1.3.1 Mission Costs Associated with Thermal Systems	32
1.3.2 Evaluation of Current Thermal Model Validation	36
1.3.3 Effect of Uncertainty Margin on Thermal System Resources	41
1.3.4 Answering the Model Validation Evaluation Questions	43
1.4 Literature Review	46
1.4.1 Model Uncertainty Propagation (UP)	46
1.4.2 Design of Experiments (DOE)	54
1.4.3 Model Calibration	59
1.4.4 Research Gap	64
1.5 Problem Statement, Research Goal, and Thesis Objectives	65
1.5.1 Problem Statement	65

1.5.2	Research Goal	66
1.5.3	Scope	66
1.5.4	Thesis Objectives	66
1.6	Thesis Roadmap	68
2	Bayesian-based Model Validation (BMV) Methodology	69
2.1	Step 1: Validation Problem Definition	71
2.2	Step 2: Uncertainty Propagation and Parameter Prioritization	73
2.3	Step 3: Experimental Goal Setting	78
2.4	Step 4: Design and Implementation of Experiments	80
2.5	Step 5: Experimental Model Calibration and Flight Model Update	84
2.6	Step 6: Validation Problem Documentation	87
3	Passive Spacecraft Radiator Case Study	89
3.1	Bayesian-based Model Validation (BMV)	89
3.1.1	Step 1: Validation Problem Definition	89
3.1.2	Step 2: Uncertainty Propagation and Parameter Prioritization—First Pass	92
3.1.3	Step 3: Experimental Goal Setting—First Pass	98
3.1.4	Step 4: Design and Implementation of Experiments—First Pass	98
3.1.5	Step 5: Experimental Model Calibration and Flight Model Update—First Pass	103
3.1.6	Step 2: Uncertainty Propagation and Parameter Prioritization—Second Pass	106
3.1.7	Step 3: Experimental Goal Setting—Second Pass	107
3.1.8	Step 4: Design and Implementation of Experiments—Second Pass	108
3.1.9	Step 5: Experimental Model Calibration and Flight Model Update—Second Pass	109
3.1.10	Step 2: Uncertainty Propagation and Parameter Prioritization—Third Pass	111
3.1.11	Step 3: Experimental Goal Setting—Third Pass	112

3.1.12	Step 6: Validation Problem Documentation	113
3.2	A Conventional Model Validation Approach	115
3.2.1	Analysis	115
3.2.2	Thermal Balance Test	117
3.2.3	Model Correlation	118
3.3	Comparison of BMV vs. A Conventional Model Validation Approach	120
4	REgolith X-ray Imaging Spectrometer (REXIS) Overview	125
4.1	Instrument Overview	125
4.2	Mission Thermal Environments	128
4.3	Solar X-ray Monitor Thermal Requirements	132
4.4	Solar X-ray Monitor Thermal Design Description	133
4.5	Summary	135
5	REXIS Solar X-ray Monitor (SXM) Case Study	137
5.1	Step 1: Validation Problem Definition	137
5.1.1	Validation Requirements	137
5.1.2	Physical Problem Documentation	138
5.1.3	Model Development and Documentation	139
5.2	Step 2: Uncertainty Propagation and Parameter Prioritization—First Pass	141
5.3	Step 3: Experimental Goal Setting—First Pass	151
5.4	Step 4: Design and Implementation of Experiments	152
5.4.1	Parameter Inference Experiment	152
5.4.2	Model Validation Experiment	164
5.4.3	Experimental Results	164
5.5	Step 5: Experimental Model Calibration and Flight Model Update	171
5.5.1	TEC Model Update	171
5.5.2	Parameter Calibration Overview	176
5.5.3	Calibration Parameter Selection: G_h Only	178
5.5.4	Calibration Parameter Selection: G_h and $G_{s,b}$	181
5.5.5	Calibration Parameter Selection: G_h and $G_{s,b}$, Relaxed $G_{s,b}$ Lower Bound	183

5.5.6	Calibration Parameter Selection: G_h , $G_{s,b}$ and G_b , Relaxed $G_{s,b}$ Lower Bound	186
5.5.7	Parameter Calibration (MCMC): G_h , $G_{s,b}$ and G_b , Relaxed $G_{s,b}$ Lower Bound	188
5.5.8	Parameter Calibration (MCMC): G_h , $G_{s,b}$ and G_b , Relaxed G_h Upper Bound and $G_{s,b}$ Lower Bound	192
5.5.9	Quantify Model Discrepancy	196
5.5.10	Flight Model Update	207
5.6	Step 2: Uncertainty Propagation and Parameter Prioritization—Second Pass	208
5.7	Step 3: Experimental Goal Setting—Second Pass	211
5.8	Step 6: Validation Problem Documentation	211
5.9	Comparison of BMV vs. A Conventional Model Validation Approach	212
6	Conclusion	217
6.1	Thesis Summary and Conclusions	217
6.2	Contributions	219
6.3	Future Work	222
7	Bibliography	225
A	Solar X-ray Monitor (SXM) Thermal Test Plan	237
A.1	Introduction	239
A.2	Engineering Model SXM Hardware Pictures	240
A.3	Test Objectives and Success Criteria	242
A.4	Personnel and Schedule	243
A.4.1	Personnel	243
A.4.2	Schedule	244
A.5	Test Program	245
A.5.1	Test Description	245
A.5.2	Test Configuration	246
A.5.3	Materials	246

A.5.4	Facility Requirements	247
A.5.5	Instrumentation	248
A.5.6	Data Requirement	252
A.6	Thermal Model Predictions	253
A.7	Red/Yellow Limits	254
A.8	Test Procedure	255
A.9	Documentation	258
A.10	Safety	260
A.10.1	Handling of SXM	260
A.10.2	General Safety Practices	260
A.10.3	Emergency Procedure	260
B	Solar X-ray Monitor (SXM) Thermal Test Data	261
C	Solar X-ray Monitor (SXM) Thermal Model Formulation	265
C.1	Lumped Parameter Formulation	265
C.2	Conduction	267
C.3	Radiation	269
C.4	Thermoelectric Cooler (TEC)	270
C.5	Model Fidelity and Important Assumptions	272

List of Figures

1-1	Spacecraft thermal environment	28
1-2	Model development process for complex system	30
1-3	Dry mass distribution of an average earth-orbiting spacecraft	33
1-4	TIRS instrument radiator	35
1-5	Comparison of flight data to temperature predictions for two spacecraft . . .	39
1-6	Comparison of flight data to model predictions for seven GSFC missions . .	40
1-7	ISS Heat Rejection System radiator	43
1-8	UQ toward validating system performance with respect to QoI	48
1-9	General global sensitivity analysis process	51
1-10	Comparison of model-based DOE methods	56
1-11	Thesis roadmap	68
2-1	BMV methodology overview	70
2-2	Mapping of physical problem, conceptual model, and simulation model . . .	72
2-3	Notional variances of parameter uncertainty distribution	74
2-4	BMV experimental goal setting	78
3-1	Physical problem for radiator case study	91
3-2	Conceptual model for radiator case study	91
3-3	Notional uniform distribution	93
3-4	Preliminary uncertainty analysis results for radiator	95
3-5	Local sensitivity analysis for isothermal radiator	96
3-6	Preliminary global sensitivity analysis results for radiator	97

3-7	Experimental utility, $U(\mathbf{d})$, contour plot of possible experiments	101
3-8	High fidelity Thermal Desktop radiator model	102
3-9	Thermal Desktop model solution for parameter inference experiment	103
3-10	Model calibration results for radiator coating emissivity	104
3-11	Contour plot of the joint distribution of β and ε	105
3-12	Uncertainty propagation results for radiator; updated coating emissivity . . .	107
3-13	Model discrepancy distributions from model validation experiment	110
3-14	Uncertainty analysis results following model validation experiment	111
3-15	Sensitivity analysis of heat flux, q , for radiator	114
3-16	Thermal Desktop results for thermal balance test	118
3-17	Model predictions of radiator temperature versus heat load	119
3-18	Timeline of BMV and conventional validation process	122
3-19	Illustration of BMV on general system over project lifecycle	123
4-1	Spectrometer design overview	127
4-2	SXM design overview	128
4-3	Isometric and side views of REXIS instrument on OSIRIS-REx	129
4-4	Solar distance versus mission time for entire 7-year mission	129
4-5	Temperatures of Bennu plotted versus longitude and latitude	131
4-6	Amptek AXR SDD package	134
5-1	Nominal thermal predictions for SXM	144
5-2	Joint cumulative distribution function for T_{sdd} and T_{O-REx}	146
5-3	Histograms and CDFs of T_{sdd} conditioned on T_{O-REx}	148
5-4	Probability of satisfying SXM requirements versus T_{O-REx}	149
5-5	Main effects global parameter sensitivities of SXM model	151
5-6	Convergence plot for experimental utility, $U(\mathbf{d})$	158
5-7	Histogram of experimental utilities and scatter plots of utilities	160
5-8	Heatmap of experimental utility for T_{O-REx} versus V_{TEC}	161
5-9	SXM sensor correlation coefficients	163
5-10	Grid of all SXM thermal test phases	165

5-11	T_{sdd} versus V_{TEC} various interface temperatures	166
5-12	T_{sdd} versus i_{TEC} for various interface temperatures	167
5-13	Comparison of Amptek performance estimates with SXM TEC data	168
5-14	T_{sdd} versus TEC power dissipation for various interface temperatures	169
5-15	Temperature difference between the SDD housing and SXM interface	170
5-16	Temperature difference between the SDD housing and the SXM housing	171
5-17	Surface fit for SDD temperature for various V_{TEC} and T_h	175
5-18	Surface fit for the TEC current draw for various V_{TEC} and T_h	175
5-19	Model calibration process overview	176
5-20	Notional prior or posterior predictive check	177
5-21	Prior predictive check for test phase T36; G_h	180
5-22	Prior predictive check for test phase T36; G_h and $G_{s,b}$	182
5-23	Bottom view of SXM housing	184
5-24	Prior predictive check for test phase T36; G_h and $G_{s,b}$ relaxed	185
5-25	Prior predictive check for test phase T36; G_h , $G_{s,b}$ relaxed, G_b	187
5-26	Plot of adaptive MCMC chain pushing up against the upper limit of G_h	191
5-27	Intermediate posterior histograms and scatterplots for calibration parameters	192
5-28	Plot of adaptive MCMC chain showing good mixing after initial burn-in	193
5-29	Final posterior histograms and scatterplots for calibration parameters	194
5-30	Posterior predictive check for test phase T36	195
5-31	Posterior predictive check for all 43 test phases	196
5-32	Comparison of GP training points and predictions	200
5-33	GP model section for bracket model discrepancy	202
5-34	GP model section for SDD housing model discrepancy	203
5-35	SDD discrepancy samples and histogram	204
5-36	Posterior predictive check for test phase T36, both with/without $\delta(\mathbf{x})$	206
5-37	Probability of satisfying SXM requirements versus T_{O-REx}	210
5-38	Illustration of BMV on REXIS SXM over project lifecycle	216
A-1	SXM structure and component overview	239

A-2	Top view of SXM interface plate	240
A-3	SXM structure showing RTD on SDD housing	241
A-4	SXM structure with all SXM RTDs	241
A-5	Final view of SXM test article with MLI blanket	242
A-6	SXM test grid	245
A-7	SSL thermal vacuum chamber	248
A-8	Notional SXM thermal test electronics/control configuration	249
A-9	SXM RTD placement	250
A-10	Model predictions for the mission Cruise Phase cold case	253
A-11	Model predictions for the mission operational hot case	254
C-1	Lumped parameter concept	266
C-2	1D mesh with uniform discretization	268
C-3	SDD temperature versus voltage for SXM TEC	270
C-4	SDD temperature versus current for SXM TEC	271
C-5	Applied voltage versus current draw for SXM TEC	272
C-6	SXM node assignments for the lumped parameter model	273
C-7	Connectivity matrix for SXM model	274
C-8	Notional SXM MLI heat flow diagrams of the MLI outer cover	275
C-9	Examination of the absorbed heat through layers of SXM MLI	278

List of Tables

1.1	Spacecraft thermal control component examples	26
1.2	Summary of flight thermal statistical data	38
1.3	Nominal values for sample radiator calculation	42
1.4	Examples of environmental test condition guidance	59
1.5	Comparison of state of the art and conventional methods	65
2.1	Observability for parameter inference experiment	83
3.1	Nominal parameter values for sample radiator problem thermal model	92
3.2	Initial parameter uncertainty characterization	93
3.3	Experimental conditions for model validation experiment	109
3.4	Summary of uncertainty analysis results	112
3.5	Initial model parameters for conventional analysis of radiator	116
3.6	Final parameters for conventional analysis of the radiator	120
4.1	Summary of REXIS thermal analysis cases	132
4.2	SXM steady state component temperature limits	133
5.1	Temperature limits for validation requirements	138
5.2	SXM model nominal parameter values	140
5.3	SXM model parameter prior uncertainty distributions	142
5.4	Thermal conductance design guidelines	143
5.5	Table of SXM parameter inference experimental conditions	155
5.6	Calibration parameter prior uncertainty distributions for MCMC	188

5.7	GP model hyperparameter regressed values	199
A.1	SXM component temperature limits	243
A.2	Personnel schedule for monitoring test chamber	244
A.3	List of RTDs for thermal test	251
A.4	SXM survival temperature limits	255
A.5	SXM operational temperature limits	255
B.1	Stabilized RTD readings for test phases T1 through T43	262
B.2	Temperature of SDD for test phases T1 through T43	263
C.1	Parameter values for SXM MLI sensitivity analysis	276

Glossary

aleatory uncertainty: model uncertainty due to intrinsic randomness [55]

complex system: a system with global emergent dynamics resulting from its many interacting elements [18]

epistemic uncertainty: model uncertainty due to lack of knowledge [55]

model calibration: the use of experimental observations of a physical system to learn about the parameters of the model [26, 27]

model correlation: the process where one gains modeling insight by observing differences in comparable quantities between model and test [26, 27]

model inadequacy: the inherent inability of the model to reproduce reality [60]

model validation: process of confirming a model is an adequate representation of the physical system and is capable of predicting the systems behavior accurately with respect to the requirements within the domain of the intended application of the model [20, 21]

model verification: process of ensuring the model implementation represents the conceptual description of the model and the model's solution [20, 21]

parameter: a quantity that determines the characteristics of a model, including external inputs to the model that are not contained in the system model itself

sensitivity analysis: the determination of how a model's parametric uncertainties contribute to its output uncertainty [43]

simulation model: mathematical representation of a conceptualized model of the real system through which model parameters and operations yield predictions for the physical response of the system

thermal balance test: dedicated test phases simulating flight conditions to gather steady state temperature predictions to verify that the thermal control system meets requirements and correlate thermal models [4, 22, 24]

thermal system: system responsible for maintaining all system component temperatures within allowable limits for all modes of operation over the entire domain of relevant mission environments [4, 5]

thermal vacuum test: performance verification of spacecraft components through functional testing during a number of hot and cold cycles at prescribed test levels in vacuum [4, 22, 24]

uncertainty analysis: the determination of a model's output uncertainty due to its uncertain parameters and its inadequacy [41]

uncertainty quantification: the quantitative characterization and reduction of uncertainty, including forward uncertainty propagation (forward problem) and model calibration (inverse problem) [17]

Nomenclature

Mathematical Definitions:

$E[\cdot]$ = expectation

Q = Quantities of Interest (QoI)

R = correlation coefficient

S_{Lj} = local sensitivity for j^{th} parameter

S_j = main effect global sensitivity for j^{th} parameter

S_{Tj} = total effect global sensitivity for j^{th} parameter

$U(\cdot)$ = utility

$V[\cdot]$ = variance

\mathbf{d} = experimental conditions

$p(\cdot)$ = probability density

\mathbf{x} = model parameters

\mathbf{y} = model output

\mathbf{z} = experimental data/observations

γ = calibration parameters

$\delta(\cdot)$ = model discrepancy

ζ = true physical process

$\eta(\cdot)$ = simulation model mapping parameters to output

θ = experimental parameters of interest

λ = Gaussian Process characteristic length

μ = mean value

σ = standard deviation

σ_0 = Gaussian Process output variance

Physical Definitions:

A = surface area

C = heat capacity

G = conductance

K_p = control gain

Q = heat load

R = electrical resistance

R_t = thermal resistance

T = temperature

V = voltage

c_p = specific heat

e = process error

i = current

k = conductivity

m = mass

q = heat flux

t = time

α = absorptivity

ε = emissivity

ε^* = multi-layer insulation (MLI) blanket effective emissivity

ϵ_m = observation error

θ = incidence angle

ρ = density

σ = Stefan-Boltzmann constant

ϕ_s = solar flux

Chapter 1

Introduction

This chapter provides introductory material for this research. Section 1.1 is a thesis primer, Section 1.2 provides background information, and Section 1.3 explains the motivation for the work. Section 1.4 reviews the current relevant literature in the area of model validation, and Section 1.5 shows the thesis objectives for this research. Finally, the thesis roadmap is given in Section 1.6.

1.1 Thesis Primer

The scope of space-based missions is significantly driven by cost. The cost of a particular mission is highly correlated to its resource consumption (e.g., mass or volume). Furthermore, resource-related costs are incurred both on the system itself and the launch vehicle. For example, the NASA and Air Force Cost Model (NAFCOM) [1] is a parametric cost estimation model based on historical data from previous space projects. In NAFCOM, mass is a significant cost driver in the subsystem-level parametric equations. Massive and/or voluminous spacecraft require large, expensive rockets to reach orbit. Launch vehicle costs persist as a significant contributor to overall mission cost. Despite the promise of next-generation launch vehicles, today we are limited to costs ranging from \$2,000 to \$10,000 per pound to low-Earth orbit [2, 3]. Process costs (e.g., system analyses, technology development, and verification and validation) are also highly correlated to mission costs. The time and organizational resources needed to develop and operate a system comprise a significant portion

of overall mission cost. Because simulation model predictions are used to allocate system resources and develop a system over the entire project lifecycle, it is important to achieve high confidence in spacecraft simulation models as early as possible. An *improvement* to the model validation process means not only improving the *form* of the system post-validation but the *processes* associated with model validation itself.

In spacecraft design, thermal control systems are developed throughout the project lifecycle and can significantly impact spacecraft form-related and process-related cost. This research focuses on improving the model validation process for spacecraft thermal systems. Thermal systems are primarily responsible for maintaining all system component temperatures within allowable limits for all modes of operation over the entire domain of relevant mission environments [4, 5]. Thermal models are used to predict performance (usually temperatures and heat flows) of the thermal system during flight. Based on these predictions, system resources, including power, volume, and mass, are allocated to satisfy requirements.

This research introduces a Bayesian-based Model Validation (BMV) methodology to improve the model validation process for spacecraft thermal systems. BMV combines the methodologies from the fields of Uncertainty Quantification (UQ) and Design of Experiments (DOE) to validate thermal models. The BMV methodology was developed with the long term goal of improving the accuracy of on-orbit predictions, making the model validation process more rigorous and systematic in addressing model uncertainties, and decreasing the resources required to meet thermal system requirements. BMV is implemented in two case studies: a passive spacecraft radiator and on the REgolith X-ray Imaging Spectrometer (REXIS) instrument solar X-ray monitor (SXM).

1.2 Background

This section introduces background information for the validation of thermal simulation models. First, an overview of thermal system engineering is discussed to examine typical design practices and conventions. Next, a description of thermal simulation models is provided. Finally, the treatment of model uncertainty and simulation model validation is presented in a general format to introduce how complex models are developed throughout the project

lifecycle.

1.2.1 Thermal System Engineering

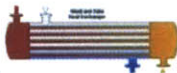
Thermal system engineering begins early in a project's lifecycle with preliminary design and analysis efforts. The early stage of design is critical because it is when the design concept develops. As the system concept matures, thermal engineers take inputs from other disciplines (e.g., structures and avionics) to develop a preliminary design. Simple analysis models are used to evaluate feasibility and allocate resources to the thermal system. As the design matures, high fidelity models are developed to predict the response of the system to its mission environments. The models are correlated with results from thermal testing to produce the final mission temperature predictions. [4, 5]

There are two main thermal control component classifications for spacecraft: active and passive. Active control systems regulate the thermal behavior of a component or subsystem by monitoring its behavior and providing control when required. Passive thermal control systems regulate the physical response of the system via static design elements such as material properties, coatings, and multi-layer insulation (MLI) blankets. Passive components cannot be changed once on-orbit and do not adapt to system or thermal environment conditions to provide thermal control. The selection of active and passive components is system-specific and depends on the thermal system requirements and configuration. For example, although passive control elements can have lower mass and cost [4], active thermal control components can have significant analysis or system performance benefits (e.g., louvers can decrease heater power).

Components selected for thermal control vary widely, ranging from those used to isolate certain components in conduction and radiation to those used to directly transfer heat within the system. Table 1.1 illustrates the spectrum of thermal control components available to engineers when designing a thermal system. The design spectrum includes components commonly implemented on satellites [4, 6] and emerging thermal technologies (e.g., electrochromics) [7]. The components in Table 1.1 are divided into the active and passive control categories and are further subdivided by how the component is typically used within the system: for isolation, heat transfer, or heat rejection to deep space (radiators). For

example, a thermal strap is a passive heat transport component used to conduct heat from a source to a sink, whereas a fluid loop is an active component that uses the fluid to transfer heat to different parts of the system. In order to achieve a thermal design, engineers select surface finishes and components to facilitate the desired heat transfer. At the most basic level, thermal design consists of sizing radiators for the hottest environments and sizing heaters for the coldest environments [8]. Radiators reject unwanted waste heat to space, and heaters are strategically placed on components and powered by the spacecraft to warm components that are nominally too cold. Generally, thermal systems are cold-biased because it is physically easier and more reliable to warm than cool components.

Table 1.1: Spacecraft thermal control component examples

Thermal Control Components	Passive Control	Active Control
Isolation	 Multi-layer Insulation  Low conductivity material	 Electrochromics
Heat Transport	 Heat Pipe  Thermal Strap	 Mechanically-pumped Fluid Loop  Heat Exchanger
Radiators	 Structural radiator  Body-mounted	 Louver  Fluid Loop

1.2.2 Thermal Simulation Models

Feasibility studies and analyses begin as soon as preliminary designs are established through the use of thermal simulation models. A simulation model is a mathematical representation of a conceptualized model of the real system through which model parameters and operations yield predictions for the physical response of the system. The goal of thermal models is to estimate the solution to the general heat transfer equation, as shown in Equation (1.1):

$$\rho c_p \frac{\partial T}{\partial t} = \nabla \cdot k(\nabla \cdot T) + Q(T, t) \quad (1.1)$$

where ρ is density, c_p is specific heat, k is the conductivity tensor, $Q(T, t)$ is the source heat term, t is time, and $T=T(x, y, z, t)$ is the spatial and temporal temperature variation. The initial conditions and boundary conditions are needed to fully solve Equation (1.1). Model parameters are quantities that determine the characteristics of the model, including external inputs to the model that are not contained in the system model itself (e.g., solar flux or thermal resistance between two components). Parameters include geometries of the system, component connectivity, and material properties that map to the k , ρ , and c_p terms.

Both conduction and thermal radiation are captured in Equation (1.1). The $\nabla \cdot k(\nabla \cdot T)$ term captures the conduction through the system. $Q(T, t)$ is both the heat transfer within the system and the heat transfer between the system and its environment. Components of $Q(T, t)$ can be categorized as shown in Equation (1.2) [9]:

$$Q(T, t) = Q_{ext} + Q_{pow} + Q_{rad} \quad (1.2)$$

where Q_{ext} captures external heating, Q_{pow} is the power dissipations of components, and Q_{rad} is radiation within the system. The terms Q_{pow} and Q_{rad} represent physics associated with the model itself. Radiation within the system is a function of the geometry. For example, the view factor from one surface to another directly affects the radiation heat transfer between the surfaces. Q_{ext} refers to the heat fluxes imposed onto the system by the space thermal environment. Although a given space mission is exposed to a thermal environment that yields unique external heating factors, there is a general thermal environment that applies to most spacecraft, as shown in Figure 1-1. Heat inputs come from three major sources: direct sunlight, radiation in the infrared spectrum from nearby planetary bodies (e.g., a planet or an asteroid), and sunlight reflected by nearby planetary bodies (i.e., albedo). The primary method of heat rejection for spacecraft is radiation to deep space. Often, Q_{ext} is given by Equation (1.3):

$$Q_{ext} = Q_{solar} + Q_{alb} + Q_{IR} \quad (1.3)$$

where the heat fluxes are Q_{solar} due to direct sunlight, Q_{IR} due to light in the infrared spectrum from a nearby planetary body, and Q_{albedo} due to reflected, or albedo, light from a nearby planetary body. Given the thermal environment, component power dissipations, and system geometry parameters, $Q(T,t)$ is completely specified. Once all parameters, initial conditions, and boundary conditions are defined, the solution to Equation (1.1) for the system can be approximated via thermal model(s).

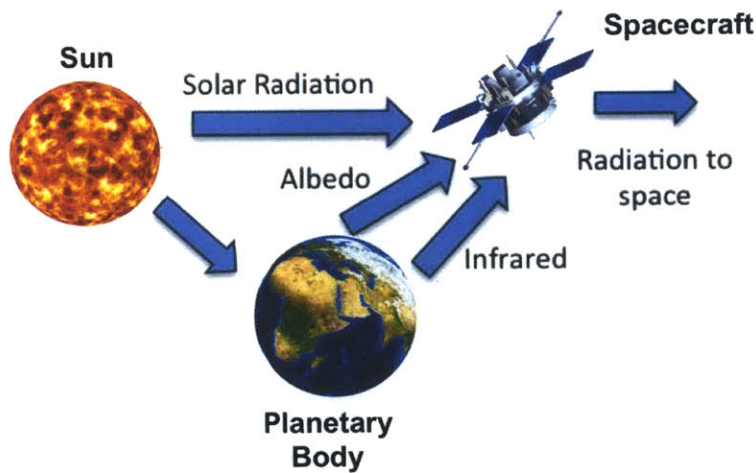


Figure 1-1: Spacecraft thermal environment [4]. In general, there can be multiple planetary bodies (e.g., an asteroid and a planet).

The fidelity of thermal models depends on the accuracy required of the model (derived from the requirements) and the thermal system complexity. Fidelity of the models often increases over the project lifecycle as design details emerge. Early in the design life cycle, preliminary analytical models [10] and lumped parameter models [11, 12] are used to evaluate system concepts, define thermal interfaces, and identify critical sensitivities. Preliminary models explore the feasibility of early designs and their impact on system resources. Because the system is immature, accounting for important model uncertainties (e.g., component power dissipations) is critical for ensuring conservative analyses. Experience and engineering judgment determine how the preliminary models are used and when to transition to higher fidelity models. Higher fidelity modeling is almost exclusively performed by commercially available software packages that offer state of the art techniques to numerically approximate the solution to Equation (1.1) [13]. While finite element methods are sometimes used [4],

the most commonly used commercial thermal model computer code is the finite difference code SINDA [14]. SINDA is commonly interfaced through the NASA standard Thermal Synthesizer System [15] or Thermal Desktop [13, 16]. Nearly all thermal models, regardless of the model fidelity and software used, generate predictions based on the parameters and mission environment.

1.2.3 Traditional Treatment of Model Uncertainty

Model uncertainty is uncertainty in aspects of a simulation model that results in uncertainty in the model's predictions. Parametric uncertainties are those uncertainties associated with not knowing the true model parameter values. Model structure uncertainties result in model error due to limitations with how the physical processes within the system are modeled (e.g., omitted physics, discretization of components or interfaces, or simplifying assumptions). Uncertainty quantification (UQ) is the quantitative characterization and reduction of uncertainty, including forward uncertainty propagation and model calibration [17]. Complete UQ requires quantification of parametric and model structure uncertainties. UQ is critical for model validation because the accuracy of a model in predicting the behavior of a physical system depends on the model's uncertainty.

Currently, a complete quantification of model uncertainties is typically not performed in the development of spacecraft thermal systems. Thermal systems are considered complex systems, which are systems with global emergent dynamics resulting from its many interacting elements [18]. The model development process of a typical complex system is depicted in Figure 1-2 [19]. A serial progression is shown, but the dashed arrows indicate that the model development processes often occur in parallel. First, the model is built based on the design of the real world system. Once the model is built, verification and validation ensure that the model was built to correctly, is in accordance with its intended purpose, and can adequately predict the real system's behavior. Once the model is finished, the remaining model uncertainties are quantified, and then the model is put into application. In most cases, uncertainties are not quantified upstream of a model. Instead, uncertainty margins are often applied to model output (i.e., downstream of the model) based on design standards and expert opinion [8] to account for unquantified parametric and model structure uncertainties.

Although not common, uncertainties are sometimes captured upstream of the model and are propagated through the model to the output. Even when uncertainties are captured upstream, uncertainty quantification usually focuses on parametric model uncertainties and does not address model structure uncertainties. The neglect of model structure uncertainties can cause important discrepancies between the model and the physical system. A systematic procedure for addressing model uncertainties upstream of the model is needed to improve the development process in Figure 1-2.

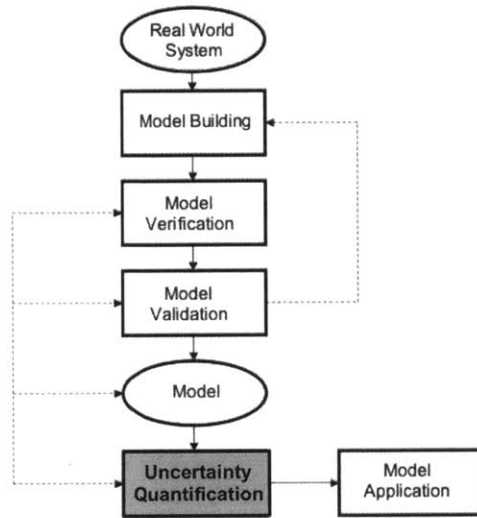


Figure 1-2: Typical model development process for a complex system. Figure modified from [19, Fig. 1-2].

1.2.4 Model Validation

Model “correctness” is addressed through verification and validation [20]. Model verification is the process of ensuring that the model implementation is consistent with the model’s output and represents the conceptual description of the model. Model validation is the process of confirming a model is an adequate representation of the physical system and is capable of predicting the systems behavior *accurately with respect to the requirements* within the domain of the intended application of the model [20, 21]. It is generally not possible to prove a simulation code correct [21], but industry standard software packages (e.g., SINDA and Thermal Desktop) are verified to a high confidence level before being put into use. The verification of a specific model’s implementation is primarily achieved through experience,

expert review, and a comparison with analytical solutions [20]. Once the model is deemed a faithful representation of what was intended, verification is complete and validation becomes the primary focus. The focus of this research is on improving the model validation process and quantifying the uncertainties associated with the validated model's output.

In the development of spacecraft thermal systems, rules and guidelines are in place to verify the system design and validate the models. Guidance includes processes for thermal model development and testing (at prototype, subsystem, and system level) for both military programs [22, 23] and NASA Goddard programs [24, 25]. Analyses focus on worst-case scenarios that are built for the hottest and coldest thermal environments in each mission phase. Thermal design margins are applied directly to the worst-case temperature predictions to account for model uncertainty. Design margins are consistent with Figure 1-2 because they are applied downstream of the model and account for both parametric and model structure uncertainties. For passive systems, military programs apply a recommended 17 °C margin (which may be reduced to 11 °C after model validation) [22] and many NASA programs must demonstrate a 5 °C margin [25] (though can be raised to 10 °C based on the specific application [8]). For active thermal control elements, heat load margin may be used in lieu of temperature margin.

The guiding philosophy for design verification testing is “test like you fly, and fly like you test” [25]. Testing in an evacuated chamber with heat sources to emulate mission environment fluxes is considered the best possible simulation of the space thermal environment. Thermal vacuum and balance tests are commonly used experimental techniques to validate a thermal system design and model. Thermal vacuum testing is performance verification of spacecraft components through functional testing during a number of hot and cold cycles at prescribed test levels. Thermal balance tests are dedicated test phases simulating flight conditions to gather steady state temperature predictions to verify the thermal control system and correlate thermal models [4, 22, 24]. From experimental data, models are calibrated and correlated. Model calibration is the use of experimental observations of a physical system to learn about the parameters of the model; model correlation is the process to gain model insights by observing differences in comparable quantities between model and test [26, 27]. The final thermal system design is realized only after models are correlated to test results

and predict that requirements are met with adequate margin. If correlated models predict that requirements are not satisfied, additional resources can be allocated (e.g., radiators made larger) to achieve required temperatures with margin. A design change late in the project lifecycle due to unexpected thermal system performance during testing (e.g., power dissipations significantly larger than expected) is expensive and can have significant schedule impacts.

1.3 Motivation

Long term, improving the spacecraft thermal model validation process can result in a reduction in form-related and process-related mission costs. This section will first discuss why the thermal system is an important component of a spacecraft's overall cost. Significant mission costs are associated with the *form* of the spacecraft and *processes* involved in its development. Next, evidence is presented that suggests current model validation practices can result in overly conservative on-orbit predictions [8, 28, 29, 30, 31]. As a result of the conservatism, thermal systems are intentionally overdesigned and consume additional mass, volume, and power. Furthermore, model inaccuracies are seen in some systems where a conventional model validation process did not reveal inadequacies with the model, analyses, and/or testing. This section will conclude by introducing and answering model validation evaluation questions to determine the effectiveness of current validation practices.

1.3.1 Mission Costs Associated with Thermal Systems

Reductions in mission costs associated with the system's resource consumption (i.e., form) and processes required to develop the spacecraft are possible by improving the thermal model validation process. The goal of this section is to explain the coupling between thermal systems and mission costs. Form-related costs are discussed first, followed by a discussion of process-related costs.

Often, thermal systems are thought to not drive the consumption of spacecraft resources relative to other systems (e.g., structures). Consequently, resource consumption reduction efforts (e.g., design optimization to minimize mass) tend to focus less on thermal systems

compared to other systems. As an example of how the thermal system impacts resources at the spacecraft level, Figure 1-3 shows the results of a study [32] that examined the composition of an average spacecraft's mass. The study found that the thermal system can comprise approximately six percent of a spacecraft's dry mass. The study in Figure 1-3 contains data from diverse mission types, including the Global Positioning System, communications satellites, and science missions. At face value, statistics such as those shown in Figure 1-3 seem to indicate that thermal systems are of second-order importance with respect to a spacecraft's overall resources (in this case mass is shown but similar statistics can be shown for power and volume). However, there can be significant physical couplings between the thermal system and other spacecraft systems (i.e., systems are not independent). Although Figure 1-3 shows that six percent of mass is *only* thermal system mass, there is mass that exists in other portions of the pie chart *for thermal reasons*. For example, a spacecraft bus structure receives design inputs from thermal analysis and also serves as a primary mechanism for heat transfer within a system. A component can be both a structural element and a significant thermal path of a spacecraft [9]. The thermal system's impact on spacecraft resources can be larger than six percent when considering the interconnectivity to other spacecraft systems.

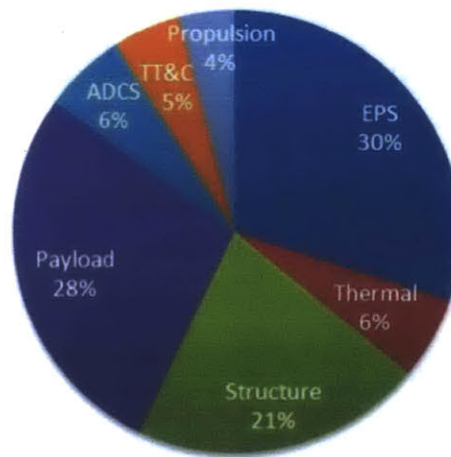


Figure 1-3: Dry mass distribution of an average earth-orbiting spacecraft. Figure from [32, Fig. 1].

Furthermore, system-specific factors such as those systems with significant thermal control challenges, those that are highly resource-constrained systems, and those that carry large uncertainty margins due to risk aversion are not captured in Figure 1-3. Such systems

often require more resources to achieve thermal requirements. For example, the James Webb Space Telescope (JWST) sun shield, only a portion of the thermal system, is approximately 12 percent of the total system mass and must be deployed in the space environment because its volume is too big to be open in the launch vehicle fairing [33]. Thermal control drives the JWST system design. For highly resource constrained systems (e.g., small satellites or payload instruments), small decreases in resource consumption are very beneficial because the power, volume, and mass budgets are very restrictive. Although the thermal system may comprise a small portion of the overall resources, design to minimize a resource on a highly resource constrained system (e.g., volume of instrument radiator) should not be overlooked. The REXIS instrument, discussed in Chapter 4, is an example of a resource-constrained instrument.

The TIRS instrument on the Landsat Data Continuity Mission [34] is a recent example of how thermal model validation can affect cost associated with resource consumption. On TIRS, an aggressive schedule, a need to procure long-lead items early, and large heat load uncertainties led to a risk reduction philosophy that emphasized large thermal design margins. In particular, the TIRS thermal team devoted significant efforts to characterizing the heat loads into the cryogenic subsystem via analysis, hand calculations, and a complex prototype-level test¹. Once the flight design was tested in thermal vacuum, better-than-expected-performance of the cryocooler led to considerable margin on the cryocooler radiator. Before launch, $\approx 60\%$ of the radiator's surface area was covered with MLI blankets to ensure that components did not violate minimum temperature limits, as shown in Figure 1-4. The excess cryocooler radiator surface area on TIRS is not only increased mass, volume, and heater power attributed to the thermal system, but the effect of the excess resources propagates through to the resources used by other subsystems (e.g., the TIRS structure must support a radiator with significantly larger mass than is needed). Reduction in the resource consumption of thermal systems is an important component of reducing a spacecraft's overall use of mass, power, and volume and thus, reducing form-related costs.

Although form-related mission costs are sometimes easier to quantify, process-related costs can be just as, if not more, significant. Process cost refers to the cost associated with

¹Veronica Otero, GSFC Thermal Engineering Associate Branch Head. Personal Interview. April, 2014.

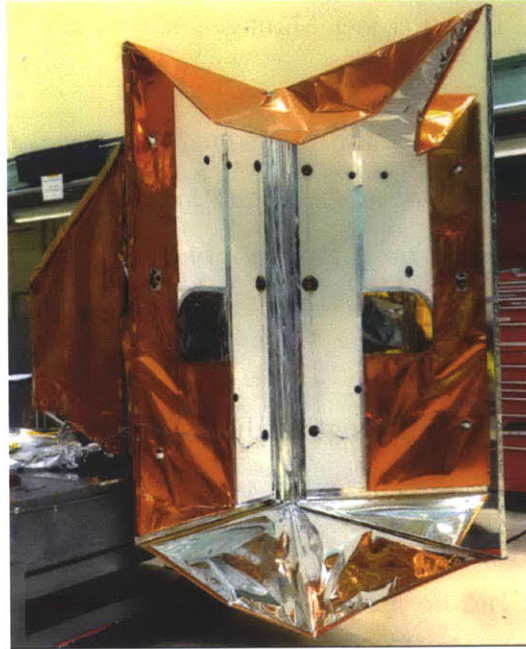


Figure 1-4: TIRS instrument radiator with multi-layer insulation blankets covering $\approx 60\%$ of radiator surface area [35]

spacecraft development and operation such as technology development, system analyses, system verification and validation, and on-orbit mission control operations. To illustrate the significance of *anticipated* process-related costs for an interplanetary mission, the operations and data analysis costs comprised approximately \$175 million of the \$680 million budget of the Mars Reconnaissance Orbiter [36]—a significant portion of the overall MRO mission budget. Model-based design and model validation play an important role in spacecraft development and operation processes and can adversely affect missions when performed inadequately.

For example, insufficient instrument-level thermal model validation led to high process-related costs on the Juno mission immediately after launch. Juno was launched in 2011 and is an interplanetary mission that accomplishes its science objectives in a polar orbit about Jupiter [37]. Soon after launch, two payload instruments began encountering warmer temperatures than expected. A conventional model validation approach did not reveal inadequacies with the thermal model, analyses, thermal balance testing, and communication of results. Extensive analyses and test efforts were made after launch to detect and mitigate

the problem. Janis Chodas, Juno Project Manager, stated²:

“An improved understanding of the Juno instruments’ thermal interactions with the spacecraft, and better instrument thermal model validation, would have decreased the amount of post-launch investigative work that the Juno team had to do when some instruments encountered thermal problems inflight.”

The instrument problems incurred during the Juno mission are just one example of the importance of model validation in the context of process costs. An improvement to the model validation process can result in not only reducing form-related costs but also a reduction in process-related costs, which can be just as if not more significant.

1.3.2 Evaluation of Current Thermal Model Validation

Given the high demand for mission success and resource efficiency, it is prudent to once again review model validation practices for current systems [38]. While Section 1.2 provides high-level information and context for the thermal model validation process, we are left with the question: *how effective are current thermal model validation practices?* Since model validation requires a comparison of the modeling world with the real world, we can evaluate our validation processes by looking at final thermal model predictions versus actual flight data. The following model validation evaluation questions arise:

- How close are post-validation model predictions and flight temperature data?
- Are there trends in the model predictions and/or data that suggest an opportunity to improve the validation process?
- Are design uncertainty margins appropriately conservative? Is there a better way to quantify and reduce the uncertainty?
- Why buck the status quo?

²Janis Chodas, Juno Mission Project Manager. Personal Interview. November, 2013.

The comparisons of thermal model predictions and flight data lead to answers for each question. The answer to each is shown in Section 1.3.4.

Current thermal model validation practices, relatively unchanged over several decades, have a long history of leading to successful space missions. However, a comparison of on-orbit temperature data and model predictions reveals limitations with the validation process. In the late 1960-70s, initial comparisons were made between thermal model predictions, thermal vacuum test data, and flight temperatures [30, 31]. Results showed that by correlating a model to test results, the standard deviation to flight data reduced from 9 °C to 5.6 °C [28]. Based on these early examinations of correlated models and flight data, the temperature margins currently in place for military programs (see Section 1.2.4) were adopted.

In 2006, Welch [28] sought to revisit the military standards [22, 23] established in the 1970s by looking at more recent programs. Thermal model predictions and on-orbit temperature data from different space programs were analyzed statistically. The study includes spacecraft from DOD programs, ESA programs, an Iridium satellite, and the NASA Thermosphere Ionosphere Mesosphere Energetics and Dynamic (TIMED) mission. The results of the study are shown in Table 1.2. The second column in the table indicates the mean difference between the model predictions and temperature data, plus/minus two standard deviations. The third column shows the derived thermal uncertainty margin to capture 95% of the flight temperatures and model prediction discrepancies. The third column is derived from the second column. DOD Programs A and B are programs from the 1980s and serve as a basis for comparison to the more recent programs shown.

The main takeaway from Table 1.2 is that the data suggest that the thermal models are not accurately predicting the flight temperatures for all missions. The derived thermal uncertainty margin refers to the error bounds on the mean of the predictions required to capture the flight temperatures. On average, the derived uncertainty margin to meet the 95% threshold is above 10 °C. For some programs, exceeding a derived uncertainty margin of 10 °C was due to a mean that was far from zero (e.g., NASA TIMED) and for others it was due to a large variance about a near-zero mean (e.g., DOD Program D). Between DOD Programs A and B and more recent missions (from the late 1990s and early 2000s), there is no obvious accuracy improvement even though modeling software tools have greatly improved

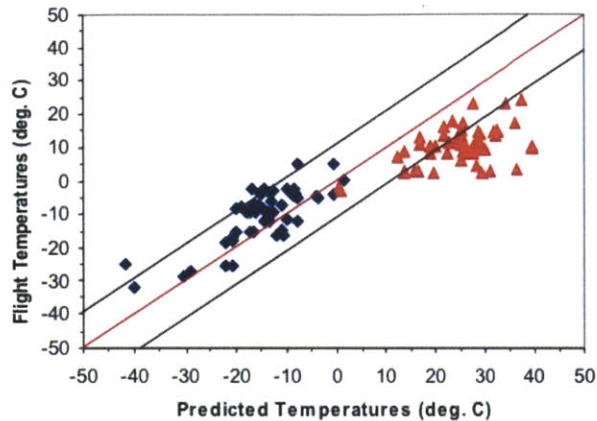
Table 1.2: Summary of flight thermal statistical data. Table from [28, Table 4].

Flight Program	Model vs. Flight Temperature Difference $\mu \pm 2\sigma$ (°C)	Derived Thermal Uncertainty Margin (°C)
DOD Program A	+5.9 ± 10.0	15.9
DOD Program B	+1.3 ± 8.4	9.7
Iridium	-3.3 ± 11.9	15.2
NASA TIMED	+4.3 ± 11.2 (cold) -13.5 ± 15.6 (hot)	15.5 29.1
DOD Program C	+6.6 ± 9.0	15.6
DOD Program D	+0.5 ± 10.0	10.5
ESA Italsat-1	+2.2 ± 7.8	10.0
ESA Italsat-2	-1.5 ± 7.7	9.2
ESA SAX	-3.1 ± 6.6	9.7

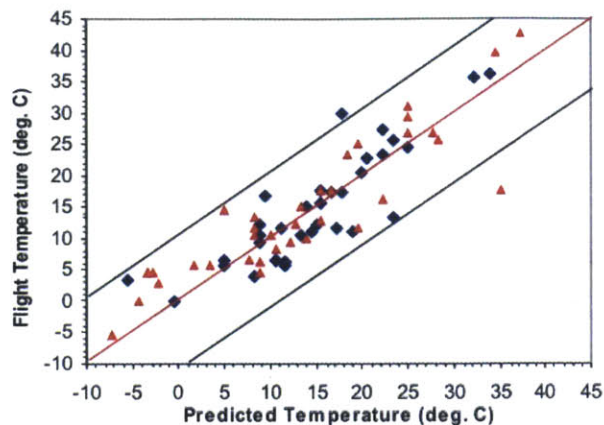
over the last two decades (i.e., modeling tool capabilities are not driving the accuracy of thermal models).

However, Table 1.2 is not a complete story. In terms of mission success, inaccurate models are not necessarily bad. As long as temperature requirements are satisfied, the mission can still be successful. To illustrate this point, Figure 1-5 shows the predictions versus flight data for the NASA TIMED and DOD Program D missions from Table 1.2. Red triangles correspond to the hot cases, and blue diamonds correspond to the cold cases. The center red line is the point of reference marking zero discrepancy between model prediction and flight temperature. The outer blue lines are the 11 °C model uncertainty margin for military programs.

Figure 1-5 highlights two different explanations for the uncertainty margin thresholds in Table 1.2. Figure 1-5a shows the NASA TIMED mission flight data near beginning of life. In this case, the thermal model was significantly biased (i.e., the mean of the predictions is shifted, for both the hot and cold cases in a stacked, worst-case fashion). In most cases, cold environment data were warmer than predicted temperatures, and hot environmental data were colder than predicted temperatures. The derived uncertainty margin to account for the model-data discrepancy is large due to the model bias, but the direction of the bias is conservative for both the warm and cold cases. In the NASA TIMED case, the bias for the hot cases (the difference between the hot case data mean and the red line) is approximately 14 °C. If the 11 °C uncertainty margin was used for design, the thermal system is



(a) NASA TIMED



(b) DOD Program D

Figure 1-5: Comparison of flight data to temperature predictions for two spacecraft. Figures from [28, Fig. 4 and Fig. 6]. Red triangles indicate hot cases, and blue diamonds indicate cold cases.

successful in terms of meeting requirements for mission success. There are drawbacks to this very conservative modeling approach. For example, sizing the thermal system components (e.g., radiator) based on model simulations with stacked, worst-case conditions can lead to excessive overdesign. The overdesigned system increases spacecraft resource consumption (e.g., increased radiator size means more heater power usage).

DOD Program D in Figure 1-5b tells a different story than the TIMED mission. In this case, the mean of the difference between model and flight temperatures was nearly zero, indicating a very small thermal model bias toward either hot or cold temperatures. While a 10.5 °C uncertainty margin was required to meet the 95% threshold in Table 1.2, no hot or cold case predictions exceeded the temperatures limits with the 11 °C margin applied. That is, similar to the TIMED case, all temperatures satisfy requirements if it is assumed that requirements are at the 11 °C uncertainty bound for the hot and cold cases. That the discrepancy between model and flight temperatures is large is evidence of model inaccuracy. Although most missions are still successful, relatively large uncertainty margins, which impact system resources, are needed to account for system and environmental uncertainties.

In 2012, Karpati et al. [8] presented an investigation (original analysis by Garrison [39]) of seven recent Goddard Space Flight Center (GSFC) missions to make a similar comparison

of flight temperatures to model predictions. For this investigation, only the daily or orbit max cases were sampled over the course of the entire mission life. Regardless of the system modes and environments from which the temperatures were measured, the temperature data is compared to the worst-case scenario model predictions. Figure 1-6 shows the results of this sampling for all seven GSFC missions, grouped by the component type: electronics, solar arrays, actuators, and structure. In Figure 1-6, entries in quadrant I mean that the predictions were warmer than actual flight temperatures, and entries in quadrant II mean that the predictions were cooler than actual flight temperatures.

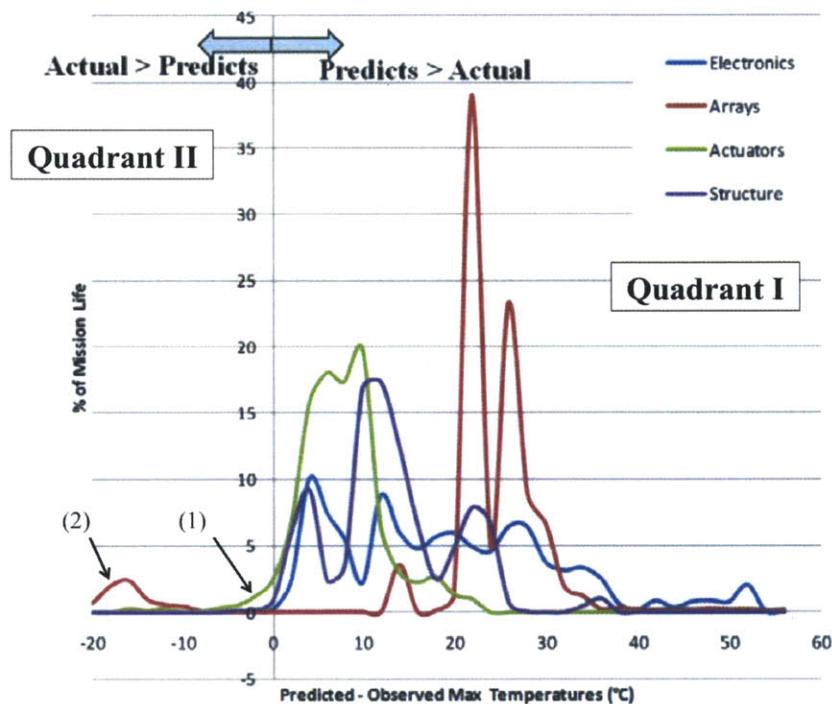


Figure 1-6: Comparison of flight data to model predictions for seven recent GSFC missions. In (1), actuators tend to run warmer than predicted by 2 °C 1% of the time, and (2) one solar array on one mission ran much warmer due to bad modeling practices. Figure from [8, Fig. 3-1].

In Figure 1-6, the mean of all the data is 16 °C (i.e., the average predicted hot case temperature was 16 °C warmer than the temperatures seen during flight). As Karpati et al. [8] notes, in all cases the predicted temperatures were greater than observed with two exceptions: (1) actuators tend to run warmer than predicted by 2 °C 1% of the time, and (2) one solar array on one mission ran much warmer due to bad modeling practices. The

study shows that the current model validation approaches result in hot case simulations that are conservative (i.e., at or above actual flight temperatures). However, there are significant differences (greater than the 5 °C NASA uncertainty margin) between worst-case predicted and actual flight temperatures, suggesting that the biased models can be too conservative. Furthermore, because the hot case model predictions are used to size components of the thermal system, significantly biased models can lead to too much overdesign.

Also in 2012, Peabody et al. [29] investigated the effects of biasing model parameters on thermal margin for the Global Precipitation Measurement (GPM) mission. The goal of the study was to examine the likelihood or frequency of the worst-case hot and cold conditions given that they are often used to size the thermal system. By systematically varying the conservatism of the values for important biasing parameters (e.g., power dissipations, beta angles, or optical property values), Peabody et al. [29] showed the effects of particular biasing parameters on thermal margin for various components of GPM. Among the biasing parameters, the power dissipations were found to be the largest driver of reduced thermal margin. The driving hot component had 18 °C margin for 95% of the mission time, whereas the stacked worst-case scenario (corresponding to 100% of the mission time) had only 7 °C margin. The study by Peabody et al. [29] indicates that the conservative approach of analyses using stacked, worst-case conditions can have a significant impact on analytical thermal margin, and thus, significantly impact the design of a thermal system.

1.3.3 Effect of Uncertainty Margin on Thermal System Resources

Before revisiting the model validation evaluation questions, we can investigate how uncertainty margins impact resource consumption (at the first-order) through example. Karpati et al. [8] estimated that the 5 °C NASA uncertainty margin [25] to hot operational limits will result in radiator mass growth between 0.3-0.7 kg per 100 W heat load; this radiator growth maps to a power draw increase of 4-6 W per 100 W heat load for survival heaters. Four radiator designs for current GSFC missions, two already built and two in preliminary design stages, were used to generate these estimates. To demonstrate this mass increase through simple example, consider the 5 °C NASA uncertainty margin. Assume a homogeneous, isothermal aluminum radiator plate with surface area, A , thickness, t , and with a full

view to deep space (assumed 0 K). The required surface area and radiator mass are given by Equation (1.4) and Equation (1.5), respectively:

$$A = \frac{Q}{\sigma \epsilon T^4} \quad (1.4)$$

$$m = \rho A t \quad (1.5)$$

where Q is the heat rejected, σ is the Stefan-Boltzmann constant, ϵ is the radiator emissivity, and ρ is the radiator density. Given the required performance characteristics, Q and T , we can determine the corresponding surface area and mass directly. By changing the nominal T value by the 5 °C uncertainty margin value, we can see the effect on mass in this simple case. Table 1.3 shows the nominal values assumed in this example.

Table 1.3: Nominal values for sample radiator calculation

Parameter/Constant	Nominal Value	Units
Heat load, Q	100	W
Stefan-Boltzmann constant, σ	5.67×10^{-8}	$\frac{W}{m^2 K^4}$
Emissivity, ϵ	0.90	–
Temperature, T	280	K
Density, ρ	2,700	$\frac{kg}{m^3}$
Thickness, t	3.18×10^{-3}	m

Using Equation (1.4), Equation (1.5), and the values in Table 1.3, the radiator surface area is 0.319 m², and the radiator mass is 2.73 kg. If the temperature is reduced by 5 °C to reflect a minimum uncertainty margin value, the radiator temperature becomes 275 K. The inflated radiator surface area is 0.343 m², and the radiator mass is 2.94 kg. The radiator mass increases by 0.21 kg. **The 5 °C uncertainty margin maps to an approximate 8% increase in radiator mass in this simple example.** The increase in radiator size will also increase heater size (i.e., system power consumption). This result is of the same order of magnitude but at the lower end of the range reported by Karpati et al. [8]. While a 0.21 kg increase may be a relatively small increase, an 8% increase in the mass of a much larger thermal system component would be significant. Although the scaling may be different for

larger systems due to geometry, material, and component interaction complexities, the 8% comparison provides a first-order approximation.

For example, one Heat Rejection System (HRS) radiator for the International Space Station is shown in Figure 1-7. Each HRS radiator has a mass of approximately 1,100 kg and measures 76 ft long and 11 ft tall [40]. Drawing from the sample calculation above, an 8% increase to the HRS radiator's mass or volume is significant. The sample calculation *does* show how current uncertainty margins can affect system resources; it *does not* capture how complexity in the radiator design (e.g., fluid loop radiators) can further increase resource consumption, nor does it capture second-order effects such as the structural or payload requirements to support the larger radiator. The radiator example is a demonstration of how the uncertainty margins required by military and NASA programs can lead to significantly increased resource consumption. An improvement to the thermal model validation process that allows for important system uncertainties to be systematically identified and managed throughout the project lifecycle could allow for reduced uncertainty margins, or margins applied in system-specific manner.



Figure 1-7: International Space Station Heat Rejection System radiator during deployment testing [40]

1.3.4 Answering the Model Validation Evaluation Questions

Having reviewed comparisons between model predictions and recent flight data and examined the effect of the uncertainty margin through example, we can now return to the model

validation evaluation questions introduced at the beginning of this section:

- How close are post-validation model predictions and flight temperature data?

Based on the flight temperature data, no generalizations can be made about final thermal model accuracy. Model accuracy is mission-specific and depends on the engineering practices of the organization developing the system. Welch [28] concludes that no appreciable improvement has been made over the last three decades in our ability to accurately predict on-orbit temperatures and recommends the continued use of the 11 °C uncertainty margin for military programs to bound 95% of all actual flight temperatures. From recent NASA-based studies [8, 29], evidence indicates that worst-case scenario predicted temperatures are often more than 10 °C different than those temperatures seen during flight in intermediate thermal environments or system modes. Even though the models are often accurate to less than 10 °C, designing to the worst-case scenarios can lead to excessive overdesign with respect to the majority of the environments/system modes.

- Are there trends in the model predictions and/or data that suggest an opportunity to improve the validation process?

Yes; current practices focus on building stacked, worst-case scenarios involving the hottest and coldest environments; uncertainty margins are then applied to these worst-case predictions. Thus, current practices can result in overly conservative model predictions, which are used to design the thermal system. A better understanding of the system concept, uncertainties, and sensitivities earlier in the design lifecycle would facilitate a reduction in conservatism during preliminary design.

- Are design uncertainty margins appropriately conservative? Is there a better way to quantify and reduce the uncertainty?

Sometimes and yes; given that important uncertainties are addressed by assigning margin to model output instead of being quantified and propagated through the thermal model, it is challenging to determine the source of the discrepancy between model predictions and flight data. For many missions, there is evidence to suggest that the worst-case scenarios (which are used for design) have low likelihood and/or low fre-

quency. *The evidence indicates that the difference between actual flight temperatures sampled randomly over many orbits is often more than 10 °C different than the worst-case predictions, which suggests that the worst-case scenarios are too conservative in some cases. By systematically identifying important model parameter uncertainties early in the design lifecycle, and furthermore focusing model validation efforts throughout the design lifecycle on reducing important uncertainties, we can allocate uncertainty margin in a system-specific manner based on expected temperature variations and the mission's risk posture.*

- Why buck the status quo?

A significant improvement to the model validation process means increasing system knowledge earlier in the design lifecycle (e.g., greater knowledge of thermal system concept, identification of critical sensitivities, or reduced model uncertainty) and/or a more efficient, systematic validation approach. Improved model validation can decrease reliance on stacked, worst-case analyses and design margin which can result in system overdesign. The validation process can be more rigorous in characterizing uncertainties upstream of the model and more systematic in managing uncertainties throughout the project lifecycle. With the driving environmental/system uncertainties quantified, thermal margin can be allocated in a system-specific manner to address particular uncertainties. Long term, improving the thermal model validation process can reduce overall mission costs that are both form-related and process-related.

The bottom line is that because worst-case thermal model predictions are often more than 10 °C different than actual temperatures from intermediate power modes and environments, designing to worst-case conditions *with uncertainty margins* can result in too much conservatism (depends if the worst-case scenarios actually happen on-orbit and if it is acceptable to exceed thermal requirements during the worst-case scenarios). Although thermal systems are typically successful, the heavy reliance on conservative analyses and uncertainty margins can lead to overdesigned systems. An improvement to the model validation process, under the cost/schedule constraints of a flight program, can result in thermal models that more accurately predict flight temperatures for specific power modes and environments.

1.4 Literature Review

This literature review will categorize the fields of uncertainty quantification (UQ) and design of experiments (DOE) into three areas: forward uncertainty propagation (UP), design of experiments (DOE), and model calibration. Whereas UP can be seen as the forward UQ problem, model calibration is the inverse UQ problem. The three literature review areas comprise the simulation model validation process and are discussed in Sections 1.4.1-1.4.3. While each area is discussed individually, none are independent: the methods of UP, DOE, and model calibration all influence one another as part of the validation process. Each of the following sections compares the state of the art model validation techniques with conventional thermal system techniques. In this thesis, a *conventional validation approach* refers to methods that are typically performed in practice to develop thermal systems. Although the exact conventional methodologies can vary between organizations and between engineers, the central themes of conventional validation approaches are discussed. Section 1.4.4 summarizes the differences between the state of the art and the thermal convention and presents the research gap.

1.4.1 Model Uncertainty Propagation (UP)

UP examines the effects of a model's uncertainty on its output through uncertainty and sensitivity analyses. Uncertainty analysis (UA) is the determination of a model's output uncertainty due to its uncertain parameters and its inadequacy [41]. Discussed later in this section, model inadequacy refers to any model error that cannot be described by parametric uncertainty [42]. Sensitivity analysis (SA) is the determination of *how* a model's parametric uncertainties contribute to its output uncertainty [43].

Uncertainty Propagation (UP)—State of the Art

Although the process does not have to be serial, the general flow of UP in the analysis of complex systems is outlined by Allaire [19]:

- UP goal setting

- Model selection and documentation
- Uncertainty classification
- Uncertainty characterization
- Uncertainty analysis
- Sensitivity analysis

The relevant literature for each component of the list is reviewed below.

Common UP model development goals address identification and reduction of parameters that most significantly create variance in the model output [19]. Quantities of Interest (QoIs) are model output quantities that map directly to requirements of the system. As an example, Figure 1-8 shows an UA product for a certain QoI for three different designs. Figure 1-8 demonstrates how this type of analysis could indicate the need for uncertainty reduction efforts for a QoI. The dots in Figure 1-8 indicate the nominal performance of each design and the brackets around the dots show the uncertainty in the QoI. Design A does not meet requirements nominally (but could meet the requirement, given its uncertainty), Design B meets requirements nominally but has uncertainty such that it might not meet requirements, and Design C meets requirements, even in a worst-case scenario. There are two ways to address the unsatisfactory performance predicted for Design B: (1) translation of the QoI nominal performance and uncertainty bounds below the requirement or (2) reduction of the width of the uncertainty bounds on the QoI. While (1) might entail allocation of resources to improve the design (e.g., increase radiator size in thermal system), approach (2) could entail experimentation to reduce important parameter uncertainties. For Design A, the nominal design must be improved because it is not predicted to meet the requirement for the QoI. SA could further focus research efforts to improve the variance or mean of a QoI by attributing the undesired behavior to a particular model parameter. The nature of the problem and the specific goals selected for UQ drive both the computational approach and the presentation of the results [44, 45].

Model selection refers to the choice of which model(s) will be used to simulate the system throughout the project lifecycle. Often the choice of model boils down to a trade between

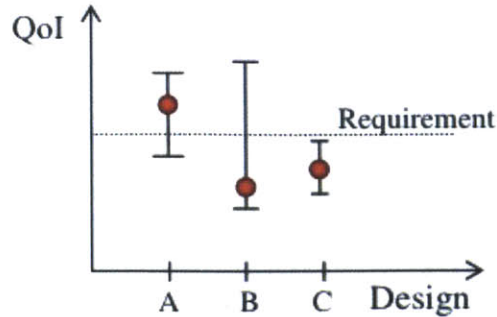


Figure 1-8: Uncertainty Quantification toward validating system performance with respect to a particular Quantity of Interest. The dots indicate nominal performance. Figure from [46, Fig. 1].

model fidelity and computational cost. Large scale simulation models are often difficult to document, are often a black box for the user (i.e., a model that can only be viewed through its inputs, outputs, and transfer characteristics), and are computationally expensive. Many system models cannot be fully utilized for all analyses because the scale and complexity are large. Howell [47] sought to balance computational cost with model fidelity by using a fidelity metric that estimated how well a finite element model approximated structural eigenvalues based on a certain mesh size. Physics-based tuning of a model's mesh size can improve computational burden, but it is not always possible to achieve the accuracy required of a model strictly by reducing the mesh size.

Surrogate models are a common alternative, offering an approximation to the full system model at reduced complexity and computational costs. According to Eldred et al. [48], surrogate models can be divided into three categories:

- Data-fit models [49]
- Reduced-order models [50, 51]
- Hierarchical models [52, 53, 54]

Hierarchical models are low fidelity models that are derived from higher fidelity models through simplification (e.g., simplified mathematical model, relaxed convergence criteria, coarser grid, or neglected physics). Hierarchical models are a common surrogate model choice for complex system modeling because of the dimensionality issues associated with

data-fit methods and the general requirement for the governing equations to be known for projection-based reduction methods.

There are many sources of uncertainty when modeling a physical process, but uncertainties in the model itself can be organized into two areas: parametric and model structure. While parametric uncertainty refers to the lack of knowledge of the true parameter values, model structure uncertainties are due to model inadequacy [42]. Model inadequacy is the model's inability to match reality with its output and includes errors caused by model fidelity, convergence, or unmodeled physical behavior. A common convention is to classify uncertainties as either epistemic or aleatory [44, 55, 56]. Kiureghian and Ditlevsen [55] examined epistemic and aleatory uncertainties in the context of model-based design and analysis: epistemic uncertainty is due to lack of knowledge, and aleatory uncertainty is due to intrinsic randomness. Although the distinction between the two classifications is not always clear, epistemic uncertainties are reducible, whereas aleatory uncertainties are not. For example, the uncertainty in the emissivity of a surface coating can be seen as epistemic, and the value of dice when rolled has aleatory uncertainty. In a typical Bayesian setting, epistemic uncertainties are defined probabilistically using the *maximum uncertainty principle* [56]. Allaire [19] states that in practice, all uncertainties are often treated as epistemic (i.e., each model parameter is assigned a probability distribution according to the uncertainty in its value, and if all uncertainty were reduced, the parameter's value would be fixed at the true value).

Uncertainty characterization focuses on how the model uncertainties, both parametric and those associated with the model structure, will be quantified. There are two general ways to characterize parametric uncertainties: probabilistically and nonprobabilistically [57]. Convex models, a nonprobabilistic approach, align with the maximum uncertainty principle: the worst-case parameter values are considered to build conservative performance predictions at the bounds of operation [58]. However, information is lost in the presentation of the results regarding the likelihood and frequency of the worst-case scenario. Probabilistic models use distributions for each parameter that capture the expected variance and mean value. Probabilistic models are utilized in many engineering applications because they fit well into many uncertainty and sensitivity analysis methods and enable users to state probabilistically if requirements will be met for the system [19, 46]. While the literature is dense for parametric

uncertainty characterization, considerably less work addresses model inadequacy. Riley and Grandhi [59] assert that fully addressing model inadequacy means quantifying uncertainty between multiple models and addressing discrepancies between model predictions and the real system. The latter is typically quantified after experimentation, though recent work by Moser and Oliver [60] has sought to predict model inadequacy by modeling the inadequacy itself (e.g., including a discrepancy function with a model parameter that is the suspected source of the model inadequacy).

Uncertainty analysis is performed by propagating model uncertainties through the model to observe the resulting uncertainty in the QoIs. The output of UA is typically the distributions of the QoIs, including mean values, variances, and histograms [45]. Various methods exist to propagate parameter uncertainties through a model, including nonsampling-based and sampling-based methods. Nonsampling-based techniques include mean-value methods [61], analytic reliability methods [62], and stochastic expansion methods (e.g., polynomial chaos [63]). For example, Gutierrez [64] used the results of local sensitivity analysis during uncertainty analysis via a constrained optimization approach to predict the worst-case RMS performance of a disturbance model of a reaction wheel assembly. While nonsampling-based methods can be more computationally efficient for linear models where the model structure is known, sampling-based methods are most commonly used for large, nonlinear models. Model parameters are often treated as independent random variables. However, if the parameters have known correlations, the covariance is used and propagated through the model [65]. Sampling-based methods are a popular choice in uncertainty analysis due to their general applicability and effectiveness [19, 44]. Monte Carlo (MC) simulations use many samples to approximate the expected value of the model output given the model's parameter uncertainties and inadequacy. Two popular methods for generating the samples are random sampling and Latin Hypercube sampling (LHS) [41].

Sensitivity analysis attributes the QoI uncertainty to the uncertainty of individuals or groups of parameters. Model parameter importance analyses generally focus on two types: local sensitivities and global sensitivities. Local sensitivity analyses examine the change in the response of the QoI due to a small variation in a single model parameter [66]. However, local sensitivities provide no global information regarding the effects of the parameter

uncertainties. Global sensitivity analysis (GSA) addresses many of the limitations of local sensitivity analysis [67]. Figure 1-9 illustrates the general GSA process. GSA apportions the observed output variance, given by $V[y]$, to the model parameter contributors, x_i .

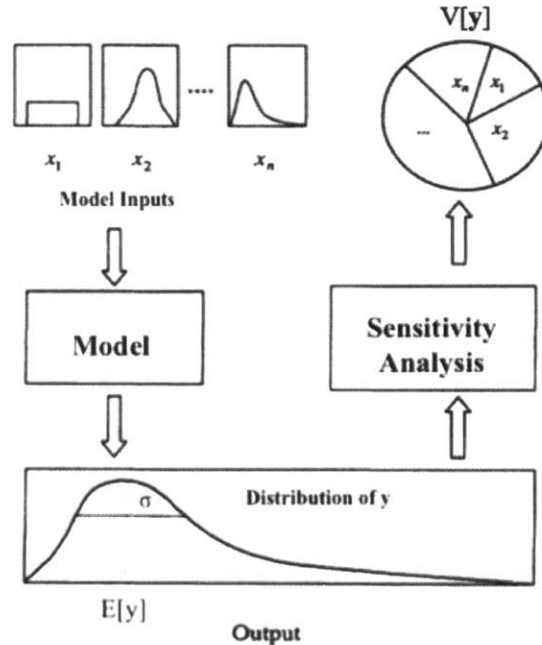


Figure 1-9: General global sensitivity analysis process. Figure modified from [67, Fig. 1].

In the context of model-based design, GSA can guide research aimed at reducing model parameter uncertainties that significantly affect expected performance and allow engineers to neglect model parameters that do not significantly affect a QoI. GSA can be broadly categorized into two groups: regression-based methods and variance-based methods (i.e., Analysis of Variance (ANOVA) methods) [45, 68]. Variance-based methods are most popular and are based on a decomposition of the model into main effects and interactions [69, 70]. The goal of most variance-based GSA is to approximate the main effect and total effect sensitivities for a given model parameter; these sensitivity indices are well established expressions for use in importance assessment and guiding future research [43, 67, 68, 69, 70, 71]. Saltelli and Tarantola [71] outline procedures for prioritizing model parameters to guide future research in cases with or without interactions (i.e., an additive model) and parameter correlations.

Uncertainty Propagation (UP)—Thermal Convention

In industry, UP is uncommon. Instead, design margins are commonly used to account for model uncertainties. While modeling and margin policies depend on the scope of the project and the governing organizations, the NASA GOLD Rules [25] summarize the philosophy invoked by most programs, including military programs. The thermal design margin policy, per GOLD rules, is summarized below:

Rule: Thermal design shall provide adequate margin between stacked worst-case flight predictions and component allowable flight temperature limits.

Rationale: Positive temperature margins are required to account for uncertainties in power dissipations, environments, and thermal system parameters.

Important language in the thermal design margin rule, shown above, includes *predictions*, *stacked worst-case*, and *margin*.

Predictions refer to the output of thermal models that are constructed and updated throughout a project's lifecycle. Geometries, material properties, and component power dissipations are all parameters that determines the model's output. The *stacked worst-case* conditions refer to a convex approach to uncertainty where the focus is on the model parameters' bounding values. For a particular mission phase hot or cold case, the most conservative model parameters are selected so that the model's output is biased to create a worst-case scenario. Model parameters and factors that are biased using the convex approach include [8, 72, 73]:

- Component power dissipations
- Material optical properties
- Environmental heat loads
- Beta angles
- Critical conductances

- MLI blanket effective emissivities

The above list is not all-inclusive, and if a critical model parameter exists that heavily drives thermal system performance, it too is biased in similar fashion. For an example of this biasing, consider a radiator's emissivity. Maximum emissivities, often Beginning of Life (BOL) values, are used for cold case simulations, and minimum emissivities, often End of Life (EOL) values, are used for hot case simulations. These assumptions ensure that the predicted temperatures of component(s) cooled by the radiator are conservative for both cold and hot cases.

The final critical element of the thermal design rule concerns the application of *margin*. Margin is applied directly to the model output to account for uncertainties in the model parameters and model inadequacy. Early in a project lifecycle, preliminary analyses use larger design margins. Once the thermal models have been correlated to thermal balance test results, design margins can be relaxed under the assumption that model uncertainty has been reduced. Guidance from the thermal design standards and handbooks [4, 72, 73] suggests that thermal engineers conduct sensitivity analyses and compare worst-case predictions with nominal cases, though no specific processes are specified. Thus, the industry thermal system convention is rooted in building very conservative models where uncertainty margins are applied to predictions to account for parameter uncertainty and model inadequacy.

Although few published references could be found on the topic, model uncertainty factors (MUFs) are often used in industry to account for model uncertainties either upstream or downstream of the model. MUFs (and test uncertainty factors (TUFs) for thermal balance testing) are essentially factors of safety to account for predictive uncertainty or design maturity (see Blair et al. [74] for example of MUFs on structural dynamic modes). MUFs are typically larger at the beginning of the life lifecycle and reduced over time. The application of MUFs directly to model parameter(s) relies heavily on experience, and if applied to the model output, MUFs are analogous to design margin. While recent work has looked at characterizing and quantifying all parametric uncertainty in spacecraft thermal models [75], the state of the art UP techniques have not been extended to a full system thermal model nor the model validation process.

Limitations

In general, UP is uncommon in the analysis of spacecraft thermal systems. Instead of rigorously addressing model uncertainty upstream of the model, uncertainties are addressed downstream and margin is applied directly to the model output. Historically, the conventional approach has been successful, but there is evidence of occasional model inaccuracy and overdesign for some systems. Consideration is rarely given to the likelihood or frequency of all these parameters actually occurring simultaneously during the mission [29]. Furthermore, it is not always clear which parameter values yield worst-case conditions. State of the art UP techniques can improve upon current thermal practices by:

- Probabilistically characterizing model parameter uncertainties and propagating uncertainties through the model
- Predicting the expected temperature uncertainty and variability
- Identification of true worst-case thermal scenarios
- Creating a general procedure to rigorously determine the importance of model parameters and prioritizing future research (e.g., experimentation) based on global sensitivity analysis
- Quantifying model inadequacy and creating basis for system-specific uncertainty margins consistent with the level of QoI uncertainty and mission risk posture

1.4.2 Design of Experiments (DOE)

Testing is a fundamental part of the model validation process. It is through experiments that the model is compared directly to a real system. This comparison reveals important information, such as the need to adjust model parameters/structure or the ability of the system to meet requirements. Design of Experiments (DOE) is the process of selecting experiments to obtain relevant information and test hypotheses. The following section will discuss classical DOE methods and more recent model-based DOE work, which focuses on Optimal Experimental Design (OED) approaches. Next, the conventional thermal system

experimental design is discussed in light of the state of the art OED approaches to identify the research gap.

Design of Experiments (DOE)—State of the Art

DOE is a comprehensive field encompassing the choice of experimental hardware, when and where to measure, measurement accuracy, and experimental conditions [76]. While DOE has origins dating back hundreds of years ago, the seminal work by Ronald Fisher [77, 78] effectively established the field. Over the last several decades, classical DOE methods have developed into the most popular approach to experimentation and should adhere to four principles [79]:

- **Randomization:** minimize the effect of all potential biases in the experiment
- **Replication:** repeat an entire experiment under the same conditions and procedures
- **Blocking:** isolate the effect of a particular unwanted input
- **Orthogonality:** contrast the effects of uncorrelated inputs

Popular classical DOE methods include full factorial and central composite designs [80]. Hu [79] comments that classical DOE methods generally use predefined experimental designs and empirical models based on the data. There is no unifying strategy to design experiments in the classical approach [81]. Taguchi methods offer an alternative methodology to classical DOE and are effective at designing an experiment around a single characteristic in the presence of “noise parameters” to identify main effects [82]. For a complete treatment of classical DOE in a general context, please see Montgomery [81].

Model-based DOE uses the model to design experiments customized to the specific system. There are two types of model-based methods, hereafter referred to as Optimal Experimental Design (OED) and Optimal Bayesian Experimental Design (OBED). Figure 1-10 summarizes how both OED and OBED fit into the larger decision theory framework for DOE. The important elements of Figure 1-10 are discussed below for both OED and OBED. The takeaway is that OED does not utilize prior parameter information, and OBED is a more general process that states outcomes probabilistically.

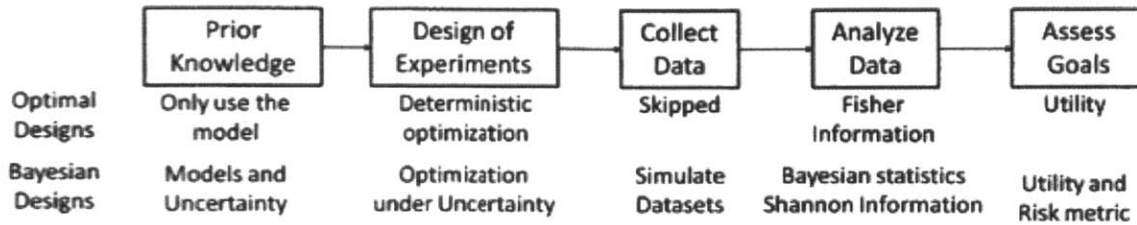


Figure 1-10: Comparison of model-based DOE methods. Figure from [79, Fig. 5-1].

OED is a commonly applied model-based experimental design method. OED does not utilize prior parameter information. Experimental design solutions are written as functionals of the Fisher information matrix [83], stated in terms of *alphabetic optimality* conditions [76]. The solutions are not dependent on the expected results of an experiment. Thus, the Collect Data step from Figure 1-10, which refers to the *expected* data collected from a particular experiment, is skipped, and the Design of Experiments step is a deterministic optimization problem. While OED improves on classical DOE by utilizing the system simulation model, OBED is needed to fully address model parameter uncertainties. Furthermore, OBED methods can be used for large systems with black box, nonlinear models to accurately calculate expected utilities of experiments. For more information on OED methods, see Atkinson and Doney [84].

Whereas in OED the experimental utility was measured by the Fisher information matrix, the utility function selection in OBED depends on the goals of the experiment. Common OBED experimental goals include [83, 85, 86]:

- Model parameter inference
- Generation of accurate model predictions
- Model discrimination

In the context of simulation model validation, model parameter inference is an important goal for calibrating models from experimental data [42].

OBED utility is formulated in a Bayesian setting where inferences are made from noisy, indirect, and incomplete data [83]. Given the prior knowledge of model parameter uncertainty,

the results of an experiment, and the likelihood of observing the result, Bayes' Theorem indicates the change in the state of knowledge of the model parameters. In this Bayesian setting, Lindley [87] suggested measuring an experiment's utility based on the expected result of an experiment, the updated model parameter knowledge, and a suitable utility function. For parameter inference, a common choice of utility function is the Kullback-Leibler (KL) divergence, a measure of relative entropy [83, 85, 88, 89]. The KL divergence is analogous, but not equal to, differential entropy and is a scalar value indicating the difference between two distributions [79]. Once the experimental utility measure is in place, the expected utility must be optimized over the design space of experimental conditions.

Hu [79] asserts that often organizations lack a rigorous treatment of uncertainty in DOE: test cases are designed to best-case, worst-case, or baseline scenarios. The thermal system convention for DOE is consistent with both Hu's assertion and classical DOE, where test cases are built around worst-case scenarios expected on-orbit.

Design of Experiments (DOE)—Thermal Convention

In practice, thermal simulation models are validated through thermal balance testing. The General Environments Verification Specification (GEVS) [24] and MIL-STD-1540 [23] are standards that govern the DOE for space-based thermal systems for NASA and military programs, respectively. While MIL-STD-1540 is a general requirements document, MIL-HDBK-340 (MIL340) [22] are guidelines that supplement the requirements and provide more instruction regarding practices of thermal balance testing. NASA programs [90, 91, 92] and military programs, such as those studied by Welch [28], must rigorously adhere to their respective standards to demonstrate validated thermal models. Furthermore, other programs that are not held to either standard, such as university space systems [93, 94], typically adhere to the same thermal model validation testing philosophy. Thus, the standards of GEVS and MIL-STD-1540/MIL-HDBK-340 represent the thermal model validation test convention philosophy for spacecraft thermal systems.

Thermal balance testing is typically performed to validate the system level model. Prototype-level thermal tests are recommended in situations when analysis uncertainty is large or for mission critical components (e.g., thermally-induced structural distortions of a structure)

[22]. The following describes the minimum requirement and objective for system level thermal balance, per GEVS and MIL340:

Minimum Requirement: At minimum, two test conditions shall be imposed: one at the mission hot case and one at the mission cold case. For NASA programs, GEVS requires one additional case selected by the thermal engineer.

Primary Objective: Validate the thermal model so that it can be used to predict tested and untested conditions spanning the entire domain of environmental conditions that the system will experience on-orbit.

At minimum, thermal balance testing for military programs and NASA programs requires two and three cases, respectively. MIL340 further suggests that if practical, additional tests including a transient and another mid-point mission case are useful for better model validation. In summary, *any* spacecraft or space-based system required to conform to GEVS or the instruction of MIL340 must perform pre-defined thermal tests to validate the thermal models.

GEVS and MIL340 further define not only the test cases, but also test levels and environmental conditions that should be applied to create the conservative hot/cold worst-case environments. Furthermore, each standard specifies a recommended thermal stabilization criteria for thermal balance. Since the actual space environment is not precisely reproducible in a thermal vacuum chamber, thermal models are modified to match the test configuration. Table 1.4 describes a few examples of how the environmental conditions are imposed. Thermal radiation heat sources, such as the sun or a planet, are simulated in test by heaters and lamps. In conduction, cold/hot plates held at a fixed, worst-case temperature are used to simulate system interfaces to payloads. Test level and environmental conditions guidance is meant to be generally applicable to any thermal balance test. While the guidelines are consistent and intuitive for engineers to apply, there are inherent limitations to these standards.

Table 1.4: Examples of environmental test condition guidance from GEVS and MIL340 [22, 24]

Environmental Condition	Heat Transfer Type	Implementation
Solar Input	Radiation	Mercury-xenon, xenon, or carbon arc source, cryopanel, and/or heaters
Planetary Input	Radiation	Skin heaters, cryopanel/heat plates, quartz lamps
Interface	Conduction	Cold/hot plates and isolation standoffs

Limitations

Thermal balance testing aligns well with classical DOE. Thermal balance tests are designed around worst-case scenarios corresponding to the hottest and coldest environments expected on-orbit. Although the goal of thermal balance testing is model validation, experiments are not designed specifically for each system. In model-based DOE, experiments are optimally designed to achieve the specified experimental goal. Limitations associated with thermal system DOE that are addressed by OED/OBED include:

- Important model parameters that significantly contribute to QoI variability are neglected in the design of the experiment.
- Test levels and environmental conditions are predetermined and can be suboptimal for model validation and parameter inference.
- More experiments may be required to validate the thermal model. No explicit guidance is given if the single thermal balance test was insufficient (ambiguous success criteria).

1.4.3 Model Calibration

Once the experiment is designed and executed, models must be calibrated to the experimental observations. The model calibration problem is commonly referred to as the inverse problem for UQ. The following sections review the literature for the state of the art model calibration and the thermal system convention.

Model Calibration—State of the Art

Over the last decade, a popular technique to calibrate thermal models to experimental data is to formulate the calibration as a parameter optimization problem. For space-based systems, one advantage of working with the physical parameters instead of working with a measurement model is the straight-forward transition from the experimental model to mission model [95]. Cullimore [96] formulates the thermal model calibration process as an optimization problem where model parameters, such as conductances, optical properties, and MLI performance, are automatically adjusted to find the best fit to experimental data. Similar approaches to Cullimore's explore the use of genetic algorithms [97] and particle swarm algorithms [98] in the optimization problem.

Parameter optimizations are limiting because all prior estimates of a parameter's value are neglected in pursuit of the best *set of parameters* to fit the data. Often, many parameter sets exist that satisfy the minimum requirement for the fitness function (e.g., root mean squared error). Thus, there is ambiguity in selecting the best parameter set that physically represents the real system. Isoperformance [99] seeks to address this issue (though introduced in the context of system design) by identifying acceptable parameter sets and choosing from among them the set that is optimal with respect to other criteria. However, establishing the criteria for parameter set selection, in the context of model calibration, is challenging because it is not always clear what the criteria should be. For example, if the parameter sets contain values outside of the parameter bounds, it is unclear how to establish the selection criteria—are the parameter values correct, even though they are outside of the expected range, or are the out-of-bounds values evidence of model inadequacy? Masterson [100] implemented a model updating methodology based upon isoperformance to select parameter values from sets of parameters that yield the same hardware performance. While parameter optimizations can be effective for parametric uncertainties, they neglect model inadequacy during the calibration process.

The development of Bayesian calibration techniques started in the 1980s and gained popularity for model validation throughout the 1990s. These calibration techniques rely upon Bayesian inference, a technique that exploits Bayes' Theorem, to update the distribution

of a random variable in light of evidence. Romanowicz et al. [101] proposed a Bayesian calibration approach that accounts for parametric uncertainties called Generalized Likelihood Uncertainty Estimation (GLUE). In GLUE, Monte Carlo (MC) sampling of input prior distributions are weighted by a likelihood function to produce estimates of the posterior predictive distribution. Similar approaches in the literature focus on finding best fit model parameters primarily associated with parametric uncertainties [102, 103]. Cox et al. [104] introduced a surrogate model interpolator in a similar fashion to improve computation time. Despite these advances, model inadequacy was not captured in the model calibration process. The fundamental limitation of this strategy is that model parameters are calibrated to match the *experimental data* instead of capturing the true physics of the *real system*.

The seminal paper in the Bayesian calibration of models is by Kennedy and O’Hagan [42]. The “Kennedy and O-Hagan approach” (K-O approach) uses a general Bayesian model calibration framework that allows for parameter and model uncertainties. The K-O approach:

- Treats the model as a black box (i.e., no exploitation of model structure).
- Identifies model parameters as either known control parameters or calibration parameters whose distributions are to be updated.
- Accounts for model inadequacy independent of the parametric uncertainties and defines inadequacy as the difference between the true process and the modeled process.
- Includes observation error to capture the uncertainties associated with an experiment (e.g., sensor error).

The K-O approach has been used for problems in disciplines such as engineering [105, 106, 107], health sciences [108], experimental physics [109], astrophysics [110], and climate modeling [111, 112]. Higdon et al. [113] applied the K-O approach to a thermal problem using a Gaussian Process model.

Since its introduction, several notable improvements to the K-O approach have been made. Brynjarsdottir and O’Hagan [26] sought to improve on the K-O approach by modeling the model inadequacy, albeit simplistically (e.g., constraining the shape of the inadequacy distribution). It was shown that without capturing model inadequacy during calibration,

models are persistently biased. By modeling the inadequacy in simplistic ways, interpolations within the input domain are unbiased but extrapolations are typically biased. Higdon et al. [114] further expanded the K-O approach to high dimensional output problems. The multivariate output is representative of systems with many QoIs and with models that are computationally expensive. Qian and Wu [115] developed a methodology for using multiple Gaussian process models to adjust models based on multiple experiments of different fidelity in a Bayesian calibration setting. Bayarri et al. [116], an extension of the work by Higdon et al. [117], generalized the K-O approach into a model validation framework. Although UP is introduced as a supplemental tool to be used for model calibration efforts, model-based DOE is not addressed. The Bayarri et al. [116] framework does not specify *how* experiments can be designed in a system-specific manner based on UP.

Model Calibration—Thermal Convention

Despite the state of the art model calibration techniques presented above, Kennedy and O’Hagan [42] assert that the traditional way of estimating unknown parameters is an ad hoc search for the best fitting parameter values. The thermal system convention aligns with this ad hoc search method. In industry, thermal model calibration is often referred to as *correlation* between the test data and model predictions. In order to prepare for the thermal balance test, the system model is modified to capture the environmental conditions and ground support equipment in the thermal balance test. Once the thermal test has occurred, model correlation begins (though it is often performed during later phases of testing to debug or make test environment changes, as necessary). Gilmore [4] outlines the conventional model correlation process followed by thermal system engineers:

1. Update the test chamber conditions, and rerun the model to update temperature and power predictions
2. For a single test phase, compare the model predictions with test data, and first adjust the model for large temperature discrepancies. Common adjustments to the model include:
 - Addition of physics that were previously omitted

- View factor geometries
 - Conductances
 - Optical property values
3. Correlate all temperature differences between model and test data to less than some threshold value (e.g., ± 3 °C per MIL340 [22])
 4. Repeat 2-3 for the remaining test phases, ensuring that changes made in each remaining phase do not undo the correlation from a previous phase

Any unresolved discrepancies persisting after the correlation process must be completely understood and documented. There are many examples in the literature of model correlation for space-based thermal systems [91, 118, 119, 120] that follow the general process outlined by Gilmore [4]. In general, industry thermal model calibration techniques do not rely on the state of the art techniques for correlation. Instead, the ad hoc search for the best fitting model parameters is completed with engineering experience and intuition. Once correlation is complete, the validated flight model is used to generate updated mission temperature predictions.

Limitations

Thermal model correlation relies heavily on engineering expertise. The model adjustments needed for proper correlation are not obvious, particularly for complex system models. Often adjustments to model parameters or the model structure can have the same desired effect of reducing the discrepancy. Thus, there is ambiguity in selecting the correct model parameter values for correlation purposes. Limitations of the thermal system model correlation process, in light of the state of the art calibration approaches, include:

- Model parameters are *tuned* to the thermal balance test data instead of representing the real system's parameters.
- Prior model parameter estimates are discarded after correlation, and no rigorous framework exists to update model uncertainties following correlation.

- Model inadequacy is not explicitly quantified.
- Multiple test cases are considered sequentially instead of simultaneously.
- Manual correlation procedures rely heavily on engineering experience and judgment.

1.4.4 Research Gap

In practice, the state of the art methods are either rarely used or used in limited capacity. There is no existing framework to combine the state of the art methods to validate the model of a complex thermal system.

The preceding sections presented the literature in the fields of UQ and DOE, divided into three areas: UP, DOE, and model calibration. These areas comprise the major elements of model validation. The literature review summarized important techniques for both the state of the art and those currently practiced by thermal system engineers in industry. Table 1.5 summarizes the literature review for all three areas.

The state of the art techniques for model validation shown in Table 1.5 include a probabilistic characterization of uncertainty, implementation of UA, and the use of GSA to identify important model parameters that greatly contribute to QoI uncertainty. OED/OBED is used to design model-based parameter inference experiments suited for a particular system. Finally, the K-O approach is used to calibrate models to experimental results, quantifying parametric uncertainties and model inadequacy.

In contrast to the state of the art techniques, the thermal system convention for model validation shown in Table 1.5 consists of building stacked worst-case scenarios *within* the model, applying margin to model output, and designing experiments to these worst-case scenarios. Models are correlated to the experimental results through a process that is largely based on manual model adjustments made by the engineer. State of the art techniques can be highly automated and are consistent in their rigorous treatment of uncertainties, whereas the conventional thermal system techniques rely heavily on engineering intuition and experience.

Table 1.5: Comparison of state of the art methods and thermal system conventions in Uncertainty Propagation, Design of Experiments, and Model Calibration

Discipline	State of the Art	Thermal Convention
<i>Uncertainty Propagation</i>	Probabilistic uncertainty characterization; UA and GSA	Convex uncertainty characterization; margin applied “downstream” of model
<i>Design of Experiments</i>	OED and OBED	Classical DOE
<i>Model Calibration</i>	Bayesian (K-O approach)	Manual model correlation

1.5 Problem Statement, Research Goal, and Thesis Objectives

Sections 1.2 and 1.3 provided the background and motivation for this research. The current validation process can lead to overly conservative or inaccurate thermal models. Now we can examine the main research topic: improving model validation for spacecraft thermal systems.

1.5.1 Problem Statement

Given the importance of validating thermal models:

How do we improve simulation model validation for spacecraft thermal systems to facilitate reduced resource consumption, efficient model validation processes, and more accurate on-orbit predictions?

More specifically, can we formulate a methodology to:

- quantify the effects of thermal model uncertainty on the mission temperature predictions?
- reduce important model uncertainties and validate the thermal design and model via experiments?

- update model parameters based on new information?
- tailor state of the art model validation methods to validate thermal system models?

1.5.2 Research Goal

The research goal for this thesis flows from Table 1.5. This research will improve the thermal model validation process by developing a tailored methodology that combines the state of the art validation methods of UQ and DOE. The research will rigorously and systematically show the effects of model uncertainty on predictions, identify important model uncertainties, produce system-specific, optimally designed experiments to learn more about important model uncertainties, and update the model following experimentation to reduce model uncertainty. The methodology will be implemented on a real thermal system (see REXIS SXM case study in Chapter 5) to demonstrate the process-related benefits to the thermal model validation process.

1.5.3 Scope

This thesis primarily deals with developing the Bayesian-based Model Validation (BMV) methodology for improving the thermal model validation process. The architecture of the thermal system designs will be considered and analyzed to some degree (for some systems, design changes may be required to validate the thermal design and/or thermal model), but previous design trades and design decisions are not evaluated in this thesis. Instead, the focus will be on validating the models of the thermal systems that are already in place (i.e., a frozen design, unless a small design change is needed).

1.5.4 Thesis Objectives

The objective of this research is to improve the thermal model validation process by creating a methodology to validate thermal simulation models using state of the art methods in UQ and DOE. Specific objectives include:

1. Quantify thermal model uncertainty associated with both the parameters and model

structure to investigate effects on thermal model predictions and identify the model parameters that require uncertainty reduction.

2. Reduce important model parameter uncertainties using optimally designed parameter inference experiments, and validate the system-level model via model validation experiments.
3. Update thermal model parameters based on experimental data while accounting for both model and experiment uncertainties.
4. Implement the methodology in industry-relevant case studies and demonstrate improvement to thermal model validation process.

As a result of the proposed methodology, the improvement to thermal model validation can be both form-related and process-related. The primary innovation of the methodology is in the improvement to the validation *process*. At the end of each case study, the process for the research methodology will be compared to a conventional approach to highlight areas of improvement. Improvement areas include:

- Information that is made available to the engineer through the new methodology that was previously unavailable following a conventional approach
- Computational techniques that are more efficient or require less thermal engineering expertise
- System-specific validation activities that might not have occurred following a conventional approach (e.g., a thermal test configured to certain experimental conditions)

An improvement to the validation process can also result in system form-related savings. Where applicable, direct comparisons will be made between the research methodology and a conventional approach in terms of resources (e.g., mass, power, or volume) gained or lost.

1.6 Thesis Roadmap

This thesis is organized into six chapters. The thesis roadmap structure is shown in Figure 1-11. Chapter 1 is the thesis introduction, including the background, motivation, literature review, and thesis objectives. Chapter 2 generally describes the Bayesian-based Model Validation (BMV) methodology used in this thesis. The first of two case studies is presented in Chapter 3 where BMV and a conventional thermal validation approach are applied to a passive spacecraft radiator. In Chapter 3, synthetic data are used in lieu of actual test data during the validation process. The REXIS instrument solar X-ray monitor (SXM) is the basis for the second case study. A general REXIS overview is given in Chapter 4. Chapter 5 presents the SXM case study where BMV is implemented, and real experiments are performed in a thermal vacuum chamber to validate the thermal model. Lastly, Chapter 6 concludes with a thesis summary, contributions, and future work.

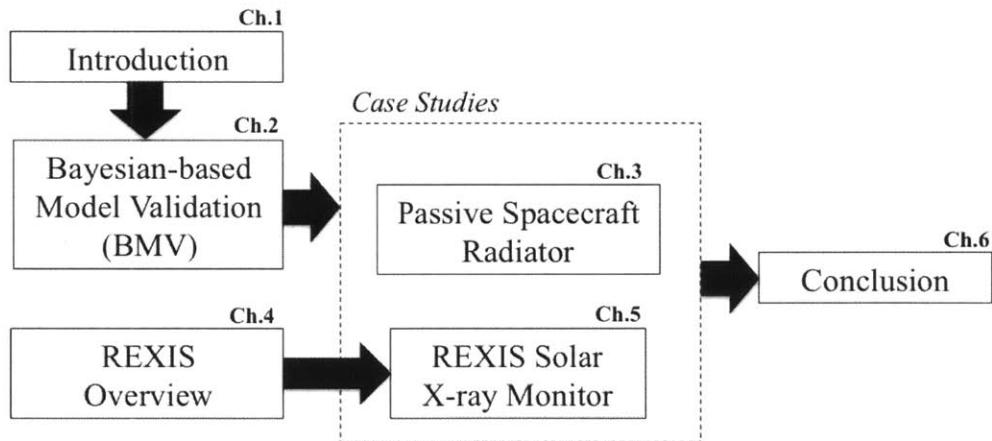


Figure 1-11: Thesis roadmap

Chapter 2

Bayesian-based Model Validation (BMV) Methodology

This chapter describes the Bayesian-based Model Validation (BMV) methodology developed to improve simulation model validation for spacecraft thermal systems. The methodology overview is shown in Figure 2-1. There are six main steps: (1) validation problem definition, (2) uncertainty propagation (UP) and parameter prioritization, (3) experimental goal setting, (4) design and implementation of experiments, (5) experimental model calibration and flight model update, and (6) validation problem documentation. The main steps are discussed in the sections below.

An important feature of the methodology is that the validation process is iterative, and the outcome of each step informs the validation procedures for the subsequent step. For example, a parameter inference experiment in step four can be performed to infer the value of parameter(s) that the forward uncertainty propagation in step two identified as being most important in creating uncertainty in the QoIs. In Figure 2-1, a system *redesign* is necessary if, in the process of experimenting with the system hardware or during calibration, it is learned that the design is architecturally flawed such that requirements cannot be met with *small* design modifications. In these cases, a redesign is necessary before validation can occur.

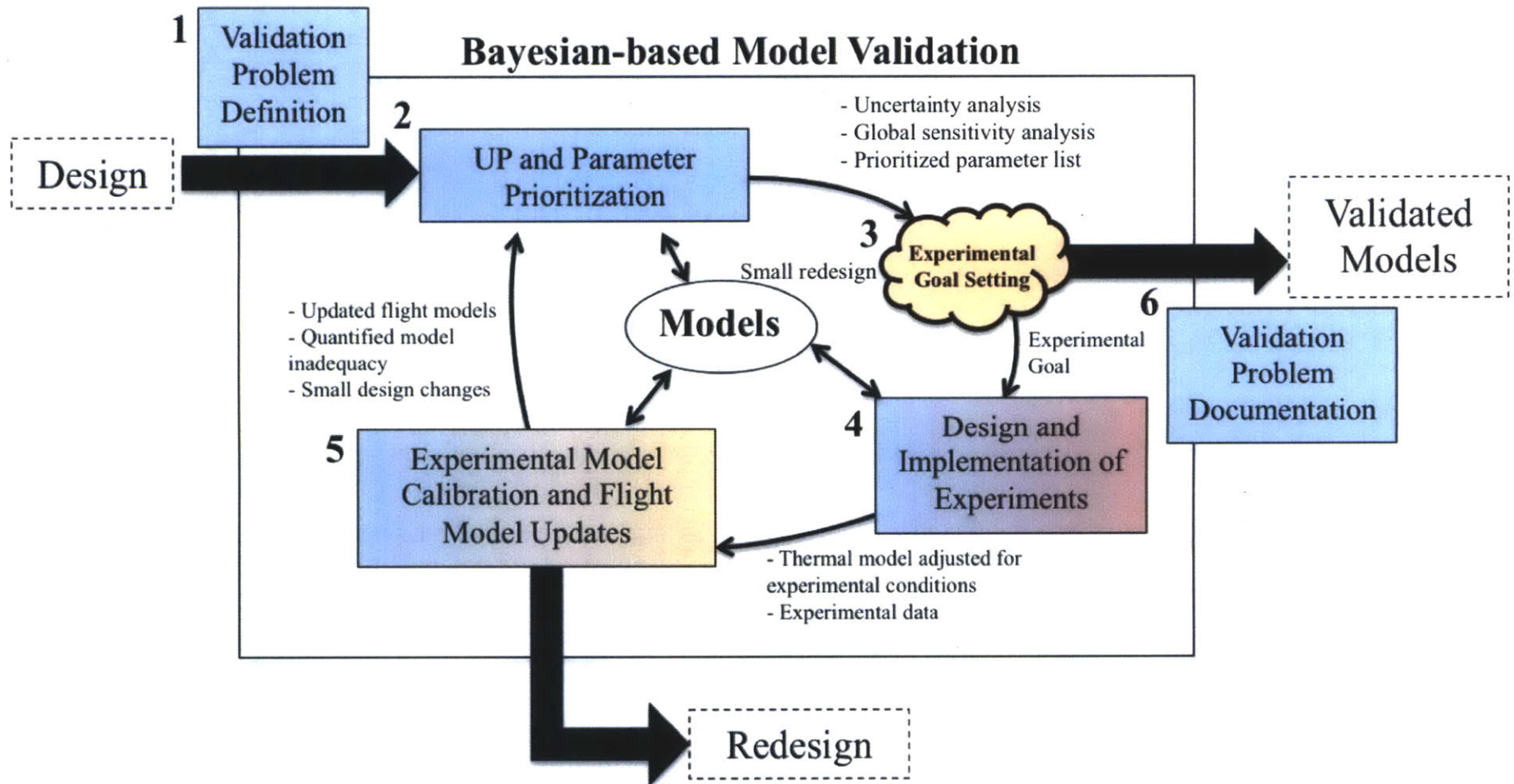


Figure 2-1: BMV methodology overview. Blue shading indicates analyses, orange shading indicates decision(s), and red shading indicates that physical hardware is involved. A model block is shown at the center of the diagram because steps two, four, and five are model-based processes within BMV.

2.1 Step 1: Validation Problem Definition

Validation problem definition is the first step of the BMV methodology. The components include:

1. Enumerate requirements for validation
2. Physical problem documentation
3. Model development and documentation

The first component is enumerating the requirements relevant to validating the model. For the thermal system, we are not concerned about the complete set of requirements for a spacecraft but only those requirements that pertain to validating the thermal system. For example, performance or functional requirements of the thermal system are relevant, whereas a requirement on material selection is not relevant because the design is considered frozen for the validation process. Understanding the requirements that the thermal system must meet is critical because uncertainty propagation will indicate the probability of satisfying the requirements. Acceptable designs are judged by comparing the mean and variance of the QoIs to the requirements. In step four of BMV, the goal of potential experiments depends on whether the QoI mean and variance are sufficient to meet the requirements.

The second component is to document the physical problem. The physical problem includes the system and the mission environment. Design information relevant to the thermal design is documented. Ultimately, a thermal model is created from this information so it is important to have a complete set of the thermally relevant design information. For example, the geometries, material properties, and surface coatings are relevant pieces of information, but the housekeeping software information is not relevant. The mission environment is equally important to document. Typically, the most extreme hot and cold environments drive the system design and analysis efforts. An understanding of the mission phases during which it is most difficult to achieve requirements is crucial to focus model validation efforts (uncertainty analysis, discussed in step two, helps to identify the driving mission thermal environments).

The third component is model development and documentation. Figure 2-2 shows how the physical problem maps to the simulation model [20]. The physical problem is how the physical system will perform during the mission. The conceptual model is an *approximation* of the physical problem and is what the engineer *intends* to capture with the simulation model. For example, physics (e.g., radiation from a surface) can intentionally be omitted from a model because it is thought to be insignificant. The simulation model approximates the solution of the conceptual model to provide *insight* into the behavior of the physical system in the mission environment. The decision of whether to include certain aspects of the physical problem into the conceptual and physical models impacts model fidelity, and model structure uncertainty.

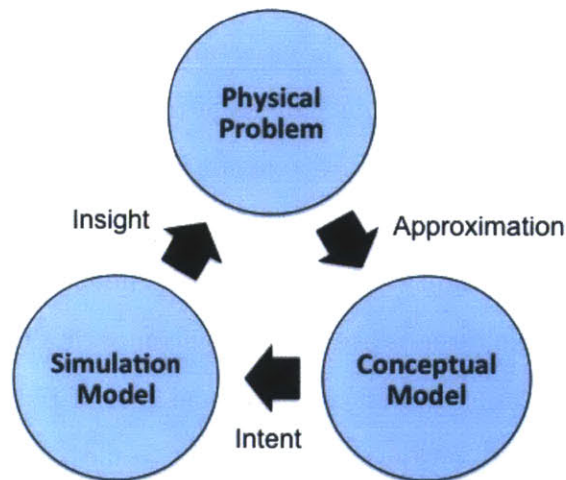


Figure 2-2: Mapping of physical problem, conceptual model, and simulation model. The conceptual model is an approximation of the physical problem and is what the engineer intends to capture with the simulation model. The simulation model predictions provide insight into the physical behavior of the system during the mission. Figure modified from [20, Fig. 2].

Prior to step two of BMV, the simulation models are constructed to provide initial indications of whether requirements will be met by the design. Equation (2.1) shows the structure of a simulation model:

$$\mathbf{y} = \eta(\mathbf{x}) \tag{2.1}$$

where \mathbf{y} is the model output, $\mathbf{x} = [x_1, x_2, \dots, x_n]^T$ is the vector of parameters, and η is the model. QoIs, denoted by \mathbf{Q} , are identified in \mathbf{y} that map to system requirements. In the context of this research, the QoIs are considered a subset of the model output, $\mathbf{Q} \subseteq \mathbf{y}$. Documenting the model structure (including fidelity of η), parameters, assumptions, and mission environments is necessary to ensure that model is implemented appropriately and is understood.

2.2 Step 2: Uncertainty Propagation and Parameter Prioritization

Once the validation problem is defined, the second step in BMV is the uncertainty propagation (UP) and model parameter prioritization process. In BMV, the UP process typically consists of the following components:

- UP goal setting
- Uncertainty classification
- Uncertainty characterization
- Uncertainty analysis
- Sensitivity analysis

The UP goal is to determine if there is adequate confidence that the requirements are met by the design, *as predicted by the model*. If there is insufficient confidence that a requirement will be satisfied, a prioritized list of model parameters is generated using the results of a global sensitivity analysis to target the parameters that are most influential in producing unsatisfactory QoI values. Later, additional research (e.g., experimentation) is performed to reduce the uncertainty in important parameters' distributions.

Before UP analysis begins, the uncertainty must be classified and characterized. Unless otherwise noted, all model parameter uncertainties are characterized probabilistically in BMV. Depending on the model parameter, information for initial parameter distributions

comes from different sources. For example, optical property values for surface coatings can be assigned initial distributions based on measured values or mission historical data. In contrast, the initial distribution for the power dissipation of an electronics board might come from analyses or developmental testing.

It is critical to ensure that the variance of the initial parameter distributions is appropriately conservative. The variance of a prior uncertainty distribution should be large enough to ensure that the true parameter value is captured, but not too large as to artificially inflate the parameter’s importance during uncertainty and global sensitivity analysis. Figure 2-3 notionally depicts two distributions for a parameter, x_j . If in reality the true variance of a parameter (blue, dashed curve) is *larger* than the initially assumed variance (red, solid curve), the model output is not only incorrect, but it is challenging to recover the true distribution variance during model calibration. If there is doubt as to whether an initial parameter distribution is conservative, a sensitivity analysis (manual adjustment of the uncertainty bounds) of the uncertainty to the QoI(s) can indicate the importance of the parameter’s variance. In some cases, it may not matter that a parameter has a large initial variance because it has little effect on the QoIs.

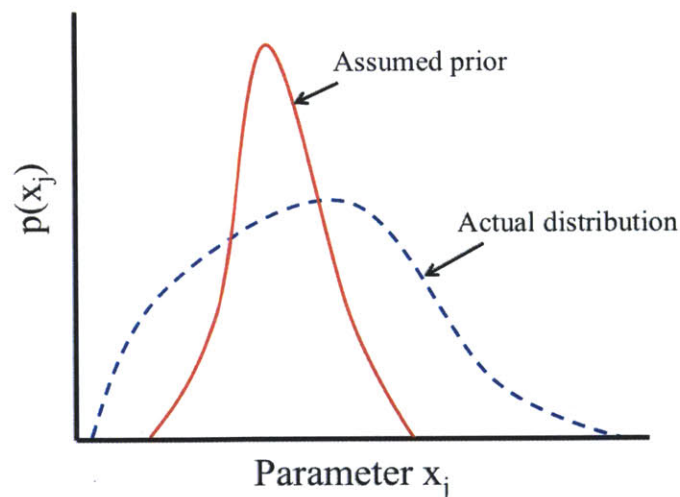


Figure 2-3: Notional depiction of a parameter, x_j , with an assumed uncertainty distribution (red, solid curve) whose variance is smaller than the actual distribution (blue, dashed curve).

In BMV, all models are assumed to be inadequate (i.e., having model structure errors). If there is prior knowledge of model inadequacy, a model discrepancy term, $\delta(\mathbf{x})$, can be included in the uncertainty and sensitivity analyses. For example, Equation (2.2) shows an

additive discrepancy function (i.e., accounted for in the model output), which accounts for all model inadequacy:

$$\mathbf{y} = \eta(\mathbf{x}) + \delta(\mathbf{x}) \quad (2.2)$$

where δ is dependent on the model parameters, \mathbf{x} . In practice, $\delta(\mathbf{x})$ can be represented in any form, though modeling $\delta(\mathbf{x})$ as a zero-mean Gaussian Process is common [26]. If there is no prior estimate of a model's inadequacy, the inadequacies of the model can be quantified and/or updated after experimentation. The final uncertainty propagation includes both parametric and model structure uncertainty.

Uncertainty and sensitivity analysis methods are used to examine the effect of uncertainty on the model output and guide future research. Uncertainty analysis (UA) indicates the expected mean and variance of the QoI(s) due to the parameter and model structure uncertainties. Monte Carlo (MC) simulations are one commonly used UA technique where many samples are drawn from the parameter distributions to approximate the characteristics of QoI distributions. To formulate MC simulations generally, the MC sample mean for an arbitrary function $h(X)$ is given by Equation (2.3):

$$\bar{h}_N = \frac{1}{N} \sum_{i=1}^N h(x_i) \quad (2.3)$$

where \bar{h}_N is the MC estimator and the samples, x_i , are randomly drawn from the parameter's probability distribution, $x_i \sim p_X(x)$. As the number of samples, N , goes to infinity, Equation (2.3) converges to the expectation in Equation (2.4) according to the law of large numbers:

$$E[h(X)] = \int h(x)p_X(x)dx \quad (2.4)$$

For example, X could be a parameter of a thermal model and $h(X)$ could be the thermal model output, $\eta(X)$. The MC sample mean in Equation (2.3) approximates the mean output value of a thermal model. Additionally, finding the variance of the thermal model evaluations, $h(x_i)$, performed during a MC simulation will provide the expected variance of the model output.

Sensitivity analysis is used to attribute the majority of the variance in the QoI(s) to the most influential parameters. Depending on the problem, sensitivity analyses consist of both local and global sensitivities. Local sensitivities explore how small perturbations in a parameter around a nominal or baseline parameter set affects model output (e.g., how a small change in a thermal conductance affects a component temperature). A common expression for the local sensitivity of a parameter to a single, scalar QoI, Q , is given by Equation (2.5):

$$S_{L,j} = \frac{\partial Q}{\partial x_j} \frac{x_{j,o}}{Q_o} \quad (2.5)$$

where x_j is the j^{th} parameter in \mathbf{x} and $\frac{\partial Q}{\partial x_j}$ is the analytical gradient (i.e., slope) of Q in the x_j direction. Q_o and $x_{j,o}$ are the nominal QoI and parameter values, respectively. The $\frac{x_{j,o}}{Q_o}$ term is included in Equation (2.5) to normalize $S_{L,j}$ so that different local parameter sensitivities can be compared non-dimensionally. Local sensitivities provide no global information regarding the effects of model uncertainties. Consequently, global sensitivity analysis (GSA) is a commonly used method for exploring global effects on model sensitivities.

GSA methods propagate parameter uncertainties through a model to capture a prescribed parameter's effect on the model output not just near a baseline solution but considering many possible solutions and the influences of many uncertain parameters. Many types of global sensitivities are used including "one-factor-at-a-time" methods (OAT) methods, Fourier Amplitude Sensitivity Test (FAST), and regression methods [45]. Variance-based GSA methods are used for guiding future research [70]. Variance-based methods rely on decomposition of the model, η , into main effects and interactions. The model is decomposed dimensionally as shown in Equation (2.6), which leads to a variance decomposition shown in Equation (2.7) [19, 69, 70]:

$$\mathbf{y} = \eta(\mathbf{x}) = \eta_o + \sum_{i=1}^n \eta_i(x_i) + \sum_{i=1}^n \sum_{j=i+1}^n \eta_{ij}(x_i, x_j) + \dots + \eta_{1,2,\dots,n}(x_1, \dots, x_n) \quad (2.6)$$

$$V_{total} = \sum_{i=1}^n V_i + \sum_{i=1}^n \sum_{j=i+1}^n V_{ij} + \dots + V_{1,2,\dots,n} \quad (2.7)$$

where the V_i are the main effect variances and the V_{ij} and higher order terms are the variances due to the parameter interactions. From this variance decomposition, Equation (2.8) and Equation (2.9) are the main effects and total global sensitivities, respectively, referred to as the Sobol' indices [121, 122]:

$$S_j = \frac{V_j}{V[Q]} = \frac{V[E[Q|x_j]]}{V[Q]} \quad (2.8)$$

$$S_{Tj} = 1 - \frac{E[V[Q|\mathbf{x}_{\sim j}]]}{V[Q]} \quad (2.9)$$

where the sensitivities are expressed for a single, scalar QoI, Q . The S_j 's are the main effects sensitivity indices, and the S_{Tj} 's are the total effects sensitivity indices. In Equation (2.9), $\mathbf{x}_{\sim j}$ are all the parameters except for the j^{th} parameter. If no interactions between parameters exist, then $\sum_{j=1}^n V_j = V[Q] = V_{total}$. In general, the sum of main effects indices is less than or equal to one (i.e., $\sum_{j=1}^n S_j \leq 1$), and the sum of total effects indices is greater than or equal to one (i.e., $\sum_{j=1}^n S_{Tj} \geq 1$).

Once the global sensitivities are found, the model parameters are prioritized by selecting those that most significantly contribute to the QoI variance. One method of prioritizing, Saltelli and Tarantola [71] outline specific procedures for using the main and total effects indices to select parameters to study. A limitation of Saltelli and Tarantola's [71] parameter prioritization procedure is that it relies on the assumption that the parameter(s) uncertainty can be completely reduced such that its value can be fixed to some point. Often, it is not possible to *completely* reduce a parameter's uncertainty. Allaire and Willcox [123] developed a variance-based sensitivity index function that prioritizes parameters based on the original main effects sensitivity, per Equation (2.8), and *the amount that a parameter's variance can be reduced through future research*. The sensitivity index function relaxes the assumption that a parameter's value can be fixed after future research and relies on previous model evaluations computed during the calculation of the original main effects sensitivities. The prioritized parameters are used to focus experimentation and calibration efforts in subsequent BMV steps.

2.3 Step 3: Experimental Goal Setting

The framework for experimental goal setting is shown in the cloud in Figure 2-1. Based on the results of UP and parameter prioritization, Figure 2-4 shows the decision tree for determining the experimental goal. There are four distinct outputs of the experimental goal setting step: (1) parameter inference experiment, (2) system-level validation experiment, (3) small redesign, or (4) validated system-level model(s).

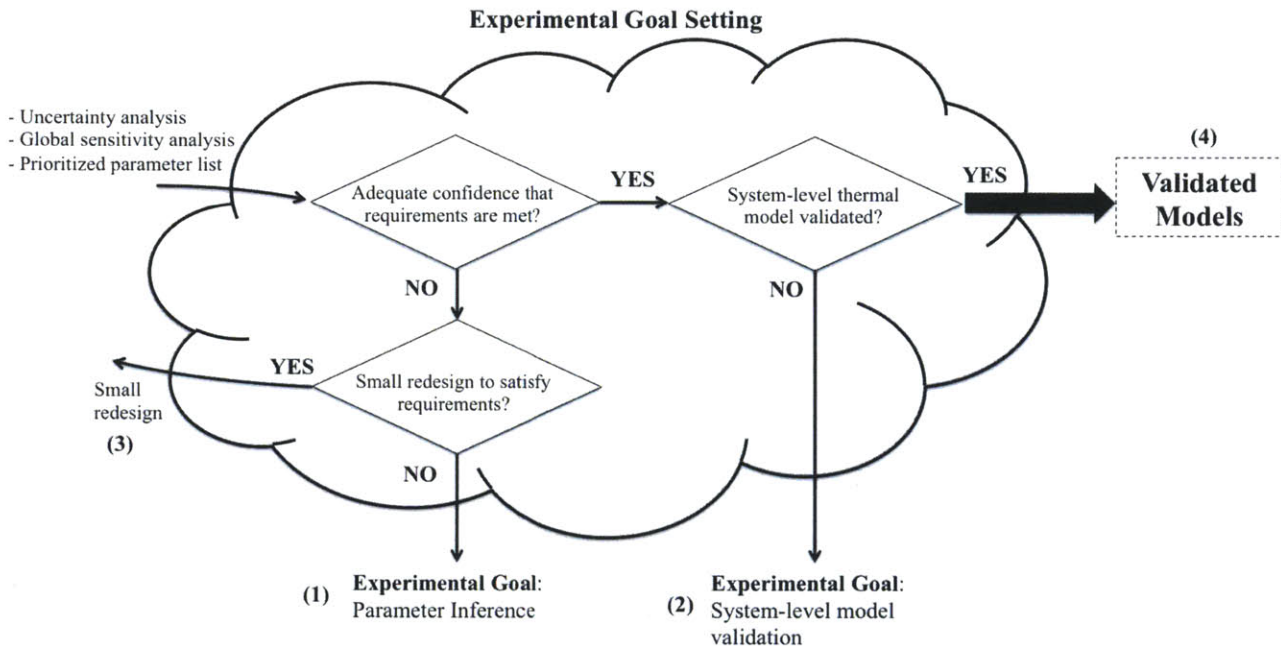


Figure 2-4: Experimental goal setting procedure for BMV methodology

The first decision gate is whether UA indicates that all QoI distributions meet requirements. While nominal QoI values must meet requirements, it is also important that there is sufficient confidence the requirement will be satisfied given the variance in the QoIs uncertainty. For example, a QoI variance that meets the requirement with 99% probability could be sufficient for a certain system. If there *is not* adequate confidence that the requirement is met, the next decision gate is whether to perform a small redesign to increase the probability of meeting requirements. A *small* redesign (e.g., surface coating change resulting in optical property changes in model or a small increase in radiator size) refers to a minor change in the thermal system design such that the system does not architecturally change, and there are little or no changes to the thermal model structure. Whether to perform a small redesign is

an engineering decision that must balance figures of merit such as the risk of change, impact to spacecraft resources and development efforts, marginal utility, and cost. For example, a change in a surface's coating could be a *small* change if thermally and mechanically feasible, but a change from a heat pipe to a mechanically-pumped fluid loop is a larger change with many system design implications at the spacecraft level.

The decision whether to implement a small redesign prior to a parameter inference experiment must consider both the potential increase in system knowledge by performing the parameter inference experiment and the cost/schedule impacts of implementing the experiment. If a small redesign is not performed, a parameter inference experiment is performed with the experimental goal of decreasing the uncertainty of an important parameter's true value. Parameter importance has already been determined from the prioritized parameter list in the previous BMV step. By measuring the parameter through the experiment, the parameter's uncertainty is decreased, reducing uncertainty in the QoI. In some cases, a small redesign may no longer be necessary after the parameter inference experiment. In other cases, a small redesign may still be necessary, but the increase in knowledge of a critical system sensitivity can be used to better inform a design change.

If there *is* adequate confidence that the requirement is met, the next decision gate is to answer whether the system-level thermal model has been validated. If the thermal model has not been validated, the experimental goal is to validate the model at the system level. To validate the model, the focus is demonstrating that the model is an adequate representation of the physical system in its mission environment. Finally, if the system-level thermal model is validated upon entering the second decision gate, no more experiments are conducted and the BMV validation steps one through five are complete.

In BMV, there are several important characteristics of a validated model:

- A model is calibrated to system-level test results where the test phases span the domain of its intended application of the model (i.e., the model is not used for extrapolation).
- With respect to the requirement(s), a validated model is accurate and the effects of uncertainty are understood and acceptable.
- Model inadequacy quantified by a discrepancy term(s), δ , either within the model, η ,

or applied to the model output as in Equation (2.2).

In many cases, it may not be possible to complete a system-level test over the entire domain of intended application of the model. For example, there are physical limitations (e.g., thermal vacuum chamber wall temperatures are achieved via liquid nitrogen or helium, which have boiling points warmer than the 2.73 K deep space temperature) and cost/schedule limitations (e.g., a single test phase for a spacecraft could require multiple days of testing and to span all possible operational modes/environments would require many test phases) with validation tests. In many cases, analysis can be done to show that extrapolation in the untested system modes/environments are very small sensitivity with respect to the QoIs. An accurate model with respect to requirements means that the predictive accuracy of the model is at least as good as the accuracy specified by the requirement. For example, model that can predict the temperature of a component to ± 3 °C is insufficient for a thermal requirement that specifies a component be held to a temperature ± 0.1 °C. Finally, the model inadequacy is quantified via a model discrepancy function using the results of the model validation experiment to account for persisting model uncertainties (e.g., parametric or model structure uncertainties). The model discrepancy function provides insight into the magnitude and direction of the model error and can be used to improve the model's predictive accuracy.

2.4 Step 4: Design and Implementation of Experiments

The objective of step four is to design and implement an experiment according to the experimental goal set in step three. Step four of BMV contains three components:

1. Adjust thermal model for experiment
2. Design of Experiments (DOE)
3. Experiment implementation

The first two components are often completed in parallel because aspects of the thermal model cannot be set until the experiment is designed. For example, the experimental power

dissipation values are a parameter of the thermal model but also can be a design condition used to maximize the experimental utility during experimental design.

The flight thermal model is modified to capture the physics of the experimental configuration. These modifications are necessary because the thermal configuration of the experiment is different than that of the mission. For example, a radiator might see a temperature of deep space of approximately 2.73 K during the mission, but the model should be modified to match the temperature of the thermal vacuum chamber walls (e.g., a radiation sink of ≈ 80 K if the walls are cooled via liquid nitrogen). Furthermore, if the experiment is performed on only a portion of the system, the components of the system that will not be included in the experiment must be removed from the model. The modifications to the model must also include ground support equipment that change the heat transfer physics of the system (e.g., temperature sensor leads to a cold portion of the system can introduce conductive parasitic heat loads that are not present on the flight model). Once modified, the thermal model is used to make predictions for the system during the experiment.

Two categories of experiments are performed based on the experiment goal: (1) parameter inference and (2) system-level thermal model validation. Parameter inference experiments use OED/OBED techniques to design system-specific experiments that reduce uncertainty in a critical system parameter(s). By reducing uncertainty in a critical parameter, system knowledge increases and uncertainty in the QoIs decreases. Parameter inference experiments are prototype-level experiments performed with hardware that is flight-like. System-level validation experiments are used to generate data to calibrate the model and quantify the model discrepancy at the system level over domain of intended application of the system. Validation testing requires the full system flight hardware.

For parameter inference experiments, Bayes' Theorem underpins all OBED techniques. To develop OBED generally, let θ be the parameters of interest, identified in step two of BMV, to be updated by the experimental data. Let \mathbf{d} be experimental design variables (i.e., the conditions selected to perform the experiment). Bayes' Theorem, given by Equation (2.10), gives the change in the state of knowledge about the parameters of interest:

$$p(\theta|\mathbf{z}, \mathbf{d}) = \frac{p(\mathbf{z}|\theta, \mathbf{d})p(\theta)}{p(\mathbf{z}|\mathbf{d})} \quad (2.10)$$

where the experiment was held at conditions, \mathbf{d} , to obtain the experimental result/data, \mathbf{z} . That is, $p(\theta|\mathbf{z}, \mathbf{d})$ are the updated values of the parameters of interest, θ , after the experiment. In Equation (2.10), $p(\theta)$ is the prior knowledge of the parameters of interest, $p(\mathbf{z}|\mathbf{d})$ is the experimental evidence, and $p(\mathbf{z}|\theta, \mathbf{d})$ is the likelihood function for observing \mathbf{z} .

In OBED, an experiment's utility is defined to find a \mathbf{d} that is optimal with respect to the experimental goal. Using a decision theory approach, Lindley [87] developed an expression for an experiment's expected utility, shown in Equation (2.11), which is the foundation for most OBED approaches:

$$U(\mathbf{d}) = \int_{\mathcal{Z}} \int_{\Theta} u(\mathbf{d}, \mathbf{z}, \theta) p(\theta|\mathbf{z}, \mathbf{d}) p(\mathbf{z}|\mathbf{d}) d\theta d\mathbf{z} \quad (2.11)$$

where $U(\mathbf{d})$ is the expected utility, \mathcal{Z} is the support of \mathbf{z} , Θ is the support of θ , and $u(\mathbf{d}, \mathbf{z}, \theta)$ is the utility function. The utility function is selected based on the experimental goal. For parameter inference experiments, a common utility function is the Kullback-Leibler (KL) divergence, a measure of relative information gain [79, 83]. Other experimental utilities include the variance of a parameter's posterior, $V[\theta|\mathbf{z}, \mathbf{d}]$, and the posterior predictive variance of the QoI(s), $V[\mathbf{Q}|\mathbf{z}, \mathbf{d}]$. The experimental utility functions, such as the utility in Equation (2.11), are generated by sampling the thermal model and provide a numerical value for experiments at different thermal conditions, \mathbf{d} . The parameter inference experiment that is feasible and yields the highest utility is selected to reduce uncertainty in the thermal parameter(s) of interest.

For parameter inference experiments, it is important to select \mathbf{z} such that the parameters of interest are highly observable in the experimental data. In general, it is not necessary that the experimental data, QoIs, and requirements all refer to the same physical quantity. In some cases, it may be advantageous to define a quantity or metric to measure that improves the parameter inference because it is more observable for a given test (i.e., \mathbf{z} is not necessarily the measured values for \mathbf{Q}). For example, Table 2.1 provides an example of how to select observable quantities for a good parameter inference experiment. The first parameter of interest is a thermal resistance, R_t , and the second parameter of interest is a specific heat, c_p (i.e., $\theta = [R_t, c_p]^T$). An experiment is performed with the goal to measure both

parameters, and there are two quantities that can be measured: a steady state temperature, $T(t = \infty)$, and system time constant, τ . The heat capacities and thermal resistance both affect the transient response of a thermal system (and thus, the time constant), but only the thermal resistance affects the steady state response. The selection of observable quantities, $\mathbf{z} = [T(t = \infty), \tau]^T$, is good because each parameter of interest has an *independent* influence on the parameters of interest.

Table 2.1: A parameter inference experiment to measure the value of two parameters. The first parameter is a thermal resistance, R_t , and the second parameter is a specific heat, c_p . It is possible to measure two physical quantities: a steady state temperature, $T(t = \infty)$, and system time constant, τ . A check indicates that the observable quantity depends on the parameter of interest.

		Observable Quantities of Interest, \mathbf{z}	
		$T(t=\infty)$	τ
Parameters of Interest, θ	R_t	✓	✓
	c_p		✓

System-level thermal model validation experiments test the system over the domain of thermal environments and modes of the mission *to quantify the uncertainty in the model predictions*. Validation experiments for a system are different from the parameter inference experiments in that they necessarily occur at the system level. Validation experiments include multiple test phases in order to: (1) demonstrate that a design will meet system requirements and (2) generate data that allow for validation through model calibration processes. The system-level experiment is critical because the system-level model's inadequacy is quantified from the results. For the thermal system, system-level validation can be formulated along the lines of classical DOE (i.e., following GEVS or MIL340) or OBED can be used. As Huan and Marzouk [83] comment, an experimental goal of making accurate predictions can be satisfied by formulating the design objective around the distribution of the model outputs conditioned on the data. Regardless of the DOE approach, the system-level validation experiment should test the system over the entire domain of its intended mission application so that once the model is calibrated, the flight predictions are not extrapolations of calibrated parameters.

Finally, the experiment is implemented to gather experimental data. Implementation includes:

- Procurement and assembly of system
- Instrumentation of the system and test bed
- Configuration of the data acquisition software and hardware
- Personnel to monitor the experiment and perform real time analyses of results (problem diagnosis, if necessary)

Based on the experiment design and modified thermal model predictions, the experiment is conducted according to detailed plans that outline all actions required in each phase of the experiment. All discrepancies during the experiment are documented and later investigated. The output of the design and implementation of experiments step includes an adjusted model representing the system under test and experimental data.

2.5 Step 5: Experimental Model Calibration and Flight Model Update

In the experimental model calibration and flight model update step of BMV, experimental results from step four are used to update the model. To calibrate a parameter, calibration parameters, γ , are identified in \mathbf{x} to be updated in the calibration process. The calibration parameters can include the experimental design parameters of interest, θ , from step four as well as other parameters identified for calibration (i.e., $\theta \subseteq \gamma$ and $\gamma \subseteq \mathbf{x}$). The remaining parameters in \mathbf{x} and not in γ are the control parameters (i.e., fixed model parameters not identified as calibration parameters) whose values are not updated by the calibration.

The general model form for the calibration and correlation follows the K-O approach [42], shown in Equation (2.12) and Equation (2.13):

$$\mathbf{z} = \eta(\mathbf{x}) + \delta(\mathbf{x}) + \epsilon_m \quad (2.12)$$

$$\zeta(\mathbf{x}) = \eta(\mathbf{x}) + \delta(\mathbf{x}) \quad (2.13)$$

where \mathbf{z} are the data, $\eta(\mathbf{x}, \gamma)$ is the model prediction, $\zeta(\mathbf{x})$ is the true physical process, \mathbf{x} is the vector of all model parameters, and ϵ_m is the observation error. Although $\gamma \subseteq \mathbf{x}$, γ is written explicitly in Equation (2.12) and Equation (2.13) to emphasize both the focus of the calibration and the model's dependency on γ . The persisting model inadequacy is grouped into the model discrepancy term, $\delta(\mathbf{x})$. The true physical process, $\zeta(\mathbf{x})$, refers to the actual thermal system QoIs during the mission (e.g., actual mission component temperatures). The model discrepancy is equal to the difference between the true physical process and the model predictions, $\zeta(\mathbf{x}) - \eta(\mathbf{x}, \gamma)$. If the model were to perfectly predict the behavior of the system, the model discrepancy would be zero, $\delta(\mathbf{x}) = 0$. For this research, $\delta(\mathbf{x})$ is additive (i.e., included with the model output), as shown in Equation (2.12). Alternatively, $\delta(\mathbf{x})$ could be included within $\eta(\mathbf{x}, \gamma)$ [60].

Bayes' Theorem is utilized as the basis for updating prior parameter information. Rewritten into the calibration problem framework, Bayes' Theorem is given by Equation (2.14):

$$p(\gamma|\mathbf{z}, \mathbf{x}) = \frac{p(\mathbf{z}|\gamma, \mathbf{x})p(\gamma)}{p(\mathbf{z}|\mathbf{x})} \quad (2.14)$$

where $p(\gamma|\mathbf{z}, \mathbf{x})$ is the posterior distribution for the calibration parameters, $p(\mathbf{z}|\gamma, \mathbf{x})$ is the likelihood, $p(\gamma)$ is the prior distribution, and $p(\mathbf{z}|\mathbf{x})$ is the evidence. Using this formulation, prior parameter distributions are updated based on experimental evidence through an inferential process. For large models, computing $p(\gamma|\mathbf{z}, \mathbf{x})$ is typically done numerically using methods such as Markov chain Monte Carlo (MCMC) methods [116] since analytical solutions are not available.

During calibration, it is not always clear whether a difference between \mathbf{z} and $\eta(\mathbf{x})$ is due to parametric uncertainty in \mathbf{x} or model inadequacy in η . Two example approaches to determine the existence of significant model inadequacy are:

- Calibrate the parameters first without $\delta(\mathbf{x})$. After calibration, $\delta(\mathbf{x})$ is introduced to account for the remaining model-data discrepancy. If there is no parameter set within the bounds set by the prior parameter distributions that cause the model to match the

data, this is evidence of significant model inadequacy.

- Define independent calibration data sets and evaluation data sets from the experiment (i.e., set up a cross-validation problem). Calibration sets are used to calibrate γ and the evaluation sets determine how well the model predictions, $\eta(\mathbf{x}, \gamma)$ match the data, \mathbf{z} . The evaluation sets are used to quantify $\delta(\mathbf{x})$.

Whether to quantify $\delta(\mathbf{x})$ after calibration, perform cross-validation, or implement a different approach, the process for identifying model structural errors during calibration is an engineering decision that depends on the nature of the specific problem. Accurately quantifying the inadequacy term is important so that the calibration parameters approximate the *true* physical values of the system. If model structural errors are neglected, the calibrated parameter distributions will be biased. The SXM case study in Chapter 5 will show how Bayesian calibration techniques can provide evidence of whether a difference between \mathbf{z} and $\eta(\mathbf{x})$ is due to parametric uncertainty or model inadequacy. Furthermore, Chapter 5 will show how the model discrepancy can be quantified to use for prediction to account for model inadequacy.

Once the experimental model is updated, it is used to update the flight model. Because the emphasis during calibration was on learning the *true* physical parameter values, the parameter values (e.g., thermal strap conductance) are updated directly. However, model adjustments that apply only to the experimental configuration are omitted. For example, test temperature sensor leads that were modeled in the experiment to account for the parasitic heat load through wires are not included in the flight model since they are not present during the mission. Furthermore, environmental factors (e.g., thermal vacuum wall emissivity) are not updated in the flight model since the mission thermal environment is different.

There are two possible outcomes of the experimental model calibration and flight model update step. First, if experimental results reveal major architectural system design flaws or model errors, redesign may be necessary if small design changes (e.g., slightly increasing a radiator's surface area) are not sufficient to show that the design will meet requirements. In this redesign scenario, the BMV methodology is exited to redesign the system. The second (and preferred) outcome of the experimental model calibration and flight model update step

is an updated flight model. The flight model contains the posterior distributions from the model calibration process. Furthermore, if the experimental goal is system-level validation of the model, the model's inadequacy is quantified (i.e., there is understanding of how well the model approximates the behavior of the real system). Finally, based on the insight gained from the experiment, small design changes can be considered, as necessary, to improve the system performance.

2.6 Step 6: Validation Problem Documentation

Validation problem documentation is the sixth and final step of the BMV methodology. Having completed steps one through five, the thermal model(s) is now validated. This step has three components:

1. Documentation of efforts made during steps one through five BMV methodology
2. Documentation of updates to requirements, the physical problem, and model
3. Recommendations for *small* design changes

The validation problem documentation step is included to communicate what was done during validation and how it changed the thermal design and/or models. Once steps one through five of BMV are documented (including all actions taken and outcomes), the elements of BMV step one must be revisited. If requirements, the physical problem, or the model have changed, the change and its effects must be well understood. For example, if based on the validation process physics that were originally omitted from the model are now included, the model structure and parameters for these physics must be added to the model documentation.

Finally, based on the validated thermal model and final UP results, *small* design changes may be desired. In this case, *small* design changes are those that require minor changes in a design to achieve better system performance. For example, small changes include a small increase to a radiator's size, more thermal gap filler between interfaces, or slightly more thermal isolation between hot and cold components. These small changes, based on information learned during the validation process, could be inexpensive from a system resource

perspective but offer large performance benefits. Large changes due to architectural flaws in a design result in models that cannot be validated for the current system. Thus, large changes are outside the scope of this step and are associated with system redesign.

Documentation is any written report, spreadsheet, code, or presentation that conveys information about the requirements, system, model, or validation process. To ensure that detailed information is captured accurately, it is critical to document throughout the validation process. Any change to a system requirement or resource parameter is typically managed by the systems engineer and must be communicated at the systems and discipline level. Milestone review presentations (e.g., Critical Design Review) are necessary but insufficient forms of documentation of the thermal system validation process. For a typical spacecraft thermal system, written reports are produced to document the model structure and parameter assumptions, thermal balance testing, and thermal model calibration after testing.

Chapter 3

Passive Spacecraft Radiator Case Study

The first case study in this thesis considers model validation for a passive spacecraft radiator. The primary objective of the radiator case study is to demonstrate the BMV methodology on a simple system. A secondary objective is to compare the implementation of BMV to a conventional validation approach and discuss the differences in the validation *processes* and in the final *form* of the radiator. Section 3.1 presents BMV implemented on a passive spacecraft radiator, and Section 3.2 presents a conventional model validation approach (i.e., model validation as it could be implemented in practice) on the same passive spacecraft radiator. The analyses in Sections 3.1 and 3.2 are independent. Section 3.3 reviews the important lessons from Sections 3.1 and 3.2 and compares BMV to conventional model validation.

3.1 Bayesian-based Model Validation (BMV)

3.1.1 Step 1: Validation Problem Definition

Validation Requirements

Consider a small, body-mounted aluminum spacecraft radiator shown in Figure 3-1. There is one relevant thermal requirement:

There shall be a probability of at least 95% that the maximum steady state radiator temperature be less than $-60\text{ }^{\circ}\text{C} = 213.15\text{ K}$.

There are two parts to the requirement: an absolute temperature and a minimum probability. In order to satisfy the radiator's thermal requirement, both parts of the requirement must be satisfied (i.e., even if nominal performance satisfies the absolute temperature part of the requirement, the minimum probability must be satisfied when model uncertainties are included in the analysis).

Although it is convention to use temperature units of Celsius ($^{\circ}\text{C}$), sometimes it is convenient in this case study to express temperatures within the model in Kelvin (K). Where model predictions are compared to the requirements, both units are used. The mapping between units is translational: $T_{\text{Celsius}} = T_{\text{Kelvin}} - 273.15$.

Physical Problem Documentation

The physical radiator problem is shown in Figure 3-1. Assume that the radiator is fixed to a truss panel via low thermal conductivity standoffs such that conduction through the standoffs is negligible. Furthermore, assume that the radiator has a distributed heat load at its center, Q_{in} , and has a full view of deep space. The radiating surface, with heat rejection, $Q_{rad,out}$, has been painted with a highly emissive white paint. There is a single mission phase under consideration corresponding to these steady state conditions. The mission life is assumed to be short such that degradation of the radiator surface coating is not a factor. The numerical values of the geometry, material properties, heat loads, and coatings are set based on the design shown in Figure 3-1.

Model Development and Documentation

Based on the physical problem in Figure 3-1, the conceptual model shown in Figure 3-2 is developed. In the conceptual model, the radiator is assumed to be isothermal (i.e., $Q_{rad,out}$ does not vary spatially). By neglecting in-plane conduction, the conceptual model is known to be inadequate. In the general case, all model inadequacies in the conceptual model are

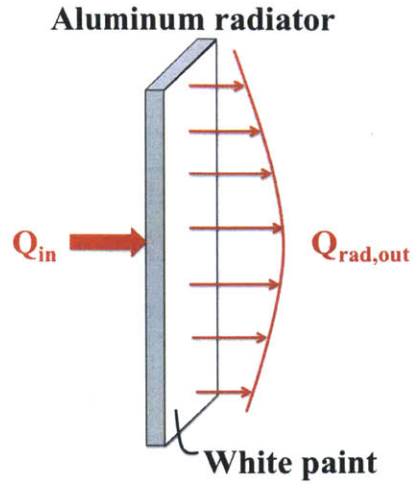


Figure 3-1: Illustration of physical problem for radiator case study

not known and those that are known are difficult to quantify prior to experimentation.

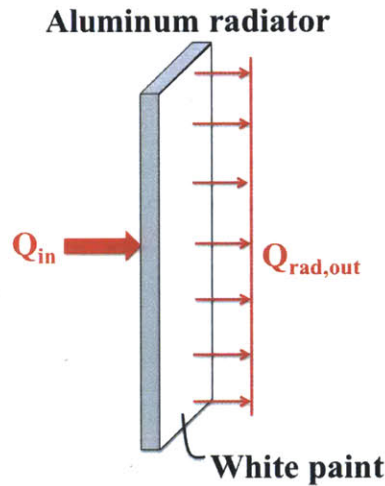


Figure 3-2: Illustration for conceptual model of radiator case study

Using the conceptual model in Figure 3-2, a thermal model is constructed to predict the maximum radiator temperature given certain model parameter values. The thermal model for the case study is the Stefan-Boltzmann equation, arranged to provide the radiator temperature as shown in Equation (3.1):

$$T_{rad} = \eta_{rad}(\mathbf{x}) = \sqrt[4]{\frac{Q_{in}}{\sigma \epsilon A} + T_{space}^4} \quad (3.1)$$

where η_{rad} is the radiator model, Q_{in} is defined above as the input heat load, σ is the

Stefan-Boltzmann constant, ε is the radiator emissivity, A is the area of the radiator, T_{rad} is the temperature of the radiator, and T_{space} is the temperature of space (i.e., the sink temperature for the radiator). There are four parameters such that $\mathbf{x} = [Q_{in}, \varepsilon, A, T_{space}]^T$. T_{rad} is the QoI for this problem and maps to the thermal validation requirement. The nominal thermal model parameters are shown in Table 3.1. The Stefan-Boltzmann constant, $\sigma = 5.67 \times 10^{-8} \frac{W}{m^2 K^4}$, is a physical constant. Given a set of parameter values, the thermal model (Equation (3.1)) will yield an estimate for T_{rad} .

Table 3.1: Nominal parameter values for sample radiator problem thermal model

Parameter/Constant	Nominal Value	Units
Heat load, Q_{in}	10	W
Emissivity, ε	0.90	–
Temperature of Deep Space, T_{space}	2.725	K
Area, A	0.1	m ²

3.1.2 Step 2: Uncertainty Propagation and Parameter Prioritization—First Pass

The radiator case study traverses BMV steps two through five more than once to validate the radiator model, as shown in Figure 2-1. The following sections present each step of BMV sequentially and each step *pass* is denoted (e.g., the second time step two is performed is referred to as step two, second pass).

The first component of the UP process and parameter prioritization is to characterize the uncertainty. In this case study, all parametric uncertainty is characterized probabilistically. All parameter values are initially defined as having uniform distributions of the form shown in Figure 3-3. The uniform distribution of a parameter, x , is given by:

$$p(x) = \begin{cases} \frac{1}{b-a} & ; x \in [a, b] \\ 0 & ; x \notin [a, b] \end{cases} \quad (3.2)$$

where a is the minimum parameter value, b is the maximum parameter value, and $p(x)$

is the probability density value. Table 3.2 characterizes the uniform distribution for each parameter. The distribution for Q_{in} is based on the maximum and minimum variation expected in the input heat load arbitrarily selected as a parameter of the larger spacecraft system. The distribution for ε is based on conservative beginning of life values for white paint [4]. Finally, the variability assumed for T_{space} is based on measurements made by the FIRAS instrument on the COBE mission [124], and the variability of A is based on the tolerance to which the radiator is machined. The Stefan-Boltzmann constant, σ , is a physical constant and does not exhibit variation.

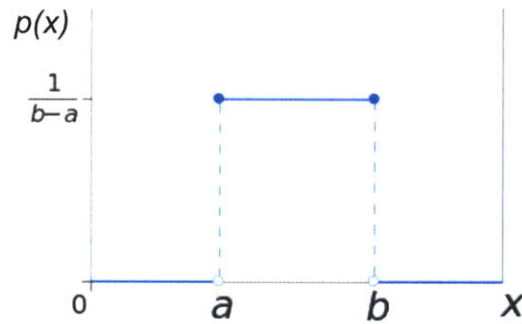


Figure 3-3: Notional uniform distribution form for initial parameter distributions in radiator case study

Table 3.2: Initial parameter uncertainty characterization for radiator thermal model. All parameter uncertainty distributions are uniform distributions. From Figure 3-3, a is the minimum value, and b is the maximum value of a parameter.

Parameter	Nominal Value	Min Value, a	Max Value, b	Units
Q_{in}	10	9.5	10.5	W
ε	0.90	0.80	0.93	–
T_{space}	2.725	2.723	2.727	K
A	0.1	0.0998	0.1002	m ²

Using Equation (3.1) and the nominal model parameter values in Table 3.2, the temperature of the radiator, T_{rad} , is approximately -62.8 °C. Nominally, the radiator design meets the required -60 °C absolute temperature. However, the parametric uncertainties, which have not yet been considered, must be propagated through the model to determine if the minimum probability of the thermal requirement is satisfied.

With the uncertainty distributions for the model parameters defined, evaluating the effects of the parameter uncertainty is next. Although the radiator model is known to be an inadequate representation of the real system during the mission, model structure uncertainties are temporarily ignored. In this case study, model inadequacy is quantified later following a model validation experiment. To perform an uncertainty analysis, a Monte Carlo (MC) simulation is performed to propagate the parameter uncertainties through the model. By tailoring Equation (2.3) for the radiator model, the expected output value is given by Equation (3.3):

$$\bar{\eta}_{rad,N} = \frac{1}{N} \sum_{i=1}^N \eta_{rad}(\mathbf{x}_i) \quad (3.3)$$

where $\bar{\eta}_{rad,N}$ is the MC estimator, the number of samples is $N = 10^5$ (shown to be sufficient via convergence analysis), and each sample, $\mathbf{x}_i = [Q_{in,i}, \varepsilon_i, A_i, T_{space,i}]^T$, is a realization of the model parameters sampled from the parameter distributions. Figure 3-4 shows the MC result for the radiator case study. Figure 3-4 is an empirical cumulative distribution function (CDF) for the QoI, T_{rad} , and the temperature requirement for the QoI value ($-60 \text{ }^\circ\text{C} = 213.15 \text{ K}$) is shown. The probability is 42% that the radiator temperature requirement will not be met based on the model parameter uncertainty.

Although it is clear that the probability does not satisfy the thermal requirement, sensitivity analysis is needed to prioritize the model parameters according to those that most significantly create variance in T_{rad} . First, the local sensitivities per Equation (2.5) are found to evaluate the effects of small perturbations about the nominal solution. Furthermore, the local sensitivity analysis will demonstrate the limitations of such an approach for guiding future uncertainty reduction efforts. Equation (3.4) shows Equation (2.5) tailored for the radiator model used to find the local sensitivities:

$$S_{L,j} = \frac{\partial T_{rad}}{\partial x_j} \frac{x_{j,o}}{T_{rad,o}} \quad (3.4)$$

where x_j is the j^{th} parameter in \mathbf{x} and $\frac{\partial T_{rad}}{\partial x_j}$ is the analytical gradient (i.e., slope of T_{rad} in the x_j direction). $T_{rad,o}$ and $x_{j,o}$ are the nominal QoI and input values, respectively. Although analytical gradients are available in this case study, analytical gradients are often

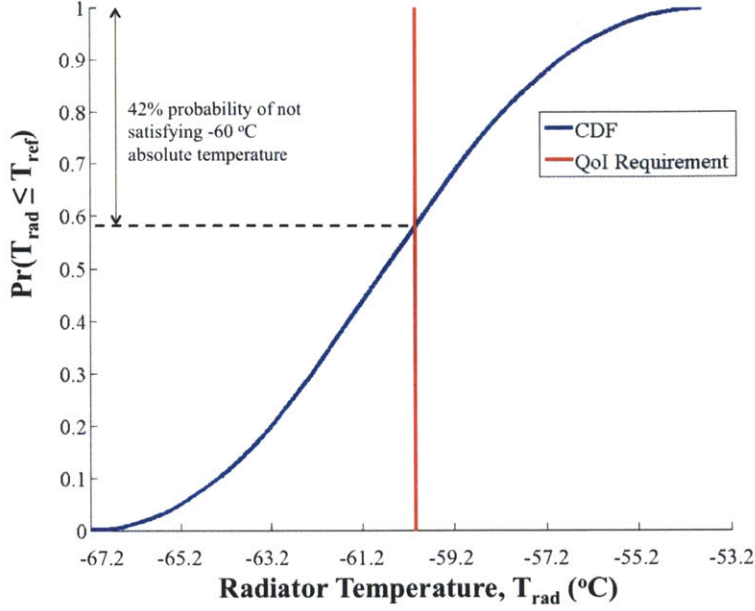


Figure 3-4: Preliminary uncertainty analysis results for radiator problem. CDF indicates the probability of the radiator temperature being less than or equal to a temperature, T_{ref} , given the radiator model’s parametric uncertainty.

not available or difficult to compute. To maintain applicability for a more general case, a first-order, forward finite differencing scheme, shown in Equation (3.5), is applied to approximate the analytical gradient in Equation (3.4) using a small perturbation in the nominal value of x_j :

$$\frac{\partial T_{rad}}{\partial x_j} \approx \frac{T_{rad}(x_{j,o} + \Delta x_j) - T_{rad}(x_{j,o})}{\Delta x_{j,o}} \quad (3.5)$$

Each parameter’s local sensitivity index, per Equation (3.4), is shown in Figure 3-5.

The normalized local sensitivities in Figure 3-5 indicate how a 1% increase in the parameter’s value affects the radiator temperature in the neighborhood of the nominal design. Based on the radiator’s local sensitivities about the nominal design, it is observed that the coating emissivity, area, and heat load are nearly equal in importance, whereas the temperature of space is insignificant. The coating emissivity, area, and heat load have the same magnitude because each parameter has the same order in Equation (3.1). Using Figure 3-5 to select parameter(s) for uncertainty reduction is misleading because it does not include the uncertainty distributions of the parameters. Local sensitivities provide no global information

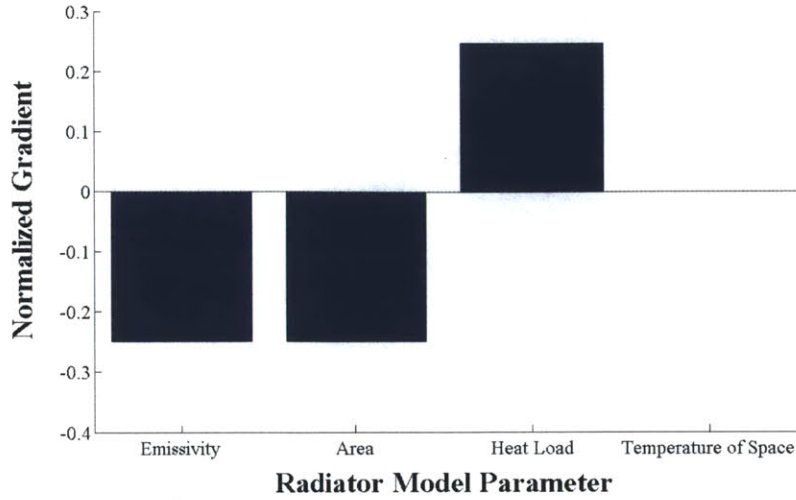


Figure 3-5: Local sensitivity analysis for isothermal radiator model parameters about nominal design

regarding the effects of model parameter uncertainties. Global sensitivities are needed to prioritize the model parameters.

A “one-factor-at-a-time” (OAT) approach is used to compute the global sensitivities for the radiator model. In an OAT setting, one parameter is perturbed while all other parameters are held at the nominal or baseline value. Saltelli and Annoni [125] explain several practical reasons for why OAT is a commonly used approach:

- The nominal values for parameters are generally the best estimate or expected values
- The approaches systematically explores the effects of one parameter at a time on model output
- The approaches are often simple to implement

Under the assumption of parameter independence, Equation (3.6) shows the sensitivity for the j^{th} model parameter using the OAT approach:

$$S_j = \frac{V[T_{rad}|\mathbf{x}_{\sim j,o}]}{V[T_{rad}]} \quad (3.6)$$

where $V[T_{rad}|\mathbf{x}_{\sim j,o}]$ is the variance of T_{rad} due to *only* the variation of the j^{th} parameter, and $V[T_{rad}]$ is the variance of T_{rad} due to all parameter uncertainty in \mathbf{x} . The $\mathbf{x}_{\sim j,o}$ term indicates

that all parameters except for the j^{th} parameter are fixed at their nominal values. $V[T_{rad}]$ normalizes the sensitivity so that $S_j \in [0,1]$. As $V[T_{rad}|\mathbf{x}_{\sim j,o}]$ increases toward $V[T_{rad}]$, S_j goes to one.

The OAT approach shown in Equation (3.6) is implemented on the four parameters of η_{rad} using random sampling of the j^{th} parameter's distribution and the values in Table 3.1 for the nominal parameter values. Figure 3-6 shows the global sensitivities for the radiator thermal model. The sensitivities for A and T_{space} are negligible due to the small variance of their initial distributions. From this point forward in the case study, the parameter values for A and T_{space} will be fixed at their nominal values. Both the radiator coating, ϵ , and the input heat load, Q_{in} , are important parameters in contributing to the variance of T_{rad} . Based on the global sensitivities, the prioritized list of model parameters are:

1. Radiator coating emissivity
2. Input heat load

The above list indicates the order in which research should be devoted toward model parameters to reduce the unsatisfactory variance in T_{rad} .

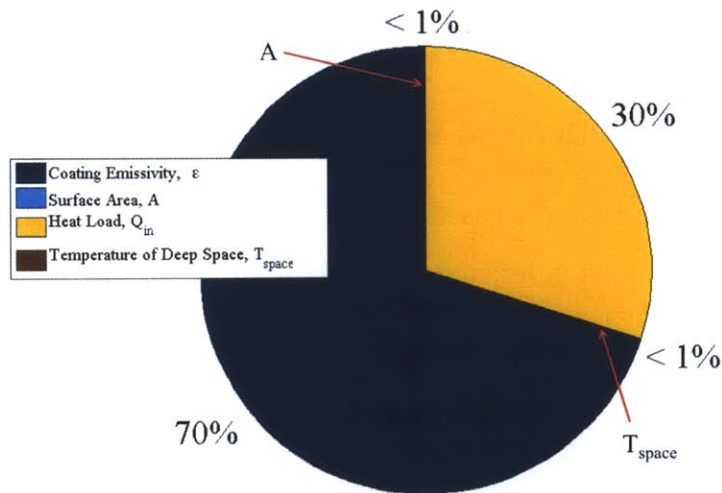


Figure 3-6: Preliminary “one-factor-at-a-time” global sensitivity analysis results for radiator problem

3.1.3 Step 3: Experimental Goal Setting—First Pass

In Figure 3-4, UA indicates that there is a 42% probability that the radiator temperature requirement will not be met. Furthermore, the global sensitivities in Figure 3-6 show that the radiator coating emissivity is the most significant contributor to the radiator temperature uncertainty. In Figure 2-4, the first decision gate is whether there is adequate confidence that the requirements are met. The answer is **no** because the 58% probability of achieving the -60°C radiator temperature is too low (requirement is 95%).

Although the radiator could be made larger to increase the probability of meeting the requirement, the sensitivity analysis indicates that because the emissivity value so strongly affects the radiator temperature, a reduction in the emissivity's uncertainty could increase the probability of meeting the requirement. Answering the second decision gate in Figure 2-4 (whether a small redesign will be performed), a small design change in the form of increasing the radiator's size will not be performed. Thus, the experimental goal is to infer the true value of the most critical parameter, the radiator coating emissivity, to reduce its variance, whereby reducing the radiator temperature variance.

3.1.4 Step 4: Design and Implementation of Experiments—First Pass

Thermal Model Modification and Experimental Design

In step four of BMV, the radiator case study shows how to modify the thermal model and design the optimal parameter inference experiment. The radiator model in Equation (3.1) is modified to match the conditions of the experiment. An important assumption of the parameter inference experiment is that the thermal configuration has the same architecture as the flight configuration (e.g., full view factor to thermal vacuum wall chamber and no conductive parasitics to radiator plate due to instrumentation/fixtures). The experimental design problem will consider the values of different experimental conditions, but not different experiment architectures. There is only one modification to the model formulation: a measurement error term, ϵ_m , is added to capture the temperature sensor error associated with measuring the QoI, T_{rad} . The experimental model is given by Equation (3.7):

$$T_{rad} = \sqrt[4]{\frac{Q_{in}}{\sigma \epsilon A}} + T_w^4 + \epsilon_m \quad (3.7)$$

where the vacuum chamber wall temperature, T_w , replaces T_{space} because the test is not in the space environment. Equation (3.7) is of the form of Equation (3.8):

$$T_{rad}(\theta, \mathbf{d}, \epsilon_m) = \sqrt[4]{\frac{d_1}{\alpha \theta}} + d_2^4 + \epsilon_m \quad (3.8)$$

where $\mathbf{d} = [d_1 \ d_2]^T = [Q_{in} \ T_w]^T$ are the experimental design conditions (the only controllable parameters to create different experiments), θ is the parameter of interest (radiator coating emissivity), and α is a constant equal to the product of A and σ . Both the parameter of interest and experimental design parameters are parameters of the model (i.e., $\theta, \mathbf{d} \subseteq \mathbf{x}$).

Values for the quantities in \mathbf{d} are selected from the set of all possible experiments.

In designing an experiment to reduce uncertainty in the coating emissivity, it is important not to artificially constrain \mathbf{d} . In the experiment, we are not limited to the range of values expected during the mission, and the optimal experiment might lie outside the mission values for \mathbf{d} . The range of values considered for each experimental design condition is shown below:

- Heat load, $d_1 = Q_{in}$: 0 to 50 W
- Thermal vacuum wall temperature, $d_2 = T_w$: 1 to 300 K

The range of values for Q_{in} and T_w exceeds the ranges in Table 3.2 to explore regions of the feasible experimental design space that could yield higher parameter inference utility. Based on the earlier results of GSA, A is fixed at the nominal design value 0.1 m^2 . The sensor error, ϵ_m , is assumed to be normally distributed with zero mean and standard deviation of 0.15 K , $\epsilon_m \sim \mathcal{N}(0, 0.15^2) \text{ }^\circ\text{C}$. Given the experimental model form in Equation (3.8) and the range of possible experimental conditions shown above, \mathbf{d} must be selected for the optimal experiment.

To design an optimal parameter inference experiment, the experimental utility function is set to the variance of T_{rad} conditioned on \mathbf{d} . That is, at conditions \mathbf{d} , the experimental utility is given by Equation (3.9):

$$U(\mathbf{d}) = V[T_{rad}|\mathbf{d}] \quad (3.9)$$

where $T_{rad}|\mathbf{d}$ is the conditional radiator temperature given experimental conditions \mathbf{d} . T_{rad} , given \mathbf{d} , is uncertain due to uncertainty in θ and ϵ_m . The experimental utility in Equation (3.9) is analogous to the high response variance criterion [126]. The optimal experiment for the radiator will maximize $U(\mathbf{d})$ to find the optimal experiment, \mathbf{d}^* . An experiment at \mathbf{d}^* means that the variability in the parameter of interest, θ , creates the maximum variability in T_{rad} such that θ is easiest to infer (i.e., the utility function makes the observable quantity very sensitive to the value of the parameter of interest).

To find \mathbf{d}^* , a brute force approach is used. A MC simulation is performed at each set of possible experimental conditions to build up $T_{rad}|\mathbf{d}$ by storing $T_{rad}(\theta_i, \mathbf{d}, \epsilon_{m,i})$ for each i^{th} sample. The $\theta_i, \epsilon_{m,i}$ terms are drawn from their respective probability distributions. Once each conditional distribution $T_{rad}|\mathbf{d}$ is built, the variance of each distribution, $V[T_{rad}|\mathbf{d}]$, is evaluated. By varying \mathbf{d} over the many possible experiments (resolution of 5 K in T_w and 1 W in Q_{in}), an experimental utility contour map is constructed as shown in Figure 3-7. The optimal experimental conditions, \mathbf{d}^* , are found to be $Q_{in} = 50$ W and $T_w = 1$ K. At temperatures below approximately 100 K, T_w has little effect on the utility. The experiment is improved mostly by increasing Q_{in} below 100 K. However, T_w is increasingly important for temperatures above 100 K and large heat loads, an intuitive trend because T_w is raised to the fourth power in Equation (3.7). In Figure 3-7, the nominal design for the radiator is shown by the blue point to illustrate how a test at these experimental conditions would be suboptimal in terms of $U(\mathbf{d})$. There are two important considerations:

- Since the experiment's design is model-based and the model is only an approximation to reality, the results are not guaranteed to be the actual optimal experiment for the real system.
- Although the optimal experiment is at $Q_{in} = 50$ W and $T_w = 1$ K, these conditions are difficult to achieve (1 K is near absolute zero). In the neighborhood of these conditions in Figure 3-7, there are conditions that are easier to achieve and will yield *nearly* the same utility (e.g., $Q_{in} = 40$ W and $T_w = 80$ K, where 77 K is the boiling point

temperature of liquid nitrogen).

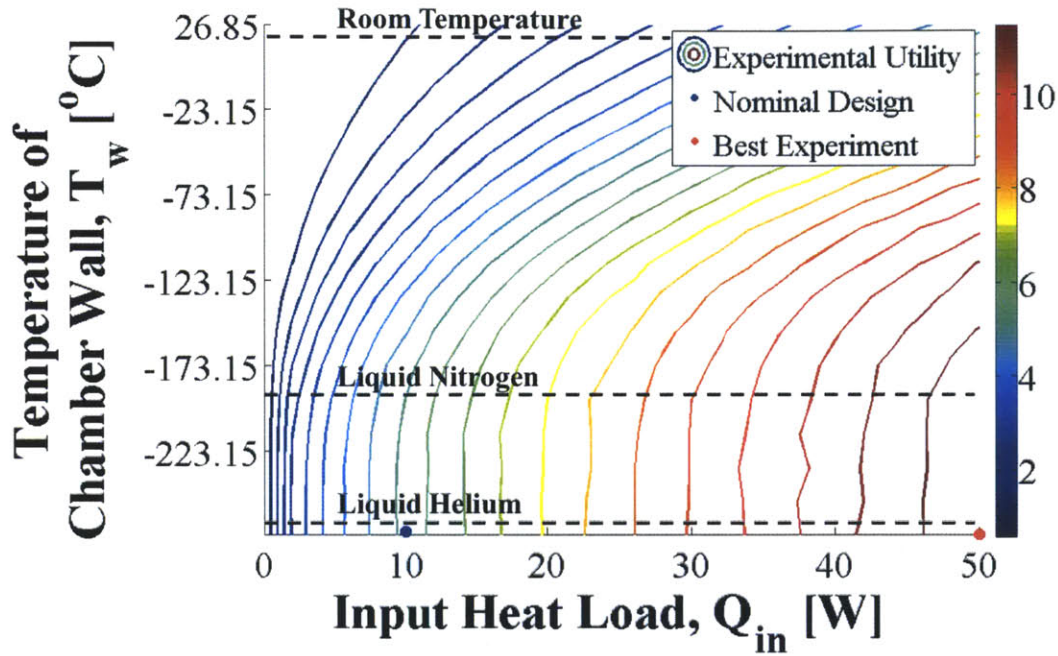


Figure 3-7: Experimental utility, $U(\mathbf{d})$, contour plot of experiments at $\mathbf{d}=[Q_{in} T_w]^T$. Units of $U(\mathbf{d})$ in °C. Number of MC samples to build $T_{rad}|\mathbf{d}$ is 10^4 . The boiling point temperatures for liquid nitrogen and helium are shown; also, room temperature is shown.

Experiment Implementation

Synthetic data are created in lieu of implementing the experiment with hardware. A numerical experiment is performed at $Q_{in} = 40$ W and $T_w = 80$ K. It is assumed that there is a minimum of one sensor (at the radiator center), and a heater applied to the radiator backside to generate the input heat load of 40 W with a footprint of approximately 20 x 20 cm. The thermal effects of instrumentation are neglected in the numerical experiment. Because the conceptual model is physically inadequate, there is an opportunity to include additional sensors to capture the in-plane gradients. From this information, the model inadequacy could be quantified for a particular \mathbf{x} , and the model structure can be modified, if necessary.

To generate the synthetic data for the experiment, a high fidelity radiator model is created using Thermal Desktop. The high fidelity model, shown in Figure 3-8, has 225 nodes and includes the effects of in-plane conduction within the radiator. To create the experimental

results for the parameter inference experiment, the high fidelity model is used in the following way:

1. Assume an arbitrary *truth* emissivity within the bounds of the prior uncertainty distribution
2. Store emissivity value and simulate parameter inference experiment at $[d_1, d_2] = [40 \text{ W}, 80 \text{ K}]$
3. Record the center radiator temperature to simulate the measurement and use the temperature as synthetic data to update the isothermal radiator model emissivity

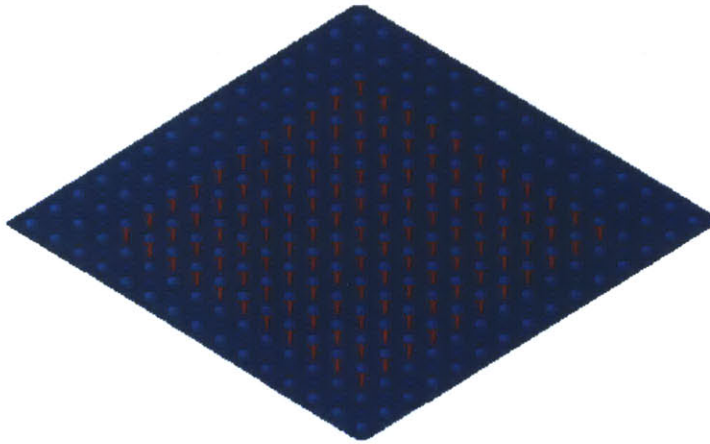


Figure 3-8: High fidelity Thermal Desktop radiator model (225 node model). Red arrows denote input heat load with footprint size 20 x 20 cm.

Following the process outlined above, the truth emissivity from the parameter inference experiment is assumed to be 0.92. The truth emissivity is within the bounds of the initial coating emissivity distribution. Figure 3-9 shows the temperature map of the radiator for the parameter inference experiment, where the warmest areas are at the radiator's center where the heat load is applied. A single steady state temperature is recorded from center of the radiator equal to 25.25 °C. In this case, it is clear that the isothermal radiator assumption is a poor assumption because the in-plane gradient is approximately 5 °C from the center to the edge of the radiator. However, the effect of in-plane gradients on validating the model may not ultimately matter. Before changing the structure of the model to increase accuracy, the effects of the model inadequacy are quantified later to determine their significance.

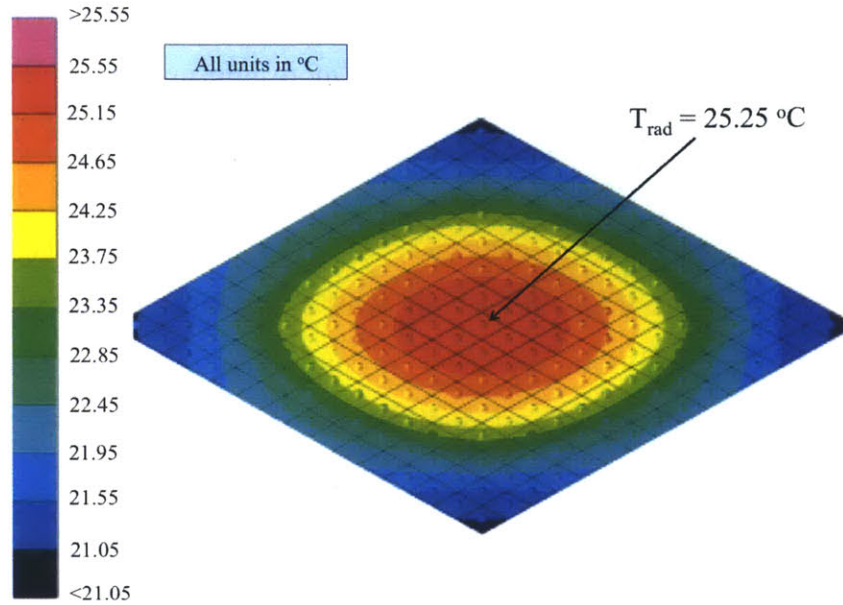


Figure 3-9: High fidelity Thermal Desktop radiator model solution for parameter inference experiment with $[d_1, d_2] = [40 \text{ W}, 80 \text{ K}]$

3.1.5 Step 5: Experimental Model Calibration and Flight Model Update—First Pass

In step five of BMV, the thermal model is calibrated to the experimental data. On this pass, the coating emissivity of the radiator is updated based on the results of the parameter inference experiment in step four. Using the K-O approach framework in Equation (2.12), the following is the nomenclature for calibration problem:

- The temperature measurement is the data/observation, $z = 25.25 \text{ }^\circ\text{C}$
- The radiator coating, ϵ , is the single calibration parameter, γ
- The radiator area, A , thermal vacuum chamber wall temperature, T_w , and input heat load, Q_{in} , are the control parameters, \mathbf{x}
- The temperature sensor measurement error is the observation error, ϵ_m
- The inadequacy term, $\delta(\mathbf{x})$, is neglected (quantified later, following model validation experiment)

Although $\delta(\mathbf{x})$ is currently unknown, if additional sensors are included in the experiment to capture in-plane gradients of the radiator, there is more information available to estimate the inadequacy of the model since the model currently assumes an isothermal radiator.

Using Bayes' Theorem as written in Equation (2.14) and a brute force, random sampling (of ε and ε_m) approach to build up each $p(z|\gamma_i, \mathbf{x})$, the uncertainty distribution for the radiator coating emissivity is updated. Figure 3-10 shows the uniform prior distribution and the posterior distribution. The prior distribution is the initial uncertainty distribution assigned to the parameter, and the posterior distribution is the uncertainty distribution that has been updated based on new information (e.g., experimental data). The posterior has a significantly smaller variance than the prior and is centered on an emissivity of approximately 0.895. Compared to the true emissivity, the emissivity is smaller because the emissivity found via the isothermal radiator model is an *effective emissivity* that includes the in-plane conduction implicitly.

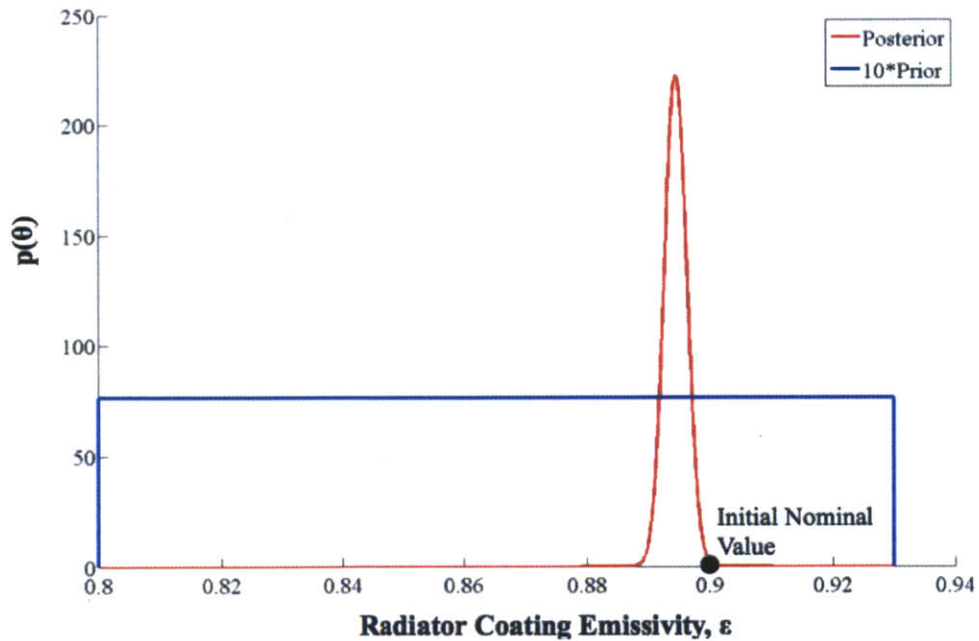


Figure 3-10: Model calibration results for radiator coating emissivity based on numerical experiment at $[d_1, d_2] = [40 \text{ W}, 80 \text{ K}]$ and a temperature measurement of $25.25 \text{ }^\circ\text{C}$.

Although Figure 3-10 illustrates an effective reduction in variance from the parameter inference experiment, the model inadequacy is neglected. Strictly following the K-O approach [42], the parameter values and a model discrepancy function, $\delta(\mathbf{x})$, are inferred simulta-

neously. Since it is known that $\delta(\mathbf{x})$ is nonzero (i.e., that the model is inadequate), it is important to ask, *how does the presence of a nonzero $\delta(\mathbf{x})$ affect the calibration shown in Figure 3-10?* To answer this question, an additive discrepancy function is temporarily included in the evaluation of $p(z|\gamma_i, \mathbf{x})$ and assumed to be normally distributed with zero mean such that $\delta(\mathbf{x}) = \delta(\beta) = \mathcal{N}(0, \beta^2)$ where β is a constant scalar. For a nonzero β , we are interested in the posterior distribution of ε (i.e., the conditional distribution of the posterior $p(\varepsilon|\delta(\beta))$). Figure 3-11 shows a contour map of the of the joint distribution of β and ε showing the density values for the radiator coating emissivity, ε , for given values of β . At $\beta = 0$, the distribution for ε is equivalent to Figure 3-10. It is clear from Figure 3-11 that as β values increase, the variance of the coating emissivity posterior increases.

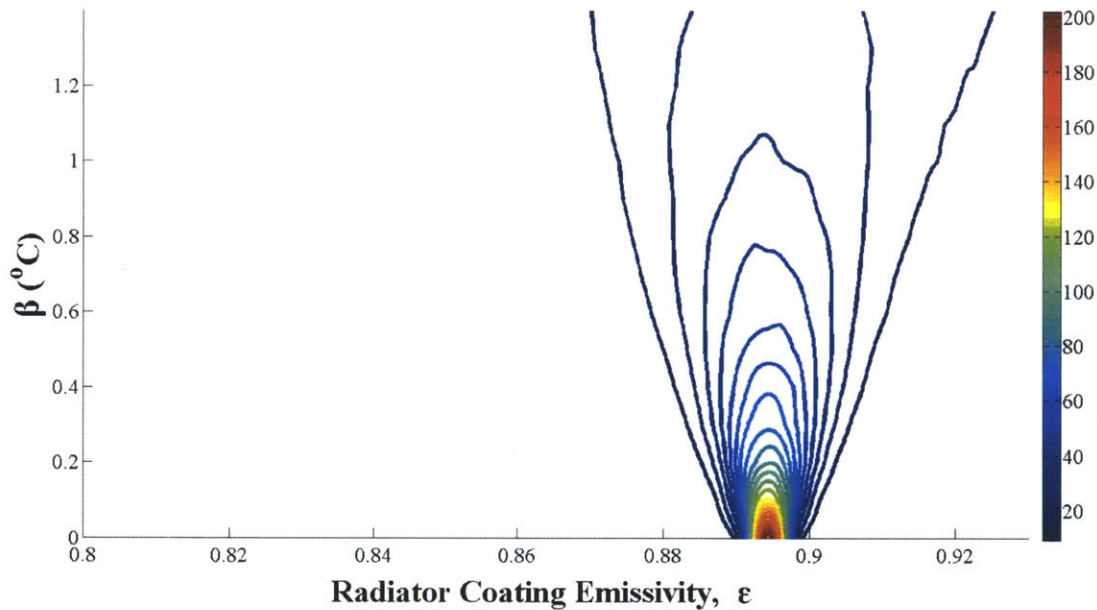


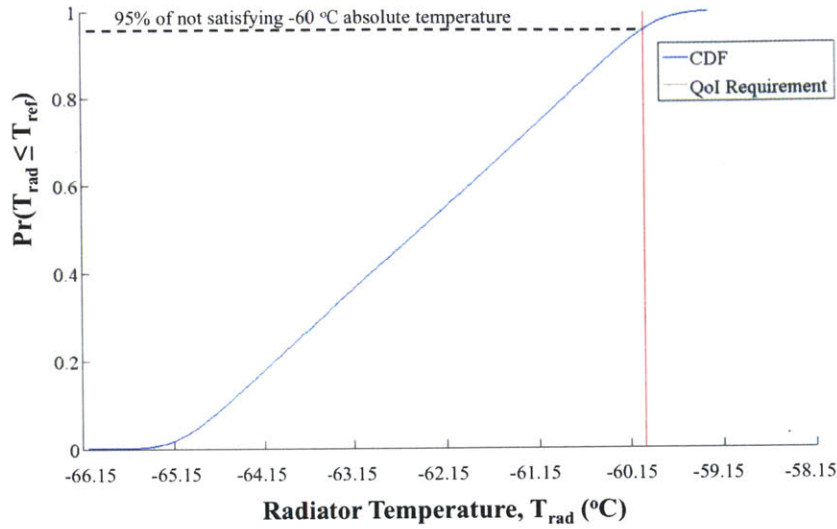
Figure 3-11: Contour plot of the joint distribution of β and ε showing the effect of increasing the variance of an additive model discrepancy, $\delta(\beta)$, on the posterior distribution for the radiator coating emissivity. Figure 3-10 shows the posterior distribution of ε for $\beta = 0$.

The posterior distribution from Figure 3-10 is carried forward in the case study. Although the effects of a nonzero $\delta(\mathbf{x})$ are shown in Figure 3-11 to be significant, there is no prior knowledge of the variance of $\delta(\mathbf{x})$. Furthermore, the parameter inference experiment is performed *outside* the domain of parameter values expected for the mission (for T_{space} and Q_{in}) so any attempt to quantify $\delta(\mathbf{x})$ from the experiment is an extrapolation of \mathbf{x} . Because

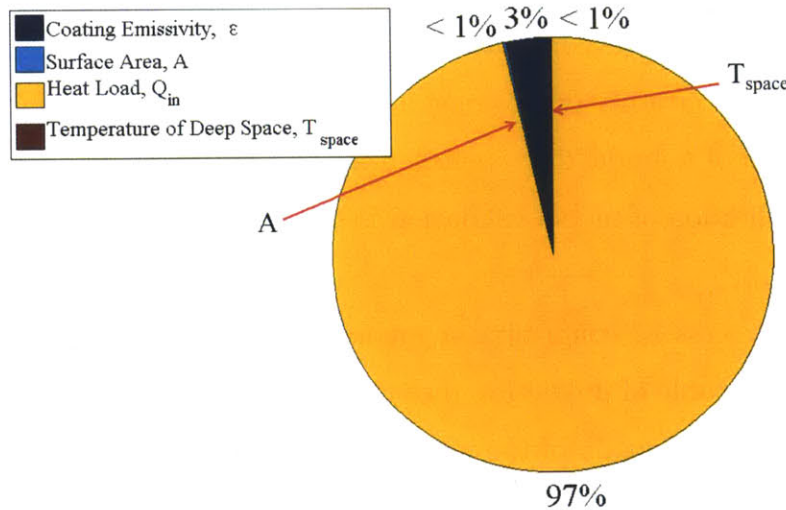
the model inadequacy is neglected here, a validation experiment that seeks to quantify $\delta(\mathbf{x})$ is still needed. Furthermore, if $\delta(\mathbf{x})$ is found to be significant, the posterior shown in Figure 3-10 is significantly biased and could be recalculated to include $\delta(\mathbf{x})$. Ultimately, $\delta(\mathbf{x})$ will be included in the final uncertainty analysis to show that, with the effects of model inadequacy included, the radiator temperature requirement is satisfied.

3.1.6 Step 2: Uncertainty Propagation and Parameter Prioritization—Second Pass

Following Figure 2-1, the next BMV step is to repeat step two with the updated thermal model. Using the posterior radiator coating emissivity shown in Figure 3-10, the initial UP from Figure 3-4 and Figure 3-6 is updated. Using Equation (3.3) and Equation (3.6) to complete the UA and GSA as before, Figure 3-12 shows updated empirical CDF and global sensitivities for the radiator problem. Whereas before UA indicated a 42% probability that the $-60\text{ }^{\circ}\text{C}$ temperature wouldn't be met, there is now a 95% probability that the temperature is met. Furthermore, Figure 3-12b indicates that majority of the remaining uncertainty is due to the uncertainty in the input heat load. The parameter inference experiment increased the probability of meeting the required $-60\text{ }^{\circ}\text{C}$ temperature and reduced the sensitivity of the coating emissivity, ϵ .



(a) Uncertainty Analysis



(b) Global Sensitivity Analysis

Figure 3-12: Uncertainty and global sensitivity analysis (OAT sensitivities) results for radiator problem with updated radiator coating emissivity distribution. CDF indicates the probability of the radiator temperature being less than or equal to a temperature, T_{ref} , given the radiator model’s parametric uncertainty.

3.1.7 Step 3: Experimental Goal Setting—Second Pass

With the results of step two of BMV updated, the next step is revisiting the experimental goal setting framework in BMV step three. In Figure 3-12, the UA indicated that there is a 95% probability that the radiator temperature requirement will be met. For the radiator case study, the answer to the first decision gate in Figure 2-4 is **yes** because the minimum

probability specified by the radiator requirement is satisfied. The second decision gate is whether the system-level thermal model has been validated. The answer to the second decision gate is **no** because the parameter inference experiment is performed outside the domain of application of the radiator (heat load, Q_{in} , is 40 W but the maximum expected on-orbit is 10.5 W) with the goal of reducing uncertainty in the coating emissivity. Thus, the experimental goal is to validate the radiator model.

3.1.8 Step 4: Design and Implementation of Experiments—Second Pass

On this pass of design and implementation of experiments, the experimental goal is to validate the isothermal radiator model. Because the calibration of the radiator coating emissivity, ϵ , does not include uncertainty due to model structure errors, validation in this context requires a quantification of a model discrepancy, $\delta(\mathbf{x})$, to account for persisting model inadequacy. The earlier definition of model validation is included here for convenience:

model validation: process of confirming a model is an adequate representation of the physical system and is capable of predicting the systems behavior accurately with respect to the requirements within the domain of the intended application of the model [20, 21]

For this case study, the key phrase is *within the domain of the intended application of the model*. Only the parameter ranges from Table 3.2 are relevant because experimental design for model validation considers interpolation, not extrapolation. The model is to be validated over the range of parameter values expected during the mission. Thus, the range of experimental conditions considered in the parameter inference experiment ($Q_{in} = 0 - 50$ W and $T_w = 1 - 300$ K) does not apply.

Experimental conditions for the model validation experiment are selected that bound the range of conditions seen on-orbit. Two test phases are performed, summarized by Table 3.3. The values for ϵ and A are not included in Table 3.3 because they are not controllable experimental conditions but are aspects of the radiator design. Although the temperature

of deep space, $T_{space} = 2.73$ K, is significantly lower than the lowest possible chamber wall temperature of $T_w = 80$ K, the chamber wall temperature for the experiment is 80 K since it is the lowest achievable temperature. In Section 3.1.11, a sensitivity analysis is performed to show that the effect of testing at 2.73 K versus 80 K is negligible with respect to the radiator's temperature due to the fourth order of the temperature of deep space in the Stefan-Boltzmann equation. Values for Q_{in} are selected at its upper and lower limit and are the only difference between the two test phases. The DOE for the validation experiment is the same as the hot and cold test cases in a conventional validation approach.

Table 3.3: Experimental conditions for each test phase of the model validation experiment

Parameter	Nominal Value	Test Phase #1	Test Phase #2	Units
Q_{in}	10	9.5	10.5	W
T_{space}	2.725	80	80	K

Following the same approach as the parameter inference experiment, the high fidelity Thermal Desktop model is used to generate synthetic data for the model validation experiment. The experiment with conditions shown in Table 3.3 is implemented using the true emissivity of 0.92 in the high fidelity model in Figure 3-8. By simulating the two validation test phases, the temperature values to be used as synthetic data are shown below:

- Test Phase 1: $T_1 = -64.8$ °C = 208.4 K
- Test Phase 2: $T_2 = -59.6$ °C = 213.6 K

The above temperatures are used to quantify the model discrepancy for the radiator model in step five of BMV.

3.1.9 Step 5: Experimental Model Calibration and Flight Model Update—Second Pass

Using the model validation experiment data points, $\mathbf{z} = [T_1, T_2]^T$, and the calibrated thermal model, the model inadequacy is quantified via an additive model discrepancy function. Rearranging Equation (2.12) to solve for $\delta(\mathbf{x})$:

$$\delta(\mathbf{x}_i) = T(\mathbf{x}_i) - \eta_{rad}(\mathbf{x}_i) - \epsilon_m \quad \text{for } i = 1, 2 \quad (3.10)$$

where $T_i = T(\mathbf{x}_i)$ are the temperature measurements (scalar), $\eta_{rad}(\mathbf{x}_i)$ is the model prediction (distribution due to variability in ϵ), and ϵ_m is the measurement noise (distribution). To calculate $\delta(\mathbf{x}_1)$ and $\delta(\mathbf{x}_2)$, the posterior distribution for the emissivity shown in Figure 3-10 and the sensor measurement uncertainty are used. Because $\eta_{rad}(\mathbf{x}_i)$ and ϵ are distributions, $\delta(\mathbf{x}_i)$ are also distributions.

The model discrepancy distributions, $\delta(\mathbf{x}_i)$, found using Equation (3.10) are shown in Figure 3-13. $\delta(\mathbf{x}_1)$ is nearly identical to $\delta(\mathbf{x}_2)$ because the difference between \mathbf{x}_1 and \mathbf{x}_2 is small but representative of the range of conditions expected for flight. Thus, from this point it is assumed that $\delta(\mathbf{x}_1) \approx \delta(\mathbf{x}_2) = \delta_{avg}$. Furthermore, because the parameter inference experiment updated the emissivity distribution under the assumption of an isothermal radiator, the *effective emissivity* found turned out to be conservative. The discrepancy, δ_{avg} , is nearly always negative and approximately -0.8 °C on average. Physically, this means that temperature of the radiator is likely slightly colder than predicted.

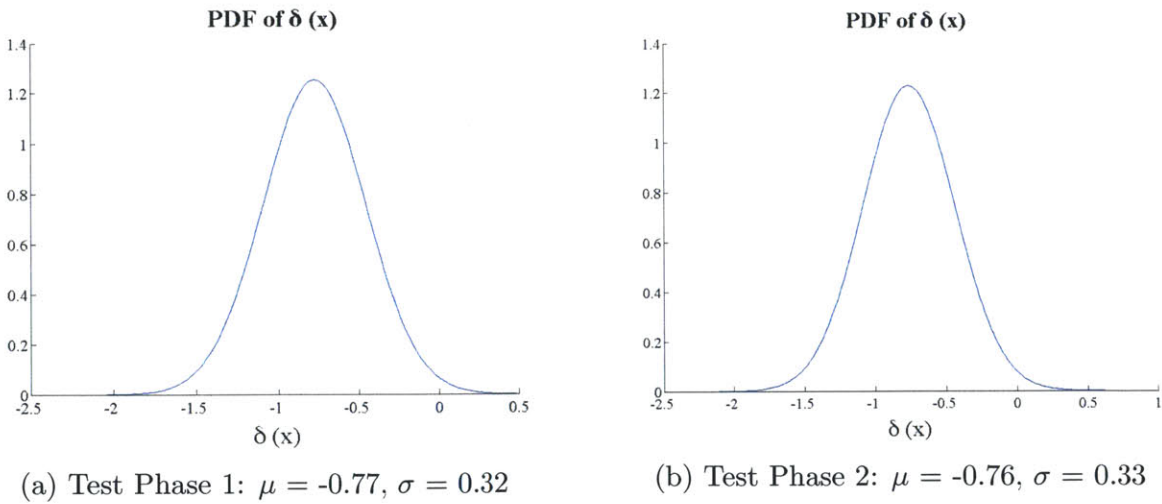


Figure 3-13: Model discrepancy distributions from model validation experiment

3.1.10 Step 2: Uncertainty Propagation and Parameter Prioritization—Third Pass

The δ_{avg} distribution from Figure 3-13 is added to the model output to predict the true physical process, $\zeta_{rad}(\mathbf{x})$, according to Equation (2.13). Equation (3.3) is once again used for the uncertainty analysis, but η_{rad} is replaced with ζ_{rad} as shown in Equation (3.11):

$$\bar{\zeta}_{rad,N} = \frac{1}{N} \sum_{i=1}^N \zeta_{rad}(\mathbf{x}_i) \quad (3.11)$$

where $\bar{\zeta}_{rad,N}$ is the MC estimator for the expected value of the true physical process. The true physical process is the summation of the model, η_{rad} , with the model discrepancy, δ_{avg} , as shown in Equation (2.13). Figure 3-14 shows the final uncertainty analysis for the radiator case study. With δ_{avg} included, the probability that the -60 °C requirement is met is 99%. The probability that the -60 °C temperature is met increased following the model validation experiment because δ_{avg} is nearly always negative.

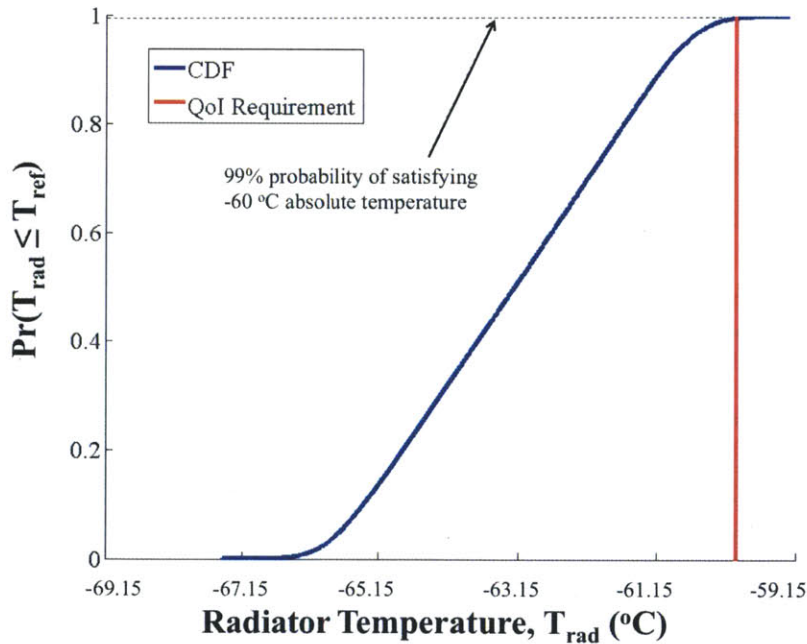


Figure 3-14: Uncertainty analysis results including model discrepancy, δ_{avg} , for radiator following model validation experiment. CDF indicates the probability of the radiator temperature being less than or equal to a temperature, T_{ref} , given the radiator model’s parametric uncertainty and model discrepancy.

To summarize the uncertainty analysis results for each pass of BMV step two, Table 3.4 shows the probability of satisfying the required $-60\text{ }^{\circ}\text{C}$ absolute radiator temperature for each pass. In both pass one and pass two, the uncertainty analysis considers only the parametric uncertainty in the radiator model. The probability increases from 58% to 95% due to the uncertainty reduction in the radiator’s coating emissivity following the parameter inference experiment. Once the model inadequacy is quantified following a model validation experiment via an additive model discrepancy function, the probability again increases to 99% because the discrepancy is nearly always negative.

Table 3.4: Summary of uncertainty analysis results for during each pass of BMV. Table shows how BMV increases the probability of satisfying the required $-60\text{ }^{\circ}\text{C}$ radiator temperature during each pass.

BMV Pass Number	BMV Procedural Location	Uncertainties Included in Uncertainty Analysis	Probability of Satisfying $-60\text{ }^{\circ}\text{C}$ Absolute Temperature (%)
1	Preliminary uncertainty analysis	Parameter only	58
2	After parameter inference experiment	Parameter only	95
3	After model validation experiment	Parameter and model discrepancy	99

3.1.11 Step 3: Experimental Goal Setting—Third Pass

In Figure 3-14, the UA results indicate that there is a 99% probability that the radiator temperature requirement will be met when model discrepancy is included. The answer to the first decision gate in Figure 2-4—whether there is adequate confidence that the requirement is met—is **yes**. The answer to the second decision gate in Figure 2-4—whether the system-level model has been validated—is **yes**, because a model validation experiment that sufficiently exercised the model over the domain of expected power dissipations has been completed.

Although it is infeasible to perform a model validation experiment with thermal vacuum chamber wall temperatures equivalent to deep space (leading to extrapolation of the validated model with respect to radiation sink temperature), analysis can show that not testing with a radiation sink temperature below 80 K is a very small sensitivity for the radiator temperature. In general, margin can be allocated (e.g., radiator made larger) depending on the risk posture

of the mission and nature of the risk when certain aspects of a model cannot be validated. In this case, sensitivity analysis via the Stefan-Boltzmann equation can reduce concern that the model inadequacy, $\delta(\mathbf{x}) \approx \delta_{avg}$, is not well characterized with respect to T_{space} . The wall temperatures of the test phases are 80 K versus the 2.73 K temperature of deep space with a radiator that operates near -60 °C. Equation (3.12) gives the heat flux from an isothermal radiating surface:

$$q = \sigma(T_{rad}^4 - T_w^4) \quad (3.12)$$

where T_w is the variable chamber wall (i.e., sink) temperature and q is a heat flux (i.e., total heat load per area). Figure 3-15a indicates the sensitivity of the heat flux, q , to changes in T_w for a radiator at -60 °C. The total flux at $T_w = 2.73$ K is near $T_w = 80$ K because T_{rad} is raised to the fourth power in Equation (3.12).

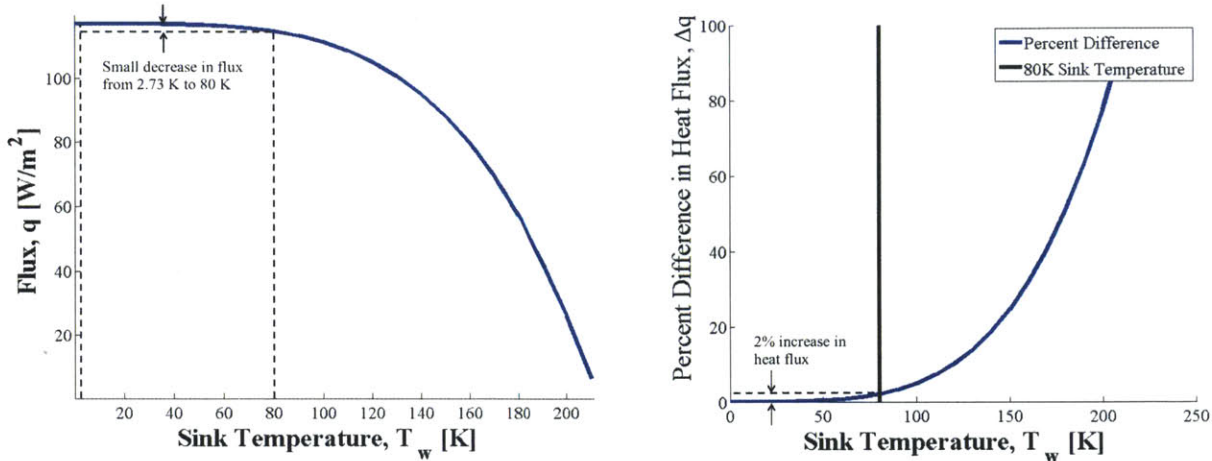
Figure 3-15b shows the results of Equation (3.13) to calculate the percent difference in flux between a radiator with sink temperature of 0 K, q_{0K} , and a radiator with sink temperature at w , q_w :

$$\Delta q = \frac{(q_{0K} - q_w)}{q_{0K}} * 100\% \quad (3.13)$$

where Δq is the percent difference. Note that there is less than a 2% difference in the flux from a radiator's surface between a 0 K and 80 K sink temperature when operating at -60 °C. Increasing the nominal heat load value of $Q_{in} = 10.0$ W by 2% (nominal values shown in Table 3.1) to $Q'_{in} = 10.2$ W, the radiator temperature, T_{rad} , increases by 1.04 K, or $\approx 0.5\%$. Thus, the effect of not validating the model with experiments using a thermal vacuum chamber wall temperature of $T_w = 2.73$ K is relatively small (i.e., the relationship between $\delta(\mathbf{x})$ and T_{space} is weak).

3.1.12 Step 6: Validation Problem Documentation

Step six of BMV includes the three components outlined in Chapter 2: documentation of steps one through five of BMV, updating requirements if necessary, and recommending small design changes for flight. For brevity, it will suffice to say that no design changes are necessary



(a) Total Flux for Infinite Isothermal Radiator

(b) Percent Difference in Flux

Figure 3-15: Sensitivity analysis of heat flux for radiator at $-60\text{ }^{\circ}\text{C}$ to illustrate the small increase in flux for a radiator emitting to a 80 K sink versus 2.73 K deep space temperature

to analytically demonstrate that the requirement is met. The posterior radiator coating emissivity, model discrepancy distributions, and completed experiments are documented.

Important takeaways from the radiator case study include:

- It is not necessary to increase the surface area, A , of the radiator in order to validate the model and design.
- Initially, the radiator coating emissivity is the most important global sensitivity, and the probability of meeting the design requirement is unsatisfactorily low.
- An optimally designed parameter inference experiment reduces the uncertainty of the radiator coating emissivity, resulting in higher probability that the requirement is met.
- The posterior distribution for ε is known to be biased. However, by adding the quantified model discrepancy, $\delta(\mathbf{x})$, to the model predictions, the isothermal radiator model is validated because both parametric and model structure uncertainties are accounted for in $\zeta_{rad}(\mathbf{x})$.
- The radiator requirement is met: the design is predicted to satisfy the $-60\text{ }^{\circ}\text{C}$ requirement with over 95% probability.

3.2 A Conventional Model Validation Approach

A conventional thermal model validation approach adheres to processes and margin policies typically performed in practice to validate a thermal design and model. Validation processes for NASA and military programs are discussed in the literature review in Chapter 1. In the radiator case study, a conventional thermal model validation approach is performed in the following three sections and is independent from BMV. The three serial steps of the conventional validation approach are analysis, thermal balance testing, and model correlation.

3.2.1 Analysis

A conventional thermal analysis focuses on stacked worst-case hot and cold scenarios. In this context, *stacked* means assuming sets of system and environmental parameter values that are most likely to violate requirements in a given case. For example, maximum expected power dissipations are assumed for hot cases, and minimum expected power dissipations are assumed for cold cases. If requirements are satisfied in the stacked worst-case scenarios, all intermediate sets of system and environmental parameter values are assumed to satisfy requirements. Because the $-60\text{ }^{\circ}\text{C}$ radiator requirement is a maximum temperature requirement (the minimum probability part of the requirement is not applicable in this conventional analysis approach), the analysis case is a hot case scenario. Consequently, the parameter values assumed for conventional analysis are those that yield maximum radiator temperatures. Table 3.5 shows the parameter value assumptions for the conventional radiator analysis. The worst-case parameter assumptions are selected from the range of parameter values given in Table 3.2. The maximum expected heat load and temperature of deep space and the minimum expected emissivity and surface area are the parameter values that yield the maximum radiator temperature.

The same radiator model used in BMV (Equation (3.1)) is used to generate predictions for T_{rad} in this conventional approach. Evaluating the radiator model for the parameter values in Table 3.5, the temperature of the radiator is predicted to be $T_{rad} = -53.8\text{ }^{\circ}\text{C} = 219.3\text{ K}$. The temperature of the radiator is not predicted to meet the $-60\text{ }^{\circ}\text{C}$ requirement. Furthermore, the design has no margin to the requirement (margin is typically required in practice).

Table 3.5: Initial model parameters for conventional thermal analysis of radiator yielding worst-case hot conditions

Parameter/Constant	Value	Units
Heat load, Q_{in}	10.5	W
Emissivity, ϵ	0.80	–
Temperature of Deep Space, T_{space}	2.727	K
Area, A	0.0998	m ²

In a conventional analysis of a general system, many parameters affect the QoIs. In the absence of a systematic method of identifying critical system parameters, prototype-level tests *might not* be performed to learn more about parameters of interest. Consequently, extra conservatism is applied in conventional analysis to capture uncertain parameter values. To maintain general applicability and demonstrate how not reducing the conservatism early can be significant, it is assumed that the coating emissivity is not investigated by a parameter inference experiment. Instead, the radiator design is changed to lower the radiator temperature prediction.

Architecturally, there are multiple ways to lower the radiator temperature prediction (e.g., changing system parameters to lower Q_{in}). However, if temperatures are trending too warm, radiators are often made larger, particularly early in the design lifecycle. Under the assumption that the radiator design is subject to a NASA Goddard passive thermal temperature margin of 5 °C [25], the radiator is re-sized so that its temperature is predicted to be $T_{rad} = -65$ °C (i.e., meeting the -60 °C requirement with 5 °C margin). The new surface area of the radiator, A_{new} , corresponding to $T_{rad} = -65$ °C is 0.1235 m². The new surface area is a 24% increase in surface area of the nominal radiator design. (Note: without the 5 °C margin, the area required for a -60 °C radiator prediction is 0.01122 m², a 12% increase in radiator area.) With the radiator design predicted to satisfy the -60 °C requirement with 5 °C of margin, the next step is to validate the model via thermal balance testing.

3.2.2 Thermal Balance Test

Thermal balance testing uses dedicated test phases to simulate flight conditions to gather steady state temperature predictions to verify that the thermal control system meets requirements and correlate thermal models [4, 22, 24]. As discussed in the literature review (Chapter 1), recommendations for the design of thermal balance tests are contained in the Goddard Environmental Verification Standard (GEVS) for many NASA programs and MIL-HDBK-340 (MIL340) for military programs. Conventional thermal balance test design adheres to the philosophy of these standards:

- **GEVS:** “The adequacy of the thermal design and the capability of the thermal control system shall be verified under simulated on-orbit worst-case hot and worst-case cold environments, and at least one other condition to be selected by the thermal engineer.” [24]
- **MIL340:** “As a minimum, two test conditions will be imposed: a worst hot case and a worst cold case.” [22]

In practice, tests occur at the mission hot and mission cold cases. The thermal balance test cases will correspond to the hot and cold environments for the resized radiator (with surface area A_{new}).

The thermal balance test phases are shown in Table 3.3 (the same test cases as those performed during model validation experiment for BMV). The minimum possible temperature of the vacuum wall chamber is assumed to be 80 K, and the worst-case hot and cold scenarios are the maximum and minimum radiator heat loads, respectively. Test Phase 1 has a heat load of 9.5 W, and Test Phase 2 has a heat load of 10.5 W. The high fidelity Thermal Desktop model of the radiator is used to generate synthetic data for the thermal balance test. The same truth emissivity of $\epsilon = 0.92$ is assumed, and the radiator area within the high fidelity model is increased to $A_{new} = 0.1235 \text{ m}^2$.

Figure 3-16 shows the results of the thermal balance tests, given the conditions in Table 3.3. The following are the measured steady state temperatures from the center of the radiator:

- Test Phase 1: $T_1 = -75.3\text{ }^\circ\text{C} = 197.9\text{ K}$
- Test Phase 2: $T_2 = -70.4\text{ }^\circ\text{C} = 202.8\text{ K}$

Comparing the results of Figure 3-16 with those from the model validation experiment in BMV, the radiator temperatures in the thermal balance tests are lower due to the increased surface area of the radiator. In the worst-case hot scenario (Test Phase 2), there is $\approx 10\text{ }^\circ\text{C}$ margin to the $-60\text{ }^\circ\text{C}$ temperature requirement. T_1 and T_2 are used to update the model structure and/or model parameters through the model correlation process.

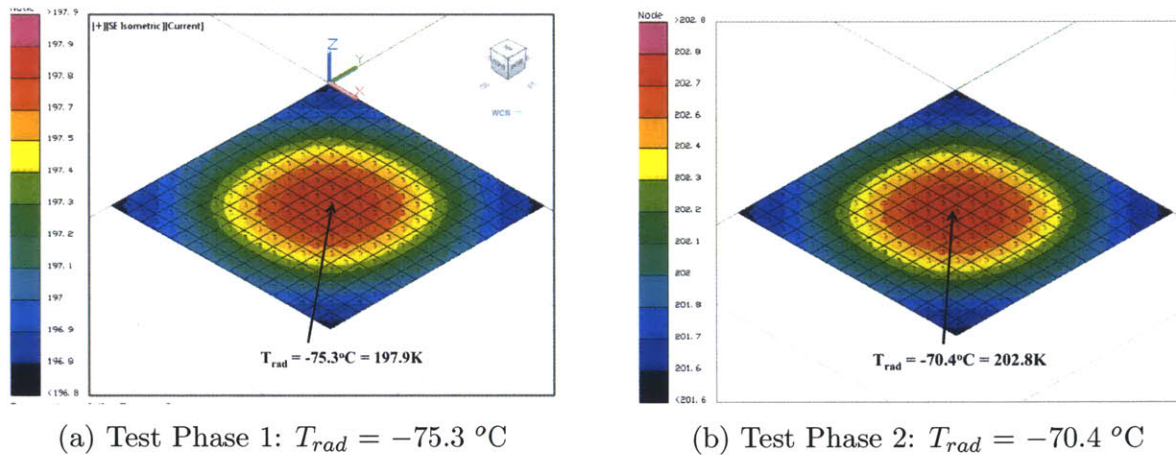


Figure 3-16: Synthetic data (generated via Thermal Desktop) results for thermal balance tests with radiator with $A_{new} = 0.1235\text{ m}^2$.

3.2.3 Model Correlation

Model correlation is the process where one gains modeling insight by observing differences in comparable quantities between model and test [26, 27]. As discussed in the literature review in Chapter 1, the thermal model correlation process is a systematic, manual process in practice. The data is used to obtain *best fitting values* for model parameters.

To correlate the radiator model to the thermal balance test results, the model parameters are updated to the conditions of the test. Of the four variable radiator model parameters, only one is significantly uncertain: the radiator coating emissivity, ε . The heat load, Q_{in} , the new radiator area, A_{new} , and the thermal vacuum chamber wall temperature, T_w , are all assumed to be known parameters of the system or test. Using the radiator model, Figure

3-17 shows the result of various coating emissivity values on the temperature of the radiation as a function of radiator heat load. The results from the thermal balance test are shown at 9.5 W and 10.5 W. The two experiments of the thermal balance test fall nearest to the line of $\varepsilon = 0.92$ in Figure 3-17, the known actual emissivity of the radiator.

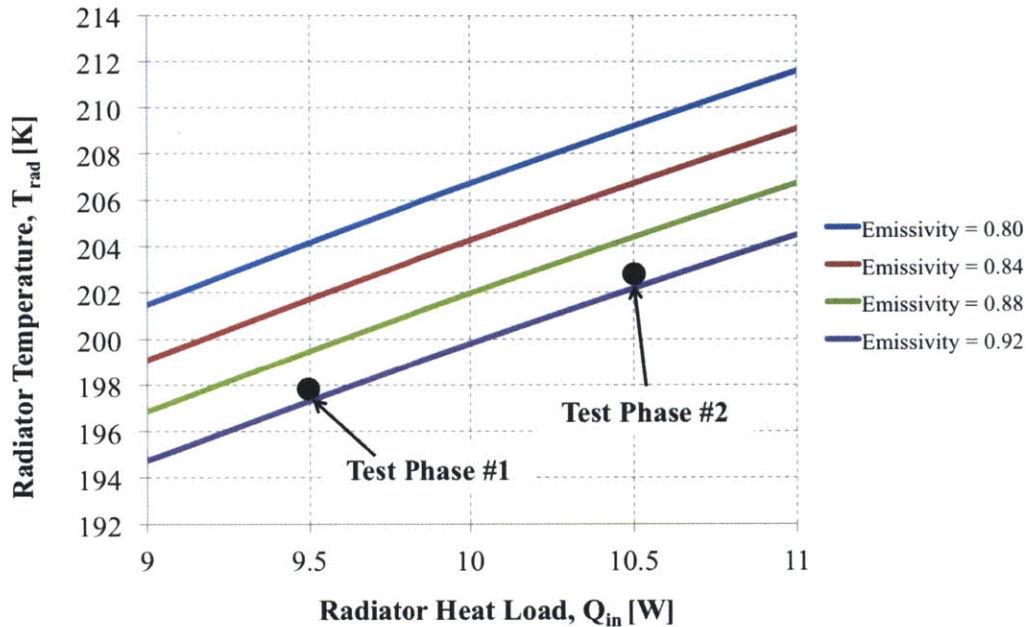


Figure 3-17: Model predictions of radiator temperature versus heat load for various coating emissivities. The thermal balance results are shown where Test Phase 1 is at 9.5 W, and Test Phase 2 is at 10.5 W. The known truth emissivity from the Thermal Desktop model is $\varepsilon = 0.92$.

Unlike in BMV where the emissivity distribution is updated to reduce the variance of the prior, a scalar value of the emissivity is selected that provides the best fit for the data. An emissivity value of $\varepsilon = 0.909 \approx 0.91$ matches both experimentally measured temperatures to within 0.1 K. Thus, the value of the emissivity in the radiator model is updated from 0.80 to 0.91.

The final post-correlation step is to regenerate flight predictions for the updated model. Using the final model parameters shown in Table 3.6, the maximum hot case radiator temperature is found to be $T_{rad} = 201.5 \text{ K} = -71.7 \text{ }^\circ\text{C}$. Thus, the radiator design has $\approx 12 \text{ }^\circ\text{C}$ margin for flight and the initial radiator model prior to thermal balance is found to be conservative. At this point, the radiator surface area could be decreased. Compared to BMV, the surface area penalty for sizing the radiator prior to the validation experiments is

0.0235 m². However, since the hardware from the thermal balance test is built and could be used for flight, the design is not changed. In practice, removing material from a radiator to decrease surface area after system-level thermal balance testing changes the mass properties of the spacecraft. Because the spacecraft design has been qualified with the larger radiator, it is often less risky and/or costly to either accept a colder radiator or apply MLI blankets to a portion of the radiators surface than re-qualify the spacecraft with a smaller radiator structure (e.g., smaller radiator has implications for both structures and attitude control systems). MLI blankets on the radiator surface are not necessary as long as the colder radiator does not cause other components to exceed lower temperature limits or unacceptably high power draws from heaters.

Table 3.6: Final, correlated model parameters for a conventional thermal analysis of the radiator

Parameter/Constant	Value	Units
Heat load, Q_{in}	10.5	W
Emissivity, ϵ	0.91	–
Temperature of Deep Space, T_{space}	2.727	K
Area, A_{new}	0.1235	m ²

3.3 Comparison of BMV vs. A Conventional Model Validation Approach

BMV and a conventional model validation approach are completed independently in Sections 3.1 and 3.2. Although the radiator does not match the size and complexity of a real spacecraft, the primary objective of the radiator case study is to demonstrate the BMV methodology on a simple system. A secondary objective is to compare the implementation of BMV to a conventional validation approach and discuss the differences in the validation *processes* and in the final *form* of the radiator. The radiator model is the Stefan-Boltzmann equation, which contains four parameters. Three of the four parameters, Q_{in} , ϵ , and A , are design parameters. In BMV, ϵ is identified as being the critical sensitivity for performance

given the large variance of its initial uncertainty distribution. Since Q_{in} is an arbitrarily assumed input heat load based on a larger spacecraft system, A is the primary resource parameter for the radiator. In general, a smaller radiator surface area is preferred because a larger radiator increases mass, heater power to warm components in cold environments, and the structure of the spacecraft required to support the radiator.

Figure 3-18 shows the state of the critical system performance parameter, ε , and the critical resource parameter, A , as a function of time during the validation process. The validation process is shown as an alternating series of analyses and tests. In BMV, an additional parameter inference experiment is performed prior to the model validation experiment. The emissivity parameter value is updated *earlier* in the validation process in BMV, following the parameter inference experiment. With the updated emissivity distribution (following the parameter inference experiment), it is not necessary to increase the radiator size. However, in the conventional approach the radiator area is initially increased in the first analysis phase to show sufficient design margin prior to the model validation experiment.

In BMV, the updated radiator coating emissivity distribution (following the parameter inference experiment) is centered on ≈ 0.895 whereas in conventional analysis, a value nearer the truth emissivity of 0.91 is found after thermal balance testing. BMV converges to a less accurate value for the coating emissivity because the parameter is calibrated to an experiment with a larger radiator heat load. While the larger heat load makes T_{rad} highly sensitive to the emissivity value, the model is inadequate because it does not account for in-plane temperature gradients. Because the gradients in the radiator are larger at higher heat loads, the isothermal radiator assumption made by the choice of model structure is better at smaller heat loads. Thus, the emissivity value found from a smaller heat load in the conventional analysis is closer to the actual emissivity of 0.92.

That conventional analysis leads to a more accurate value for the coating emissivity is less a byproduct of the methodology and more a physical implication of performing the parameter inference experiment in BMV *outside the domain of intended application of the system* (i.e., Q_{in} is greater than the maximum expected value of 10.5 W). Although the model discrepancy, $\delta(\mathbf{x})$, accounted for the less accurate ε value in BMV, a different experimental utility for the parameter inference experiment or a second calibration of ε following the

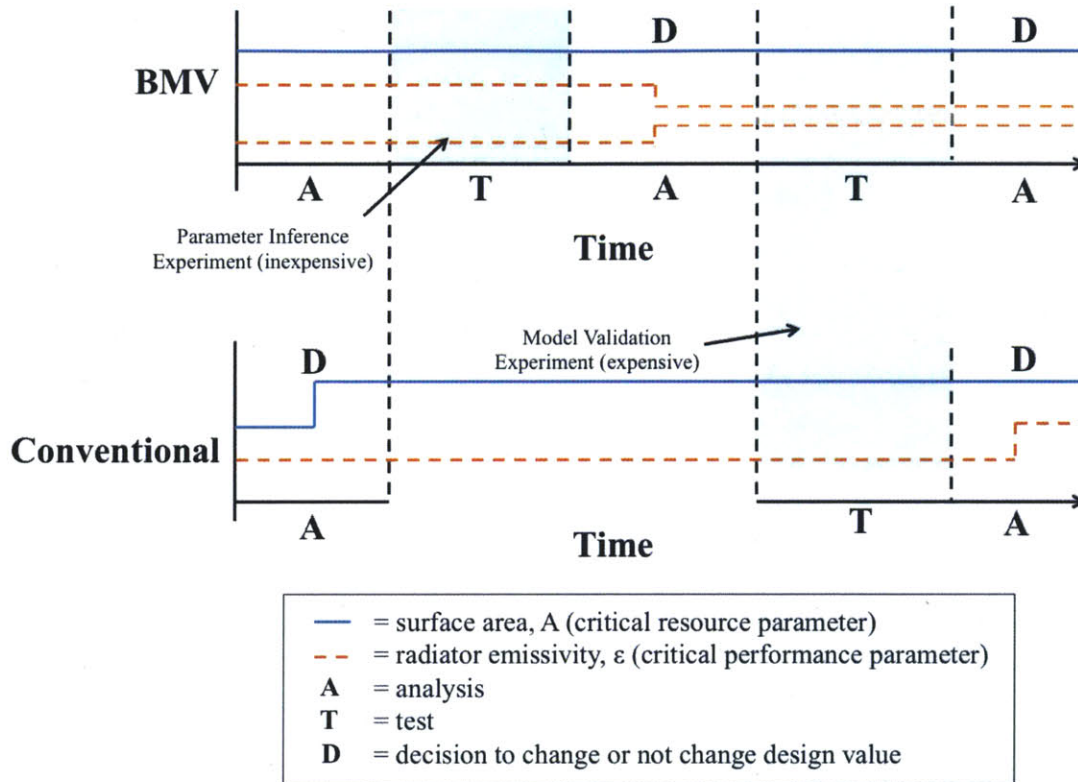


Figure 3-18: Timeline of BMV and a conventional validation approach illustrating the change in values of critical resource and performance parameters, area and coating emissivity, respectively.

model validation experiment could result in a more accurate posterior distribution for ε , if desired.

The aim of BMV is to improve the validation processes of a thermal system. Figure 3-19 illustrates that a conventional validation approach *can* result in a design that consumes more resources (e.g., mass) because design decisions are based on the early analysis of stacked worst-case scenarios when less is known about the system. Figure 3-19 is a notional depiction of knowledge of the system and design freedom versus project lifecycle time to illustrate qualitative, process-related improvements made by BMV to the model validation process.

For the radiator case study, the green star indicates the design decision to maintain the same size or increase the radiator's surface area. BMV provides a rigorous, systematic framework for identifying and reducing the uncertainty of critical system parameters *prior to* the system-level model validation experiment. By learning the true values of critical system sensitivities earlier in the project lifecycle, system knowledge increases. In a conventional

validation approach, true parameter value estimates are updated *after* the model validation experiment when the system is later in the design lifecycle. BMV can provide engineers more knowledge of the system when making important design decisions in the early phases of a project's lifecycle.

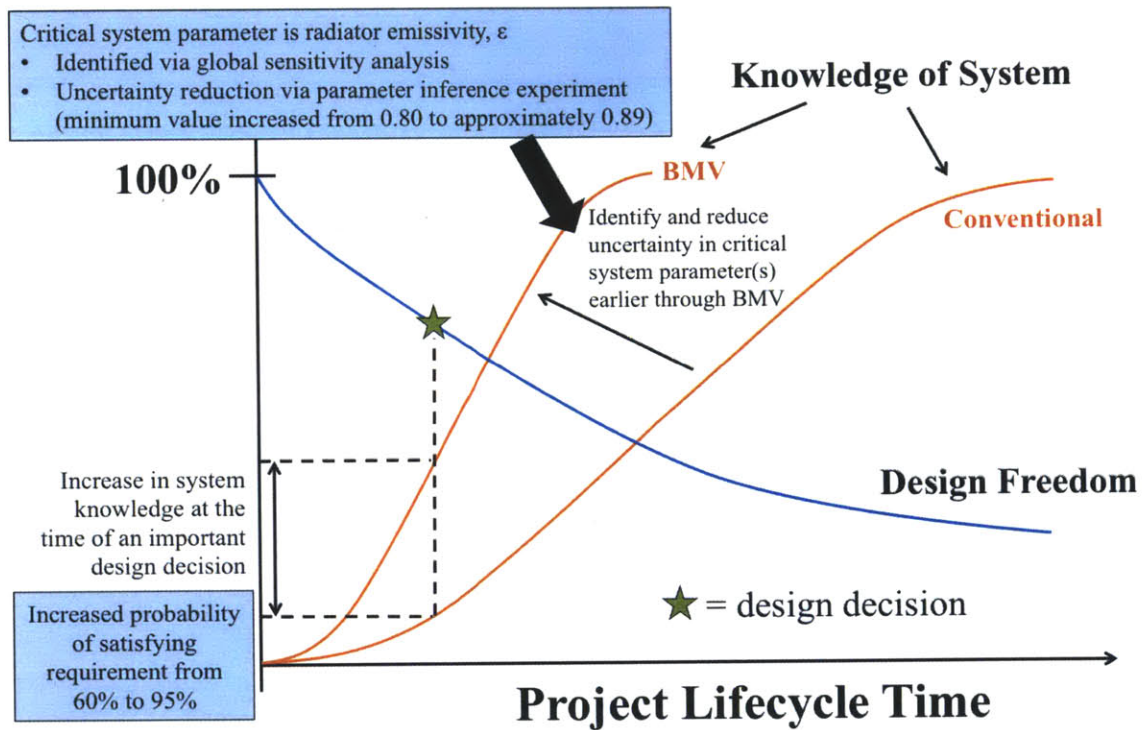


Figure 3-19: Notional illustration of BMV on general system over project lifecycle with respect to knowledge of system and design freedom. Plot qualitatively shows that system knowledge is increased early in the lifecycle due to a systematic, rigorous approach to identifying and reducing important system uncertainties.

For the radiator problem, implementation of BMV increases the probability of satisfying the radiator temperature requirement from 58% to 99% because the updated uncertainty distribution in the radiator coating emissivity—the critical system parameter—has an increased minimum value of 0.89 over the prior minimum value of 0.80. Thus, it is not necessary to increase the radiator area to validate the thermal design and model. Conventional analysis results in a larger radiator that is colder during flight. If the temperature requirement for the system is such that colder is better, it may not be bad, from a thermal performance perspective, that the additional margin exists from conventional validation. However, a large radiator ultimately maps to higher form-related cost. Furthermore, additional surface

area could be added to the radiator from the BMV process if margin is needed to account for un-modeled physics of the flight environment. Although conventional validation requires less computational cost, BMV uses model-based computational approaches to rigorously and systematically focus analysis and test efforts.

Chapter 4

REgolith X-ray Imaging Spectrometer (REXIS) Overview

The second case study in this thesis (Chapter 5) demonstrates BMV on the REgolith X-ray Imaging Spectrometer (REXIS) instrument solar X-ray monitor (SXM). This chapter provides a general REXIS instrument overview, a description of the mission thermal environments, SXM thermal requirements, and SXM thermal design.

4.1 Instrument Overview

The REXIS instrument is one of five payload instruments on the Origins, Spectral Interpretation, Resource Identification, and Security-Regolith Explorer (OSIRIS-REx) asteroid sample return mission. OSIRIS-REx is a 7-year mission that launches in 2016, arrives at the asteroid Bennu in 2018 for proximity operations, samples Bennu in 2019, and returns the sample to Earth by 2023. From the sample that OSIRIS-REx provides, the organic chemistry and geochemistry of Bennu will be well-characterized, providing knowledge fundamental to understanding planet formation and the origin of life [127]. REXIS is a Class D payload¹ and a student-led project with the primary goal of providing flight hardware experience to science and engineering students. The REXIS instrument observes the X-ray fluorescence emitted from Bennu in the 0.5-7.5 keV soft X-ray band. It uses X-ray spectroscopy to char-

¹Per the document NPR 8705.4—Risk Classification for NASA payloads

acterize Bennu among the known meteorite groups and coded aperture imaging to map the surface elemental distribution [128]. The REXIS science goals complement and enhance the science data collected by the other instruments on OSIRIS-REx.

REXIS consists of two assemblies: the spectrometer and the solar X-ray monitor (SXM) [129]. The spectrometer is the primary sensor for the REXIS instrument. It observes the X-ray fluorescence from the asteroid Bennu via four charge-coupled devices (CCDs) and a coded aperture mask. The SXM is the secondary sensor for REXIS. It observes the highly variable solar X-ray spectrum via a silicon drift detector (SDD) to provide context to the spectrometer measurements.

The spectrometer, shown in Figure 4-1 without multi-layer insulation (MLI) blankets, consists of two subassemblies: the electronics box and the tower. The electronics box has a footprint of approximately 5.6 x 7.9 in and is mechanically and thermally coupled to the OSIRIS-REx instrument deck. The electronics box contains three boards: two detector electronics (DE) boards for driving and reading data from the CCDs and the main electronics board (MEB). The MEB electrically interfaces with the OSIRIS-REx avionics so that the spacecraft can power the REXIS instrument, transmit REXIS data to Earth, and send commands. The tower is connected to the electronics box via four titanium standoffs, houses the CCDs, and supports the coded aperture mask. The tower consists of the detector assembly support structure (DASS) and four truss panels. The spectrometer detector plane is comprised of a 2 x 2 array of back illuminated CCDs within the detector array mount (DAM). The DAM is connected to the DASS via four Torlon 5030 standoffs. The tower supports the mask assembly 20 cm above the detector array. The mask assembly consists of the coded aperture mask, the mask frame, and the radiation cover deployment system. The radiation cover protects the detectors from radiation exposure during the cruise to Bennu. A one-time deployable device opens the cover to a 110° angle (toward +X) upon arrival at the asteroid. A Frangibolt actuator is used to break a notched bolt that pins the cover closed, and a spring rotates the door about the hinge-line out of the field of view of the spectrometer [130]. A single-string heater, powered by OSIRIS-REx, is used to keep the radiation cover system warm prior to and during deployment.

The SXM, shown in Figure 4-2, is located separately from the spectrometer on a sunward

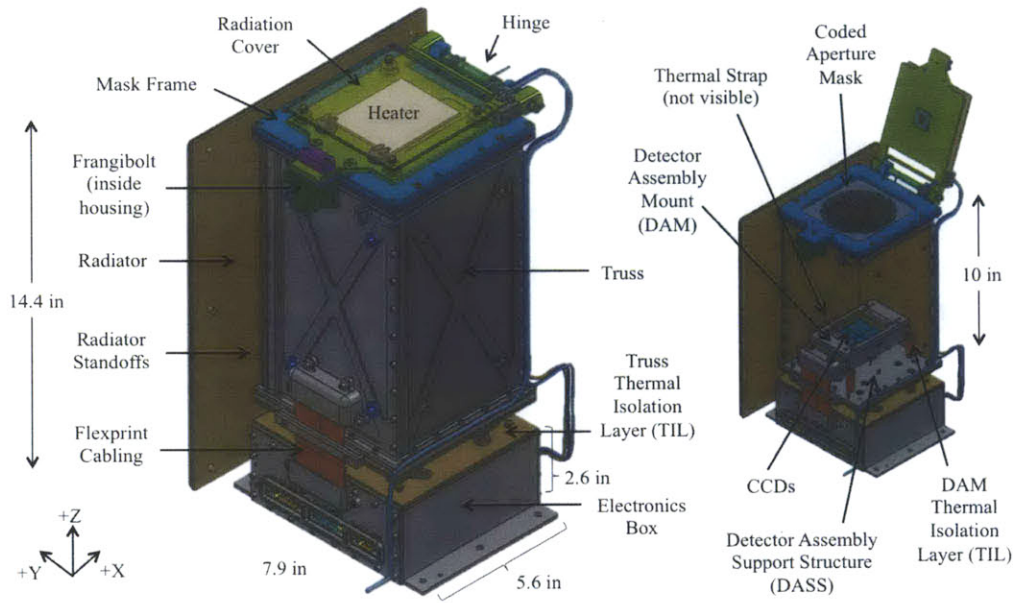


Figure 4-1: Spectrometer design overview (shown without MLI)

facing gusset of OSIRIS-REx. Cables extend along the outer surface of the instrument deck to connect the spectrometer MEB to the local support electronics of the SXM. The bracket is mechanically and thermally coupled to the spacecraft gusset, and is constructed at an angle to orient the SDD boresight to the +X axis of OSIRIS-REx, the nominal direction of the sun during the REXIS science observations. The SXM assembly is attached to the bracket and consists of the housing, a collimator, the SDD and the SXM electronics board (SEB). The SXM housing contains the SDD and SEB and protects the SEB from the radiation environment. The SDD is housed in a commercially available package from Amptek, Inc. The AXR SDD includes the SDD and a thermoelectric cooler (TEC) to cool the SDD. The SDD data is readout by custom designed electronics on the SEB and transmitted to the REXIS MEB for further processing through the intra-instrument harness. The SEB filters noise from the power input to the Amptek package and amplifies the analog output signal from the SDD to the spectrometer MEB.

The spectrometer and SXM are mounted externally to OSIRIS-REx but in different locations, as shown in Figure 4-3. The spectrometer is located near the edge of the instrument deck to provide the radiator a near full view of deep space (note: the radiator is located on the +Y side of the spectrometer). Furthermore, it is rotated 10° counterclockwise about the

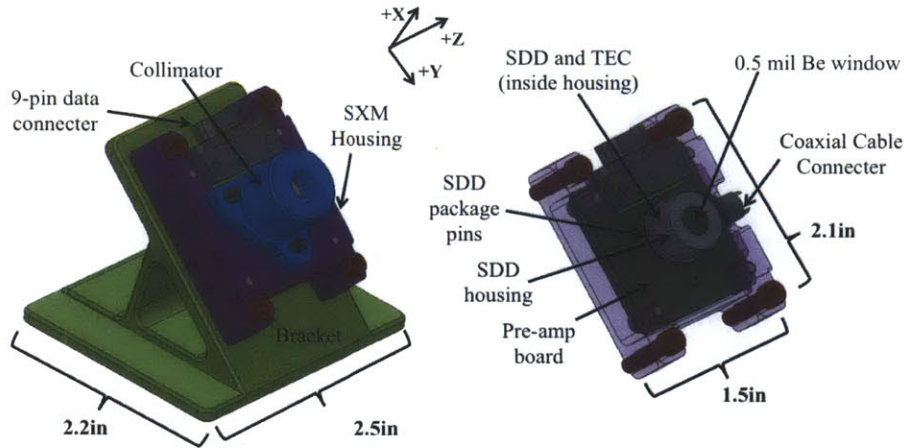
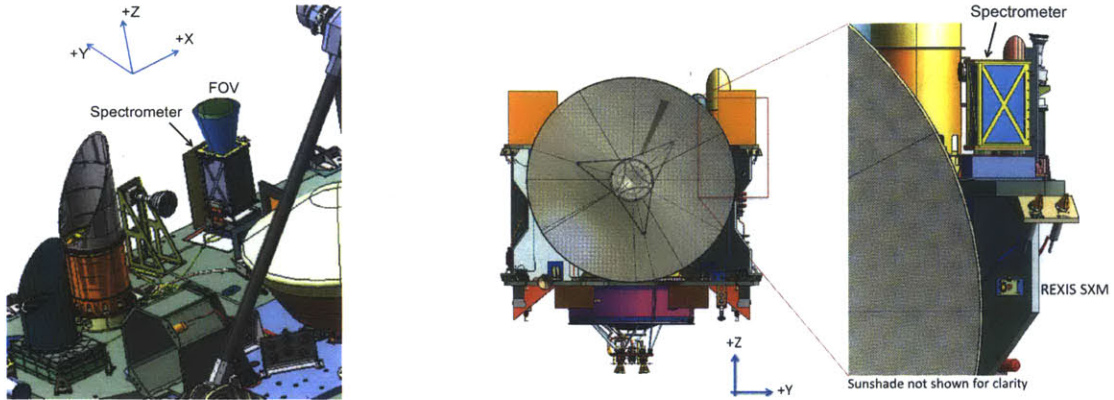


Figure 4-2: SXM design overview (shown without MLI)

spacecraft $+Z$ axis in order to minimize the view factor of the radiator to the warm solar arrays. Nominally, the sun is in the direction of $+X$ during science operations at the asteroid. Figure 4-3b shows the SXM and instrument deck sunshade behind which the spectrometer is mounted. Observing the spacecraft from the $+X$ direction, the spectrometer is completely hidden by a sunshade on the instrument deck when the radiation cover is closed. The sunshade greatly reduces the total absorbed solar flux of the spectrometer. Figure 4-3b also illustrates the position of SXM on a sun-facing gusset of OSIRIS-REx. Although the SXM will be illuminated by the sun for the majority of the mission, all but the SXM collimator is underneath spacecraft MLI blankets (not pictured in Figure 4-3b). Note that the sunshade has been removed from the right figure in Figure 4-3b to show a clear view of both REXIS assemblies.

4.2 Mission Thermal Environments

The OSIRIS-REx mission consists of three periods: Outbound Cruise, Proximity Operations, and Return Cruise. Each period consists of multiple mission phases. Figure 4-4 shows the solar distances versus time for the entire 7-year mission. The spacecraft launches in 2016, and after a brief check-out following launch, is placed on a 2.5-year heliocentric transfer orbit to Bennu, referred to as Outbound Cruise. Shortly after arrival at the asteroid, OSIRIS-REx



(a) Isometric view of spectrometer (b) View OSIRIS-REx/REXIS from sun (+X)

Figure 4-3: Isometric and side views of REXIS instrument on OSIRIS-REx

is placed in a captured orbit about Bennu for science operations during the Orbit Phase A and Orbit Phase B. Next, the mission enters Reconnaissance Phase and various sampling rehearsals leading up to the actual sampling of the asteroid in 2019. Finally, the spacecraft is once again placed in a heliocentric transfer orbit to Earth to return the sample, referred to as Return Cruise. The minimum and maximum solar distances for the entire mission are 0.77 AU and 1.39 AU, respectively.

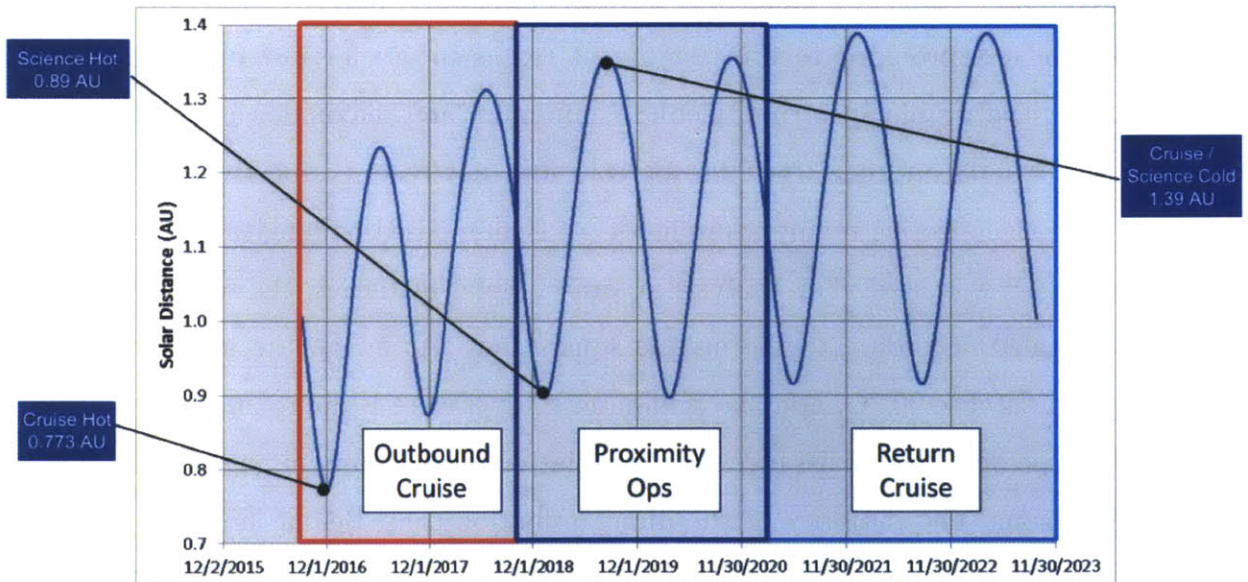


Figure 4-4: Solar distance versus mission time for entire 7-year mission consisting of Outbound Cruise, Proximity Operations, and Return Cruise periods

The primary REXIS science mission occurs during the Orbit and Reconnaissance phases within Proximity Operations. Prior to its science mission and during Outbound Cruise, REXIS is mostly off and survival is the key concern. Periodically during the 2.5-year Outbound Cruise, REXIS is turned on to perform internal calibrations using ^{55}Fe sources that are built into the instrument. During these calibrations, REXIS must satisfy the thermal requirements corresponding to its science operation (e.g., cool the CCDs to its prescribed operating temperature range).

Prior to performing its science mission and during Proximity Operations, REXIS is turned on and the Frangibolt actuated to deploy the radiation cover during Detailed Survey Phase. REXIS will operate during Orbit Phase and Reconnaissance Phase for a minimum duration of 420 hours. During REXIS science operation, OSIRIS-REx is in a 1 km terminator orbit about Bennu, and the spectrometer boresight is nadir-pointed at Bennu. Once the science mission of REXIS is complete, the instrument returns to a survival mode for the remainder of the OSIRIS-REx mission.

During science operation, the thermal environment of REXIS includes both the albedo and infrared radiation effects of Bennu. Bennu's thermal effects, which are germane only for operational cases, are important but not design-driving. A conservative asteroid thermal model was provided to the instrument teams to use for instrument modeling efforts [131]. For the visible spectrum, Bennu's minimum and maximum assumed albedo factors are $\alpha_{min} = 0.03$ and $\alpha_{max} = 0.06$ for cold and hot cases, respectively. For the infrared spectrum, the effective temperature model of Bennu based on longitude and latitude shown in Figure 4-5 was used. For analysis at various solar distances, the temperatures in Figure 4-5 are scaled according to the inverse square law. At 1 AU, the maximum temperature is approximately 100 °C, and the minimum temperature is approximately -70 °C. During Orbit Phase and Reconnaissance Phase, radiation from Bennu impinges on REXIS from the +Z direction. The majority of the direct radiation from Bennu impinges on mask, mask frame, radiation cover, and CCDs (traveling through the coded regions of the mask).

The bounding thermal analysis cases for the REXIS mission through operation are shown in Table 4.1. During Outbound Cruise (i.e., Cruise Phase) REXIS is primarily off, and the hot and cold cases are the minimum and maximum solar distances, respectively. The

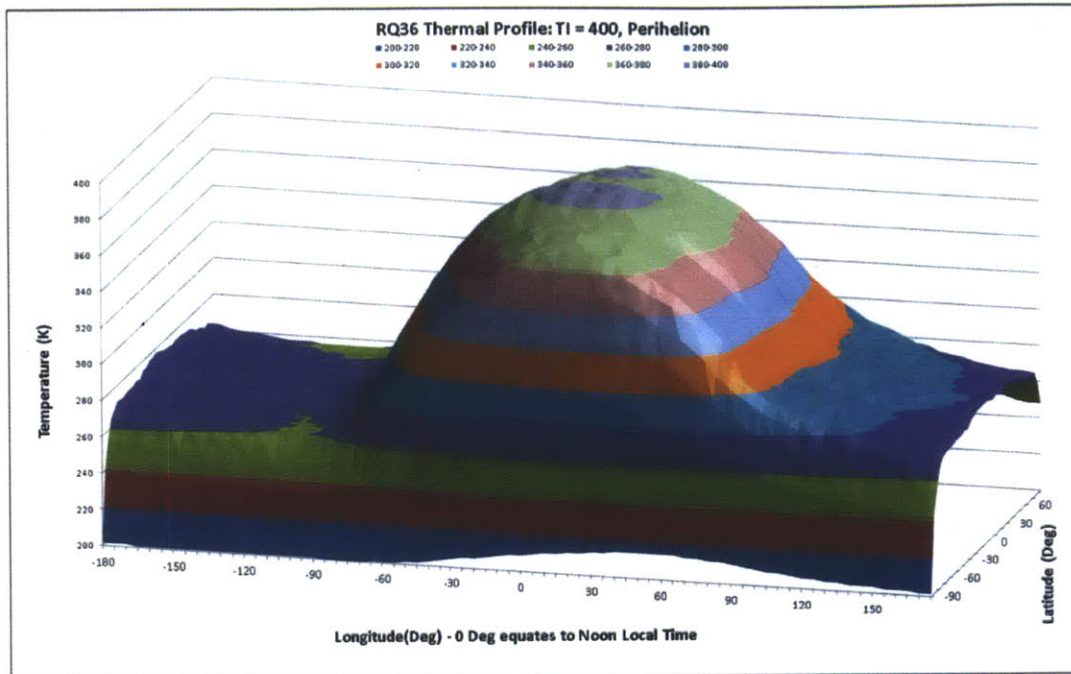


Figure 4-5: Temperatures of Bennu plotted versus longitude and latitude at a solar distance of 1 AU [131]

radiation cover is closed and the heater is on to warm the radiation cover deployment system. Although the spectrometer is protected from direct sunlight by a sunshade, as shown in Figure 4-3, shorter solar distances warm the external features of the spacecraft (e.g., solar arrays). Thus, shorter solar distances marginally warm the spectrometer also because REXIS has view factors to the spacecraft. Once in Proximity Operations at Bennu, the radiation cover is deployed during Detailed Survey (DS) Phase and the heater is turned off. In Orbit Phase B, REXIS is on and taking science data. The hot case is when Bennu is at perihelion, and the cold case is when Bennu is at aphelion. Bennu's radiation effects are included for hot case analysis and neglected in cold case analysis for conservatism since the asteroid is significantly warmer than REXIS during operation. REXIS also operates during the Reconnaissance phase. However, that phase is not shown separately in Table 4.1 because the thermal environment in which REXIS will operate is identical to that in Orbit Phase B.

From this point forward, the thermal requirements and design are presented of *exclusively the REXIS SXM*. Because the spectrometer is not a case study in this thesis, a detailed design description, summary of thermal requirements, and analyses can be found in Stout

Table 4.1: Summary of REXIS thermal analysis cases for each mission environment

Analysis Case	Case Description	Sun Distance (AU)	Solar Intensity (W/m ²)	Sun Offpoint from +X (deg)	Bennu Altitude	REXIS State	REXIS Cover/Heater
Cruise Phase							
Cruise, Hot	Perihelion, arrays at 45deg	0.773	2322	0	--	Off	Closed/On
Cruise, Cold	Aphelion, arrays at 45deg	1.387	700	0	--	Off	Closed/On
Orbit Phase B							
Orb B, Hot	Min Bennu range and max temp profile, arrays at +45deg	0.897	1752	0	750m	On	Open/Off
Orb B, Hot Offpoint	Min Bennu range and max temp profile, arrays at +45deg, 5hrs	0.897	1752	20 (+Z)	750m	On	Open/Off
Orb B, Cold	Max Bennu range, arrays at +45deg, no Bennu	1.387	700	0	--	On	Open/Off

and Masterson [132].

4.3 Solar X-ray Monitor Thermal Requirements

The SXM thermal system requirements are the steady state component temperature ranges shown in Table 4.2. The SDD package (i.e., SDD housing) refers to the bulk temperature of the Amptek AXR SDD package and is thermally equivalent to the base (i.e., hot side) of the TEC. The temperature limits for the SDD housing are provided by the manufacturer. For conservatism, the limits of the SEB are driven by the most restrictive electrical component. If the SDD housing or SEB requirements are not satisfied, the risk is failure of the component. During science operation, the maximum SDD temperature is the driving SXM thermal requirement because the hot side of the TEC must be sufficiently cool so that the TEC can drive a temperature difference to achieve less than -30 °C. Failure to cool the SDD below -30 °C broadens the SXM spectral resolution, which degrades the ability to accurately predict the X-ray solar spectrum during post-processing (which provides context to the measurements of Bennu’s fluorescence made by the spectrometer). For more information regarding the SXM science performance and background on the REXIS science mission, see Inamdar et al. [133] and Allen et al. [128].

Table 4.2: SXM steady state component temperature limits

Component	Non-Operational (°C)		Operational (°C)	
	Min	Max	Min	Max
SDD Housing	-65	150	-40	100
SEB	-55	100	-40	85
SDD	–	–	-100	-30

The ability of the SXM design to achieve its thermal requirements is driven by the spacecraft interface temperature. The range of allowable interface temperatures was negotiated between the REXIS instrument team and OSIRIS-REx spacecraft developers prior to the REXIS Critical Design Review. When the instrument is on or off, the minimum allowable interface temperature is $-30\text{ }^{\circ}\text{C}$, and the maximum allowable interface temperature is $50\text{ }^{\circ}\text{C}$. The $50\text{ }^{\circ}\text{C}$ limit drives the ability of the SXM to achieve the driving $-30\text{ }^{\circ}\text{C}$ SDD temperature requirement during operation.

4.4 Solar X-ray Monitor Thermal Design Description

The thermal control system for the SXM is decoupled from that of the spectrometer because the two assemblies are not collocated. The thermal design challenge of the SXM is cooling the SDD during operation. Cooling the SDD is difficult because the detector must face the sun to observe its X-ray spectrum, but the incident solar flux warms the detector and its package. Because the SXM structure is exposed to the sun during operation, the entire SXM except for the collimator is beneath the spacecraft MLI blanket to isolate the structure from direct sunlight. When the SXM is not operating, all power dissipations are zero and the entire structure is relatively isothermal. During operation, the power dissipations primarily come from the SEB and TEC. The maximum expected total dissipation is 2.75 W (estimate prior to test). Given that approximately 90% of this power comes from the TEC, cooling the SDD effectively during operation requires that the TEC power dissipation be efficiently removed from the SXM.

The SDD (i.e., the SXM detector) is located on the cold side of the TEC within the Amptek AXR SDD package, as shown in Figure 4-6. The mounting stud allows the package

to be fastened to the SXM housing, and the pins are attached to the SEB. The TEC base rests on the base of the SDD housing. The TEC itself has two stages and cools the SDD. A transmissive Beryllium window is brazed to the +X side of the SDD housing. Operationally, sunlight passes through the Beryllium window and impinges on the SDD. The primary thermal path of the SDD package is through conduction from the package into the SXM housing, through the SXM housing into the bracket, and through the bracket into the OSIRIS-REx gusset to which the SXM is mounted. A sensitivity analysis (manual sensitivity analysis prior to testing) of the SDD temperature to the thermal paths of the SXM revealed that the contact resistance at the package interface is the critical thermal sensitivity for the SXM. In order to satisfy the maximum SDD operating temperature of $-30\text{ }^{\circ}\text{C}$, Cho-Therm 1671 gap filler is applied to the gap between the package and the SXM housing to decrease contact resistance. The OSIRIS-REx gusset is the primary thermal sink for the SXM, and the spacecraft is responsible for accepting and dissipating the total SXM heat load and maintaining the interface temperature within its allowable range (from $-30\text{ }^{\circ}\text{C}$ to $50\text{ }^{\circ}\text{C}$).

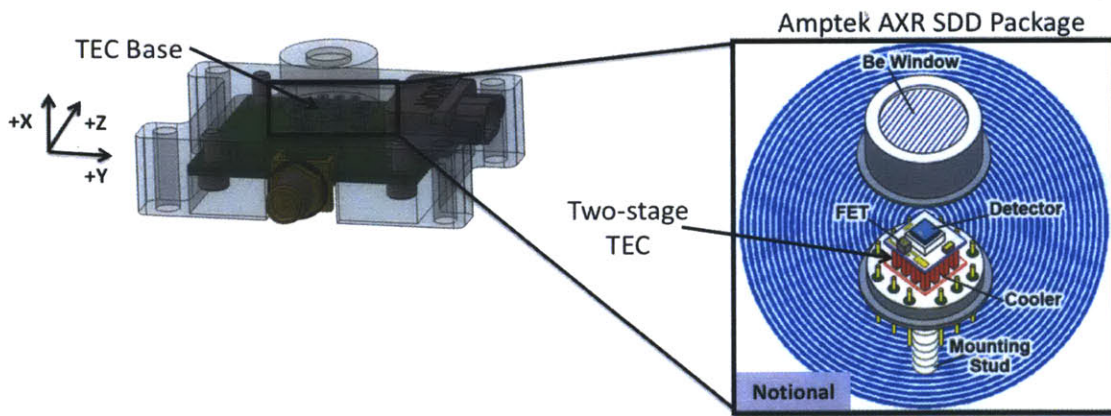


Figure 4-6: Amptek AXR SDD package. The *Detector* is the SDD, and the *Cooler* is the TEC in this figure. Image courtesy of Amptek, Inc. (accessible at <http://www.amptek.com/drift.html>).

4.5 Summary

This chapter provided a REXIS instrument overview, description of the thermal environments, summary of SXM thermal requirements, and SXM thermal system description. The REXIS instrument consists of the spectrometer and the SXM assemblies, which are mounted in different locations on the spacecraft OSIRIS-REx. REXIS must survive a 2.5 yr cruise period and then perform its science mission during Proximity Operations about the asteroid Bennu. During operation, the SXM is pointed directly at the sun to provide context to the measurements made by the spectrometer.

The second case study in this thesis implements BMV on the SXM thermal system model. The SXM is thermally coupled to the spacecraft deck, and a TEC cools the SDD to its operating requirement during the REXIS science mission. The driving thermal requirement during operation is the SDD hot temperature limit, which is driven by the detector spectral resolution requirement. To verify that the design will satisfy the requirements, analyses and tests are performed to validate the SXM thermal models in Chapter 5 by implementing BMV.

Chapter 5

REXIS Solar X-ray Monitor (SXM)

Case Study

The REXIS SXM thermal system is the second case study in this thesis. Sections 5.1-5.8 present BMV implemented on the SXM. Section 5.9 reviews the important lessons from Sections 5.1-5.8 and compares the BMV process to a conventional model validation approach.

5.1 Step 1: Validation Problem Definition

5.1.1 Validation Requirements

The complete list of thermal requirements for the SXM is shown in Table 4.2. The SXM does not internally dissipate power when off in a survival mode. Because the SXM structure is beneath the OSIRIS-REx MLI blankets, all components are approximately isothermal with the spacecraft interface temperature. Consequently, this case study will focus validation efforts on the operational temperature requirements of the SXM, restated in Table 5.1. The SXM requirements relevant for validation are stated probabilistically:

There shall be a probability of at least 99% that the component limits in Table 5.1 are satisfied during REXIS instrument operation.

The probability associated with satisfying a requirement is a systems engineering decision that must flow down from the mission’s risk posture. In this context, the probability of satisfying a requirement is analogous to thermal design margin. A probability of 99% for the REXIS SXM is selected because REXIS is a class D payload¹.

Table 5.1: Operational temperature limits for validation requirements

Component	Operational (°C)	
	Min	Max
SDD Housing	-40	100
SEB	-40	85
SDD	-100	-30

In this case study, the SXM model developed will be validated using the temperature limits in Table 5.1. As noted in Chapter 4, during operation the SXM electronics board (SEB) is more thermally restrictive than the SDD housing (i.e., if the SEB limits are satisfied, the SDD housing limits are satisfied). Analysis will show that the hot operational temperature limit of the SDD will drive the SXM thermal design.

5.1.2 Physical Problem Documentation

In Chapter 4, the thermal environments and SXM thermal system design are documented. Because the validation problem requirements consider the thermal response of the SXM *only* during operation, the relevant mission phases are Orbit Phase and Reconnaissance Phase, whose thermal environmental parameters are shown in Table 4.1. Nominally, the sunlight impinges on the SXM directly from the +X direction (see Figure 4-2), and the spacecraft solar distance ranges from 0.89 AU to 1.39 AU. The model validation efforts will consider thermal environment and SXM power modes for Orbit/Reconnaissance Phase only. As mentioned in Chapter 4, the thermal environments of Orbit Phase B and Reconnaissance Phase, *when REXIS performs science observations*, are identical.

¹Per the document NPR 8705.4—Risk Classification for NASA payloads

5.1.3 Model Development and Documentation

This section explains the selection of SXM thermal model structure and parameters. The SXM thermal model formulation, including its physical assumptions, details of the model structure, and descriptions of model fidelity are provided in Appendix C. The final product of this section is a ready-to-use model that generates mission temperature predictions for the components of the SXM that can be compared to the Table 5.1 limits.

A lumped parameter (i.e., network) model of the SXM is selected for BMV because it is physics-based and not computationally expensive. The model formulation for the SXM lumped parameter model is obtained by re-writing Equation (2.1):

$$\mathbf{y} = \eta_{SXM}(\mathbf{x}) \quad (5.1)$$

where \mathbf{x} is the complete set of model parameters including all system parameters (e.g., geometries and material properties), initial conditions, and boundary conditions, η_{SXM} is the SXM lumped parameter model, and \mathbf{y} is the output vector of node temperatures and heat flows. For a detailed description of the model underlying Equation (5.1), see Appendix C. The three QoIs for this case study are the steady state temperature predictions of the components shown in Table 5.1 where T_h is the temperature of the SDD housing, T_{SEB} is the temperature of the SEB, and T_{sdd} is the SDD temperature (i.e., $\mathbf{Q} \subset \mathbf{y}$ and $\mathbf{Q} = [T_h, T_{SEB}, T_{sdd}]^T$).

The SXM model parameter values are based on the system design that includes geometry and material properties, the interface with the spacecraft, and the space thermal environment. Table 5.2 shows the nominal model parameters for the SXM model; there are 38 total parameters. Depending on the parameter, *nominal* either refers to the parameter's default design value, an uncertain parameter's current best estimate, or a median value for the parameter. Examples of each type of nominal parameter values include:

- **Default design value:** the number of screws between the SXM housing and the bracket, $N_{s,b}$, is fixed because the design is frozen and is equal to four screws.
- **Current best estimate:** the conductance between the spacecraft and the SXM

bracket, G_b , is uncertain, but the best estimate of its value comes from empirical contact conductance data [4, 134] and is $2,000 \frac{W}{m^2 K}$.

- **Median parameter value:** the solar flux, ϕ_s , depends on the heliocentric radius of the spacecraft, which varies throughout the mission. A median value is $\phi_s=1,367 \frac{W}{m^2}$, which corresponds to a radius of 1 AU.

The model output corresponding to the parameters in Table 5.2 is referred to as the nominal model output.

Table 5.2: SXM model nominal parameter values

Parameter Name	Parameter Variable	Value	Units	Parameter Name	Parameter Variable	Value	Units
TEC Control Parameters				Area between SDD housing and SXM housing	A_{sdd}	1.824e-4	m ²
TEC Controller Gain	K_p	0.05	V/°C	Conductance between O-REx and bracket	G_b	2,000	W/m ² -°C
SDD Temperature Control Set Point	T_s	-30	°C	Number of screws between SXM housing and bracket	$N_{s,b}$	4	--
Controller Update Frequency	f_c	0.03	Hz	Conductance per screw between bracket and SXM housing	$G_{s,b}$	0.42	W/°C
Initial Applied TEC Voltage	V_{TEC}	3.0	V _{DC}	Conductance per screw between SEB and SXM housing	$G_{s,pa}$	0.26	W/°C
Node Specific Heats				Bracket Interface Surface Area	A_b	0.0035	m ²
Bracket Specific Heat	$c_{p,1}$	961	J/kg-K	Number of screws between SEB and SXM housing	$N_{s,pa}$	4	--
SXM Housing Specific Heat	$c_{p,2}$	961	J/kg-K	Conductivity of pins on SDD package	k_{pins}	400	W/m-°C
SEB Specific Heat	$c_{p,3}$	800	J/kg-K	Area of pins on SDD package	A_{pins}	1.968e-6	m ²
SDD Housing Specific Heat	$c_{p,4}$	461	J/kg-K	Length of pins on SDD package	L_{pins}	0.00762	m
Collimator Specific Heat	$c_{p,5}$	961	J/kg-K	Conductance between SDD housing and SXM housing	G_h	2,000	W/m ² -°C
Node Masses				Temperature of OSIRIS-REx	T_{O-REx}	40	°C
Bracket Mass	m_1	0.1082	kg	Number of screws between collimator and SXM housing	$N_{s,coll}$	3	--
SXM Housing Mass	m_2	0.0192	kg	Radiation Parameters			
SEB Mass	m_3	0.0060	kg	Solar Flux	ϕ_s	1,367	W/m ²
SDD Housing Mass	m_4	0.0120	kg	Collimator External Surface Area	A_{coll}	0.000246	m ²
Collimator Mass	m_5	0.0090	kg	Temperature of Deep Space	T_{space}	2.73	K
Power Dissipations				Collimator Absorptivity	α_c	0.5	--
SDD Heat Load	Q_{sdd}	0.01	W	Collimator Emissivity	ϵ_c	0.8	--
SEB Heat Load	Q_{pa}	0.20	W	SDD Housing Area Exposed to Direct Sunlight	A_h	3.9e-5	m ²
Conduction Parameters				SDD Housing Absorptivity	α_h	0.5	--
Conductance per screw between collimator and SXM housing	$G_{s,coll}$	0.21	W/°C	Effective IR Radiation Area of Collimator	$A_{coll,eff}$	0.00128	m ²

5.2 Step 2: Uncertainty Propagation and Parameter Prioritization—First Pass

The SXM case study traverses BMV steps two through five more than once to validate the SXM thermal model, as shown in Figure 2-1. The following sections present each step of BMV sequentially and each step *pass* is denoted (e.g., the second time step two is performed is referred to as step two, second pass). The goals of UP and parameter prioritization for the SXM are:

- To determine the probability that the design requirement will be met
- To identify important model parameters that require additional research or experimentation to reduce their uncertainties

First, the SXM model parameter distributions are assigned prior uncertainty distributions. Next, uncertainty analysis (UA) and global sensitivity analysis (GSA) are performed for the SXM. Finally, a prioritized list of parameters is provided based on the results of GSA.

Before UA and GSA, the uncertainty for each model parameter is characterized. In total, the SXM model contains 38 parameters, of which 18 parameters are uncertain or exhibit natural variability (e.g., solar flux). As an example of a known model parameter value, the number of the screws between the SXM housing and bracket is known to be four. For the uncertain parameters, distribution type and ranges must be specified in order to probabilistically propagate the uncertainties through the model. Table 5.3 shows all 18 uncertain or naturally varying SXM model parameters and their initial probability distribution parameters. In all cases, it is possible to conservatively estimate the maximum and minimum expected values for the parameter, but no shape information for the probability distributions is known. Consequently, all 18 initial parameter distributions are assigned uniform distributions. To place a value on the minimum and maximum parameter values, lookup tables [4, 5, 134, 135] are used for the node specific heats, conduction parameters, and radiation parameters. The lookup tables provide estimates based on a historical data for a measured value. The minimum and maximum values are consistent with the worst hot and cold case assumptions used in conventional model validation thermal analysis. Finally, the

power dissipations are based on power analyses of the SEB circuitry and the Amptek package thermoelectric cooler (TEC).

Table 5.3: SXM model nominal parameter values and initial parameter distribution values

Parameter Number	Name	Variable	Units	Nominal Value	Distribution Type	Parameter 1 (minimum)	Parameter 2 (maximum)
Node Specific Heats							
1	1 - Bracket	$c_{p,1}$	J/kg-K	961	Uniform	921	972
2	2 - SXM Housing	$c_{p,2}$	J/kg-K	961	Uniform	921	972
3	3 - SEB	$c_{p,3}$	J/kg-K	800	Uniform	378	880
4	4 - SDD Housing	$c_{p,4}$	J/kg-K	461	Uniform	378	461
5	5 - Collimator	$c_{p,5}$	J/kg-K	961	Uniform	921	972
Power Dissipations							
6	SDD	Q_{SDD}	W	0.01	Uniform	0	0.01
7	SEB	Q_{PA}	W	0.20	Uniform	0	0.25
Conduction Parameters							
8	Temperature of O-REx Deck	T_{O-REx}	°C	40	Uniform	-30	50
9	Conductance between O-REx and bracket	G_b	W/m ² -C	2,000	Uniform	100	4,000
10	Conductance per screw between bracket and SXM housing	$G_{s,b}$	W/C	0.42	Uniform	0.11	1.32
11	Conductance per screw between SEB and SXM housing	$G_{s,pa}$	W/C	0.26	Uniform	0.07	0.80
12	Conductivity of pins on SDD package	k_{pins}	W/m-°C	400	Uniform	350	405
13	Conductance between SDD housing and SXM housing	G_h	W/m ² -C	2,000	Uniform	100	4,000
14	Conductance per screw between collimator and SXM housing	$G_{s,coll}$	W/C	0.21	Uniform	0.03	0.42
Radiation Parameters							
15	Solar Flux	ϕ_s	W/m ²	1,367	Uniform	700	1,752
16	Collimator Absorptivity	α_c	--	0.50	Uniform	0.31	0.60
17	Collimator Emissivity	ϵ_c	--	0.80	Uniform	0.78	0.82
18	SDD Housing Absorptivity	α_h	--	0.50	Uniform	0.30	0.52

To provide an example of how the minimum and maximum parameter values are derived for the uniform distributions, Table 5.4 shows the recommended conductance values for an aluminum bolted interface (with no gap filler). For a given screw size, small stiff surfaces yield greater conductance across a bolted interface than large thin surfaces. Consider the conductance, per screw, across the interface between the SXM housing and the bracket, $G_{s,b}$: while strictly looking at the screw size 6-32, provides the nominal value, the maximum value is selected from a small stiff surface two sizes larger (10-32) and the minimum value is selected from a large thin surfaces two sizes smaller (2-56). Thus, the minimum and maximum values in Table 5.3 for $G_{s,b}$ from Table 5.4 are 0.105 and 1.32, respectively. The screw sizes two sizes larger/smaller are used is to increase the likelihood that the true conductance value is

contained within the bounds of the initial probability distribution.

Table 5.4: Thermal conductance design guidelines from TRW for an aluminum bolted interface. Table from [4, Table 8.4]

Screw Size	Conductances (W/K)	
	Small Stiff Surfaces	Large Thin Surfaces
2-56	0.21	0.105
4-40	0.26	0.132
6-32	0.42	0.176
8-32	0.80	0.264
10-32	1.32	0.527
1/4-28	3.51	1.054

The screw conductance example illustrates the philosophy in selecting the initial distribution variances: the minimum and maximum range should be selected so that the true parameter value is contained, but not so large that the parameter’s sensitivity is artificially inflated. In practice, adjusting the variances may be necessary as the model is run. Furthermore, a sensitivity analysis *to a particular parameter’s uncertainty distribution* can be performed if there is poor prior knowledge of a parameter’s value to determine the influence of the parameter’s uncertainty on the output.

The SXM model is first run for the nominal parameter values in Table 5.2. The nominal temperature predictions are shown in Figure 5-1, and steady state temperatures are achieved after approximately 10 minutes. The temperatures of the SEB and SDD housing are 41 °C and 42 °C, respectively. The temperature of the SDD is –30 °C. All requirements from Table 5.1 are satisfied for the nominal parameter values.

Although the requirements are met in the nominal case, the requirements *may* not be satisfied when the parameter uncertainties are considered. As in the radiator case study in Chapter 3, the model structure uncertainty is temporarily neglected and only parameter uncertainties are considered for the first uncertainty propagation. A Monte Carlo (MC) simulation is performed to propagate the parameter uncertainties through the SXM model. Rewriting Equation (2.3) for this MC analysis, Equation (5.2) shows the MC formulation for the parameter uncertainty distributions in Table 5.3:

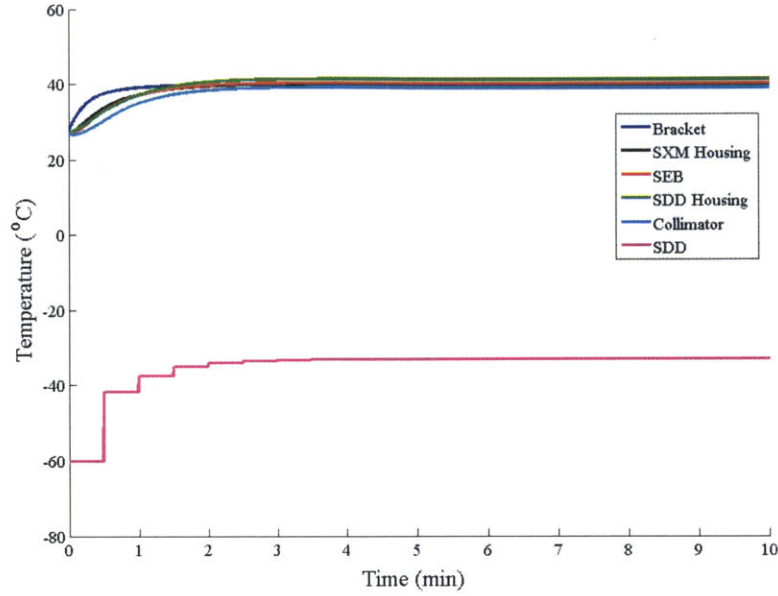


Figure 5-1: Thermal predictions for SXM using nominal parameters from Table 5.2 where a hot start is assumed with initial node temperatures of 27 °C. The initial SDD temperature is -60 °C.

$$\bar{\eta}_{SXM,N} = \frac{1}{N} \sum_{i=1}^N \eta_{SXM}(\mathbf{x}_i) \quad (5.2)$$

where η_{SXM} is the SXM model and \mathbf{x}_i is the i^{th} randomly sampled set of parameters. The MC estimator, $\bar{\eta}_{SXM,N}$, is the expected output value of the model.

To select a suitable number of random samples, N , the MC standard error is computed. The minimum allowable probability for satisfying each temperature requirement is 99%. When the probability of *not* satisfying the requirements is much greater than $p = 0.01$ (i.e., probability of 1%), fewer MC samples are required because the estimated probability is larger. Thus, we are interested in the number of samples, N , required to accurately estimate probabilities of $p = 0.01$ because it drives the minimum allowable N value. For the SXM, a MC standard error of 0.001 is sufficient because the error in the probability estimate will not effect decisions/analyses made later in the case study. The MC standard error is shown in Equation (5.3):

$$e_{MC} = \sqrt{\frac{p(1-p)}{N}} \quad (5.3)$$

where e_{MC} is the MC standard error and p is the specified probability of *not* satisfying the temperature requirements (e.g., $p = 0.01$ for the SXM). For $N = 10,000$, the MC standard error is $e_{MC} = 0.001$. A MC simulation that predicts a probability of $p = 0.01$ of satisfying the requirement has a 3σ confidence interval of [0.007, 0.013]. The number of MC random samples used for uncertainty analysis is $N = 10,000$.

After running the MC analysis, all three component temperatures in Table 5.1 are satisfied with the required 99% probability given the SXM thermal model's parametric uncertainty. At this stage in BMV, step three (Figure 2-4) dictates that a model validation experiment be performed to validate the model since all requirements are predicted to be met. However, this case study will relax the bounds on the interface temperature with the spacecraft OSIRIS-REx, T_{O-REx} , to determine *at what temperature limits the interface could be set using BMV*. The maximum allowable value of T_{O-REx} is important because:

- The SDD temperature is the driving thermal system requirement for the SXM, and the upper limit of T_{O-REx} is the most critical parameter in determining whether the SDD temperature requirement is achievable.
- The allowable flight temperatures for T_{O-REx} range from [-30,50] °C and are requirements of the spacecraft thermal system. The temperature range was negotiated between REXIS and the spacecraft during preliminary design (before the Critical Design Review). The 50 °C limit is driving because the region where the SXM is mounted is illuminated by the sun during the mission. The 50 °C limit resulted in design changes and potential operational constraints on the spacecraft that may have not been necessary for a higher upper limit. The design changes to the spacecraft resulted in an increase to the spacecraft accommodations cost for REXIS.

BMV is used to validate the model of the SXM and re-evaluate the limits of T_{O-REx} to see if the 50 °C limit is an appropriate upper interface temperature limit. Furthermore, an increase of the 50 °C limit, if allowable once the model has been validated, represents a cost savings that *could have* occurred when the ranges of T_{O-REx} were set. For a more detailed discussion of the design changes and operational constraints due to the 50 °C limit, see Section 5.9.

The first step is to repeat the MC analysis in Equation (5.2) for various T_{O-REx} temperatures. In order to find the T_{O-REx} upper limit at which the requirements in Table 5.1 are no longer satisfied. Figure 5-2 shows the joint cumulative distribution function (CDF) of the SDD temperature, T_{sdd} , and the spacecraft interface temperature, T_{O-REx} . The joint CDF is created by performing MC analyses at discrete values of T_{O-REx} , and the number of samples for each MC simulation is $N = 10,000$. For a given spacecraft interface temperature, the contour value is the probability that the SDD temperature is equal to or less than the y-axis value. For example, the probability that the SDD temperature is at or below -28 °C for an interface temperature of 80 °C is approximately 90%. From Figure 5-2, the thermal design of the SXM is unable to achieve the -30 °C SDD temperature limit with at least 90% probability near an interface temperature of $T_{O-REx} = 75$ °C.

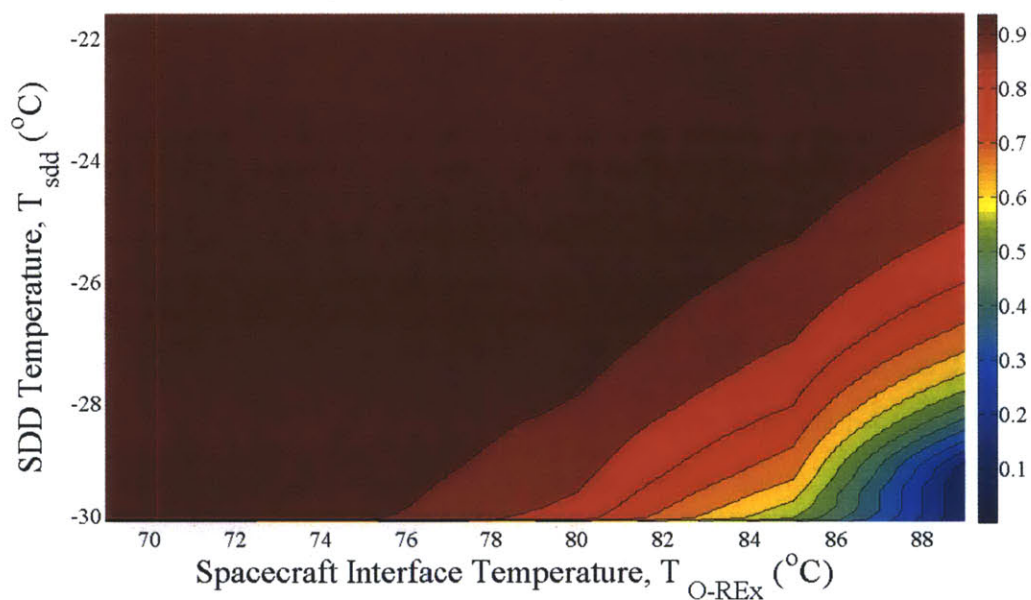
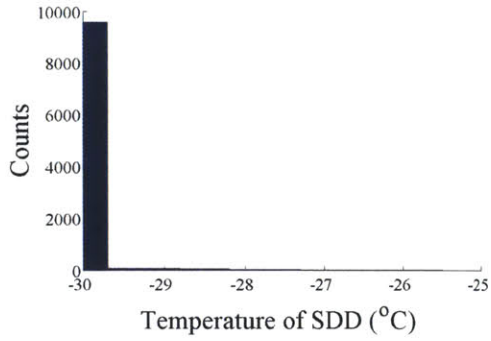


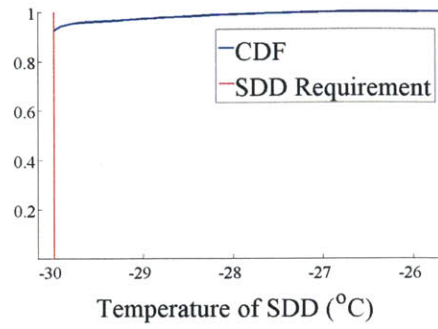
Figure 5-2: Joint cumulative distribution function for SDD temperature and the temperature of the spacecraft deck, T_{O-REx}

MC simulations at discrete T_{O-REx} values are shown in Figure 5-3. The spacecraft interface temperature, T_{O-REx} , ranges from 75 °C to 90 °C in increments of 5 °C. On the left, histograms are shown at each temperature to illustrate the number of model evaluations at or near the -30 °C limit. At 90 °C, no model evaluations yield a temperature prediction for the SDD of -30 °C (i.e., the probability of meeting the requirement is zero). CDFs

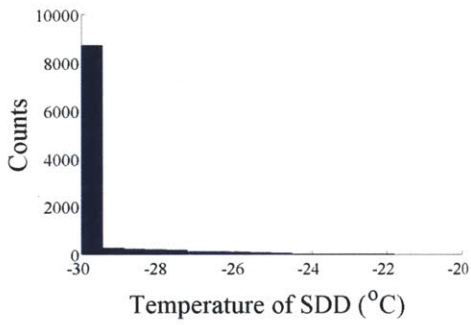
are shown on the right side of Figure 5-3 using the same data from the histograms. Each empirical CDF shows the probability that the $-30\text{ }^{\circ}\text{C}$ limit is satisfied.



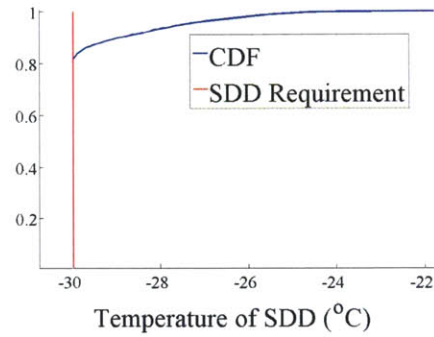
(a) Histogram, $T_{O-REx} = 75 \text{ }^\circ\text{C}$



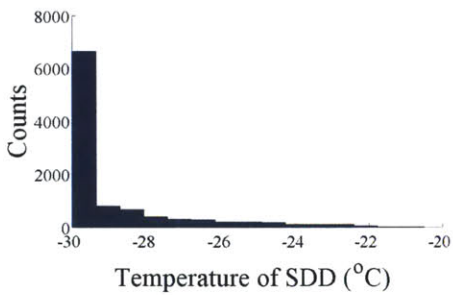
(b) CDF, $T_{O-REx} = 75 \text{ }^\circ\text{C}$



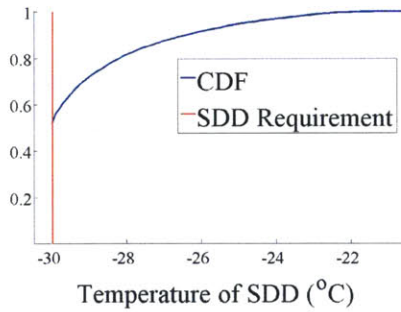
(c) Histogram, $T_{O-REx} = 80 \text{ }^\circ\text{C}$



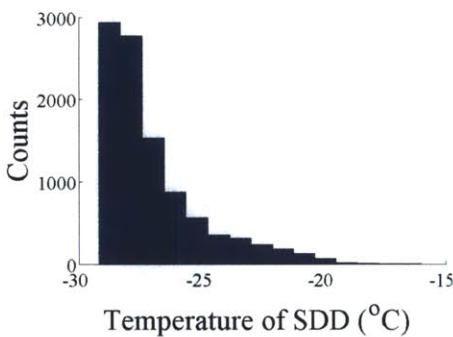
(d) CDF, $T_{O-REx} = 80 \text{ }^\circ\text{C}$



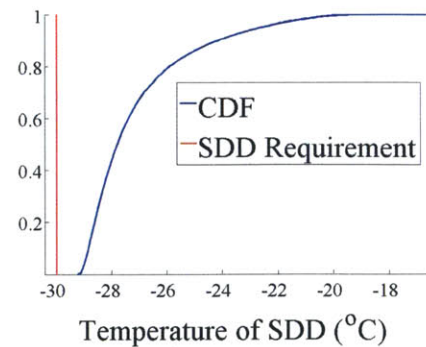
(e) Histogram, $T_{O-REx} = 85 \text{ }^\circ\text{C}$



(f) CDF, $T_{O-REx} = 85 \text{ }^\circ\text{C}$



(g) Histogram, $T_{O-REx} = 90 \text{ }^\circ\text{C}$



(h) CDF, $T_{O-REx} = 90 \text{ }^\circ\text{C}$

Figure 5-3: Histograms and CDFs of T_{sdd} conditioned on T_{O-REx} . MC simulation results shown for 10,000 samples at each T_{O-REx} value.

The CDF of the SDD temperature *conditioned on* T_{O-REx} is found for $T_{sdd} = -30$ °C by taking the $T_{sdd} = -30$ °C section from Figure 5-2 (i.e., selecting the CDF values from Figure 5-3 that intersect at -30 °C). Figure 5-4 shows the conditional CDF at $T_{sdd} = -30$ °C. The MC results for the SEB and SDD housing temperatures are included in Figure 5-4 to confirm that the SDD temperature is the most restrictive QoI. Because the SDD temperature is the QoI that has the lowest T_{O-REx} temperature corresponding to a 99% probability, the SDD temperature is the most thermally restrictive QoI. At 63 °C, the SDD requirement is no longer satisfied with sufficient probability. At ≈ 75 °C, the probability that the -30 °C limit is satisfied decreases relatively sharply to zero at approximately 90 °C. If there were no parameter uncertainties (model structure uncertainties are not yet considered), the distributions in Figure 5-4 would instead be a single T_{O-REx} value at which the model predicts the requirements are not met. Reducing the uncertainties in key SXM model parameters will reduce the uncertainty in the upper limit of T_{O-REx} .

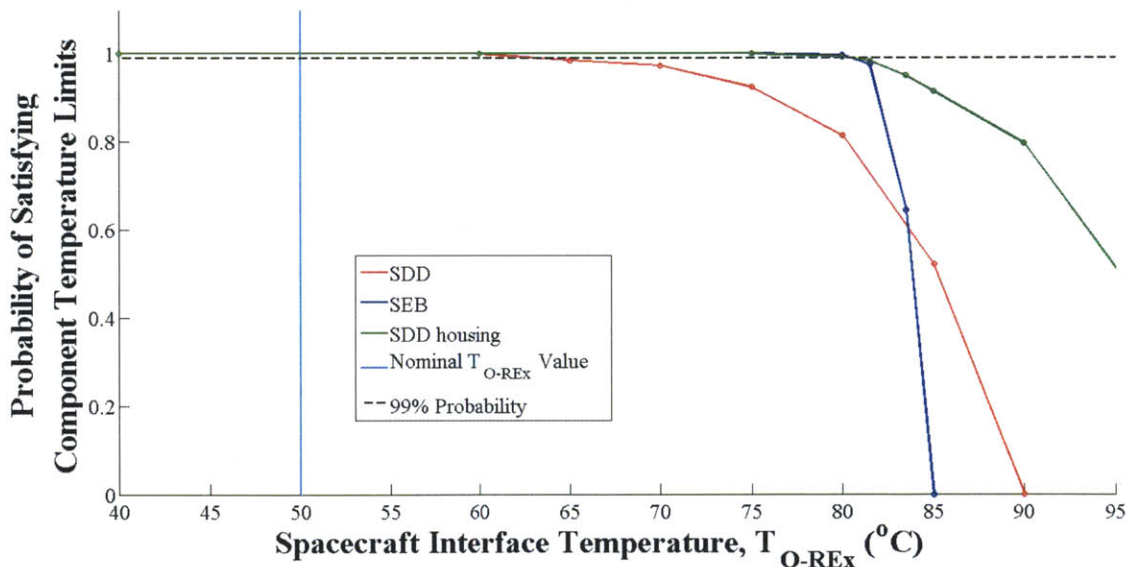


Figure 5-4: Probability of satisfying the upper limits of the Table 5.1 temperature ranges versus T_{O-REx} for all three SXM QoIs based on MC simulations with $N = 10,000$ samples to propagate parametric uncertainties through the SXM thermal model

GSA is used to identify key SXM model parameter(s) that heavily influence the variability observed in the QoIs. The GSA method used for the SXM case study is the Sobol' method [121]. The main effect and total effect sensitivities, shown in Equations (2.8) and (2.9),

respectively, account for both a parameter's sensitivity and its uncertainty by quantifying its effect on the model QoIs. The Sobol' method is commonly used for identifying important model parameters and guiding future research and testing [71]. The main effects and total effects sensitivities are evaluated using the numerical procedure outlined by Saltelli et al. [122]. The global sensitivities for the uncertain parameters in Table 5.3 are found for all three QoIs.

Figure 5-5 shows the main effect global sensitivities for $T_{O-REx} = 85$ °C. For all three QoIs, the sensitivity indices of the specific heats, $c_{p,i}$, are zero. That the sensitivities for $c_{p,i}$ are zero is an intuitive result because the QoIs are steady state values and do not functionally depend on the specific heats, which affect the system's thermal time constant. The largest sensitivity index for the SDD is the conductance between the SDD housing and the SXM housing, $S_{G_h}^{SDD} = 0.96$. The SDD housing to SXM housing conductance is also the largest sensitivity for the SDD housing with a sensitivity of $S_{G_h}^{SEB} = 0.97$. That these sensitivities are near one indicates that nearly all uncertainty in the two QoIs at $T_{O-REx} = 85$ °C is due to the parameter G_h . Furthermore, it is intuitive that G_h dominates because the power dissipation for the TEC inside the SDD housing is a large portion of the overall SXM power dissipation, and the conductance between the SDD housing to the SXM housing is the primary thermal path to remove the heat load.

For the SEB temperature, the second most restrictive QoI, three parameters have the most influence: the SDD housing to SXM housing conductance, G_h , the conductance between the housing and SEB (per screw), $G_{s,pa}$, and the conductance between the bracket and SXM housing, $G_{s,b}$. For all three QoIs, the sum of the main effects sensitivities is nearly one, indicating that the effects of the interactions are small. To confirm that the effects of interactions are small, the total effects indices are found for all three QoIs. All total effects indices are identical to the main effects indices to the second decimal place, confirming that the parameter interactions are negligible. While the model has 18 uncertain parameters, making it initially unclear which parameters to target in a parameter inference experiment, the GSA results in Figure 5-5 show how the variability in the QoIs can be attributed to only a few of the 18 parameters, G_h being the most significant.

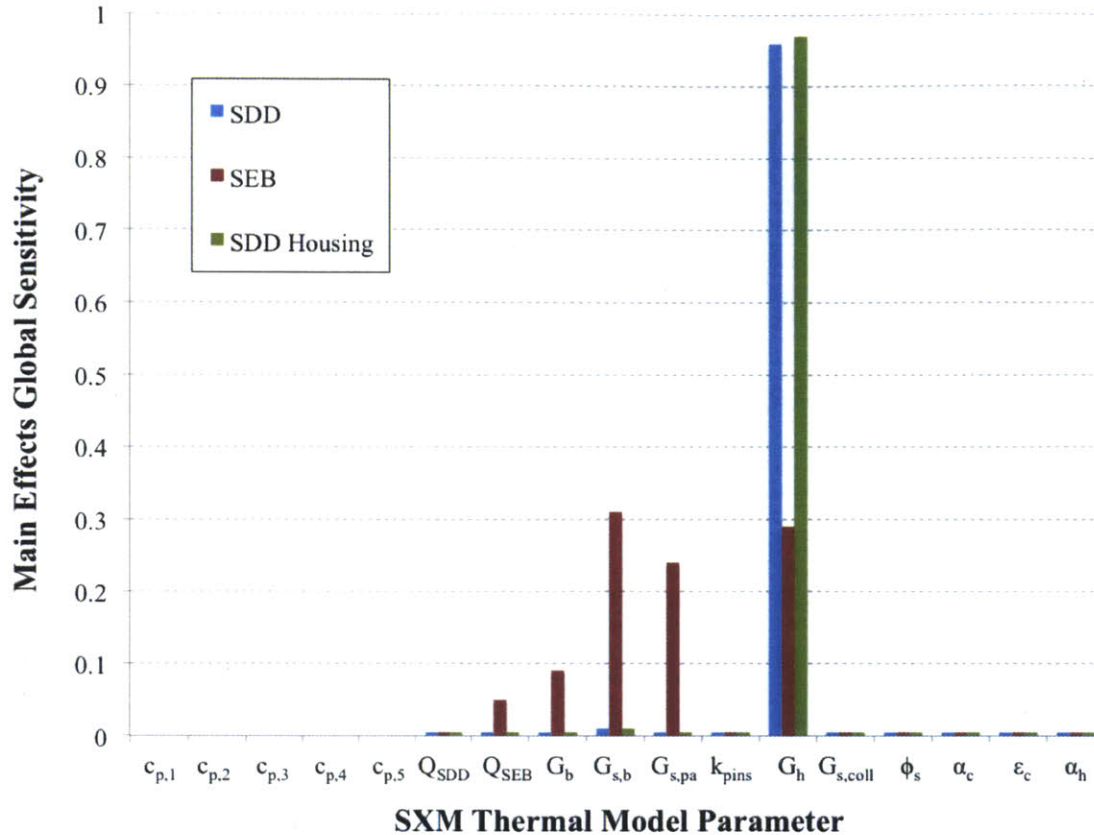


Figure 5-5: Main effects global parameter sensitivities of SXM model for all three QoIs at $T_{O-REx} = 85 \text{ }^\circ\text{C}$. The parameter variable names are defined in Table 5.3. The spacecraft interface parameter, T_{O-REx} , is omitted since it is held constant for this GSA.

5.3 Step 3: Experimental Goal Setting—First Pass

In step two of BMV, UA indicates that the requirements will be met when accounting for *all* parameter uncertainties. Thus, the answer to the first gate in Figure 2-4—whether there is sufficient confidence that the requirements are met—is **yes**, and the answer to the second gate—whether the system-level model is validated—is **no**. However, the upper limit on the spacecraft interface temperature, T_{O-REx} , is relaxed. The case study validates the model of the REXIS SXM and looks back in the design lifecycle to find the upper temperature limit of T_{O-REx} at which the interface *could have been set* using BMV.

With T_{O-REx} variable, the SDD temperature is found to be the driving QoI as T_{O-REx} increases. From Figure 5-4, $T_{O-REx} = 63 \text{ }^\circ\text{C}$ is the value at which the SDD requirement is no longer satisfied with at least 99% probability. From GSA, the uncertainty in the conductance

between the SDD housing and the SXM housing, G_h , most significantly contributes to the variability in the SDD temperature. A parameter inference experiment will be performed to reduce the uncertainty in G_h to reduce uncertainty in T_{sdd} (in accordance with Figure 2-4). In addition to the parameter inference goal, the case study will formulate a system-level model validation experiment to validate the thermal model of the SXM.

5.4 Step 4: Design and Implementation of Experiments

Step four of BMV is divided into three sections. First, an optimal parameter inference experiment is designed to reduce the uncertainty in the SXM conductance parameter G_h . Second, a model validation experiment is formulated to validate the SXM thermal model over the domain of thermal environments and operational modes expected during the mission. The parameter inference and model validation experiments are completed during the same test session to reduce the total time required to complete both experiments. The validation experiment consists of 45 test phases, and the parameter inference experiment is one of the 45 phases. Third, the experimental results are shown for all test phases. Appendix A shows the SXM thermal test plan, and Appendix B contains the raw SXM thermal test data.

5.4.1 Parameter Inference Experiment

Development of Experimental Thermal Model

The first component of Design of Experiments (DOE) for the parameter inference experiment is to modify the model structure to match the conditions of the experiment. Pictures and detailed descriptions of the test thermal vacuum chamber are provided in the test plan in Appendix A. The important features of the test environment include a baseplate that can be temperature controlled to a fixed temperature (emulating the spacecraft interface), an evacuated chamber below 1×10^{-5} torr, and nominally room temperature walls. An MLI blanket with a hole cut-out for the collimator is draped over the SXM and baseplate to simulate the spacecraft MLI blanket. Consequently, there are four major changes to the SXM thermal model:

1. Addition of observation error term, ϵ_m , to the temperature predictions to account for random noise in the temperature sensors.
2. The temperature of deep space, T_{space} , in Table 5.2 becomes the temperature of the thermal vacuum chamber wall, T_w .
3. Sunlight is not simulated in the chamber so the solar flux, ϕ_s , and all related SXM parameters are removed (e.g., α_h).
4. For the experiment, the TEC will not be software controlled but instead set to a constant direct current voltage value. Thus, for the experimental design the TEC voltage, V_{TEC} , can be manually set to any value.

As in the radiator case study in Chapter 3, ϵ_m is based on the characteristics of the sensors used. For all temperature measurements except for the SDD, resistance temperature detectors (RTDs) are used to make temperature measurements. Based on manufacturer specifications of the RTDs used, $\epsilon_m \sim \mathcal{N}(0, \sigma_m^2) = \mathcal{N}(0, 0.15^2)$ °C. For the diode on the cold side of the TEC used to measure the SDD temperature, $\epsilon_m = \mathcal{N}(0, 0.25^2)$ °C based on specifications from Amptek, Inc. The results of GSA indicated that the sensitivities to the optical property parameters for all three QoIs are small. Thus, it is acceptable to neglect the thermal effects of the sun in this test.

OBED Formulation for Parameter Inference Experiment

Bayes' Theorem, stated in the OBED form in Equation (2.10), is used to update the knowledge of parameter(s) of interest in light of experimental data. Model inadequacy is temporarily neglected to design the parameter inference experiment, so the observations are equal to the model output plus the observation error:

$$\mathbf{z} = \eta(\mathbf{x}, \theta, \mathbf{d}) + \epsilon_m \quad (5.4)$$

where the terms in Equation (5.4) are:

- \mathbf{x} : all SXM model parameters, including experimental design conditions and experimental parameters of interest. All SXM model parameters are shown in Table 5.2.

- $\eta(\mathbf{x}, \theta, \mathbf{d})$: model evaluation for a realization of SXM model parameters
- \mathbf{z} : experimental result or data
- θ : the parameter of interest (i.e., those parameters in \mathbf{x} that are specifically targeted by the parameter inference experiment). Note: $\theta \subset \mathbf{x}$ and $\theta = G_h$.
- \mathbf{d} : experimental conditions (i.e., parameters in \mathbf{x} that can be set to create different types of experiments). Note: $\mathbf{d} \subset \mathbf{x}$.

The parameter of interest is the conductance between the SDD housing and the SXM housing, $\theta = G_h$. Through GSA, it is determined that the effects of all other parametric uncertainties on the QoIs are small. Consequently, all parameters in \mathbf{x} , except G_h , are fixed at their nominal values.

The experimental data, \mathbf{z} , are steady state temperatures of the SXM. Practically, a minimum of one temperature measurement is necessary to reduce uncertainty in G_h . However, it is relatively easy to include multiple sensors in this test, so six sensors are assumed when designing the optimal parameter inference experiment. Later, analysis is performed to find the sensors that are most important with respect to inferring G_h . An RTD is allocated to each node in the model (see Figure C-6) to provide a temperature measurement for each SXM component. For exact RTD locations, see Appendix A. Assuming multiple RTDs for each node provides no added information in the context of designing this parameter inference experiment because the model will predict the output of the sensors to have identical distributions. Including multiple sensors for each model node is beneficial during calibration to check the assumption that all material within a node's region is isothermal; thus, additional sensors are included on certain SXM components when feasible (see Appendix A). A diode within the Amptek package on the cold side of the TEC provides the best possible temperature measurement of the SDD. Thus, the data vector, \mathbf{z} , is a 6x1 vector consisting of temperature measurements for the bracket, SXM housing, SEB, SDD housing, collimator, and SDD.

Parameters in \mathbf{x} that describe either the thermal environment or SXM configuration are identified as experimental conditions, \mathbf{d} , and their values are selected to find the optimum experiment. Table 5.5 describes the three experimental conditions for the parameter inference

experiment. The three parameters in \mathbf{d} that are used to create different experiments are the chamber interface plate temperature (simulating the interface temperature with the spacecraft deck, T_{O-REx}), the TEC voltage setting (effectively controlling TEC power), V_{TEC} , and the temperature of the thermal vacuum wall, T_w . The experimental conditions are all contained in a vector \mathbf{d} such that $\mathbf{d} = [d_1, d_2, d_3]^T = [T_{O-REx}, V_{TEC}, T_w]^T$.

Table 5.5: Table of experimental conditions, \mathbf{d} , and the range of possible values for each d_i

Name	Variable	DOE Variable	Units	Nominal Value	Minimum Value	Maximum Value
Temperature of O-REx Deck	T_{O-REx}	d_1	$^{\circ}\text{C}$	40	-100	75
TEC Voltage	V_{TEC}	d_2	V_{DC}	3.0	0	4.5
Temperature of Thermal Vacuum Chamber Wall	T_w	d_3	$^{\circ}\text{C}$	23	23	80

By design, the range of values for each experimental condition in Table 5.5 is not necessarily the same as the range expected during the mission because there may be experimental conditions outside the expected mission range that result in higher parameter inference utility. The chamber baseplate temperature, T_{O-REx} , is regulated by a controller that uses the baseplate heater and liquid nitrogen plumbing to warm and cool the baseplate, respectively. The temperature limits for T_{O-REx} are constrained by the component limits on the SEB. To analytically explore how the utilities change for lower T_{O-REx} values, a minimum of $-100\text{ }^{\circ}\text{C}$ is shown in Table 5.5. However, the minimum allowable lower limit is $-30\text{ }^{\circ}\text{C}$ to prevent failure of SEB components. The upper limit of $T_{O-REx} = 75\text{ }^{\circ}\text{C}$ for the experiment is $25\text{ }^{\circ}\text{C}$ higher than the original upper limit of $T_{O-REx} = 50\text{ }^{\circ}\text{C}$. The SDD TEC voltage range shown is 0-4.5 V to analytically explore a large range of possible voltages. Based on the range of voltages in the performance estimates provided by the manufacturer in Figure C-3, the maximum allowable TEC voltage will be constrained to 4.0 V when the final experimental conditions are selected. Lastly, the temperature of the thermal vacuum chamber wall, T_w , is nominally room temperature since the walls of the chamber are externally exposed to ambient air and are not cooled by liquid nitrogen. However, an IR heater plate can be added to the chamber with a full view factor to the collimator such that the effective wall temperature can be up to $80\text{ }^{\circ}\text{C}$, if shown to be important in the experiment’s design.

The next component of this BMV step is to implement an OBED method to find the

optimal parameter inference experiment. Following the approach of Huan and Marzouk [83] for a parameter inference experiment, the Kullback-Leibler (KL) divergence is chosen as the utility function, $u(\mathbf{d}, \mathbf{z}, \theta)$, in Equation (2.11). The KL divergence is a scalar, non-negative measure of information difference between two distributions and is commonly used as the utility function in parameter inference experiments [79, 83]. Huan and Marzouk [83] show that an estimate for $U(\mathbf{d})$ can be achieved via MC sampling:

$$U(\mathbf{d}) \approx \frac{1}{n_{out}} \sum_{i=1}^{n_{out}} \left(\ln[p(\mathbf{z}_i|\theta_i, \mathbf{d})] - \ln[p(\mathbf{z}_i|\mathbf{d})] \right) \quad (5.5)$$

where $p(\mathbf{z}_i|\theta_i, \mathbf{d})$ is the i^{th} sample of the likelihood, and $p(\mathbf{z}_i|\mathbf{d})$ is the i^{th} sample of the evidence, both terms in Bayes' Theorem in Equation (2.10). In Equation (5.5), the subscript i denotes a realization of the parameter of interest, θ_i , (randomly drawn from the uncertainty distribution) which results in a single realization for the experimental outcome, \mathbf{z}_i . The evidence, $p(\mathbf{z}_i|\mathbf{d})$, in Equation (5.5) is approximated using nested MC sampling:

$$p(\mathbf{z}_i|\mathbf{d}) \approx \frac{1}{n_{in}} \sum_{j=1}^{n_{in}} p(\mathbf{z}_i|\theta_{i,j}, \mathbf{d}) \quad (5.6)$$

where n_{out} is the number of evaluations in the outer loop and n_{in} is the number of evaluations in the inner loop. A new set of realizations for the parameter of interest is drawn, and each realization, $\theta_{(.,j)}$, is used to evaluate the conditional probability in Equation (5.6). The probability is evaluated using the experimental result corresponding to the set of parameter realizations in Equation (5.5), \mathbf{z}_i . All quantities in \mathbf{z} are *conditionally independent* of G_h (i.e., for a given realization of G_h , the experimental model is deterministic). Thus, the likelihood terms in Equations (5.5) and (5.6) are equivalent to the product of individual likelihood terms for each quantity in \mathbf{z} :

$$p(\mathbf{z}_i|\theta_i, \mathbf{d}) = \prod_{k=1}^{M=6} p(z_i^k|\theta_i, \mathbf{d}) \quad (5.7)$$

where the individual likelihood terms come from the fact that there are multiple sensors used in the experiment. There are six independent component temperature measurements in \mathbf{z} , so $M = 6$. The superscript k is used to iterate over each component's estimated measurement

value, z_i^k , given an experiment at \mathbf{d} and a realization of the parameter of interest, θ_i .

In Equations (5.5) and (5.6), the shape of the conditional distributions are not known in general because there are additional uncertain parameters in \mathbf{x} (e.g., nuisance parameters), not in \mathbf{d} or θ , that contribute to the output variance. However, all uncertain parameters in this experimental design problem, except G_h , in \mathbf{x} are fixed at their nominal values. Consequently, the shape of the conditional distributions is identical to the shape of the observation error distributions. The samples in Equation (5.7), z_i^k , are evaluated on Gaussian distributions that are centered on the expected experimental result with variance equal to the variance of ϵ_m (i.e., sampled from $\mathcal{N}(\eta(\mathbf{x}, \theta_i, \mathbf{d}), \sigma_m^2)$).

With the experimental utility defined by Equation (5.5), the goal is to find the maximum utility, U^* , by selecting a single set of the experimental conditions, \mathbf{d}^* . To compute $U(\mathbf{d})$ for a particular \mathbf{d} , the computational cost is $\mathcal{O}(n_{out}n_{in})$. To reduce the number of model evaluations to $\mathcal{O}(n_{out})$, the implementation follows the recommendation of Huan and Marzouk [83] to constrain the sampling to $n_{out} = n_{in}$ and use the same batch of samples of θ for the outer loop as the inner loop. Over the domain of possible experimental conditions, $\mathbf{d} \in \mathcal{D}$, a \mathbf{d}^* is sought such that:

$$\mathbf{d}^* = \arg \max_{\mathbf{d} \in \mathcal{D}} U(\mathbf{d}) \quad (5.8)$$

In general, solving Equation (5.8) via grid search can be computationally infeasible (e.g. \mathbf{d} has high dimension or $U(\mathbf{d})$ requires many model evaluations and each model evaluation is computationally expensive). Several optimization algorithms such as the simultaneous perturbation stochastic approximation (SPSA) [136, 137] and the Nelder-Mead nonlinear simplex (NMNS) [138] have been proposed to solve Equation (5.8), allowing for the noisy objective function, $U(\mathbf{d})$. However, for the SXM parameter inference problem, \mathbf{d} has only three dimensions. While $U(\mathbf{d})$ is computationally expensive to evaluate, it is feasible to solve Equation (5.8) via grid search .

Selection of Optimal Parameter Inference Experiment

There are four remaining questions to answer to design the optimum parameter inference experiment:

1. What is the sample size, n_{out} and n_{in} , required to accurately evaluate $U(\mathbf{d})$?
2. What is the nature of the objective space? What is the optimum experiment, \mathbf{d}^* , to learn $\theta = G_h$?
3. What experimental design condition(s) is most important?
4. What temperature sensor location(s) is most important?

To answer the first question, the convergence of $U(\mathbf{d})$ is examined for a fixed value of \mathbf{d} . Fixed median experimental design conditions are selected so that $\mathbf{d} = [T_{O-REx}, V_{TEC}, T_w]^T = [30\text{ }^\circ\text{C}, 3\text{ V}, 30\text{ }^\circ\text{C}]^T$. Figure 5-6 shows the experimental utility versus the number of samples to evaluate the utility. At approximately $n_{out} = n_{in} = 1,000$, $U(\mathbf{d})$ converges to within ± 0.1 . A sample size of $n_{out} = 1,000$ is sufficient for this parameter inference experiment design problem because $U(\mathbf{d})$ is convex with one global minimum on the boundary of the domain of \mathbf{d} (as we will later show).

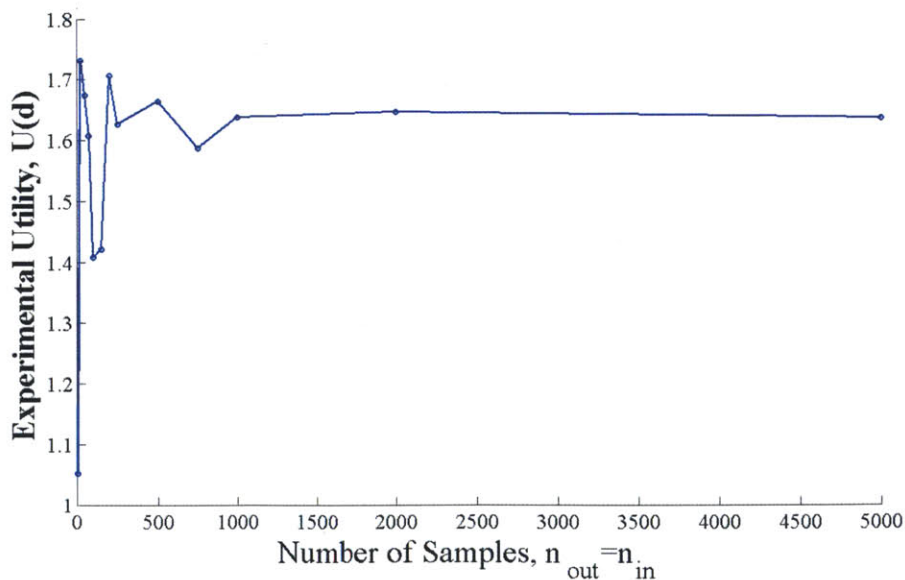


Figure 5-6: Convergence plot for experimental utility, $U(\mathbf{d})$, versus number of samples

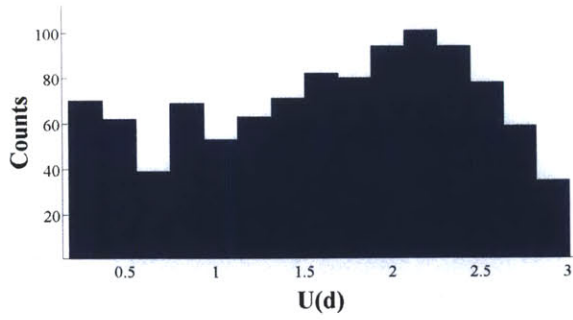
To answer questions two and three, a grid search is performed to find the optimum experiment and determine which experimental conditions are most important. Possible experiments are evaluated on a coarse grid consisting of 1,050 points (i.e., $U(\mathbf{d})$ evaluations) where the experimental conditions considered are:

- **Chamber baseplate, T_{O-REx} :** from -100 °C to 80 °C in 20 °C increments
- **TEC Voltage, V_{TEC} :** from 1 V to 4.5 V in 0.25 V increments
- **Chamber wall temperature, T_w :** from 20 °C to 80 °C in 10 °C increments

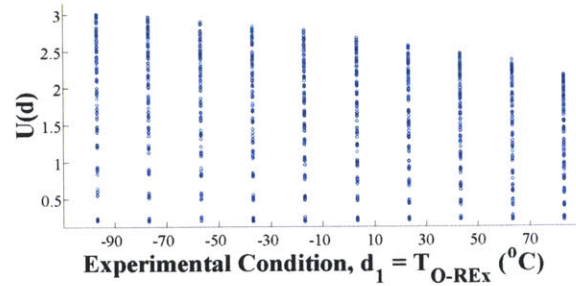
The grid of experimental conditions is selected to both bound and uniformly investigate the entire domain of \mathbf{d} .

Figure 5-7 shows the results of the experimental design analysis where $U(\mathbf{d})$ is evaluated on a grid. Figure 5-7a shows the histogram of all 1,050 $U(\mathbf{d})$ evaluations. The maximum utility is near three and the minimum utility is just greater than zero. Many different experiments yield utilities greater than two, so if the optimum experiment is infeasible (e.g., violation of SEB component temperature limits), a sub-optimal experiment can be performed with nearly the same utility. Figure 5-7b, Figure 5-7c, and Figure 5-7d are scatter plots of $U(\mathbf{d})$ versus each experimental design condition. There is a medium strength correlation between $U(\mathbf{d})$ and chamber baseplate temperature, strong correlation between $U(\mathbf{d})$ and TEC voltage, and weak correlation between $U(\mathbf{d})$ and chamber wall temperature. The highest utility experiments correspond to low chamber baseplate temperatures and high TEC voltage values. The chamber wall temperature is effectively an option to add an IR heater plate to the chamber if shown through the experimental design to be advantageous. Because there is a weak correlation between $U(\mathbf{d})$ and the wall temperature in Figure 5-7d, no IR heater plate is added to the chamber. The chamber wall temperature is kept at room temperature for the experiment.

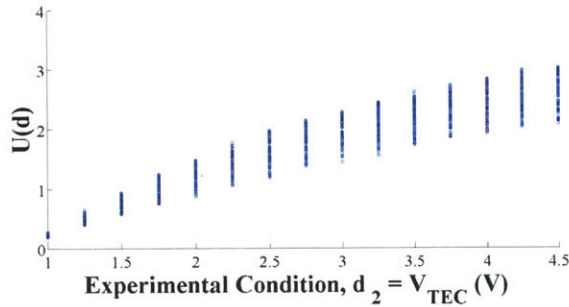
Figure 5-8 shows a heatmap of experimental utilities for T_{O-REx} and V_{TEC} for the same 1,050 $U(\mathbf{d})$ evaluations (the dimensionality of \mathbf{d} is now two because T_w is fixed at room temperature). Without constraints, the optimum parameter inference experiment is at $T_{O-REx} = -100$ °C and $V_{TEC} = 4.5$ V. The correlations between $U(\mathbf{d})$ and the design



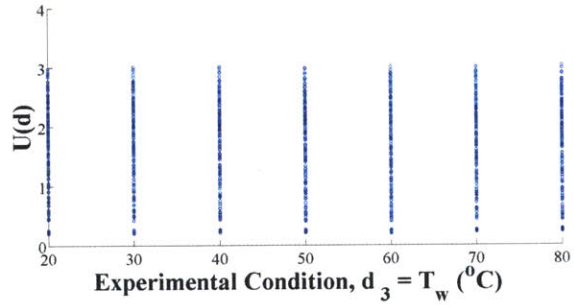
(a) Histogram of experimental utilities



(b) Chamber baseplate temperature



(c) TEC voltage



(d) Chamber wall temperature

Figure 5-7: Histogram of experimental utilities and scatter plots of utilities versus each experimental design condition

conditions first shown in Figure 5-7 are apparent: the TEC voltage is the primary driver of high utility experiments but the chamber baseplate temperature is also important in maximizing utility. The dashed vertical line indicates that the lowest possible value of T_{O-REx} is at $-30\text{ }^\circ\text{C}$ to prevent failure of components on the SXM electronics board. Furthermore, the horizontal dashed line indicates that the largest possible TEC voltage is 4.0 V . The optimum experiment within the domain of allowable \mathbf{d} is $T_{O-REx} = -30\text{ }^\circ\text{C}$ and $V_{TEC} = 4.0\text{ V}$ with an experimental utility of $U(\mathbf{d}) = U^* = 2.4$. Although the utility of an experiment at $T_{O-REx} = -100\text{ }^\circ\text{C}$ and $V_{TEC} = 4.5\text{ V}$ is higher, its utility of $U(\mathbf{d}) = 2.9$ is only slightly higher than the utility within the domain of allowable \mathbf{d} .

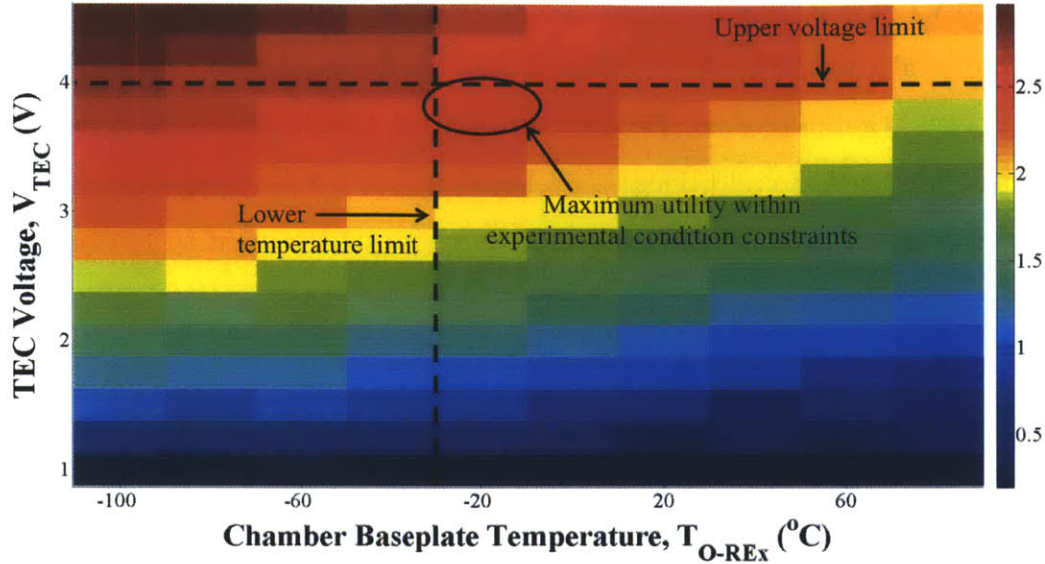


Figure 5-8: Heatmap of experimental utility for chamber baseplate temperature (simulating OSIRIS-REx temperature, T_{O-REx}) versus TEC voltage, V_{TEC} . Dashed lines indicate lower temperature limit at -30 °C and upper voltage limit at 4.0 V to indicate the domain of allowable \mathbf{d} .

Sensor Importance Study

Note that all $U(\mathbf{d})$ evaluations assume six temperature measurements on the SXM: one RTD on each SXM model node and one diode on the SDD. In general, it is useful to evaluate which sensors are most important with respect to an experiment's utility. Reasons for analytically investigating the importance of each sensor include:

- It may be difficult or problematic to install a sensor intended for a particular component
- The actual testbed may not support as many sensors as originally intended, resulting in the need for sensor prioritization
- If a particular measurement is important for achieving the experiment's objective(s), redundant sensors could be added as a contingency if one or more sensors fails during the test

To evaluate the importance of each temperature measurement of the SXM with respect to U^* , the experimental conditions are fixed at the optimum conditions, $\mathbf{d}^* = [T_{O-REx}, V_{TEC}, T_w]^T$

$= [-30 \text{ }^\circ\text{C}, 4.0 \text{ V}, 20 \text{ }^\circ\text{C}]^T$. For the fixed design conditions, the experimental utility in Equation (5.5) is re-evaluated for each sensor set so that there is an experimental utility associated with each permutation of sensors. Because the original 1,050 $U(\mathbf{d})$ evaluations assumes that all six sensors are used, no additional model evaluations are required to evaluate Equation (5.5). The stored model evaluations corresponding to \mathbf{d}^* are used to recompute the likelihoods using Equation (5.7), so the computational cost of the sensor importance analysis is low. All possible sets of the six temperature sensors are considered. A 64-row matrix of sensor permutations is constructed:

$$\begin{pmatrix} \text{Bracket} & \text{SXM Housing} & \text{SEB} & \text{SDD Housing} & \text{Collimator} & \text{SDD} \\ 0 & 0 & 0 & 0 & 0 & 1 \\ 0 & 0 & 0 & 0 & 1 & 0 \\ 0 & 0 & 0 & 0 & 1 & 1 \\ \vdots & \vdots & \vdots & \vdots & \vdots & \vdots \\ 1 & 1 & 1 & 1 & 1 & 1 \end{pmatrix}$$

where zero indicates that the sensor measurement is not available, and one indicates that the sensor is providing a temperature measurement. Each row is a unique sensor set.

The final step of the sensor importance analysis is to correlate the presence of a sensor with the calculated experimental utility. The Pearson correlation coefficient is used to obtain an averaged importance rating for each sensor:

$$R_{A,B} = \frac{\text{cov}(A, B)}{\sigma_A \sigma_B} \quad (5.9)$$

where A and B are arbitrary variables, and $R_{A,B}$ is the correlation coefficient whose magnitude ranges from zero to one. Zero indicates no correlation, and a magnitude of one indicates strong correlation between data A and B . The correlation coefficient is computed between all the 64 utilities from the sensor permutation matrix and the column of the permutation matrix corresponding to each sensor location. Figure 5-9 shows a bar graph of each correlation coefficient. Sensor correlation coefficients with large magnitude indicate that the experimental utility tends to be higher when that sensor is included. The sensor with the

largest correlation coefficient is the SDD housing at 0.91, and the sensor with the second largest coefficient is the SDD at 0.26. All other sensor coefficients have a correlation coefficient magnitude below 0.05, so the SDD housing and SDD temperature measurements are significantly more important with respect to achieving U^* . During integration of the SXM hardware, it was not possible to include an RTD on the SEB because there is not sufficient surface area on the board to attach the sensor head. Because it has small correlation with $U(\mathbf{d})$, no additional hardware modifications are performed and the SEB RTD is omitted.

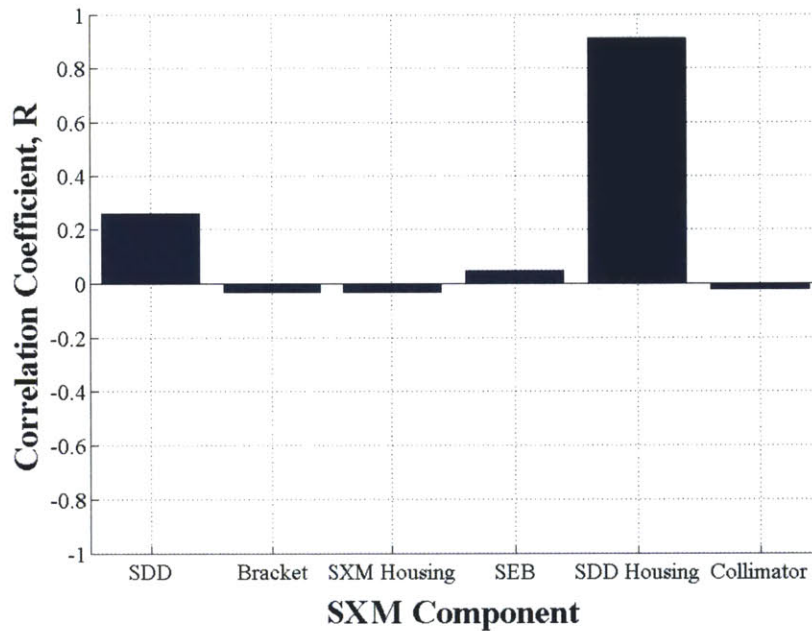


Figure 5-9: Correlation coefficients, per Equation (5.9), between experimental utility, $U(\mathbf{d})$, and each possible temperature sensor location

The summary of the optimal parameter inference experiment design problem is shown below:

- The thermal model of the SXM is modified to match the testbed environment.
- The Kullback-Leibler (KL) divergence is selected as the utility function for the experimental design problem.
- The experimental utility, $U(\mathbf{d})$, is maximized using a grid search. The optimum experiment consists of a chamber baseplate at $-30\text{ }^{\circ}\text{C}$, an applied TEC voltage of 4.0 V, and a thermal vacuum chamber wall temperature of $20\text{ }^{\circ}\text{C}$.

- The optimum experiment lies on the boundary of the domain of possible experimental conditions.
- Although all temperature sensor locations provide utility, the sensors for the SDD and SDD housing are the most important with respect to achieving high $U(\mathbf{d})$

The SXM thermal test plan includes additional details for the parameter inference experiment and is given in Appendix A.

5.4.2 Model Validation Experiment

A full factorial experimental design approach, in-line with classical DOE, is adopted for the model validation experiment. The model validation experiment takes place in the SSL thermal vacuum chamber (same as parameter inference experiment, see Appendix A for chamber description) and explores the largest feasible number of combinations of T_{O-REx} and V_{TEC} over the domain of intended application of the SXM. The experiment does not simulate the thermal effects of the sun and deep space, but analysis shows that these parameters are insignificant for the SXM thermal system QoIs. Figure 5-10 shows the 45 planned test phases for the SXM model validation experiment; 45 test phases is feasible due to the relatively small time constant of the SXM thermal response. Each cross represents a single steady state test phase of the model validation experiment. Five different chamber baseplate temperatures at nine different TEC voltages are tested. All crosses are model validation experiment tests; the red cross indicates that T36 also corresponds to the parameter inference experiment to reduce uncertainty in G_h .

5.4.3 Experimental Results

The parameter inference and model validation experiments are executed per the test plan in Appendix A. Appendix B shows the raw data from each test phase. The data from the parameter inference and model validation experiments are used in step five of BMV to calibrate the SXM experimental thermal model, quantify the calibrated model's inadequacy, and update the flight model. In this section, plots are shown to provide a high-level summary

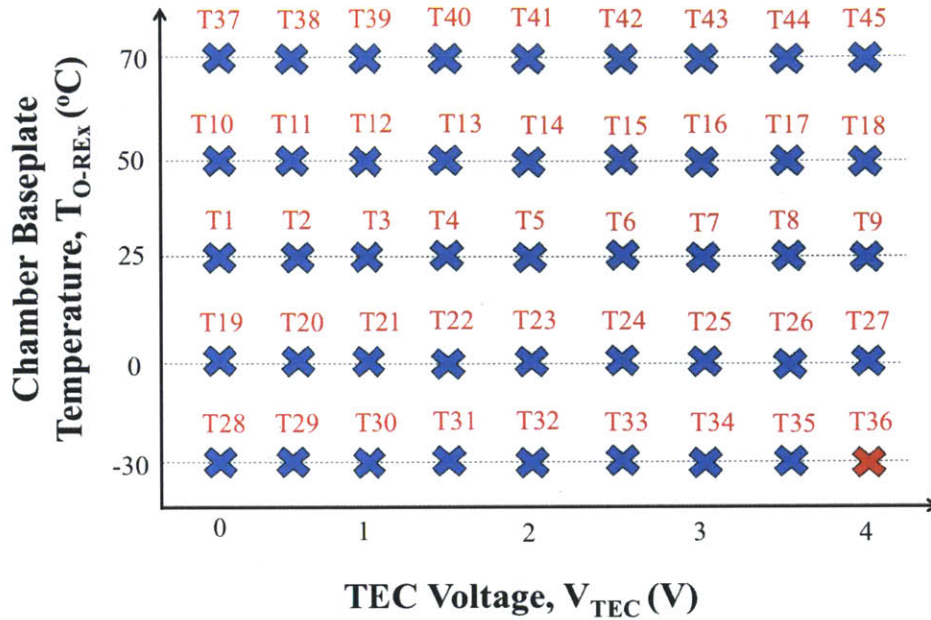


Figure 5-10: Grid of all SXM thermal test phases, including parameter inference experiment (red cross) and model validation experiment (all crosses, both blue and red). Model validation experiment coarsely grids the domain of expected TEC voltages and SXM interface temperatures.

of SXM thermal performance during the tests. First, plots are shown to illustrate how the SDD temperature changes with the SXM interface temperature and applied TEC voltage. Next, the experimental data are overlaid with the Amptek TEC performance data to show how close the initial TEC model was to reality. Finally, temperature plots for the SXM structure are shown to indicate where the largest temperature differentials occur as heat flows from the Amptek package to the SXM interface.

From Figure 5-10, test phases T1 through T43 were successfully executed to steady state conditions (typical stabilization is ± 0.1 °C/hr for at least 30 min). Test phases T44 and T45 were not accomplished because an electrical short caused a failure in the SDD package. The failure of the SDD package is not a problem associated with the SXM thermal system, experimental temperatures, or the thermal system requirements. Consequently, the only impact to the overall model validation problem is that data is not available for the final two test phases. Calibration in step five of BMV continues as planned with data from phases T1 through T43.

The relationship between SDD temperature and voltage/current at various chamber base-

plate temperatures is shown in Figure 5-11 and Figure 5-12. The black dotted line on each plot indicates the SDD requirement. An important takeaway from Figure 5-11 is that for a maximum spacecraft interface temperature of 50 °C, the TEC is capable of achieving the -30 °C SDD temperature requirement. At an interface temperature of 50 °C, Figure 5-12 shows that the current draw for $V_{TEC} = 4$ V is approximately 0.5 A. Thus, the maximum expected power dissipation of the TEC is approximately 2 W. When the interface temperature is below 50 °C, the applied TEC voltage is lower than 4 V because the TEC requires less power to achieve its set point.

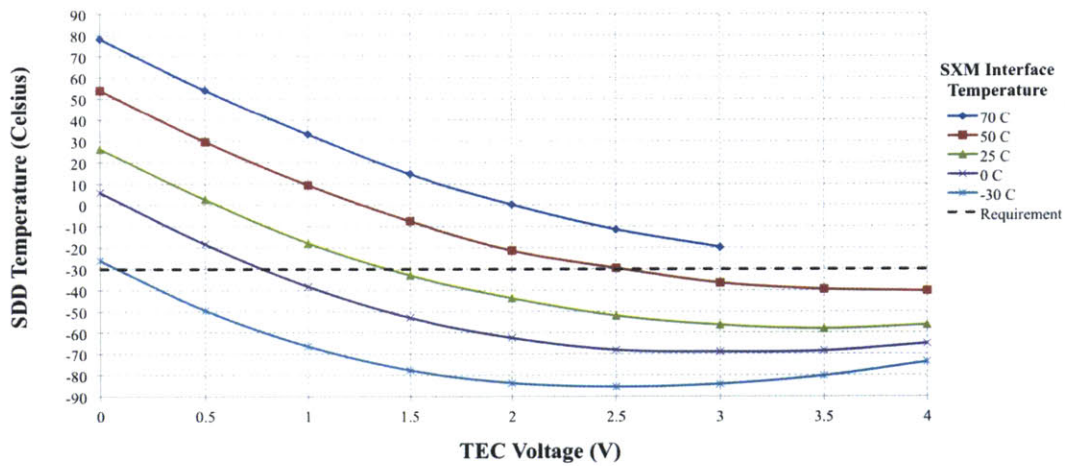


Figure 5-11: SDD temperature, T_{sdd} , versus TEC voltage, V_{TEC} , for various SXM interface temperatures ranging from 70 °C to -30 °C. There is a zero-mean Gaussian observation error associated with each data point that is not shown for the data in this figure.

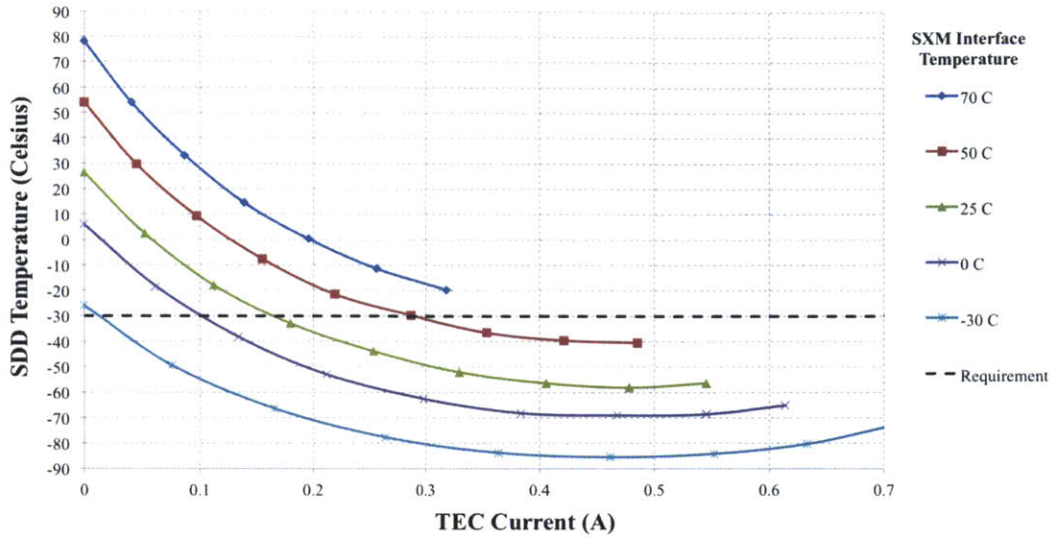


Figure 5-12: SDD temperature, T_{sdd} , versus TEC current draw, i_{TEC} , for various SXM interface temperatures ranging from 70 °C to -30 °C. There is a zero-mean Gaussian observation error associated with each data point that is not shown for the data in this figure.

The experimental data are compared to the original TEC performance estimates to see if the original performance curves are conservative or optimistic. Figure 5-13 shows the 50 °C and 70 °C performance curves from Figure C-3 overlaid on a contour plot of the experimental data. A surface fit of the data is required for a direct comparison because during the experiment, the SXM bracket interface, not the TEC hot side temperature, was controlled. For a given SXM bracket interface temperature, the TEC hot side temperature changes with the TEC voltage value, so the data need to be interpolated to show lines of constant hot side temperature. Figure 5-13 shows that for less than 3 V, the data, represented by the contour lines, match the 50 °C and 70 °C performance curves well. For voltages greater than 3 V, the differences between the data and the initial estimates are significant and greater than 5 °C in some areas. The original TEC performance estimates are a good representation of the actual TEC performance for <3 V and are optimistic for >3 V.

To find the TEC heat load flight envelope, Figure 5-11 and Figure 5-12 are combined to plot the SDD temperature versus TEC heat load (i.e., power dissipation) in Figure 5-14. As discussed earlier, at 50 °C the maximum heat load is nearly 2 W. The SXM thermal system has approximately 10 °C margin to the SDD requirement in the hottest possible

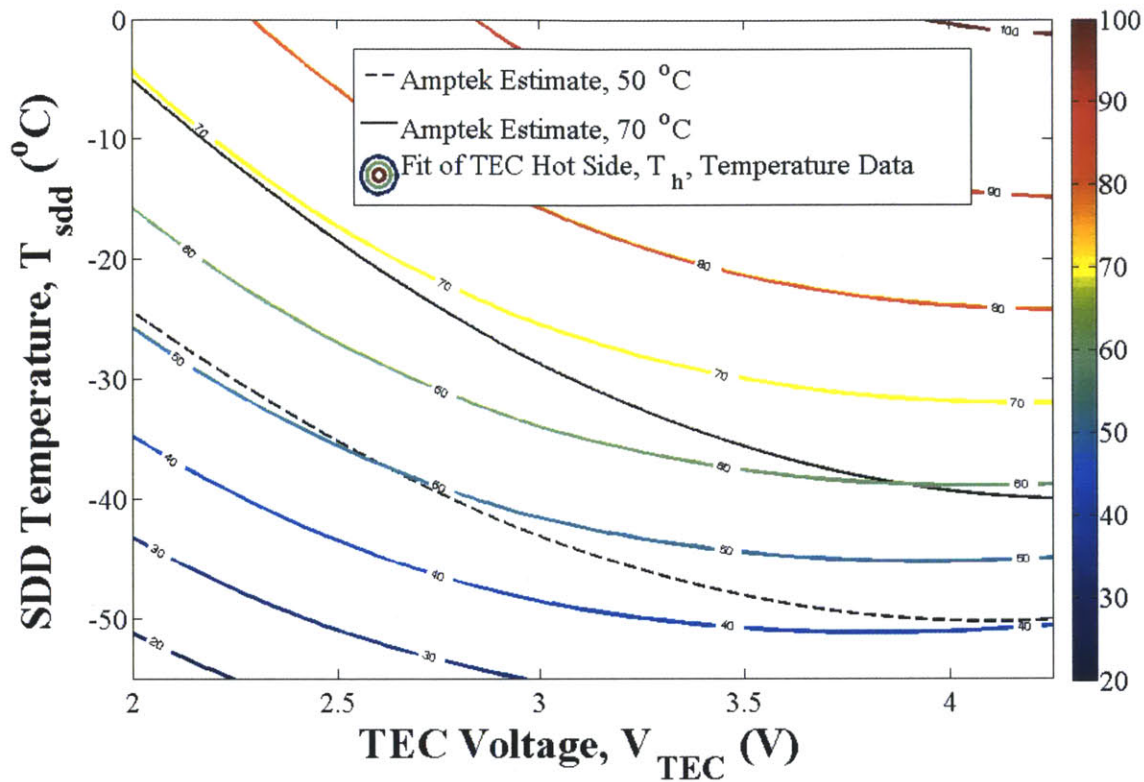


Figure 5-13: Comparison of Amptek, Inc. performance estimates from Figure C-3 to SXM thermal test TEC data. Plot shows contour plot of TEC hot side temperatures versus SDD temperature and applied TEC voltage. The contour lines are a third-order surface fit to the data obtained during the experiment; RMS error between fit and data is approximately 1 $^{\circ}\text{C}$.

operating case for the SXM. Operating the TEC below 1.5 W is more efficient for interface temperatures below 50 $^{\circ}\text{C}$ because the SDD temperature decreases very little for increasing heat loads. In fact, increasing the power to the TEC can *increase* the SDD temperature for various hot side temperatures and heat load values (e.g., the slope of the -30°C curve is positive at 1.5 W).

The primary method of heat rejection for the SXM is conduction to the bracket interface. In addition to providing the TEC more power, another way to achieve lower SDD temperatures is to decrease the TEC hot side temperature (i.e., SDD housing temperature) by decreasing the overall temperature difference between the interface and SDD housing. Figure 5-15 shows the temperature difference between the SDD housing and SXM interface plate as measured during the experiment. The temperature difference is larger for decreasing

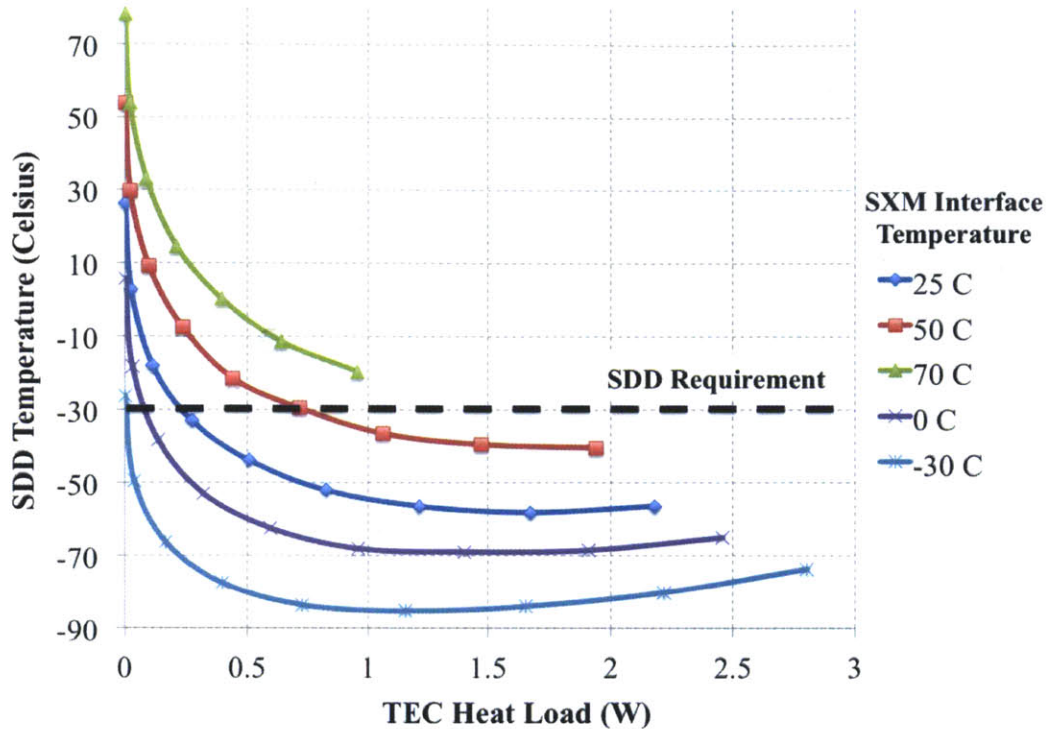


Figure 5-14: SDD temperature, T_{sdd} , versus TEC power dissipation for various SXM interface temperatures ranging from 70 °C to -30 °C. There is a zero-mean Gaussian observation error associated with each data point that is not shown for the data in this figure.

chamber baseplate temperatures and increasing TEC power. With 0 V applied to the TEC, the temperature difference is approximately zero, but with 4 V applied to the TEC, the temperature differences range from 6-12 °C. Figure 5-16 shows the temperature difference between the SDD housing and the SXM housing. As in Figure 5-15, the larger temperature differences occur for colder chamber baseplate temperatures. However, the magnitude of the temperature differences is smaller than in Figure 5-15. Because the SDD housing to SXM housing thermal path is an intermediate thermal path of the SDD housing to SXM interface thermal path, Figure 5-16 reveals that the majority of the temperature difference in Figure 5-15 is due to thermal resistance between the SXM housing and the interface.

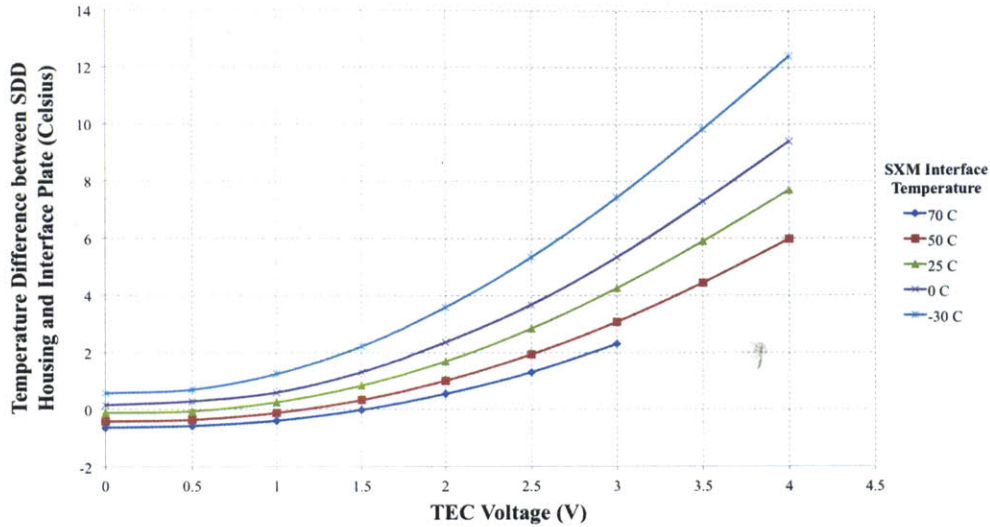


Figure 5-15: Temperature difference between the SDD housing, T_h , and SXM interface, T_{O-REx} , versus TEC voltages, V_{TEC} , for various SXM interface temperatures. There is a zero-mean Gaussian observation error associated with each data point that is not shown for the data in this figure.

Figure 5-16 confirms the intuition that the optimal parameter inference experiment conditions, \mathbf{d}^* , for inferring G_h are a chamber baseplate temperature of -30 °C and a TEC voltage of 4 V. Heat transfer across G_h , between the SDD housing and SXM housing, is approximately one dimensional. For one dimensional conduction, Equation (C.8) shows that the temperature difference between the two components is proportional to the conductance, $\Delta T \propto G_h$. Because the observations are noisy, maximizing the temperature difference between the SDD housing and SXM housing is important to reduce the variance in the G_h posterior as much as possible (i.e., making observables highly sensitive to the quantities we want to infer, G_h).

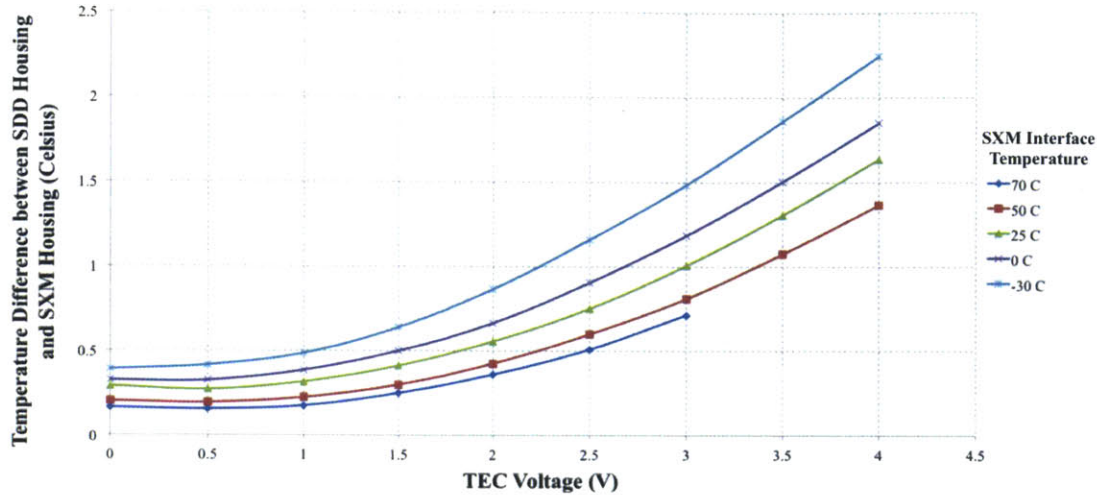


Figure 5-16: Temperature difference between the SDD housing, T_h , and the SXM housing versus TEC voltages, V_{TEC} , for various SXM interface temperatures. There is a zero-mean Gaussian observation error associated with each data point that is not shown for the data in this figure.

5.5 Step 5: Experimental Model Calibration and Flight Model Update

With the parameter inference and model validation experiments complete, the next step is to calibrate the model parameters and quantify the calibrated model’s inadequacy. First, the TEC model is updated. Second, the SXM thermal model parameters are calibrated to match all experimental data. Next, the thermal model discrepancy is quantified by examining the differences between the calibrated model predictions and the experimental data. Lastly, the flight model is updated based upon changes that are made during the calibration of the experimental thermal model.

5.5.1 TEC Model Update

Prior to thermal testing, the TEC model is based on interpolating the performance curves (Figure C-3 and Figure C-4) provided by the SDD package manufacturer. Because the prior model does not contain performance estimates for TEC hot side temperatures below 50 °C (thus, requiring large extrapolations for performance estimates down to -30 °C) and

is shown experimentally to inaccurately estimate the TEC's performance above 3 V (see Figure 5-13), it is replaced by a new TEC model based on the experimental data from test phases T1 through T43.

A TEC model is needed that relates TEC voltage, V_{TEC} , and hot side temperature, T_h , to the cold side temperature (i.e., temperature of detector), T_{sdd} , and current draw, i_{TEC} , as shown in Equation (5.10):

$$[T_{sdd}, i_{TEC}] = f(V_{TEC}, T_h) \quad (5.10)$$

A first step in developing the new TEC model is to examine the analytical relationships between the physical quantities in Equation (5.10). Goldsmid [139] provides the basic voltage and cooling capacity equations for a one-layer thermoelectric module. The model assumes no electrical resistance between the thermo-elements and metal links and that the links themselves have zero resistance. Thermal resistance between the couple and the heat source and sink is neglected, so that the heat transferred between the source and sink is only through the couples. Given these assumptions, the voltage equation shown in Equation (5.11) and the cooling capacity equation in Equation (5.12) for a one-layer thermoelectric module are:

$$V = S(T_h - T_c) + iR \quad (5.11)$$

$$Q_c = iST_c - \frac{1}{2}i^2R - k(T_h - T_c) \quad (5.12)$$

where V is voltage, i is current, Q_c is the TEC cooling capacity, and T_h and T_c are the TEC hot and cold side temperatures, respectively. Note that the Seebeck coefficient, S , electrical resistance, R , and thermal conductivity, k , are temperature independent. In Equation (5.11), the first term captures the Peltier effect and the second term is Ohm's law. In Equation (5.12), the first term is the Peltier effect, the second term describes the Joule heating, and the third term is conducted heat through the TEC. Rearranging Equation (5.12) to solve for the cold side temperature:

$$T_c = \frac{T_h + \frac{i^2 R}{2k} + \frac{Q_c}{k}}{1 + \frac{iS}{k}} \quad (5.13)$$

In Equation (5.11) with constant current, the hot side temperature is linearly related to voltage. At constant hot and cold side temperatures, current is linearly related to voltage. In Equation (5.12), the TEC cold side is linearly dependent on the hot side and quadratically dependent on current (and thus, voltage also from Ohm's law). However, Huang et al. [140] found that for a one-layer TEC module over a wide range of hot side temperatures, T_h , and TEC power values, Equation (5.12) does not fit empirical data well due to the inaccuracy of the simplifying assumptions. Instead, Huang et al. [140] established an empirical relationship for T_c that is 3rd order with respect to TEC current draw, i .

Following the framework of Huang et al. [140], an empirical TEC model is constructed using polynomial regression for the two-layer TEC inside the SDD package. Many other physical or empirical TEC model options are possible (e.g., alternative regression models, Gaussian process models, or finite elements models of the TEC). Although alternative methods offer potentially higher accuracy and/or model structure more suited for probabilistic analysis, the TEC polynomial model structure is selected for its simplicity and accuracy. The model is structured so that the output quantities in Equation (5.10) are generated via two independent polynomial functions:

$$\begin{aligned} T_{sdd} &= f_1(V_{TEC}, T_h) \\ i_{TEC} &= f_2(V_{TEC}, T_h) \end{aligned} \quad (5.14)$$

where each function, f_1 and f_2 , returns a scalar value. Before regression can be performed, a polynomial order must be selected to match the experimental data well but not overfit the data. Overfitting the data can result in a TEC model that does not well match the underlying physical processes and has poor predictive performance.

Polynomial regression is performed for polynomials of increasing order using the experimental data. The RMS error between the polynomial functions, f_1 and f_2 , and the TEC data is calculated. For T_{sdd} , the RMS error is 1.27 °C for a polynomial of order three and the

maximum residual is below 3.5 °C. A third order polynomial, as shown by Equation (5.15), is selected for f_1 :

$$T_{sdd} = f_1(V_{TEC}, T_h) = \alpha_1 + \alpha_2 V_{TEC} + \alpha_3 T_h + \alpha_4 V_{TEC}^2 + \alpha_5 V_{TEC} T_h + \alpha_6 T_h^2 + \alpha_7 V_{TEC}^3 + \alpha_8 V_{TEC}^2 T_h + \alpha_9 V_{TEC} T_h^2 + \alpha_{10} T_h^3 \quad (5.15)$$

where α_1 - α_{10} are the ten polynomial coefficients whose values and associated confidence intervals are obtained via polynomial regression. For i_{TEC} , the RMS error is 0.008 A for a polynomial of order two and the maximum residual is 0.015 A. A second order polynomial consisting of six additional coefficients β_1 - β_6 , as shown by Equation (5.16), is selected for f_2 :

$$i_{TEC} = f_2(V_{TEC}, T_h) = \beta_1 + \beta_2 V_{TEC} + \beta_3 T_h + \beta_4 V_{TEC}^2 + \beta_5 V_{TEC} T_h + \beta_6 T_h^2 \quad (5.16)$$

The final polynomials from Equation (5.15) and Equation (5.16) are plotted as surfaces against the experimental data in Figure 5-17 and Figure 5-18. The polynomial models can be used to predict T_{sdd} and i_{TEC} given values for V_{TEC} and T_h . The TEC model is now updated, and the coefficients are fixed at their regressed values.

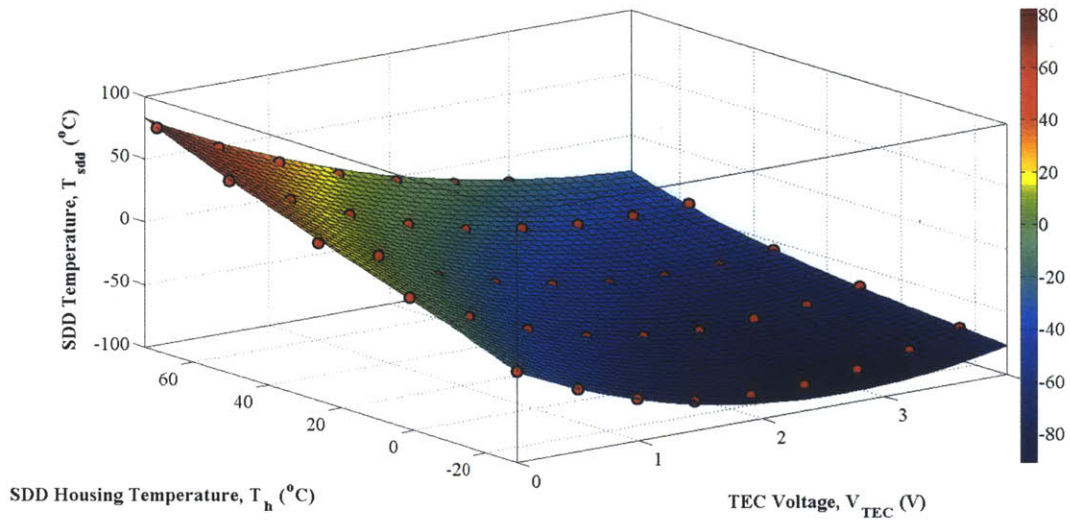


Figure 5-17: Surface fit for the SDD temperature, T_{sdd} , for various TEC voltages and SDD housing temperatures. The experimental data are marked with red points and the surface is constructed via Equation (5.15). There is a zero-mean Gaussian observation error associated with each data point that is not shown for the data in this figure.

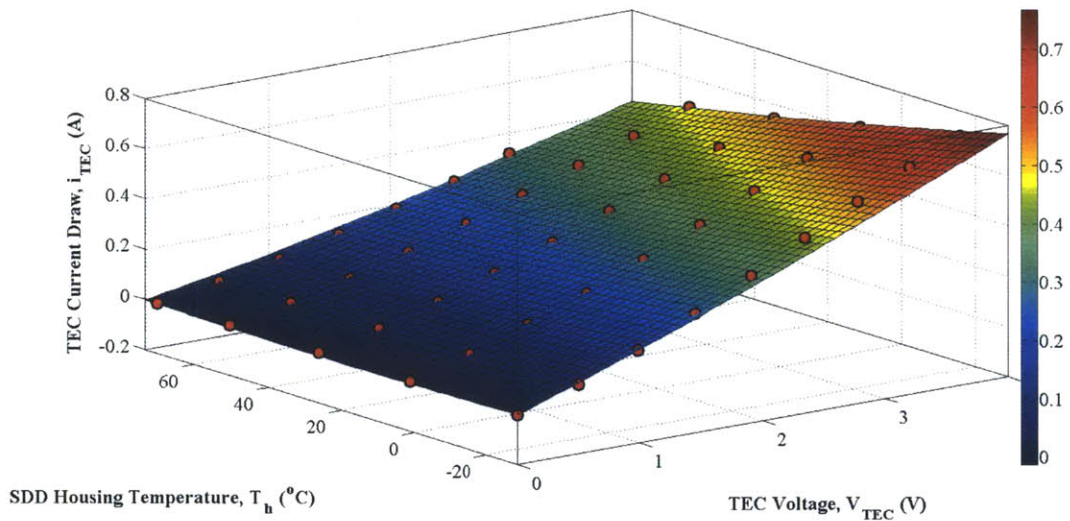


Figure 5-18: Surface fit for the TEC current draw, i_{TEC} , for various TEC voltages and SDD housing temperatures. The experimental data are marked with red points and the surface is constructed via Equation (5.16). There is a zero-mean Gaussian observation error associated with each data point that is not shown for the data in this figure.

5.5.2 Parameter Calibration Overview

With the TEC model updated, the next step is to calibrate the parameters of the SXM thermal model. The SXM thermal model is calibrated to match all of the experimental data from the parameter inference and model validation experiments. Figure 5-19 illustrates the process used to calibrate the SXM thermal model parameters. The calibration process is iterative: the model is calibrated, then checked against the experimental data, and then updated if the model predictions do not match the data well (goodness of fit judged with respect to probability measure on temperature requirements).

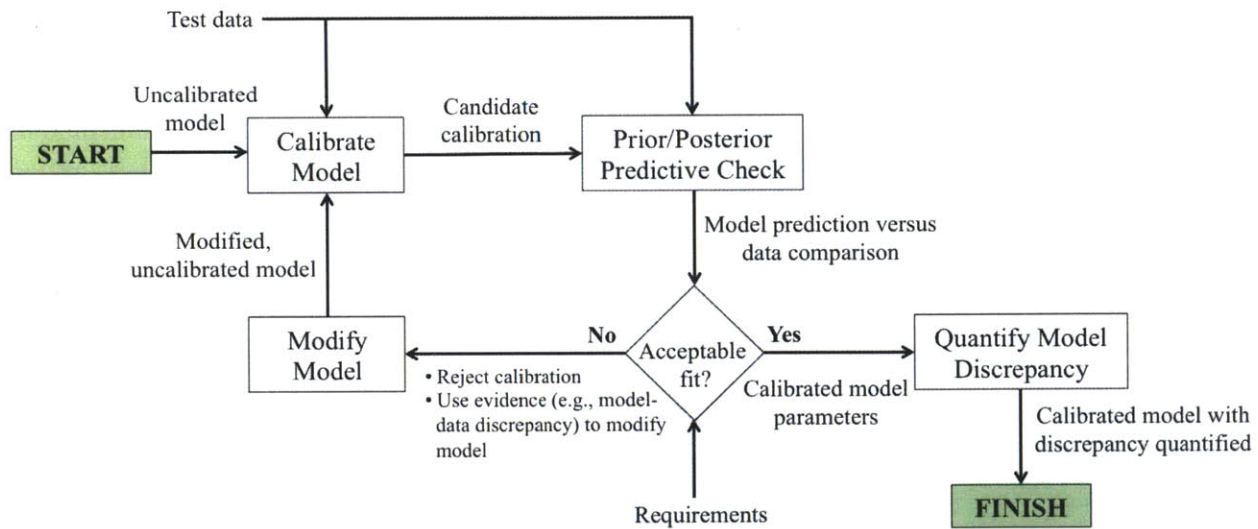


Figure 5-19: Model calibration process overview

First, the uncalibrated model is calibrated using Bayesian inference techniques (e.g., Markov chain Monte Carlo (MCMC) methods). The resulting candidate model is used in a prior or posterior predictive check where the model predictions and data are overlaid. Based on the predictive check, a decision is made as to whether the fit is acceptable. An acceptable fit must be judged while considering the thermal system requirements. For example, if the model is accurate to ± 0.1 °C, but the requirement is to control a component’s temperature to a particular set point ± 0.01 °C, the fit is unacceptable. If the model predicts accurately to ± 0.1 °C and shows 10 °C margin in a worst-case scenario, the fit is acceptable. If unacceptable, the candidate calibration is rejected. The model modification step is an engineering decision that uses evidence in the experimental data or the prior/posterior predictive check

to update the model in a physically accurate manner (e.g., increase parameter distribution limits, include the effects of additional parameter uncertainty, or change the model structure). Once the parameter calibration produces an acceptable fit, the model discrepancy is quantified using the calibrated model predictions and the experimental data. Strictly following the K-O approach [42], the parameter values and model discrepancy are inferred simultaneously. For this case study, the model discrepancy is quantified after the parameter calibration because there is no prior information regarding the magnitude of the discrepancy. With the calibrated SXM model and quantified model discrepancy, the calibration process is complete and the flight model can be updated.

To illustrate the concept of a prior or posterior predictive check, Figure 5-20 notionally shows a distribution for a single model output, y , plotted with a single, steady state data point. A prior predictive check is valuable in determining whether the prior model uncertainty *is sufficient* to explain the experimental data prior to updating the model. A posterior predictive check is useful for determining *how well* the updated model describes the data. Figure 5-20a shows a predictive check where the data is plausible under the model output distribution; in Figure 5-20b, the data is implausible under the model output distribution. In Figure 5-20b, if the distance between the distribution and data point is large, there is evidence of significant model inadequacy. If the distance between the distribution and data point is small, the calibration may still be acceptable.

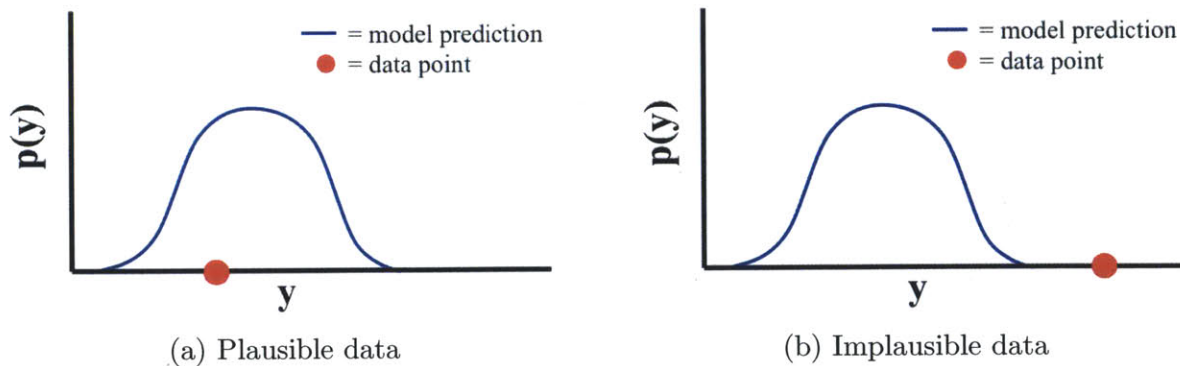


Figure 5-20: Notional prior or posterior predictive check for a single model output and a single data point demonstrating plausible and implausible data under a single model output distribution

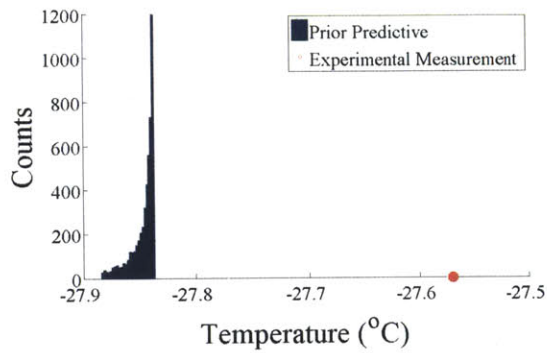
5.5.3 Calibration Parameter Selection: G_h Only

Calibration parameter(s) are selected before the model is calibrated. Prior predictive checking (observing the differences between the model predictions and data using the prior parameter uncertainty distributions) is utilized in Sections 5.5.3-5.5.6 to systematically determine the SXM thermal model parameters that require calibration. In step two of BMV, the conductance between the SDD housing and SXM housing, G_h , is identified as the most significant parameter in creating variance in the driving QoI: the SDD temperature, T_{sdd} . Consequently, the first parameter calibration of the SXM thermal model considers only the parametric uncertainty in G_h —all other SXM thermal model and TEC model parameter values are fixed.

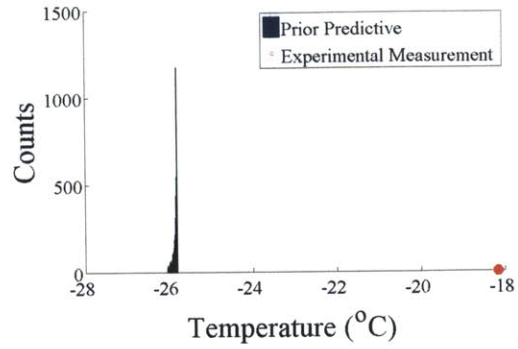
Before calculating the posterior distribution for G_h , the prior uncertainty distribution (see Table 5.3 for distribution parameters) is propagated through the SXM experimental model to perform a prior predictive check. For simplicity, test phase T36, corresponding to the optimal parameter inference experiment for inferring G_h with conditions $V_{TEC} = 4.0$ V and $T_{O-REx} = -30$ °C, is the only test phase considered for the prior predictive check. Once the data for T36 are plausible during the prior predictive check, more test phases will be added to the model check.

Figure 5-21 shows the results of the prior predictive check with G_h as the only uncertain parameter. Because the observation error variance is small, the prior predictive check in Figure 5-21 (and those that follow) show the data as single points instead of a Gaussian distribution centered on the data point; later in the calibration procedure, the observation error variance is captured when computing the posterior parameter distributions. As expected, the SDD (Figure 5-21e) and SDD housing (Figure 5-21c) are well covered (i.e., are plausible) by the prior predictive distribution. Because GSA indicates that both components are highly sensitive to the uncertainty in G_h and because the optimal parameter inference experiment is designed to make the temperature of the SDD and SDD housing highly observable to G_h values, it is intuitive that the data are plausible and that the variances of the distributions about the data points are large. However, the uncertainty in G_h is not enough to describe the data for bracket (Figure 5-21a), SXM housing (Figure 5-21b), and collimator (Figure

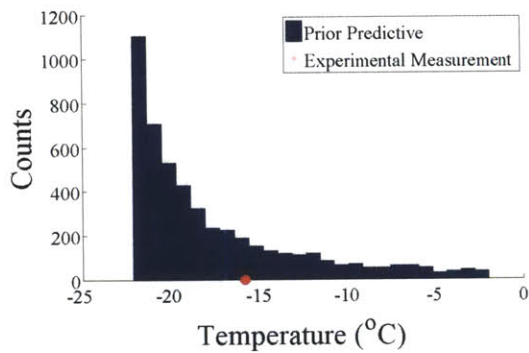
5-21d). The data for these three components are implausible under the model output distributions, and the SXM housing and collimator distributions are cold-biased by approximately 8 °C. The final, validated SXM model must not only be able to accurately predict the SDD and SDD housing temperatures but also the SXM electronics board (SEB) since it too is a QoI. Because SXM housing is the direct thermal sink for the SEB, validating the predictive capabilities of the thermal model with respect to the SXM housing is imperative. The 8 °C cold-bias is unsatisfactory. Additional model uncertainty must be introduced to account for the inadequacy before the posterior parameter distribution(s) can be calculated.



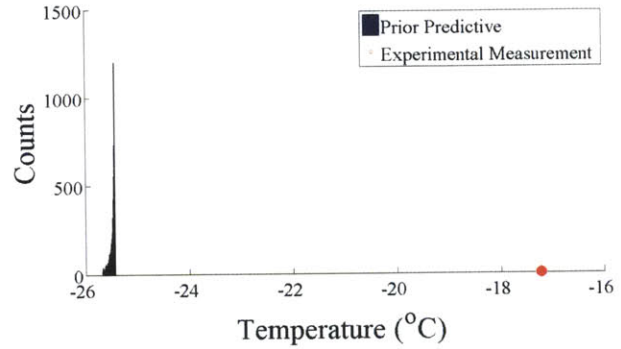
(a) Bracket



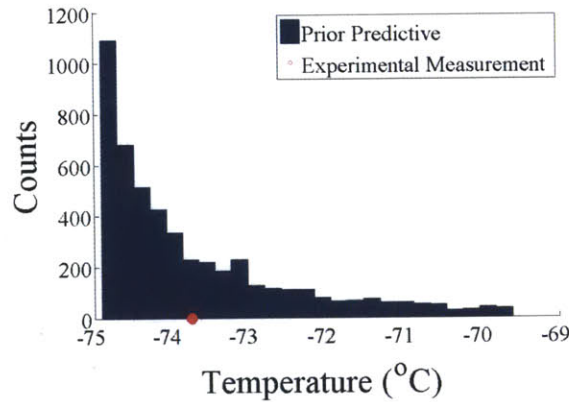
(b) SXM housing



(c) SDD housing



(d) Collimator



(e) SDD

Figure 5-21: Prior predictive distribution check for each SXM component for test phase T36. Results are based on the propagation of prior parametric uncertainty in G_h only. Model output histograms are generated via Monte Carlo sampling (5,000 samples) of the calibration parameter's prior distribution. There is a zero-mean Gaussian observation error associated with each data point that is not shown for the data in this figure.

5.5.4 Calibration Parameter Selection: G_h and $G_{s,b}$

The uncertainty in G_h alone is insufficient to explain the experimental data in T36, so additional uncertainty (e.g., parametric, model structure, or observational error) must be introduced to match the data. There are two pieces of evidence that suggest that the unacceptable fit is due to parametric uncertainty in the conductance, per screw, between the SXM housing and bracket, $G_{s,b}$. First, the sensitivity analysis from step two of BMV (see Figure 5-5) shows that the most sensitive parameter for the SEB is $G_{s,b}$. Since the SEB's only thermal connection is conduction to the SXM housing, $G_{s,b}$ is also a large sensitivity for the SXM housing and collimator. Second, the SXM housing and collimator prior predictive distributions in Figure 5-21 are significantly biased. Because the primary mode of heat transfer for the SXM is conduction to the bracket baseplate, the single parameter that controls the efficiency of the heat transfer between the SXM housing and bracket, $G_{s,b}$, is a likely cause of the persisting bias. Based on these two pieces of evidence, the conductance, per screw, between the SXM housing and bracket, $G_{s,b}$, is assigned the uniform uncertainty distribution to which it was initially assigned in step two of BMV ranging from 0.11-1.32 $\frac{W}{C}$.

Propagating parametric uncertainties in both G_h and $G_{s,b}$ through the model, Figure 5-22 shows an updated prior predictive check for T36. As before, the SDD housing (Figure 5-22c) and SDD (Figure 5-22e) data points are plausible under the model output distributions. The approximate 8 °C model bias for the SXM housing (Figure 5-22b) and collimator (Figure 5-22d) from Figure 5-21 is reduced, but the data points are not covered by the model output distributions. Furthermore, the 0.3 °C bias in the predictive distribution for the bracket (Figure 5-22a) persists. Introducing the uncertainty in $G_{s,b}$ decreased the discrepancy between model and data for T36, but the uncertainty in the current G_h and $G_{s,b}$ distributions alone is not enough to make the data for all five components plausible.

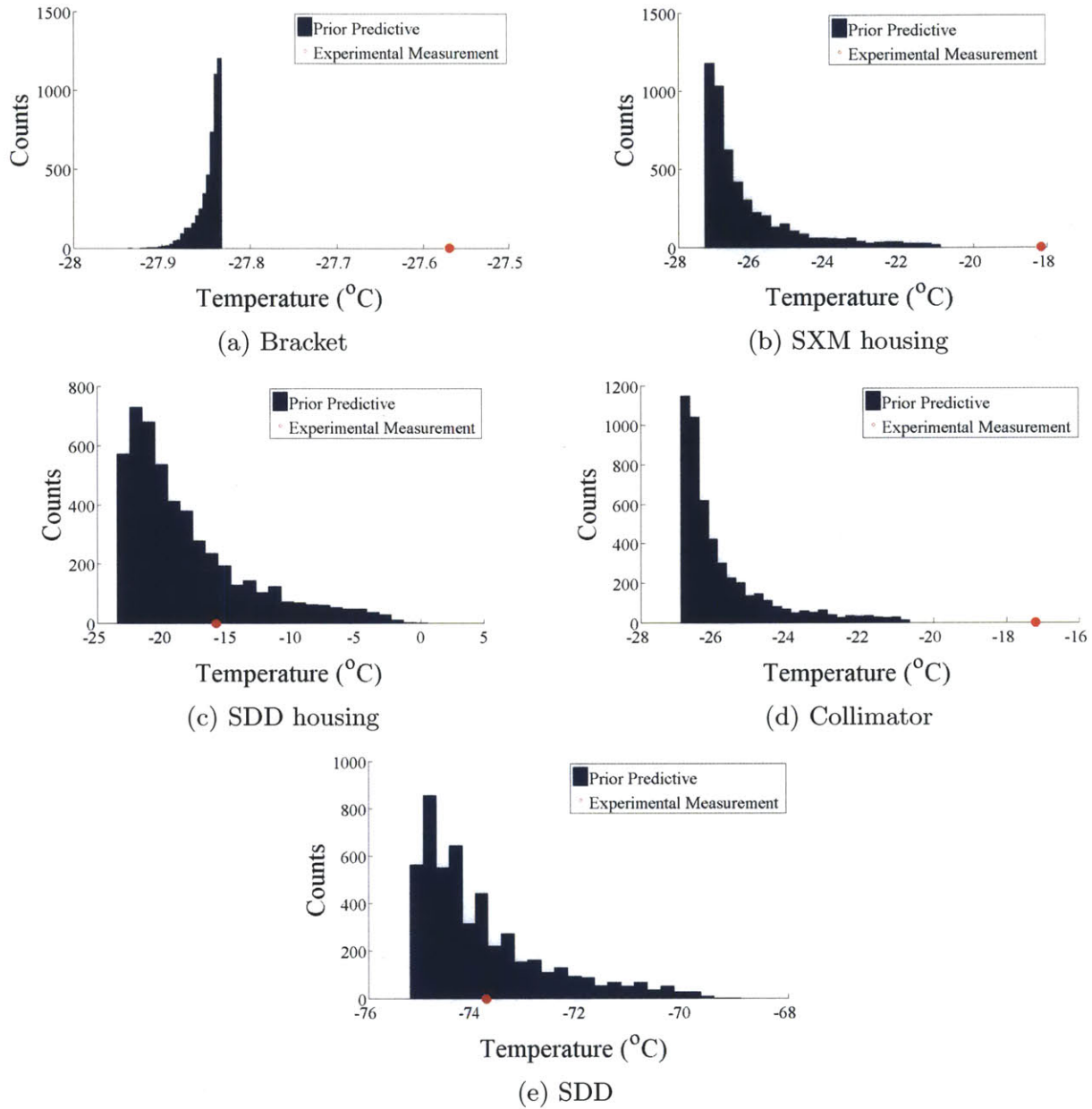


Figure 5-22: Prior predictive distribution check for each SXM component for test phase T36. Results are based on the propagation of prior parametric uncertainty in G_h and $G_{s,b}$. Model output histograms are generated via Monte Carlo sampling (5,000 samples) of the calibration parameters' prior distributions. There is a zero-mean Gaussian observation error associated with each data point that is not shown for the data in this figure.

5.5.5 Calibration Parameter Selection: G_h and $G_{s,b}$, Relaxed $G_{s,b}$ Lower Bound

As before, additional uncertainty (e.g., parametric, model structure, or observational error) must be introduced to explain the data. Introducing the prior uncertainty of $G_{s,b}$ reduced the cold-biased model predictions from approximately 8 °C to a minimum of 3 °C. There is evidence in the experimental data and in the design of the SXM housing itself to suggest that the initial lower bound of the $G_{s,b}$ distribution does not bound the true value of the conductance. From Figure 5-15 and Figure 5-16, the experimental temperature difference from the SXM housing to the bracket interface is approximately 10 °C, which is larger than the temperature difference predicted by the model with $G_{s,b}$ at its lower limit of 0.11 $\frac{W}{C}$. That $G_{s,b}$, at its minimum value, does not yield the correct temperature difference between the SXM housing and bracket suggests that the true value is below the 0.11 $\frac{W}{C}$ lower limit (since the conduction is approximately 1D).

Furthermore, a bottom-view inspection of the SXM housing, shown in Figure 5-23, reveals a small surface area near the fastener holes that connect the housing to the bracket. For conduction across an aluminum-to-aluminum bolted interface, the majority of the heat transfer occurs between the contacting material near the fastener [4]. Because there is very little material near the fastener holes, the lower limit of $G_{s,b}$ may not conservatively bound the true value of the conductance per screw. The lower bound of $G_{s,b}$ is relaxed to zero so that the true value is contained in the uniform distribution ranging from 0-1.32 $\frac{W}{C}$. Although not considered in this case study, the temperature difference between the SXM housing and bracket could be reduced by increasing the surface area along the bottom of the housing. The increase in area near the fastener holes could result in a lower, final SDD temperature (i.e., a higher allowable interface temperature, T_{O-REx} , for a given SDD temperature and TEC power dissipation).

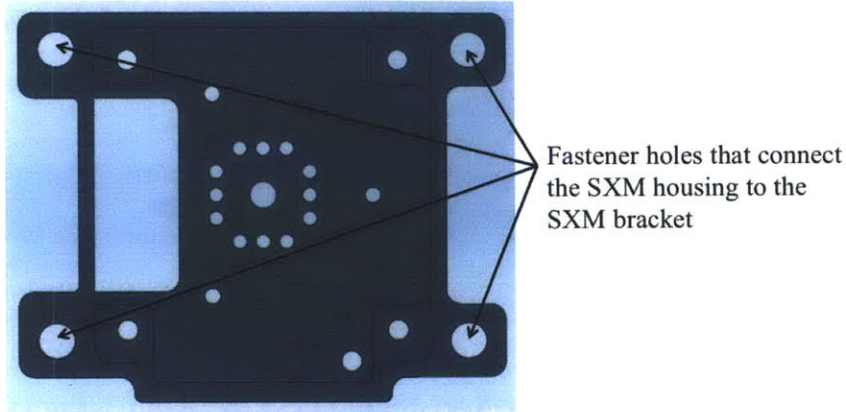


Figure 5-23: Bottom view of SXM housing illustrating the small surface area around the fasteners that connect the housing to the bracket

With the prior uncertainty of G_h and the uncertainty of $G_{s,b}$ with a relaxed lower bound, the results of the prior predictive check are updated for T36 as shown in Figure 5-24. As before, the data points for the SDD housing (Figure 5-24c) and SDD (Figure 5-24e) are covered by the prior predictive distributions. Relaxing the lower limit of $G_{s,b}$ based upon the observed temperature gradients in the data and physical inspection of the design had the desired effect of making the data plausible under the distributions for the SXM housing (Figure 5-24b) and collimator (Figure 5-24d). The predictions for the bracket (Figure 5-24a) are again cold-biased by approximately 0.3 °C. Although an additional change to the model is needed to obtain a plausible prior predictive check for the bracket, the results of Figure 5-24 suggest that the calibrated model for T36 has a small model discrepancy for the four other components.

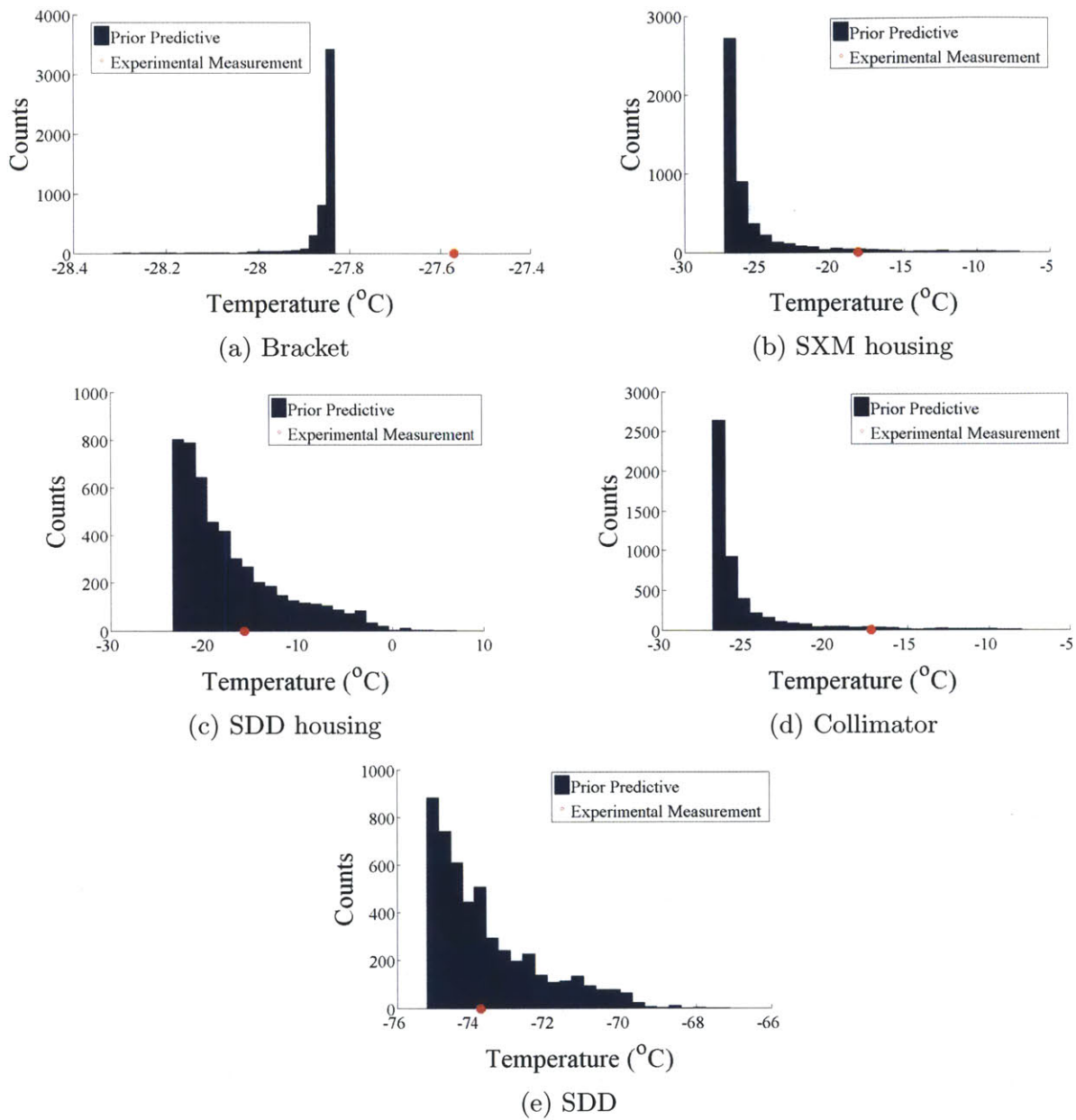


Figure 5-24: Prior predictive distribution check for each SXM component for test phase T36. Results are based on the propagation of prior parametric uncertainty in G_h and $G_{s,b}$ with relaxed lower bound. Model output histograms are generated via Monte Carlo sampling (5,000 samples) of the calibration parameters' prior distributions. There is a zero-mean Gaussian observation error associated with each data point that is not shown for the data in this figure.

5.5.6 Calibration Parameter Selection: G_h , $G_{s,b}$ and G_b , Relaxed $G_{s,b}$ Lower Bound

There is one remaining conductance parameter between the SXM housing and the bracket (whose uncertainty is not yet accounted for) that was previously fixed at its nominal value: the conductance per area between the bracket and the chamber interface plate, G_b . The prior predictive distributions in Figure 5-21, Figure 5-22, and Figure 5-24 are cold-biased by approximately 0.3 °C, suggesting that the nominal value of $G_b = 2,000 \frac{W}{m^2-C}$ is higher than the true value. The parameter G_b is now unfixed from its nominal value and assigned its prior uncertainty distribution from step two of BMV, a uniform distribution ranging from 100-4,000 $\frac{W}{m^2-C}$.

The prior predictive check is updated for T36 once more by considering the uncertainty in G_h , $G_{s,b}$ with relaxed lower bound, and G_b , as shown in Figure 5-25. As in Figure 5-24, the data for the SXM housing (Figure 5-25b), SDD housing (Figure 5-25c), collimator (Figure 5-25d), and SDD (Figure 5-25e) are plausible under the prior predictive distributions. In Figure 5-25, the bracket data point is also plausible under the prior predictive distribution now that there is uncertainty in G_b . For test phase T36, the test phase corresponding to the optimal parameter inference experiment in terms of information gain for G_h , the data for all five components are now plausible for the parametric uncertainty considered.

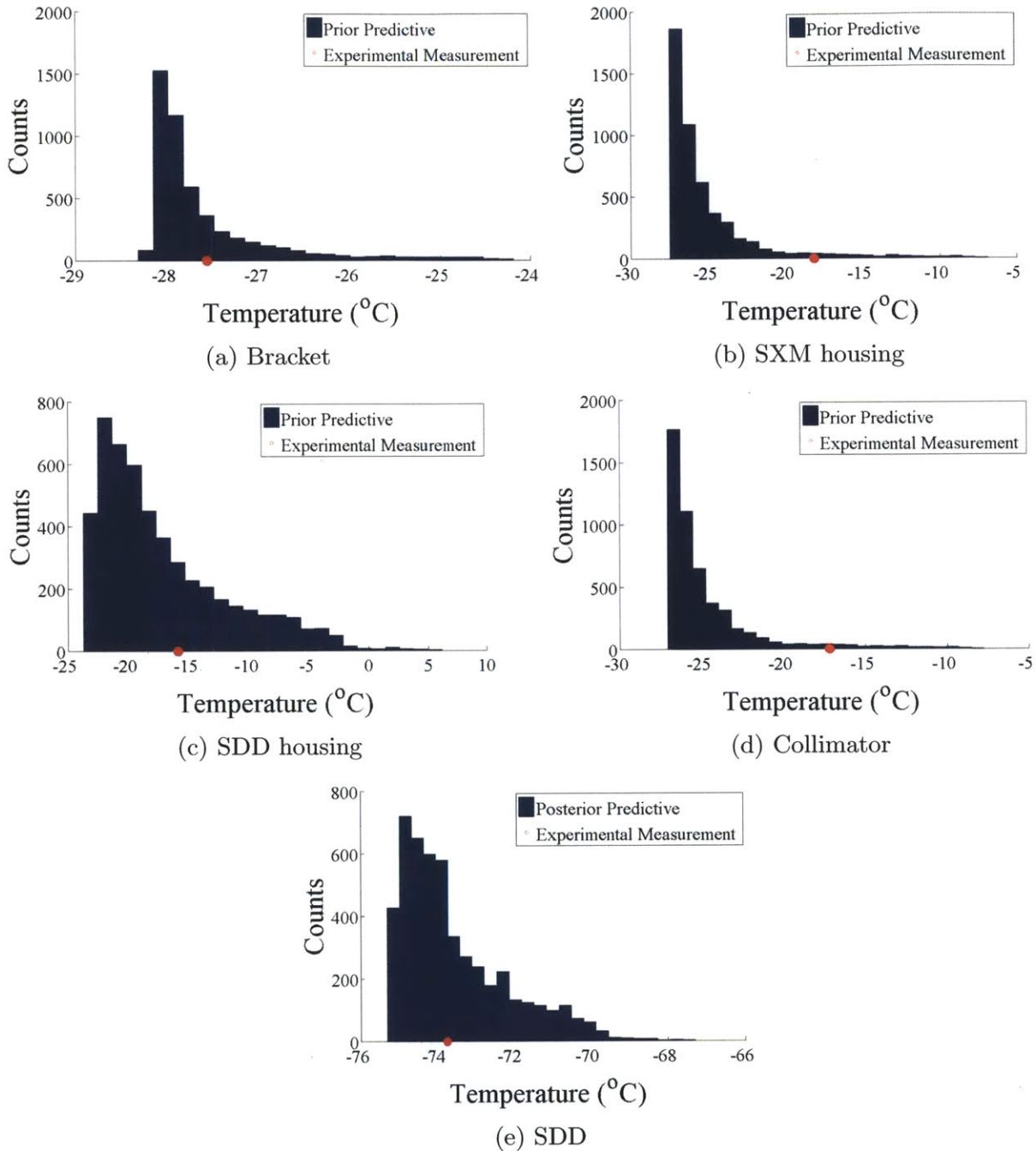


Figure 5-25: Prior predictive distribution check for each SXM component for test phase T36. Results are based on the propagation of prior parametric uncertainty in G_h , $G_{s,b}$ with relaxed lower bound, and G_b . Model output histograms are generated via Monte Carlo sampling (5,000 samples) of the calibration parameters' prior distributions. There is a zero-mean Gaussian observation error associated with each data point that is not shown for the data in this figure.

5.5.7 Parameter Calibration (MCMC): G_h , $G_{s,b}$ and G_b , Relaxed $G_{s,b}$ Lower Bound

From Figure 5-19, the next steps in the calibration procedure are to obtain posterior distributions for G_h , $G_{s,b}$ and G_b by calibrating to multiple test phases and perform posterior predictive checks to determine if the fit is acceptable. To sample the posterior distributions for the calibration parameters, $\gamma = [G_h, G_{s,b}, G_b]^T$, the Metropolis-Hastings [141, 142] algorithm for Markov chain Monte Carlo (MCMC) method is used. A summary of the prior uncertainty distributions (resulting from the prior predictive checks in previous sections) for each parameter in γ is shown in Table 5.6. For more information on implementing MCMC algorithms in practice, see Andrieu et al. [143]. Once the posterior distributions are obtained, a posterior predictive check is performed.

Table 5.6: Calibration parameter prior uncertainty distributions for MCMC. All three parameters have uniform prior uncertainty distributions.

Parameter	Units	Min Value	Max Value
G_h	$\frac{W}{m^2-C}$	100	4,000
$G_{s,b}$	$\frac{W}{C}$	0	1.32
G_b	$\frac{W}{m^2-C}$	100	4,000

It is important to begin MCMC with a good starting point, γ_0 , that lies on the support of the posterior distributions of the calibration parameters to reduce the number of samples for burn-in and for proper operation of the algorithm. To find the MCMC starting point, optimization is performed to find the set of calibration parameter values that minimizes the sum square of residuals:

$$\gamma_0 = \gamma^* = \arg \max_{\gamma \in \Gamma} \sum_{i=1}^P \sum_{j=1}^M (z_{i,j} - y_{i,j})^2 \quad (5.17)$$

where the starting point of the MCMC algorithm, γ_0 , is the solution to the optimization problem, γ^* . The search space, Γ , is the domain covered by the prior distributions for the calibration parameters, shown in Table 5.6. Equation (5.17) shows a double summation

of residuals squared over P total test phases and M total components where $z_{i,j}$ are the experimental data and $y_{i,j}$ are the model evaluations achieved for discrete values of the calibration parameters. In Equation (5.17), the subscript i iterates over the test phases, and the subscript j iterates over the components of the SXM. For the SXM test, there are five total components from which measurements were made, and up to 43 total test cases are available for calibration (i.e., $M = 5$ and P can be 1 to 43 based on how many test phases, T1 to T43, are chosen for calibration).

Once the starting point, γ_0 , is obtained, MCMC is performed to find the posterior distributions for the calibration parameters. The algorithm below outlines the adaptive Metropolis-Hastings algorithm implemented for the SXM calibration:

1. **Draw proposal, γ_{new} , from $q(\gamma_{new}|\gamma_{old})$**

2. **Calculate acceptance ratio:**

$$\alpha(\gamma_{old}, \gamma_{new}) = \left[1, \frac{\pi(\gamma_{new})q(\gamma_{old}|\gamma_{new})}{\pi(\gamma_{old})q(\gamma_{new}|\gamma_{old})}\right]$$

3. **Set the next value in the chain:**

$$\gamma_{n+1} = \begin{cases} \gamma_{new} & \text{with probability } \alpha(\gamma_{old}, \gamma_{new}) \\ \gamma_{old} & \text{with probability } 1 - \alpha(\gamma_{old}, \gamma_{new}) \end{cases}$$

In the MCMC algorithm, $\alpha(\gamma_{old}, \gamma_{new})$ is the acceptance ratio and $\pi(\gamma)$ is short-hand notation for the posterior distribution (i.e., $\pi(\gamma) = p(\gamma|\mathbf{z}, \mathbf{d}) \propto p(\mathbf{z}|\gamma, \mathbf{d})p(\gamma)$). Each new proposal, γ_{new} , is drawn from the Gaussian proposal distribution $y \sim q(\gamma_{new}|\gamma_{old}) = \mathcal{N}(\gamma_{old}, C)$, where $C = S_d \text{cov}(\gamma_{1:n}) = \frac{2.4^2}{d} \text{cov}(\gamma_{1:n})$. The covariance, C , is a function of the calibration parameters dimension, d . In this case study, $d = 3$. The approach is adaptive because the proposal is drawn from a multivariate Gaussian whose covariance is updated periodically by using the previous samples in the chain. Because the proposal distribution is symmetric, $\frac{q(\gamma_{old}|\gamma_{new})}{q(\gamma_{new}|\gamma_{old})} = 1$ so the calculation of the acceptance ratio simplifies to $\alpha(\gamma_{old}, \gamma_{new}) = \left[1, \frac{\pi(\gamma_{new})}{\pi(\gamma_{old})}\right]$. The MCMC algorithm above is implemented to sample $p(\gamma|\mathbf{z}, \mathbf{d})$ for measurements on the five major SXM components (bracket, SXM housing, SDD housing, collimator, and SDD) and any combination of test phases, T1 to T43.

Before implementing MCMC on the SXM thermal model, calibration test cases are selected. Calibrating to all 43 test cases is not computationally infeasible, but is burdensome. From inspection of Figure 5-14, Figure 5-15, and Figure 5-16, the experimental data are smooth. Smoothness in the data over many points indicates that there is redundant information in the data and suggests that not all the data are critical for calibrating the parameters in γ . To mitigate the computational burden of calibrating to all 43 test phases, a subset of the test phases is selected for calibration. Although not considered here, a more rigorous, model-based test phase selection would be to implement OBED methods. Now that there are more calibration parameters than just G_h , step four of BMW could be repeated to select the optimal experiment(s) for information gain in γ . While the OBED framework would be similar to before (using the KL divergence as a measure of expected information gain for a given experiment), the selection of multiple test phases could be extended to a dynamic programming problem to select the optimal *set* of test phases for inferring γ .

The down-select procedure to choose the calibration test phases follows the classical DOE central composite (CC) designs for response surface methodology [144]. The selection of test phases for calibration is patterned after a CC experimental design because CC designs are used to empirically model relationships, of moderate dimensionality, between experimental design variables and output variables, requiring significantly fewer points than full factorial approaches. Based on a two-factor CC design pattern overlay onto the model validation experiment grid in Figure 5-10, the following nine test phases are used for calibration:

- **Center point:** T5
- **Factorial points:** T12, T16, T21, T25
- **Axial points:** T1, T9, T32, T41

In addition to the nine test phases corresponding to the CC design, T36 is included because it is the optimal experiment in terms of information gain for G_h (shown in step four of BMV), one of the three calibration parameters. Thus, ten total test phases, of the possible 43 test phases, are used when implementing MCMC to calibrate γ .

The adaptive MCMC algorithm is implemented for the ten calibration test phases using the measured steady state temperatures on the five major SXM components. The observation

error of each sensor is included when computing the likelihood term, $p(\mathbf{z}|\gamma)$, in the MCMC acceptance ratio. Figure 5-26 shows the mixing of the MCMC chain for G_h , and Figure 5-27 shows the posterior histograms and scatterplots for the three conductance parameters contained within γ . Although the mixing of G_h appears good, the samples versus iteration of the MCMC chain in Figure 5-26 are asymmetric, appearing to hit a “wall” at $4,000 \frac{W}{m^2-C}$. Figure 5-27 confirms that G_h is pushing against the boundary of the prior uncertainty distribution. Due to the moderate correlation between the parameters, the scatterplots also appear asymmetric.

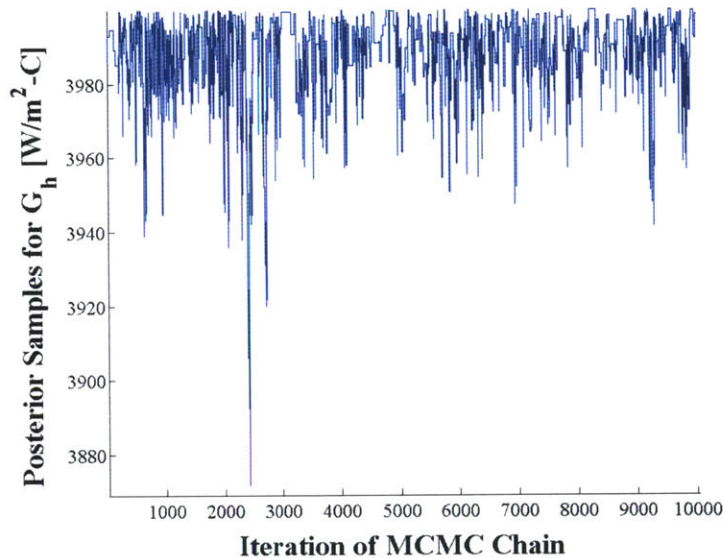


Figure 5-26: Plot of adaptive MCMC chain showing good mixing after initial burn-in period but pushing up against the boundary of the prior uncertainty distribution for G_h

The results in both Figure 5-26 and Figure 5-27 are evidence of either inaccurate prior bounds on G_h or significant model structure error. That the posterior samples for G_h are pushing up against the $4,000 \frac{W}{m^2-C}$ upper limit of the prior uncertainty distribution is because the upper limit is not large enough. Although originally thought to be an *optimistic* value for the upper limit of the conductance between the SDD housing and SXM housing, Glasgow and Kittredge [145] showed through gap filler performance testing that Cho-Therm 1671 has a conductance near its vendor-specified conductance of $6,700 \frac{W}{m^2-C}$. In step two of BMV, the upper limit of the uncertainty distribution for G_h is incorrectly set. Evidence [145] suggests that the prior upper limit does not capture the true value of G_h , the error in the results from

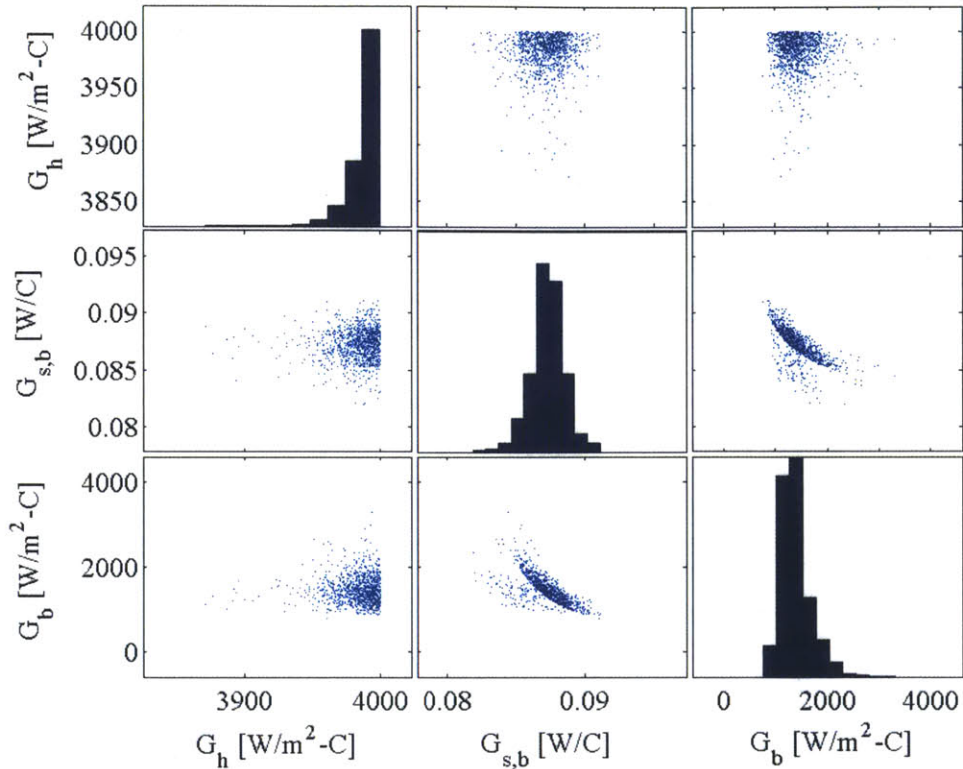


Figure 5-27: Posterior histograms and scatterplots for the three SXM calibration parameters

Figure 5-26 and Figure 5-27 is associated with the G_h parameter of the SXM thermal model, not the model structure. Therefore, the upper bound of G_h is relaxed to $10,000 \frac{W}{m^2-C}$, and the posterior distributions for the calibration parameters, γ , are re-sampled via MCMC.

5.5.8 Parameter Calibration (MCMC): G_h , $G_{s,b}$ and G_b , Relaxed G_h Upper Bound and $G_{s,b}$ Lower Bound

Once again, the adaptive MCMC algorithm discussed in Section 5.5.7 is implemented for the 10 calibration test phases and all five major SXM components. The prior uncertainty distributions for the calibration parameters are shown in Table 5.6, except the upper limit of G_h is increased to $10,000 \frac{W}{m^2-C}$. The updated MCMC mixing plot for G_h is shown in Figure 5-28. After an initial burn-in requiring approximately 1,000 samples, Figure 5-28 shows good mixing for G_h . Although not shown here, the mixing for $G_{s,b}$ and G_b is similar to G_h : good mixing after an initial 1,000 sample burn-in period. For conservatism, the first

2,000 samples of the posterior distributions are discarded when using samples or computing posterior statistics to be sure that the burn-in period is removed.

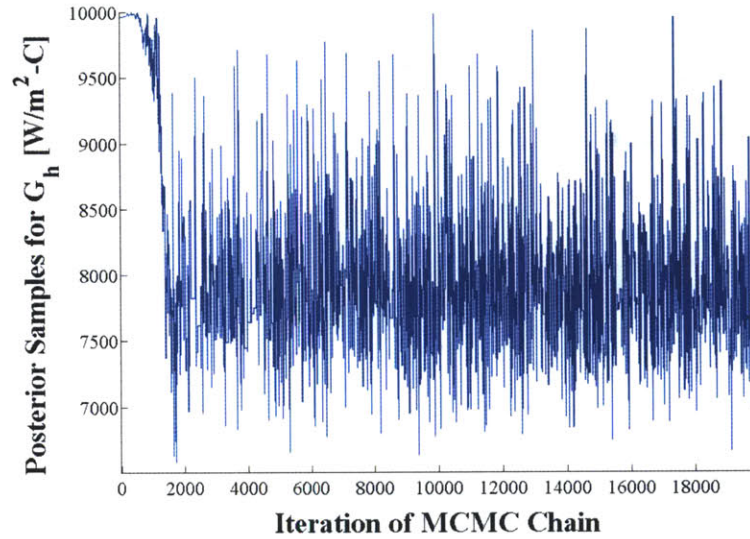


Figure 5-28: Plot of adaptive MCMC chain showing good mixing after initial burn-in period

The updated posterior histograms and scatterplots are shown in Figure 5-29. By inspection, the posterior distributions for G_h and $G_{s,b}$ are approximately Gaussian, whereas G_b has a non-Gaussian shape. The posterior mean for G_h is $7,900 \frac{W}{m^2-C}$, which is slightly higher than the value measured by Glasgow and Kittredge [145]—an intuitive result because the applied torque across the G_h joint, and thus the contact pressure, is larger than that measured by Glasgow and Kittredge experimentally. The posterior mean for $G_{s,b}$ is $0.079 \frac{W}{C}$, just below the initial $0.11 \frac{W}{C}$ lower limit for the prior distribution. The posterior mean for G_b is $1,376 \frac{W}{m^2-C}$, which is $623 \frac{W}{m^2-C}$ less than where G_b was fixed prior to calibration (before the uncertainty in G_b was considered during calibration, it was fixed at $2,000 \frac{W}{m^2-C}$). Using Equation (5.9), the correlation coefficients for the three calibration parameter posteriors are $R_{G_h, G_{s,b}} = -0.54$, $R_{G_h, G_b} = 0.0009$, $R_{G_{s,b}, G_b} = -0.64$. The correlation between G_h and $G_{s,b}$ and between $G_{s,b}$ and G_b is moderate, and the correlation between G_h and G_b is small. The correlation is intuitive because the SDD housing temperature can be increased by decreasing the value of either G_h , $G_{s,b}$, or G_b . Thus, for the SDD housing temperature, the parameters are correlated because the value of one affects the range of possible values for the other parameters. The next step in the calibration process is to determine how well the calibrated

model fits the data.

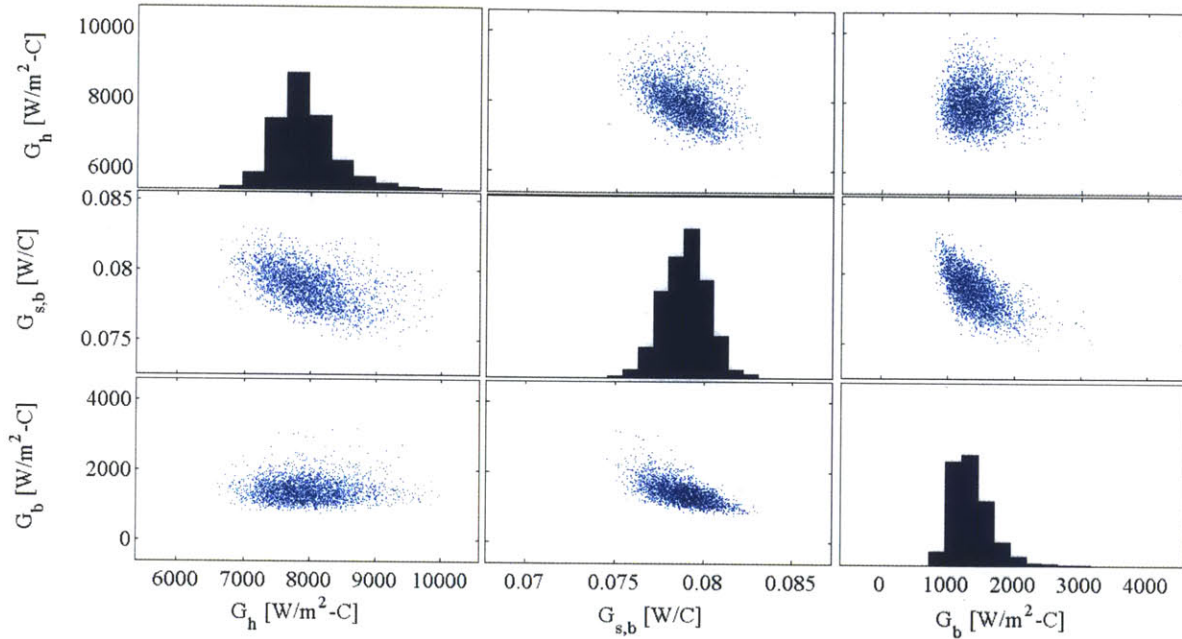


Figure 5-29: Posterior histograms and scatterplots for the three SXM calibration parameters

Following Figure 5-19, the next step is to perform a posterior predictive check with the candidate calibration. First, a posterior predictive check for T36, shown in Figure 5-30, is completed to show how the calibrated parameters fit a single test phase. Under the posterior predictive distributions, the data point for the bracket (Figure 5-30a) in T36 is plausible, and the data for the SXM housing (Figure 5-30b), SDD housing (Figure 5-30c), collimator (Figure 5-30d), and SDD (Figure 5-30e) are implausible (i.e., the data are not covered by the distributions, as shown notionally in Figure 5-20b). Although the model is overconfident and yields distributions that are centered on the incorrect temperatures, the distance between the distribution and the data is small—less than 1.5 °C. Although the implausibility of the data in T36 for the SXM housing, SDD housing, collimator, and SDD suggests that the model is inadequate, the *magnitude* of the inadequacy for all four components is small and acceptable. The inadequacy of the model is accounted for via an additive model discrepancy term, $\delta(\mathbf{x})$, in the next step of the calibration process.

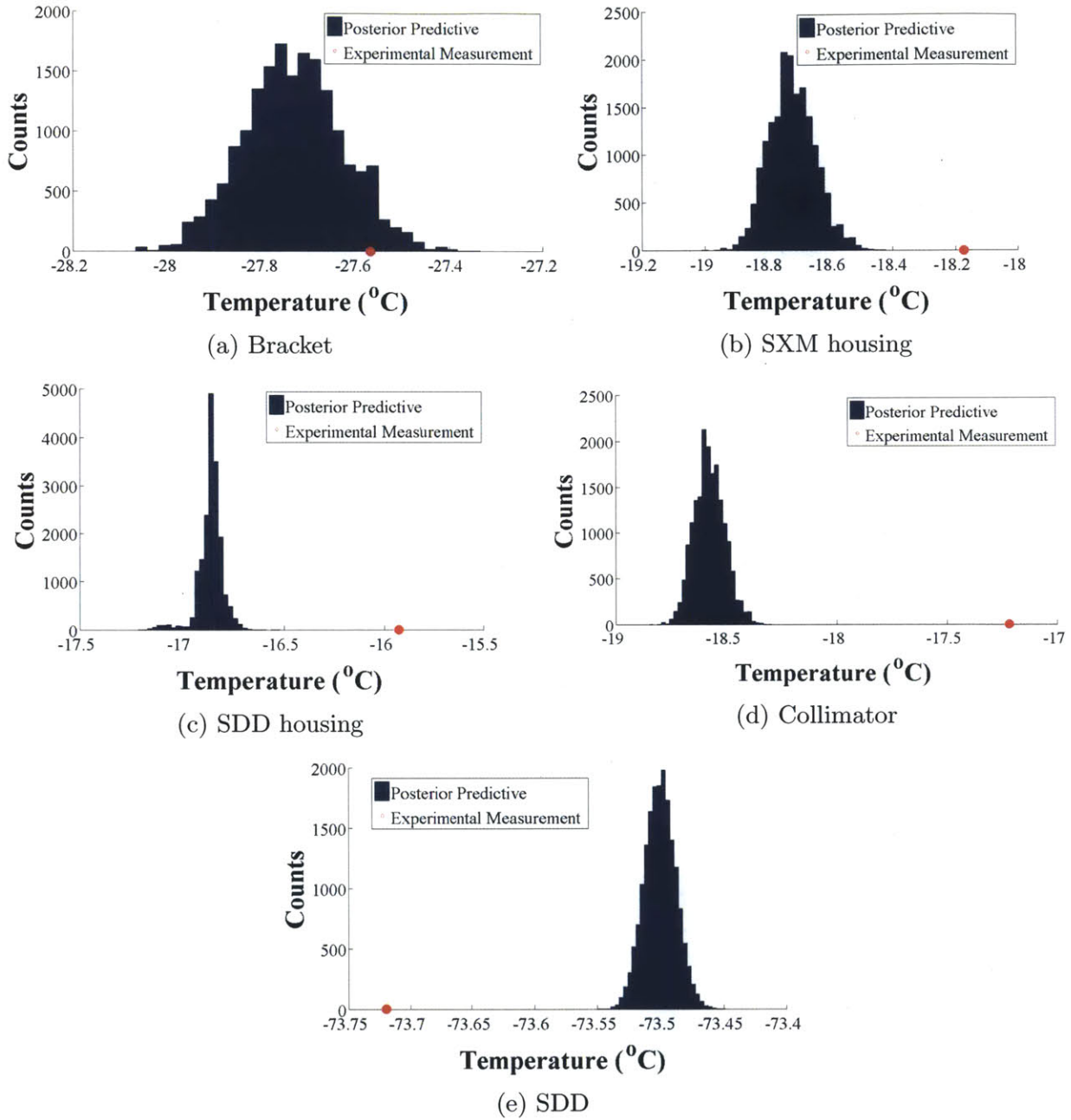


Figure 5-30: Posterior predictive distribution check for each SXM component for test phase T36. Results are based on the propagation of the posterior parametric uncertainty in G_h , $G_{s,b}$, and G_b . Model output histograms are generated via MCMC (18,000 samples of the parameters' posterior distributions). There is a zero-mean Gaussian observation error associated with each data point that is not shown for the data in this figure.

Unlike the previous prior predictive checks where the model is calibrated and checked against a single test phase (T36), the posterior distributions in Figure 5-29 are obtained by

calibrating to 10 test phases. Ideally, we would perform a posterior predictive check to all 43 test phases. To obtain an averaged sense for how well the calibrated model fits the data for all 43 test phases, Equation (5.18) shows the calculation for the magnitude of an average temperature difference for a single component and P test cases:

$$|\Delta T_{avg}| = \frac{1}{P} \sum_{i=1}^P |E[\eta_{SXM}(\mathbf{x}, \mathbf{d}_i)] - z_i| \quad (5.18)$$

where $E[\eta_{SXM}(\mathbf{x}, \mathbf{d}_i)]$ is the expected value of the model output for experimental conditions given by \mathbf{d}_i , and z_i is the data point for the i^{th} test phase. Equation (5.18) is implemented for all five components of the SXM for $P = 43$ test phases, and the results are shown in Figure 5-31. The largest $|\Delta T_{avg}|$ value is the SDD, and the smallest $|\Delta T_{avg}|$ is the bracket. Thus, on average, the predictive capabilities for the calibrated model are the worst for the SDD and the best for the bracket. On average, the mean of the posterior and the data agree to less than 1 °C for all five SXM components. The fit is acceptable for the SXM and based on Figure 5-19, the next step is to quantify the model discrepancy.

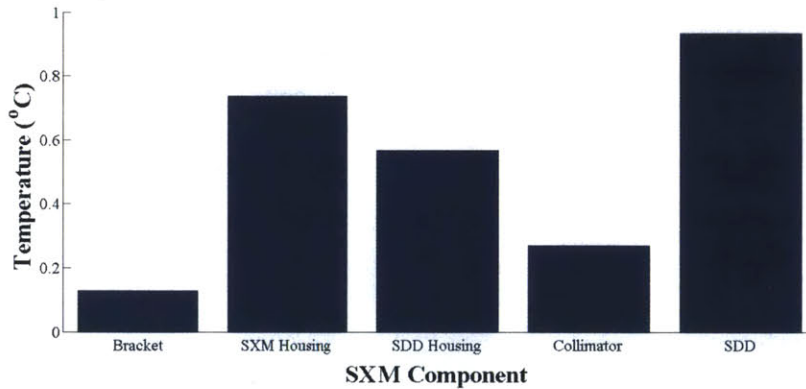


Figure 5-31: Absolute value of temperature difference between experimental data and mean of posterior predictive distribution (see Equation (5.18)) for all 43 test cases

5.5.9 Quantify Model Discrepancy

The final step in the SXM thermal model calibration procedure is to quantify the model discrepancy. The model discrepancy function, $\delta(\mathbf{x})$, is additive, as shown in Equation (2.13). Rearranging Equation (2.13) to solve for the discrepancy:

$$\delta(\mathbf{x}) = \mathbf{z} - \eta_{SXM}(\mathbf{x}) - \epsilon_m \quad (5.19)$$

As before, \mathbf{z} is the experimental data for each of the five major SXM components, \mathbf{x} are all of the model parameters, η_{SXM} is the SXM thermal model and ϵ_m is the observation error. The only parametric uncertainty considered in η_{SXM} is the uncertainty of the posterior distributions of the calibration parameters, γ , because the non-calibration parameters in \mathbf{x} have such low sensitivities with respect to the QoIs that their uncertainties are not significant. All calibration parameters, γ , are contained in \mathbf{x} (i.e., $\gamma \subset \mathbf{x}$). The dimension of each term in Equation (5.19) is 5x1 because there are five SXM components from which direct measurements were made during the model validation experiment.

The discrepancy function is a function of the experimental conditions, \mathbf{d} , (which are a subset of \mathbf{x}) because the magnitude and sign of the discrepancy function depends on the conditions of a particular test phase. Furthermore, the discrepancy function for each component is assumed to be independent of the other components' discrepancy functions. Consequently, the discrepancy function in Equation (5.19) can be written as:

$$\delta(\mathbf{d}) = \begin{pmatrix} \delta_b \\ \delta_{sxm,h} \\ \delta_{sdd,h} \\ \delta_{coll} \\ \delta_{sdd} \end{pmatrix} \quad (5.20)$$

where δ_b , $\delta_{sxm,h}$, $\delta_{sdd,h}$, δ_{coll} , and δ_{sdd} are the discrepancies of the bracket, SXM housing, SDD housing, collimator, and SDD, respectively. Using Equation (5.19) to solve for samples of $\delta(\mathbf{d})$ for each of the 43 test phases, the means of the discrepancy distributions are plotted against V_{TEC} and T_{O-REx} for each component, as shown in Figure 5-32 (a, c, e, g). By inspection, there is a smooth dependence on \mathbf{d} for the discrepancy of each component. For the SDD discrepancy, there is no observable dependence on \mathbf{d} so it is addressed separately.

A Gaussian Process (GP) model, as shown in Equation (5.21), is selected for the discrepancy functions for the bracket, SXM housing, SDD housing, and collimator. Advantages of

GPs include that they are nonparametric in that they do not assume a form for $\delta(\mathbf{d})$, are computationally tractable for moderate to some high dimensional problems, and probabilistically interpolate between observation values [146]. The GP model formulation is:

$$\delta(\mathbf{d}) \sim \mathcal{GP}(m(\mathbf{d}), k(\mathbf{d}, \mathbf{d}')) = \mathcal{GP}(0, k(\mathbf{d}, \mathbf{d}')) \quad (5.21)$$

where the mean function, $m(\mathbf{d})$, is assumed to be zero for all four discrepancies, δ_b , $\delta_{sxm,h}$, $\delta_{sdd,h}$, and δ_{coll} . GP models are highly flexible models often used to fit a wide range of smooth surfaces. The covariance kernel, $k(\mathbf{d}, \mathbf{d}')$, completely governs the behavior of the GP because the mean is zero. A squared-exponential Automatic Relevance Determination (ARD) kernel is used for the GP for each SXM component discrepancy:

$$k(\mathbf{d}, \mathbf{d}') = \sigma_0^2 \exp \left\{ -\frac{1}{2} \left(\frac{V_{TEC} - V'_{TEC}}{\lambda_1} \right)^2 + -\frac{1}{2} \left(\frac{T_{O-REx} - T'_{O-REx}}{\lambda_2} \right)^2 \right\} \quad (5.22)$$

where σ_0^2 is the output variance, and λ_1 and λ_2 are the characteristic lengths. The σ_0^2 and λ variables are referred to as hyperparameters for the GP. The characteristic lengths control how rapidly values of $\delta(\mathbf{d})$ change for different values of \mathbf{d} . If λ is large in a particular direction, that parameter in \mathbf{d} is less influential to the value of the GP. The squared-exponential ARD kernel is one of several options. For example, an empirical kernel based on the covariance of the discrepancy samples or the Matérn covariance function are alternative choices for a GP kernel.

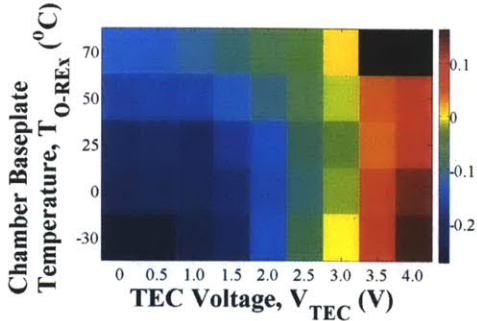
GP regression is performed using the Gaussian Processes for Machine Learning (GPML) Toolbox [147] to find the value for the hyperparameters in Equation (5.22) so that the discrepancy functions can be used for prediction. For regression, discrepancy samples are generated using Equation (5.20), and the mean and variance of the samples are used for each set of experimental conditions, \mathbf{d} . For more information on GP regression, see [148]. Table 5.7 shows the resulting hyperparameter values for the GP associated with the discrepancy function for each component. The characteristic lengths for voltage are approximately two or three times larger than those of the SXM interface temperature. The magnitude of the output variance for the bracket is much smaller than the other three components because the

model matches the data more closely (i.e., the magnitudes of the discrepancy are smaller); an intuitive result given that the bracket data point for T36 (and other test phases as well) is plausible under the posterior predictive in Figure 5-30. With the values for the hyperparameter values in Table 5.7, Equation (5.21) can now be used for prediction.

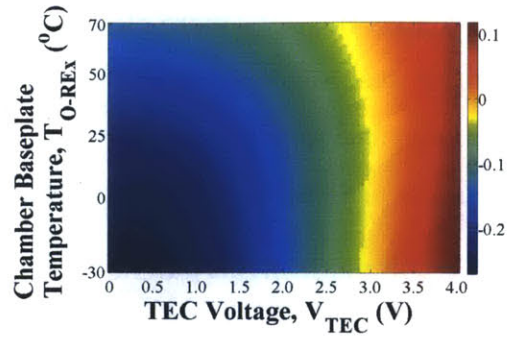
Table 5.7: GP model hyperparameter regressed values where the σ_0 's are the output standard deviations, and the λ 's are the characteristic lengths. For regression, all values of T_{O-REx} on the training point grid are normalized by 50 °C.

Component	σ_0	$\lambda_1 (V_{TEC})$	$\lambda_2 (T_{O-REx})$
Bracket, δ_b	0.032	2.792	1.220
SXM Housing, $\delta_{sxm,h}$	0.728	2.433	0.794
SDD Housing, $\delta_{sdd,h}$	0.602	2.272	0.714
Collimator, δ_{coll}	0.460	2.435	0.675

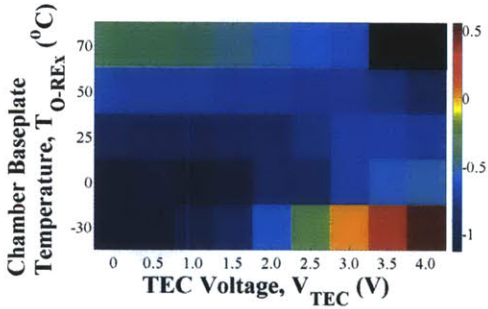
To compare the resulting GP models to the training points for δ_b , $\delta_{sxm,h}$, $\delta_{sdd,h}$, and δ_{coll} , the plots on the right side of Figure 5-32 show the mean of the GP models for a fine grid. By inspection, the mean of each of the four discrepancy functions are well represented by the GP mean. The GP model discrepancy function values and topologies appear to match the coarse training point heatmaps well over the entire domain of V_{TEC} and T_{O-REx} , even extrapolating for test phases T44 and T45 (3.5-4.0 V, 70 °C) where no data is available. The discrepancy values for the bracket are strongly correlated with the TEC voltage, and at higher voltage values and lower chamber baseplate temperatures, the discrepancy values for the SXM housing, SDD housing, and collimator are strongly correlated with the baseplate temperature.



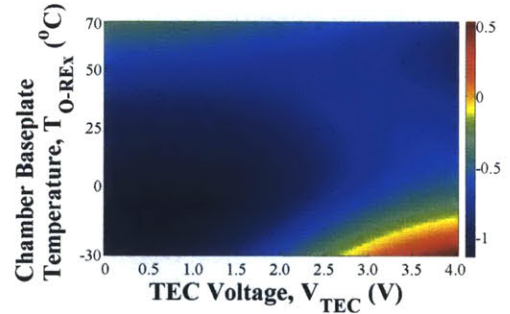
(a) Bracket, mean of training points



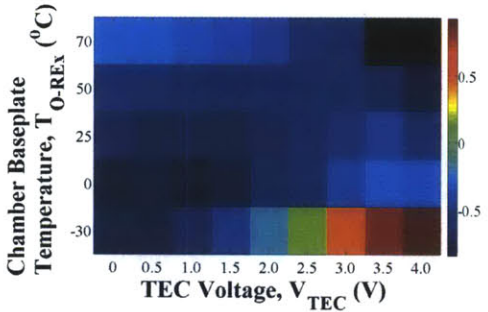
(b) Bracket, GP mean



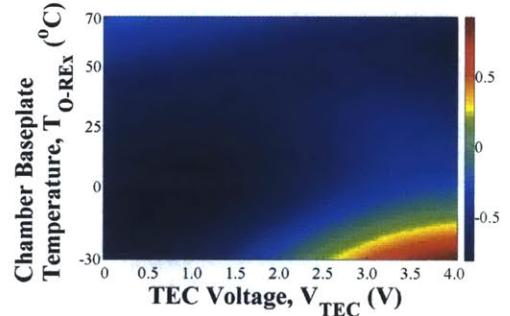
(c) SXM Housing, mean of training points



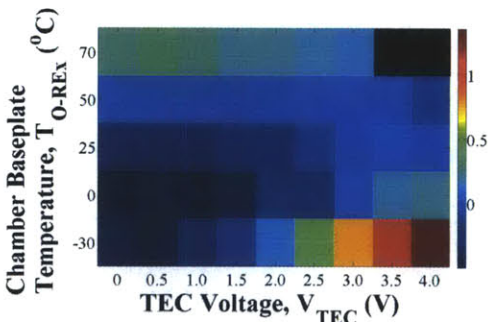
(d) SXM Housing, GP mean



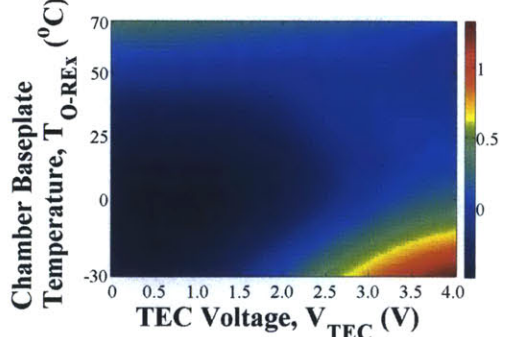
(e) SDD Housing, mean of training points



(f) SDD Housing, GP mean



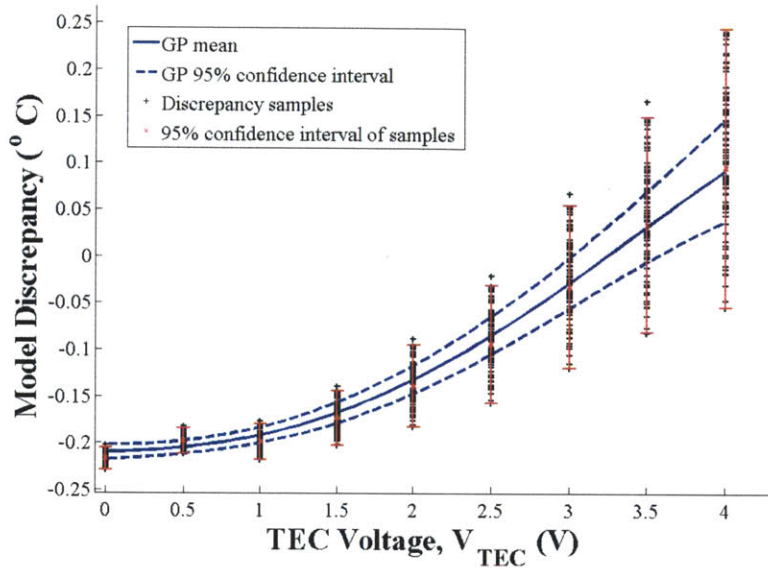
(g) Collimator, mean of training points



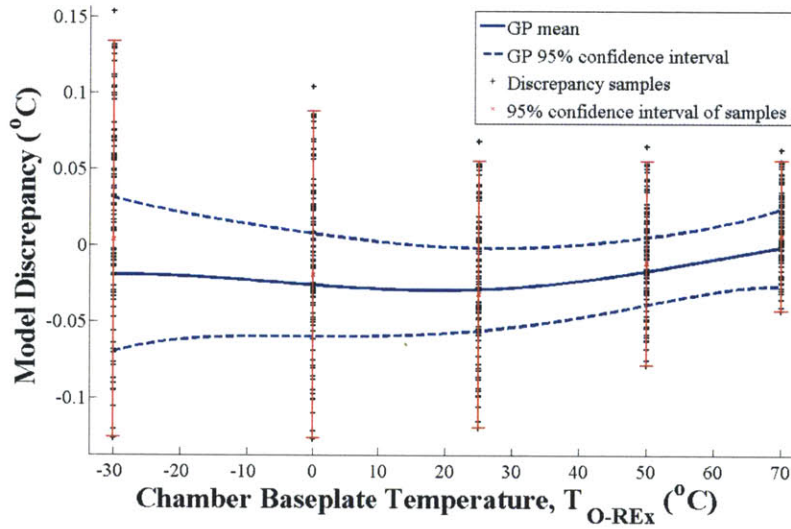
(h) Collimator, GP mean

Figure 5-32: Side-by-side comparison of Gaussian process discrepancy training points and resulting GP model discrepancy mean values for four SXM components over various TEC voltages, V_{TEC} , and chamber baseplate temperatures, T_{O-REx} . GP training points found using Equation (5.19) with the experimental data. All heatmap values are in units of $^{\circ}\text{C}$.

Sample sections of the GP random fields in Figure 5-32 are considered to determine how the GP model is matching the variance of the discrepancy samples. Figure 5-33 and Figure 5-34 show sections from the GP models for the bracket and the SDD housing, respectively. Figure 5-33a and Figure 5-34a show the model discrepancy for increasing voltage and constant $T_{O-REx} = 25$ °C. Figure 5-33b and Figure 5-34b show the model discrepancy for increasing T_{O-REx} and constant $V_{TEC} = 3$ V. In all four plots, the GP model 95% confidence interval lies inside of the 95% confidence interval for the discrepancy samples. The variance reduction in the GP is expected because the model uses not only the discrepancy training points at the same V_{TEC}, T_{O-REx} locations but also at other experimental condition locations to improve information gain. In both Figure 5-33 and Figure 5-34, the mean of the GP models well approximate the trends in the discrepancy samples. For example, Figure 5-33a shows both the discrepancy values increasing and the discrepancy sample variance increasing; the GP model captures both of these trends. In summary, the GP models with the hyperparameter values in Table 5.7 provide model discrepancy estimates for δ_b , $\delta_{sxm,h}$, $\delta_{sdd,h}$, and δ_{coll} for any set of V_{TEC}, T_{O-REx} over the entire domain of intended application of the SXM thermal model.

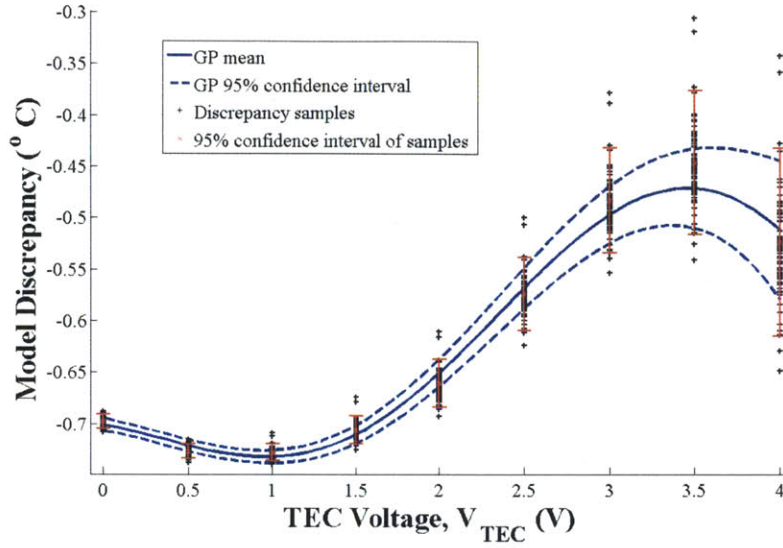


(a) Variable voltage, constant $T_{O-REx} = 25\text{ }^{\circ}\text{C}$

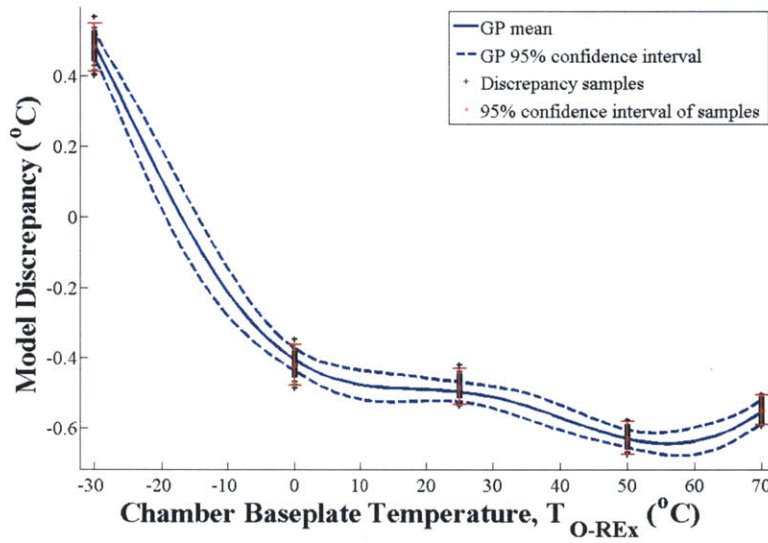


(b) Variable T_{O-REx} , constant $V_{TEC} = 3\text{ V}$

Figure 5-33: GP model section for bracket model discrepancy, δ_b . The GP model is plotted with 50 discrepancy samples, per Equation (5.19), at each location.



(a) Variable voltage, constant $T_{O-REx} = 25\text{ }^{\circ}\text{C}$



(b) Variable T_{O-REx} ; constant $V_{TEC} = 3\text{ V}$

Figure 5-34: GP model section for SDD housing model discrepancy, $\delta_{sdd,h}$. The GP model is plotted with 50 discrepancy samples, per Equation (5.19), at each location.

The final discrepancy function in $\delta(\mathbf{d})$ that must be addressed is δ_{sdd} . As shown by Figure 5-35a, there is not a clear relationship between the δ_{sdd} and the experimental conditions, V_{TEC} and T_{O-REx} . Furthermore, δ_{sdd} does not appear to be smooth. The SDD discrepancy values are different from the other SXM components because the TEC model, which is a polynomial regression model, is used to estimate the SDD temperature. For some

experimental conditions, the TEC model underestimates the actual TEC cold side temperature, and for other experimental conditions, the TEC model overestimates the actual TEC cold side temperature. There is no apparent physical tie between the experimental conditions and the under/overestimation of the TEC model cold side temperature. The values of the discrepancy samples at each experimental condition are plotted in a single histogram, shown in Figure 5-35b. The mean of the data is $\mu = 0.12$ °C, and the standard deviation is $\sigma = 1.10$ °C. The Gaussian distribution in Figure 5-35b is used as the SDD discrepancy function (i.e., $\delta_{sdd} \sim \mathcal{N}(0.12, 1.10^2)$ °C) because it is smooth, conservative over the entire domain of possible V_{TEC} and T_{O-REx} values, and computationally cheap to generate samples.

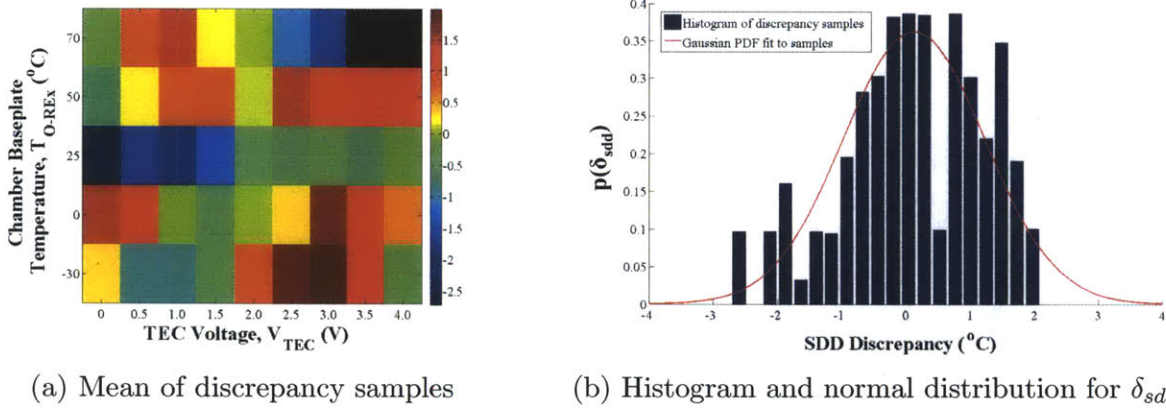


Figure 5-35: SXM SDD discrepancy samples and histogram. Because there is no clear correlation between δ_{sdd} and the experimental conditions, V_{TEC} and T_{O-REx} , a Gaussian distribution, fit to the discrepancy samples, is used for predictions of δ_{sdd} .

The model discrepancy functions are added to the predictions made by the SXM thermal model to account for model inadequacies remaining after calibrating the model parameters. To demonstrate how the model discrepancy functions are used for prediction, Figure 5-36 shows the same posterior predictive check as in Figure 5-30, but a histogram including the additive model discrepancy is also shown. Samples of the model discrepancy functions, $\delta(\mathbf{x})$, are generated by sampling the GP models for δ_b , $\delta_{sxm,h}$, $\delta_{sdd,h}$, and δ_{coll} for the experimental conditions of test phase T36. Samples of δ_{sdd} are generated by sampling the Gaussian distribution for δ_{sdd} from Figure 5-35b (18,000 samples total for Figure 5-36). The red histograms in Figure 5-36 are the same as the histograms in Figure 5-30. Without the additive discrepancy, only the data point for the bracket is plausible under the predictive

posterior distribution. However, with the model discrepancy functions included, the blue histograms in Figure 5-36 cover the data for all five SXM components, highlighting the importance of including a model discrepancy term when making final model predictions. Now, all five data points for test phase T36 (and all other test phases, although not shown) are plausible under the predictive posterior distribution with additive model discrepancy. The SXM thermal model discrepancy is quantified and the calibration procedure, per Figure 5-19, is complete.

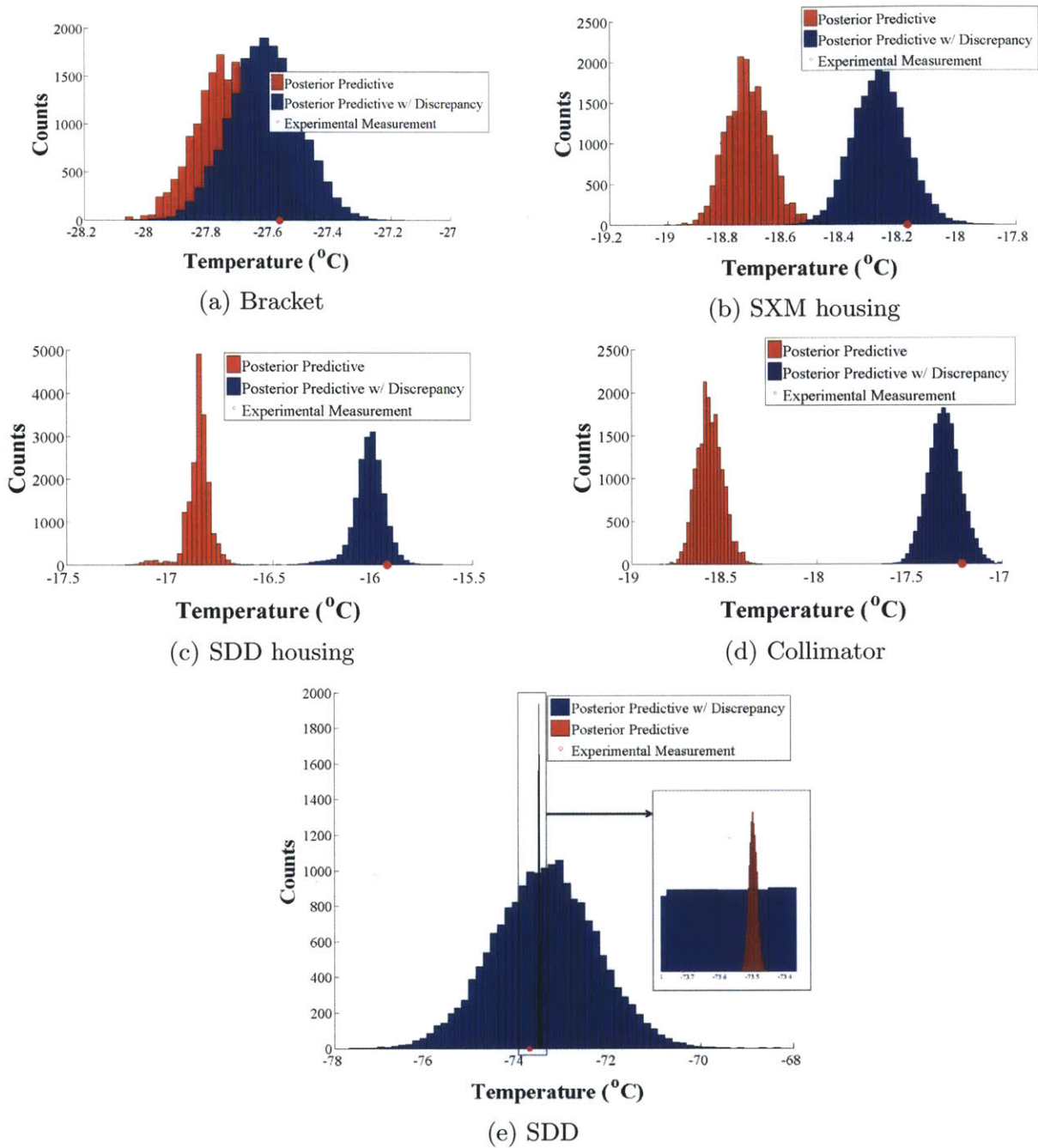


Figure 5-36: Posterior predictive distribution check for each SXM component for test phase T36, both with and without an additive model discrepancy function, $\delta(\mathbf{x})$. Model output histograms are generated via MCMC (18,000 samples of the parameters' posterior distributions). There is a zero-mean Gaussian observation error associated with each data point that is not shown for the data in this figure.

5.5.10 Flight Model Update

The final component of step five of BMV is to update the flight model based on changes made to the experimental thermal model during the calibration process. Prior to calibration, the only uncertain parameter in the SXM thermal model is G_h because GSA indicates that most of the uncertainty in the SDD temperature is due to G_h . However, the parameter calibration process reveals that uncertainty in G_h alone is not enough to accurately fit all of the experimental data *for all three QoIs*. During the model calibration process, the changes made to the SXM thermal model included three parametric changes and an additive model discrepancy:

- Uncertainty distribution for conductance, per area, between SDD housing and SXM housing, G_h , changes from uniform distribution ranging from 100-4,000 $\frac{W}{m^2-C}$ to distribution shown in Figure 5-29
- Uncertainty distribution for conductance, per screw, between SXM housing and bracket, $G_{s,b}$, changes from uniform distribution ranging from 0.11-1.32 $\frac{W}{m^2-C}$ to distribution shown in Figure 5-29
- Uncertainty distribution for conductance, per area, between bracket and spacecraft interface, G_b , changes from uniform distribution ranging from 100-4,000 $\frac{W}{m^2-C}$ to distribution shown in Figure 5-29
- An additive model discrepancy term, $\delta(\mathbf{x})$, is included with the model predictions to account for thermal model inadequacies over the entire domain of expected mission TEC voltages, V_{TEC} , and spacecraft interface temperature, T_{O-REx} .

Each of the four changes above are made to the flight model, so the remaining uncertainty in the flight thermal model is due uncertainty in the three calibration parameters and the model discrepancy functions. All parameters, except G_h , $G_{s,b}$, and G_b , remain fixed at their nominal values. The model discrepancy values are added to the model output. With the changes to the flight SXM thermal model complete, the next BMV step is to perform uncertainty propagation again to determine if requirements are met. Furthermore, the final uncertainty propagation indicates the final, maximum allowable temperature of the interface, T_{O-REx} .

5.6 Step 2: Uncertainty Propagation and Parameter Prioritization—Second Pass

The final analysis step of BMV is to propagate the calibrated model uncertainties (parametric and model discrepancy) through the model to ensure that all thermal requirements are satisfied. Furthermore, the final uncertainty propagation will indicate the maximum allowable spacecraft interface temperature, T_{O-REx} , at which the SXM can meet requirements with 99% probability. First, MC simulations using Equation (5.2), as in the *first pass*, are performed to update the results of Figure 5-4, excluding the model discrepancy, $\delta(\mathbf{d})$. This time, only the uncertainty in the posterior distributions of the calibration parameters is propagated through the model. The updated uncertainty analysis results are shown in Figure 5-37a. Each point in Figure 5-37a is found by performing a full MC simulation with $N = 10,000$ samples for a fixed interface temperature, T_{O-REx} . Compared to Figure 5-4 the curves are significantly sharper, indicating that the parametric uncertainty is significantly reduced. Because the range of temperatures over which the probability falls from 100% to 0% is small, there is less uncertainty in the QoIs as the interface temperature increases. The SDD maximum allowable operational temperature of -30 °C is still the driving thermal requirement for the SXM. Based on Figure 5-37a, the maximum allowable temperature for T_{O-REx} is 63.5 °C, which is the temperature at which the probability of satisfying the SDD requirement drops below 99%.

The uncertainty analysis results in Figure 5-37a are incomplete because they do not include the effects of the model's inadequacy in predicting the QoIs. The additive model discrepancy functions from step five are included with the model predictions to capture the inadequacy:

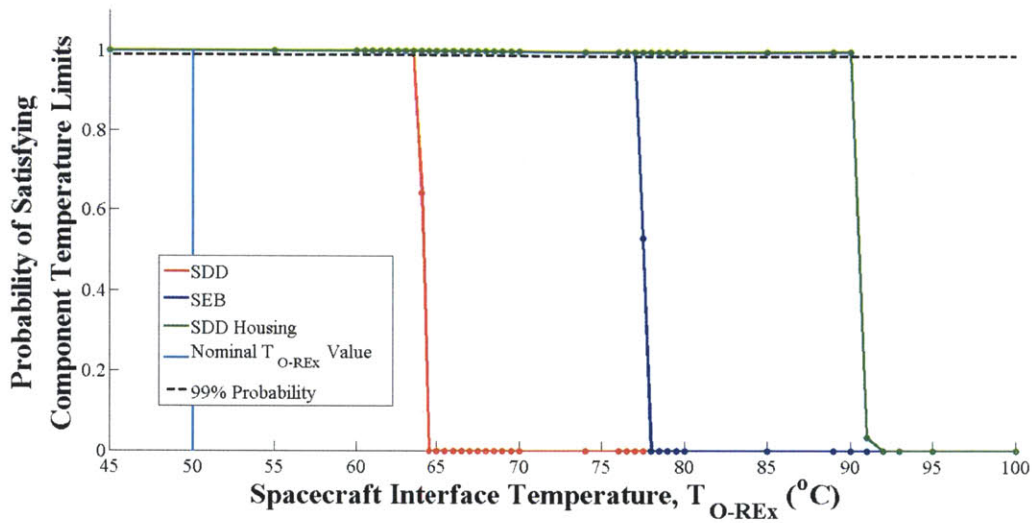
$$\zeta_{SXM}(\mathbf{x}) = \eta_{SXM}(\mathbf{x}) + \delta(\mathbf{d}) = \eta_{SXM}(\mathbf{x}) + \delta(V_{TEC}, T_{O-REx}) \quad (5.23)$$

where ζ_{SXM} is the prediction of the true physical process. For the second uncertainty analysis, the prediction of the true physical process is used in the MC simulations:

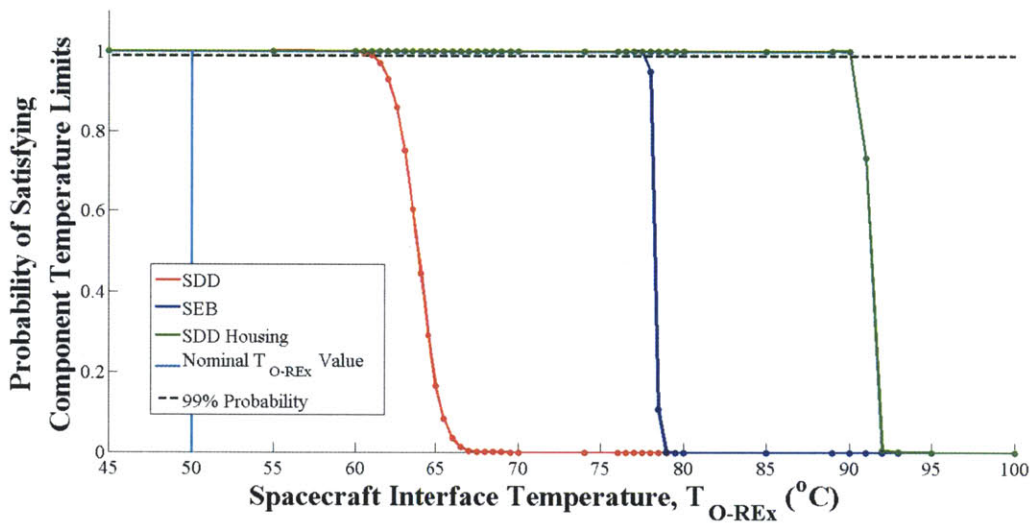
$$\bar{\zeta}_{SXM,N} = \frac{1}{N} \sum_{i=1}^N \zeta_{SXM}(\mathbf{x}_i) \quad (5.24)$$

where $\bar{\zeta}_{SXM,N}$ is the MC estimator for the true physical process and N is the number of MC samples. The model discrepancy functions for the bracket, δ_b , and the collimator, δ_{coll} , are not needed for the uncertainty analysis because they do not correspond to a QoI. The discrepancy function for the SXM housing, $\delta_{sxm,h}$, is used for the SEB because it was not possible to measure the SEB temperature directly during the experiment (thus, not easy to construct an explicit discrepancy function). Because the only thermal path from the SEB is to the SXM housing, $\delta_{sxm,h}$ is a good proxy for the discrepancy of the SEB.

The revised uncertainty analysis results, which include the effects of the model discrepancy, $\delta(\mathbf{d})$, are shown in Figure 5-37b. The additive discrepancy increases the domain of T_{O-REx} values over which the probability decreased from 100% to 0% (i.e., make the curves slightly less sharp), particularly for the SDD curve. With the model discrepancy included with the model predictions, the maximum allowable temperature for T_{O-REx} corresponding to a 99% probability of meeting all requirements is 60.8 °C, which is 2.7 °C less than in Figure 5-37a. The maximum allowable interface temperature decreases when the model discrepancy is included because the SDD discrepancy distribution has a mean of approximately zero but standard deviation of 1.1 °C, as shown in Figure 5-35b. Therefore, at interface temperatures of slightly warmer than 60.8 °C, a slightly positive δ_{sdd} value could result in not satisfying the -30 °C requirement. By inspection, the effect of the model discrepancy for the SEB and SDD housing is small. That the SEB and SDD housing discrepancy effects are small is intuitive because the mean values of both discrepancy functions have magnitudes that are less than 0.5 °C (for T_{O-REx} greater than 50 °C and V_{TEC} greater than 2.0 V). Over the range of allowable interface temperatures, $T_{O-REx} \in [-30, 60.8]$ °C, uncertainty analysis with the calibrated model (additive discrepancy included) shows that all SXM operational thermal requirements will be satisfied.



(a) $\delta(d)$ excluded



(b) $\delta(d)$ included

Figure 5-37: Probability of satisfying the upper limits of the Table 5.1 temperature ranges versus T_{O-REx} for all three SXM QoIs based on MC simulations to propagate parametric uncertainties through the SXM thermal model (with and without additive model discrepancy)

Although not completed in this thesis, a second GSA on the SXM could be performed to update the list of prioritized, high sensitivity parameters. Following model calibration (BMV step five), only three SXM parameters are uncertain. For a general system (not necessarily the SXM), there could be a large number of uncertain parameters following model calibration. Furthermore, design changes or additional model validation efforts could be required to

validate the design and/or models. In such a scenario, a second GSA will indicate the updated high sensitivity parameters, allowing for a second parameter prioritization. For example, a second GSA will indicate if the original parameter(s) targeted for variance reduction from the first uncertainty propagation are still the highest sensitivity, or if another parameter or set of parameters have the highest sensitivity. For the SXM, uncertainty analysis in Figure 5-37 shows that all SXM operational thermal requirements will be satisfied, and GSA is not required.

5.7 Step 3: Experimental Goal Setting—Second Pass

Uncertainty analysis indicates that the requirements will be met when accounting for *all remaining* parametric uncertainty in the calibrated SXM thermal model and the model's inadequacy. The maximum allowable interface temperature of the spacecraft is found to be $T_{O-REx} = 60.8$ °C. Thus, the answer to the first gate in Figure 2-4—whether there is sufficient confidence that the requirements are met—is **yes**.

In Section 5.4, a model validation experiment is performed by coarsely and uniformly gridding applied TEC voltages and spacecraft interface temperatures so that test phases in the model validation experiment cover the entire domain of intended application for the SXM. All 43 test phases in the model validation experiment are used to calibrate the model and quantify the model discrepancy functions. Posterior predictive checks of the model against the test data show that the model is an accurate representation of the SXM thermal system over the entire domain of intended application. Thus, the answer to the second gate in Figure 2-4—whether the system-level model is validated—is **yes**.

5.8 Step 6: Validation Problem Documentation

Step six of BMV consists of three components, as outlined in Chapter 2: documentation of steps one through five of BMV, updating requirements if necessary, and recommending small design changes for flight. For brevity, it will suffice to say that no design changes are necessary to meet requirements. The experimental results, posterior uncertainty distributions for the

three calibration parameters, and model discrepancy functions for the QoIs are documented.

Important takeaways from the SXM case study include:

- A lumped parameter thermal model is constructed to estimate temperatures of the QoIs for the SXM thermal system
- A preliminary propagation of model uncertainties indicates that all requirements for the SXM are met for spacecraft interface temperatures ranging from $-30\text{ }^{\circ}\text{C}$ to $50\text{ }^{\circ}\text{C}$ and that the conductance between the SDD housing to SXM housing, G_h , is the critical thermal system sensitivity
- The interface temperature, T_{O-REx} , upper limit of $50\text{ }^{\circ}\text{C}$ is relaxed and BMV is used to find the maximum temperature at which the interface could have been set (while still meeting the driving $-30\text{ }^{\circ}\text{C}$ operational SDD requirement)
- An optimal parameter inference experiment to learn G_h and a model validation experiment are implemented and the data are used to calibrate the parameters of the SXM thermal model and quantify the calibrated model's inadequacy
- The calibrated model and model discrepancy function are used in a final uncertainty analysis to show that all requirements are satisfied for a maximum spacecraft interface temperature of $60.8\text{ }^{\circ}\text{C}$, which is over $10\text{ }^{\circ}\text{C}$ warmer than the original upper limit for T_{O-REx}

5.9 Comparison of BMV vs. A Conventional Model Validation Approach

In the SXM case study, BMV differs from a conventional validation approach in both *process* and potentially, the *resource consumption* of the system. First, the BMV validation process in Sections 5.1-5.8 is compared to a conventional validation approach. Then, the impact to resource consumption is discussed, including the implications of the $50\text{ }^{\circ}\text{C}$ interface limit on the spacecraft design and operation.

In the SXM case study, there are several major differences between the BMV validation *process* and a conventional approach. Prior to testing and during step two of BMV, all model parameter uncertainties (including system and environmental parameters) are estimated via probability distributions and propagated through the model. The model is sampled many thousands of times, spanning both bounding and intermediate thermal environments and system power modes. It is shown that for a spacecraft interface temperature of $T_{O-REx} \in [-30, 50]$ °C, the three SXM operational requirements are always satisfied. In a conventional approach, there would likely be only two analysis cases—the worst-case hot and cold cases. For some systems, it can be unclear which sets of parameters yield the true worst-case hot and cold scenarios. For example, in cooling the SXM SDD, it is not immediately clear whether it is more efficient to decrease TEC power and hot side temperature or increase TEC power and accept a warmer interface temperature. The uncertainty analysis approach in BMV can indicate which parameter sets yield the true bounding (i.e., worst-case) thermal scenarios. Once the upper limit of T_{O-REx} is relaxed, BMV indicates that at $T_{O-REx} = 63$ °C, the probability of satisfying the SDD requirement is below the required 99% probability. Furthermore, the uncertainty in the SDD temperature prediction is found via GSA to be primarily due to the uncertainty in the conductance between the SDD housing and SXM housing, G_h . In a conventional approach, there is no systematic approach for finding the high sensitivity parameter(s). Although an experienced engineer *could* find G_h manually, BMV uses all of the information within the model to systematically identify the important parameters, even those that are intuitively not obvious.

The results of the uncertainty propagation in step two are used in step four, design and implementation of experiments, to *optimally* reduce uncertainty in G_h and validate the SXM model. Unlike in a conventional approach, the parameter of interest, G_h , is targeted by an experiment whose conditions are set so that information gain is maximized. Whereas in a conventional approach a thermal engineer might test at the hot case conditions (i.e., maximum T_{O-REx} and maximum power dissipations), the KL divergence experimental utility function is maximized at minimum T_{O-REx} and maximum power dissipations. For the model validation experiment, the focus of conventional approaches is often bounding the environments in a worst-case sense. However, the focus of BMV is spanning the entire domain

of operational modes and conditions. For example, while a maximum T_{O-REx} and minimum power dissipations case might be of little interest with respect to qualifying the SXM thermal design, it is useful for model calibration because it ensures that the validated model is not extrapolating for relatively high T_{O-REx} values and relatively low power dissipations. Because the time constant of the SXM is small, the BMV model validation experiment follows a full factorial experimental design approach (which did contain the conventional worst-case hot and cold test phases).

In BMV, the experimental results from step four are used in step five to calibrate the model parameters and quantify the model discrepancy. Instead of following the thermal system convention for model correlation, which often heavily relies on manual model adjustments from an experienced engineer, the SXM model parameters are updated using a MCMC method, a method for Bayesian inference. The calibration parameters are selected based on the results of GSA in step two and are systematically updated through a Bayesian calibration process. MCMC methods are advantageous because they are highly automated, reveal correlations between calibration parameters, and can indicate when unrealistic values of the calibration parameters are needed to fit the data. Unlike in a conventional approach where parameter values are replaced by new values that yield a better fit to the data, the prior parameter distributions are *updated* based on information in the data in BMV. After the model parameters are updated, the remaining model inadequacy is quantified using Gaussian Process (GP) Models. The GPs are probabilistic estimates of the model discrepancy and are added to the model output. Using BMV, the quantified model discrepancy allows the engineer to probabilistically estimate, based on a given environment and system power mode, how well the calibrated SXM thermal model approximates the actual temperatures. In contrast, a conventional approach typically requires a model correlated to some threshold value (e.g., ± 3 °C)—the model is then deemed an adequate representation of the true thermal system and the inadequacy is not quantified.

In the SXM case study, BMV led to additional information being available to the engineer at each major step of the validation process. BMV provides a more rigorous quantification of model uncertainties before and after testing. The output information of one validation step is the input to the next, and validation efforts target the most important uncertainties

in the SXM thermal system.

Although the primary innovation of BMV is to the model validation process, the implementation of BMV early in the project lifecycle could have led to system resource savings. Because the SXM has small mass and volume, the primary “resource” parameter is the spacecraft interface temperature, T_{O-REx} (SXM is thermally coupled to spacecraft). The spacecraft interface temperature upper limit of $T_{O-REx} = 50\text{ }^{\circ}\text{C}$ has spacecraft design implications and possibly introduces additional operational constraints. Following a conservative, conventional approach, the interface temperature maximum limit was set based on the simulation results of a worst-case hot operational scenario using a preliminary SXM Thermal Desktop model. Given the uncertainty in the maximum power dissipation of the TEC, thermal performance of the TEC, and SXM conductances, the interface limits were set so that the SDD requirement had greater than $10\text{ }^{\circ}\text{C}$ margin. Because the SXM is nominally facing the sun, cooling the SXM interface to $50\text{ }^{\circ}\text{C}$ with the GEVS [24] standard thermal design margin of $5\text{ }^{\circ}\text{C}$ (i.e., predictions must show a maximum interface temperature of $45\text{ }^{\circ}\text{C}$ or less) is the driving thermal system accommodation for the REXIS SXM. Due to the $50\text{ }^{\circ}\text{C}$ upper limit, design changes to the spacecraft near the SXM interface included:

- Heat spreader and RTV added to interface to decrease thermal resistance across interface
- Changes in surface coatings near the SXM to help cool the mounting structure
- Redesign of MLI blankets near the interface to increase heat rejection from structure to cooler parts of spacecraft

If the upper limit were relaxed to a warmer temperature, some or all of the above design changes to the spacecraft may have not been necessary, thus decreasing accommodations costs for REXIS. Furthermore, the operational mission plan has changed since the $50\text{ }^{\circ}\text{C}$ upper limit was set. Although current predictions indicate that the interface temperature will be satisfied, analysis by the spacecraft indicates that power cycling of the REXIS SXM *could* be necessary if temperatures are slightly warmer than expected. If the interface temperature upper limit were higher, there is a higher probability that the SXM would remain on and ready for observations.

As shown in Figure 5-38, BMV increases knowledge of the system early in the project lifecycle when important design decisions are made. For the SXM, the critical system parameter, G_h , is identified, and the uncertainties in the parameter distributions for G_h , $G_{s,b}$, and G_b are reduced during calibration. Furthermore, the calibrated model discrepancy is quantified. After the implementation of BMV, it is shown in the SXM case study that the maximum allowable interface temperature could be up to $T_{O-REx} = 60.8\text{ }^\circ\text{C}$, which is $10\text{ }^\circ\text{C}$ warmer than the original limit. Instead of implementing a standardized thermal design margin, thermal margin, if needed, could be applied to the SXM to address specific SXM uncertainties (e.g., degradation of SDD performance due to radiation damage during the interplanetary mission). As discussed above, the maximum T_{O-REx} value has implications for the spacecraft thermal design and potentially, the operation of the SXM. If implemented, BMV could have potentially saved REXIS accommodations cost to the spacecraft by allowing for a larger T_{O-REx} upper limit.

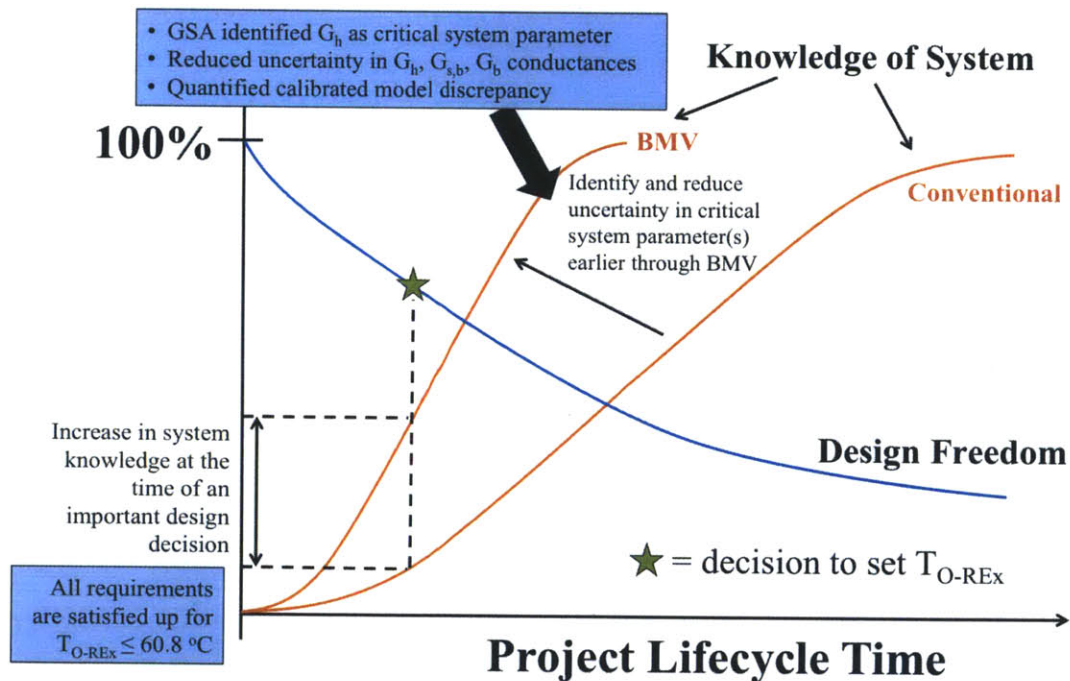


Figure 5-38: Illustration of BMV on REXIS SXM over project lifecycle with respect to knowledge of system and design freedom

Chapter 6

Conclusion

6.1 Thesis Summary and Conclusions

Over the last several decades of space flight, spacecraft thermal system modeling software has significantly advanced, but the *model validation process*, in general, has changed very little. Although most thermal systems flown are successful, there is evidence of some model inaccuracy and thermal system overdesign due to the conservatism of the current (i.e., conventional) validation process. A significant improvement to the model validation process can result in the reduction of resource-related (e.g., mass, volume, or power) or process-related (e.g., design, verification and validation, operations) mission costs. This thesis proposes a Bayesian-based Model Validation (BMV) methodology as a tailored framework that combines the state of the art model validation methods within the fields of Uncertainty Quantification (UQ) and Design of Experiments (DOE) to improve the thermal model validation process.

In Chapter 2, each of the six BMV steps are described for a general system: (1) validation problem definition, (2) uncertainty propagation (UP) and parameter prioritization, (3) experimental goal setting, (4) design and implementation of experiments, (5) experimental model calibration and flight model update, and (6) validation problem documentation. In BMV, model uncertainties are rigorously quantified *upstream* of the model and propagated through the model to determine their influence on the quantities of interest (QoIs). Critical system parameters that most significantly create variance in the QoIs are identified. Optimal parameter inference experiments, implemented prior to system-level model validation exper-

iments, target the critical system parameters to learn more about the system earlier in the project lifecycle. Finally, Bayesian inference methods are utilized to systematically update the model given experimental data. BMV is model-based and takes advantages of system-specific information. Furthermore, the validation process is iterative, and the outcome of each step informs the validation procedures for the subsequent step.

Chapter 3 presents the first of two case studies and the system under study is a passive spacecraft radiator. The radiator is a simple, notional system, and the primary objective of the case study is to demonstrate the basic aspects BMV methodology. After a preliminary uncertainty propagation, it is shown that the $-60\text{ }^{\circ}\text{C}$ radiator temperature requirement is not satisfied when considering the model's parametric uncertainties. Furthermore, the radiator's emissivity is identified as primary global sensitivity in creating uncertainty in the radiator's temperature. A parameter inference experiment is simulated, generating synthetic data, to reduce the uncertainty in the radiator emissivity. With the reduced emissivity uncertainty, the radiator requirement is satisfied. A model validation experiment is implemented to validate the radiator thermal model over the domain of intended application of the radiator. The final, validated radiator model predicts that the $-60\text{ }^{\circ}\text{C}$ requirement is satisfied with sufficient probability. For comparison, a conventional model validation approach is also implemented on the radiator. It is shown that through BMV that analyses, test conditions, and decision-making during the validation process can differ from a conventional validation approach because more information is available to the engineer. By identifying and reducing uncertainty in the critical system parameter (the radiator's emissivity) early in the lifecycle, the case study shows that the final radiator's mass and volume could be lower than a conventional approach.

The second case study of the thesis is the REgolith X-ray Imaging Spectrometer (REXIS) Solar X-ray monitor (SXM). Chapter 4 provides an overview of the REXIS instrument and a description of the thermal mission environments. Furthermore, the REXIS SXM thermal system requirements and design are discussed as background information for the SXM case study.

Chapter 5 presents the second case study where BMV is implemented on the REXIS SXM. In the SXM case study, the driving thermal system parameter, the maximum inter-

face temperature with the spacecraft, T_{O-REx} , is relaxed to determine the maximum value that T_{O-REx} could have been set to using BMV. Of the three operational SXM requirements, uncertainty analysis reveals that the detector temperature is the driving QoI as T_{O-REx} increases. Global sensitivity analysis reveals that the uncertainty in a conductance within the SXM thermal system (i.e., G_h) most significantly contributes to uncertainty in the detector temperature. Both an optimum parameter inference experiment to reduce the conductance's uncertainty and a model validation experiment are implemented in a thermal vacuum chamber. A model calibration procedure utilizing prior predictive checking and a Markov Chain Monte Carlo (MCMC) method is used to systematically update the model parameters. Finally, once the model parameters are updated, a discrepancy term, modeled via Gaussian Process models, is added to the model output to account for the persisting model inadequacy. The validated SXM model is used predictively to show that the maximum value of T_{O-REx} could have been set up to 10 °C warmer than the original upper limit. Chapter 5 concludes by contrasting the implementation of BMV on the SXM with a conventional thermal model validation approach.

The primary innovation of BMV is the model validation *process*. BMV is a rigorous, systematic validation methodology that can identify and reduce important model uncertainties in a spacecraft thermal system. BMV can increase knowledge of the system early in the project lifecycle when important design decisions are made by focusing research and testing efforts on critical system sensitivities. Because how model uncertainties affect the QoIs is better understood, margin, if needed, can be applied in a system-specific manner to address particular system or environmental uncertainties.

6.2 Contributions

The primary contribution of this thesis is the development of the BMV methodology which integrates methods of UQ and DOE to improve the spacecraft thermal model validation process. First, this thesis introduces a new way of thinking for how thermal model uncertainties and experimental uncertainties are addressed in an integrated way throughout validation. The focus is on quantifying the model uncertainty at its source and exploring its effects

on the model output. Information from previous model validation steps enhances efforts in current/subsequent steps. Second, model uncertainty is rigorously and systematically managed throughout the validation process. BMV enhances engineering intuition by providing additional information to the engineer and increases the rigor of uncertainty quantification throughout the validation process. Third, the new methodology is implemented on a real, industry-relevant thermal system to demonstrate potential system form and validation process improvements. BMV is practical for real systems under realistic project constraints.

The contributions of the thesis, with respect to each thesis objective outlined in Chapter 1, are discussed below each thesis objective:

1. Quantify thermal model uncertainty associated with both the parameters and model structure to investigate effects on thermal model predictions and identify the model parameters that require uncertainty reduction.

Contribution: Development of methodology to probabilistically characterize thermal model parameter and model structure uncertainties *upstream* of the model. Uncertainty analysis and global sensitivity analysis are applied to evaluate the effects of the model uncertainties on the QoIs. For thermal systems, the methodology enables thermal engineers to systematically identify:

- The true worst-case thermal mission scenarios that tend to drive sizing of the thermal system
 - The frequency and/or likelihood of the worst-case thermal mission scenarios
 - High sensitivity model parameter(s) and prioritize parameter(s) that require uncertainty reduction
2. Reduce important model parameter uncertainties and validate the system-level thermal design and model using optimally designed experiments.

Contribution: Application of Optimal Bayesian Experimental Design (OBED) methods to design parameter inference experiments that yield maximum information gain

in high sensitivity parameter(s). OBED thermal experiments have system-specific designs with utility functions that are formulated in accordance with the experimental objective. OBED methods enable thermal engineers to:

- Identify experimental conditions (e.g., input power) that best accomplish specific thermal test objectives
 - Trade the difficulty of implementing particular experimental conditions with the expected utility
 - Determine the placement location and required accuracy of sensors based on the experimental utility measure
3. Update thermal model parameters based on experimental data while accounting for both model and experiment uncertainties.

Contribution: Development of methodology that utilizes prior/posterior predictive checking and Bayesian inference methods to systematically calibrate thermal model parameters. The persisting model inadequacy in the calibrated model is quantified using the experimental data. The methodology enhances thermal engineering judgment and experience during the calibration process by:

- Utilizing information from global sensitivity analysis to determine which parameters to calibrate
 - Updating, not replacing, prior parameter value estimates based on the information available in the data
 - Providing evidence of either unrealistic parameter bounds or model structural errors
 - Quantifying persisting model inadequacy following calibration to improve accuracy of predictions
4. Implement the methodology in industry-relevant case studies and demonstrate improvement to thermal model validation process.

Contribution: Application of BMV on a real system, the REXIS SXM, during the project lifecycle. Using BMV, the critical thermal system parameter of the SXM, G_h , is systematically identified via global sensitivity analysis and reduced via an optimum parameter inference experiment and Bayesian calibration. Under a conventional approach, the identification and reduction of uncertainty in G_h relies on the judgment, experience, and manual analysis of the thermal engineer. Using the validated SXM thermal model, it is shown that through BMV the maximum value of the spacecraft interface temperature, T_{O-REx} —an important spacecraft thermal system design parameter—could have been set up to 10 °C warmer than the original upper limit (which was set using a conservative conventional approach). As discussed in Chapter 5, a warmer T_{O-REx} upper limit could result in fewer spacecraft thermal design changes or potential operational constraints.

6.3 Future Work

The recommendations for future work focus on three main areas: (1) broadening the applicability of BMV, (2) enhancing the capability of BMV, and (3) scaling of BMV to address the complexity of large systems seen in industry. An itemized list of specific recommendations are provided below:

1. Broadening the applicability of BMV
 - Demonstration of BMV on larger, complex thermal system (i.e., a thermal system with many component interactions, high dimensional parameter and QoI vectors, and global emergent dynamics) to show how BMV enhances engineering intuition and can be tailored to models with moderate or expensive computational cost
 - Implementation of BMV on a thermal system with:
 - Prior parameter uncertainty distributions with large variances
 - Many mission thermal environments
 - Time-dependent temperature and/or heat flux requirements

- Large thermal mass, limiting the number of test phases during experimentation
- Application of BMV on other spacecraft systems (e.g., structures)

2. Enhancing the capability of BMV

- Create prior uncertainty distributions for thermal system parameters (e.g., absorptivity and emissivity of coated surface) based on historical and/or test data for use in preliminary thermal analysis
- Create and implement variance-based parameter prioritization procedure on system with many high-sensitivity parameters
- Extend OBED methods to design optimal, system-specific model validation experiments
- Quantify the model discrepancy, $\delta(\mathbf{x})$, *during* parameter calibration

3. Scaling of BMV to address large, complex thermal systems

- Identify methods of Uncertainty Quantification (UQ) and Design of Experiments (DOE) utilized by BMV that require fewer model evaluations and allow for high dimensional parameter and model output vectors
- Create procedure for reducing size/complexity of thermal model using surrogate model approaches to improve the computational cost of the model and the efficiency of reduced model construction
- Modify the way thermal engineers interface with the inputs/outputs of a Thermal Desktop model so that BMV methods can be applied using industry standard modeling tools

Chapter 7

Bibliography

- [1] S.D. Winn and J.W. Hamcher. NASA / Air Force Cost Model. *Propulsion for Space Transportation for the 21st Century (SAIC)*, May 2002. Versailles, France.
- [2] D. Drachlis. Advanced Space Transportation Program: Paving the Highway to Space. *National Aeronautics and Space Administration*, April 2008.
- [3] D. Kestenbaum. Spaceflight is Getting Cheaper. But It's Still Not Cheap Enough. *National Public Radio*, July 2011.
- [4] D. Gilmore. *Spacecraft Thermal Control Handbook, Volume I: Fundamental Technologies*. The Aerospace Press, El Segundo, CA, second edition, 2002.
- [5] R. Karam. *Satellite Thermal Control for Systems Engineers*, volume 181. American Institute of Aeronautics and Astronautics, Danvers, MA, 1998.
- [6] V. Baturkin. Micro-satellites thermal control-concepts and components. *Acta Astronautica*, 56(1):161–170, 2005.
- [7] T. D. Swanson and G.C. Birur. NASA thermal control technologies for robotic spacecraft. *Applied Thermal Engineering*, 23(9):1055–1065, 2003.
- [8] G. Karpati, T. Hyde, H. Peabody, and M. Garrison. Resource Management and Contingencies in Aerospace Concurrent Engineering. *AIAA SPACE 2012 Conference and Exposition*, September 2012.
- [9] K. Stout. Design Optimization of Thermal Paths in Spacecraft Systems. Master's thesis, Massachusetts Institute of Technology, June 2013.
- [10] J.R. Tsai. Overview of Satellite Thermal Analytical Model. *Journal of Spacecraft and Rockets*, 41(1):120–125, January 2004.
- [11] T. Smith. Thermal Analysis of PANSAT. Master's thesis, Naval Postgraduate School, December 1997.
- [12] K&K Associates. Thermal Network Modeling Handbook. Technical report, Prepared for NASA under contract NAS 9-10435, 1999.

- [13] J. Richmond. Adaptive Thermal Modeling Architecture for Small Satellite Applications. Master's thesis, Massachusetts Institute of Technology, June 2010.
- [14] B. A. Cullimore, S. G. Ring, and D. A. Johnson. SINDA/Fluint User's Manual Version 5.6. Technical report, C&R Technology, May 2013.
- [15] P.E. Cleveland and K.A. Parrish. Thermal System Verification and Model Validation for NASA's Cryogenic Passively Cooled James Webb Space Telescope. *Society of Automotive Engineers, Inc.*, 2005. Report No. 2005-01-3042.
- [16] T.D. Panczak, S.G. Ring, M.J. Welch, D. Johnson, B.A. Cullimore, and D.P. Bell. Thermal Desktop User's Manual. Technical report, C&R Technology, April 2013.
- [17] R.C. Smith. *Uncertainty Quantification: Theory, Implementation, and Applications*. Society for Industrial and Applied Mathematics, Philadelphia, PA, 2013.
- [18] N. Boccara. *Modeling complex systems*, volume One. Springer, New York, NY, 2010.
- [19] D. Allaire. Uncertainty Assessment of Complex Models with Application to Aviation Environmental Systems. Phd thesis, Massachusetts Institute of Technology, June 2009.
- [20] R. Sargent. Verification and validation of simulation models. *Proceedings of the 37th conference on Winter Simulation Conference*, 2005.
- [21] S. Blattnig, L. Green, J. Loukring, J. Morrison, R. Tripathi, and T. Zang. Towards a Credibility Assessment of Models and Simulations. *49th AIAA/ASME/ASCE/AHS/ASC Structures, Structural Dynamics, and Materials Conference*, (AIAA No. 092407):2156–2172, 2008.
- [22] Test Requirements for Launch, Upper-stage, and Space Vehicles. *Department of Defense*, 1999. MIL-HDBK-340A (USAF).
- [23] Product Verification Requirements for Launch, Upper Stage, and Space Vehicles. *Department of Defense*, 1999. MIL-STD-1540D.
- [24] General Environmental Verification Standard (GEVS). *NASA Goddard Space Flight Center*, 2013. GSFC-STD-7000A.
- [25] Rules for Design, Development, Verification, and Operation of Flight Systems. *NASA Goddard Space Flight Center*, 2013. GSFC-STD-1000F.
- [26] J. Brynjarsdottir and A. O'Hagan. Learning about physical parameters: The importance of model discrepancy. *Inverse Problems*, 30(11), 2014.
- [27] R. Mayes. Model Correlation and Calibration. *Proceedings of the 27th International Modal Analysis Conference, Society for Experimental Mechanics Inc.*, February 2009.
- [28] J. Welch. Comparison of Recent Satellite Flight Temperatures with Thermal Model Predictions. *36th International Conference on Environmental Systems (ICES)*, July 2006. Report No. 2006-01-2278.

- [29] H. Peabody, J. Rodriguez-Ruiz, and V. Benitez. Thermal Margin Study for the Global Precipitation Measurement Spacecraft. *42nd International Conference on Environmental Systems*, pages 3625–3636, July 2012.
- [30] J.M. Vickers and R.R. Garipay. Thermal Design Evolution and Performance of the Surveyor Spacecraft. *AIAA 5th Annual Meeting and Technical Display*, (AIAA No. 68-1029), October 1968.
- [31] R.D. Stark. Thermal Testing of Spacecraft. Technical report, The Aerospace Corporation, 1971. Report No. TOR-0172(2441-01)-4.
- [32] J. Saleh, D. Hastings, and D. Newman. Spacecraft Design Lifetime. *Journal of Spacecraft and Rockets*, 39:244–257, 2002.
- [33] J. Gardner, et al. The James Webb Space Telescope. *Space Science Reviews*, 123:485–606, 2006.
- [34] V. Otero, C. Mosier, and D. Neuberger. Thermal Infrared Sensor (TIRS) Instrument Thermal Subsystem Design and Lessons Learned. *43rd International Conference on Environmental Systems*, (AIAA 2013-3445), July 2013.
- [35] NASA. Landsat’s Thermal Infrared Sensor (TIRS) Instrument, May 2014. <https://www.flickr.com/photos/gsfcr/6875673083/in/set-72157629316332651>.
- [36] Mars Reconnaissance Orbiter. Technical report, NASA, 2005. Report No. 55390.
- [37] R.S. Grammier. A look inside the Juno mission to Jupiter. *IEEE Aerospace Conference*, (IEEEAC No. 1582), 2009.
- [38] D. Thunnissen and G. Tsuyuki. Margin Determination in the Design and Development of a Thermal Control System. 2004. SAE Report No. 2004-01-2416.
- [39] M. Garrison. Statistical Analysis of Thermal Analysis Margins. *Thermal and Fluids Analysis Workshop*, 2011.
- [40] Boeing Defense and Space Group. International Space Station: Active Thermal Control System Overview. 2000. <http://www.nasa.gov/pdf/473486mainissatcsoverview.pdf>.
- [41] D. Thunnissen. *Propagating and Mitigating Uncertainty in the Design of Complex Multidisciplinary Systems*. PhD thesis, California Institute of Technology, 2005.
- [42] M.C. Kennedy and A. O’Hagan. Bayesian Calibration of Computer Models. *Journal of the Royal Statistical Society*, 63(3):425–464, 2001.
- [43] A. Saltelli, M. Ratto, T. Andres, F. Campolongo, J. Cariboni, D. Gatelli, M. Saisana, and S. Tarantola. *Global Sensitivity Analysis: The Primer*. John Wiley and Sons Ltd., West Sussex, England, 2008.

- [44] J. Helton. Conceptual and Computational Basis for the Quantification of Margins and Uncertainty. Technical report, SANDIA National Laboratories, 2009. Report No. SAND2009-3055.
- [45] J.C. Helton, J.D. Johnson, C.J. Sallaberry, and C.B. Storlie. Survey of sampling-based methods for uncertainty and sensitivity analysis. *Reliability Engineering and Systems Safety*, 91(10):1175–1209, 2005.
- [46] S.A. Uebelhart, D. Miller, and C. Blaurock. Uncertainty Characterization in Integrated Modeling. *AIAA Structures, Structural Dynamics and Materials Conference*, 46:2005–2142, April 2005.
- [47] D.J. Howell. *Spatial Nyquist Fidelity Method for Structural Models of Opto-Mechanical Systems*. PhD thesis, Massachusetts Institute of Technology, 2007.
- [48] M.S. Eldred, A.A. Giunta, S.S. Collis, N.A. Alexandrov, and R.M. Lewis. Second-Order Corrections for Surrogate-Based Optimization with Model Hierarchies. *Proceedings of the 10th AIAA and ISSMO Multidisciplinary Analysis and Optimization Conference*, (No. 2004-4457), 2004.
- [49] N.V. Queipo, R.T. Haftka, W. Shyy, T. Goel, R. Vaidyanathan, and P.K. Tucker. Surrogate-based analysis and optimization. *Progress in Aerospace Sciences*, 41(1):1–28, 2005.
- [50] E. Grimme. *Krylov Projection Methods for Model Reduction*. PhD thesis, University of Illinois at Urbana-Champaign, 1997.
- [51] A.C. Antoulas. *Approximation of Large-Scale Dynamical Systems*. Society for Industrial and Applied Mathematics, Philadelphia, PA, 2009.
- [52] A.I.J. Forrester and N.W. Bressloff and A.J. Keane. Optimization using surrogate models and partially converged computational fluid dynamics simulations. *Proceedings of the Royal Society A: Mathematical, Physical and Engineering Science*, 462(2071):2177–2204, 2000.
- [53] N.M. Alexandrov and R.M. Lewis. An Overview of First-Order Model Management for Engineering Optimization. *Optimization and Engineering*, 2(4):413–430, 2001.
- [54] R.M. Lewis and S.G. Nash. Model Problems for the Multigrid Optimization of Systems Governed by Differential Equations. *SIAM Journal on Scientific Computing*, 26(6):1811–1837, 2005.
- [55] A.D. Kiureghian and O. Ditlevsen. Aleatory or epistemic? Does it matter? *Structural Safety*, 31(2):105–112, 2009.
- [56] B.M. Ayyub and G.J. Klir. *Uncertainty Modeling and Analysis in Engineering and the Sciences*. Taylor & Francis Group, Boca Raton, FL, 2006.

- [57] Y. Ben-Haim. A non-probabilistic concept of reliability. *Structural Safety*, 14(4):227–245, 1994.
- [58] Y. Ben-Haim and I. Elishakoff. *Convex Methods of Uncertainty in Applied Mechanics*. Elsevier Science Publishers, 1990.
- [59] M. Riley and R. Grandhi. Quantification of Modeling-Induced Uncertainties in Simulation-Based Design. *AIAA Structures, Structural Dynamics, and Materials Conference*, 52(1):195–202, April 2012.
- [60] R.D. Moser and T.A. Oliver. Representing Uncertainty due to Inaccurate Models. Presentation from Predictive Engineering and Computational Sciences, University of Texas at Austin, May 2013.
- [61] A. Mailhot and J.P. Villeneuve. Mean-value second-order uncertainty analysis method: Application to water quality modeling. *Advances in Water Resources*, 26(5):491–499, 2003.
- [62] Y. Jang, N. Sitar, and A.D. Kiureghian. Reliability analysis of contaminant transport in saturated porous media. *Water Resources Research*, 30(8):2435–2448, 1994.
- [63] S.K. Choi, R.V. Grandhi, R.A. Canfield, and C.L. Pettit. Polynomial chaos expansion with Latin hypercube sampling for estimating response variability. *AIAA*, 42(6):1191–1198, 2004.
- [64] H. Gutierrez. *Performance Assessment and Enhancement of Precision Controlled Structures During Conceptual Design*. PhD thesis, Massachusetts Institute of Technology, 1999.
- [65] B. Ochoa and S. Belongie. Covariance Propagation for Guided Matching. *Proceedings of the Workshop on Statistical Methods in Multi-Image and Video Processing (SMVP)*, 2006.
- [66] T. Turanyi. Sensitivity Analysis of Complex Kinetic Systems. Tools and Applications. *Journal of Mathematical Chemistry*, 5(3):203–248, 1990.
- [67] A. Saltelli, S. Tarantola, and K.P.-S. Chan. A Quantitative Model-Independent Method for Global Sensitivity Analysis of Model Output. *Technometrics*, 41(1):39–56, 1999. American Statistical Association and the American Society for Quality.
- [68] U. Reuter and M. Liebscher. Global sensitivity analysis in view of nonlinear structural behavior. *Proceedings of the 7th German LS-DYNA Forum*, (No. F-I-11-23), 2008.
- [69] J. Oakley and A. O’Hagan. Probabilistic sensitivity analysis of complex models: a Bayesian approach. *Journal of the Royal Statistical Society*, 66(3):751–769, 2004.
- [70] K.P.-S. Chan, A. Saltelli, and S. Tarantola. Sensitivity Analysis of Model Output: Variance-based Methods make the Difference. *Proceedings of the 1997 Winter Simulation Conference*, IEEE Computer Society, 26:261–268, 1997.

- [71] A. Saltelli and S. Tarantola. On the Relative Importance of Input Factors in Mathematical Models: Safety Assessment for Nuclear Waste Disposal. *Journal of the American Statistical Association*, 97(459):702–709, 2002.
- [72] A. Avila. JPL Thermal Design Modeling Philosophy and NASA-STD-7009 Standard for Models and Simulations - A Case Study. *41st International Conference on Environmental Systems*, 41(No. 20120013535), July 2011.
- [73] W. Ousley. Requirements for Thermal Design, Analysis, and Development. Technical report, NASA Thermal Engineering Branch, 2005. 545-PG-8700-2-1A.
- [74] M.A. Blair, J. W. Sills Jr, and A. E. Semple. Determination of the Model Uncertainty Factor Using Cross-orthogonality and Overall Load Factor Decomposition. *Proceedings of the 12th International Modal Analysis*, 2251, 1994.
- [75] D. Thunnissen, S. Au, and G. Tsuyuki. Uncertainty Quantification in Estimating Critical Spacecraft Component Temperatures. *Journal of Thermophysics and Heat Transfer*, 21(2):422–430, 2007.
- [76] J.A. Jacquez. Design of Experiments. *The Franklin Institute*, 335(2):259–279, 1998.
- [77] R.A. Fisher. *The Arrangement of Field Experiments*, volume 33. 1926.
- [78] R.A. Fisher. *The Design of Experiments*. Oliver and Boyd, London, England, second edition, 1935.
- [79] K.T. Hu. *Bayesian Design of Experiments for Complex Chemical Systems*. PhD thesis, Massachusetts Institute of Technology, 2011.
- [80] R.H. Myers and C.M. Anderson-Cook. *Response surface methodology: process and product optimization using designed experiments*, volume 705. John Wiley and Sons, Hoboken, NJ, 2009.
- [81] D.C. Montgomery. *Design and Analysis of Experiments*. Wiley, Hoboken, NJ, seventh edition, 2009.
- [82] J. Antony. Taguchi or classical design of experiments: a perspective from a practitioner. *Sensor Review*, 26(3):227–230, 2006.
- [83] X. Huan and Y.M. Marzouk. Simulation-based optimal Bayesian experimental design for nonlinear systems. *Journal of Computational Physics*, 232(1):288–317, 2012.
- [84] A.C. Atkinson, A.N. Donev, and R.D. Tobias. *Optimum Experimental Designs*. Oxford University Press, with SAS, Oxford, England, 2007.
- [85] K.P. Burnham and D.R. Anderson. *Model selection and multi-model inference: a practical information-theoretic approach*. New York, NY, second edition, 2002.
- [86] L. Pronzato. Optimal experimental design and some related control problems. *Automatica*, 44(2):303–325, 2008.

- [87] D.V. Lindley. *Bayesian Statistics, A Review*. Philadelphia, PA, 1972.
- [88] K. Chaloner and I. Verdinelli. Bayesian experimental design: a review. *Statistical Science*, 10(3):273–304, 1995.
- [89] K.P. Burnham and D.R. Anderson. Kullback–Leibler information as a basis for strong inference in ecological studies. *Wildlife Research*, 28(2):111–119, 2001.
- [90] J.M. Defise and P. Rochus. Lessons learned from the thermal design of an instrument (EIT, the Extreme-UV Imaging Telescope) on board SOHO. *27th International Conference on Environmental Systems*, (SAE Technical Paper No. 972528), 1997.
- [91] M. Choi. Thermal Vacuum/Balance Test Results of Swift BAT with Loop Heat Pipe Thermal System. *Second Intersociety Energy Conversion Engineering Conference (IECEC)*, (AIAA Paper No. 5683), August 2004.
- [92] M. Maschmann. Cryogenic Thermal Test of the James Webb Space Telescope (JWST) Near Infrared Spectrograph (NIRSpec). *40th International Conference on Environmental Systems*, (AIAA 2010-6165), 2010.
- [93] B.A. Moffitt and C. Batty. Predictive Thermal Analysis of the Combat Sentinel Satellite. *16th AIAA/USU Conference on Small Satellites*, pages 295–301, August 2002.
- [94] M.F.D. Aguado, J. Greenbaum, W. Fowler, and G. Lightsey. Small Satellite Thermal Design, Test, and Analysis. *Proceedings of the Modeling, Simulation, and Verification of Space-based Systems Conference*, (6221), 2006.
- [95] D.W. Miller, E.F. Crawley, J.P. How, K.Liu, M.E. Campbell, S.C.O. Grocott, R.M. Glaese, and T.D. Tuttle. The Middeck Active Control Experiment (MACE). *Proceedings of the Fifth NASA and DOD CSI Technical Conference*, (AIAA-92-2138-CP), 1996.
- [96] B.A. Cullimore. Optimization and Automated Data Correlation in the NASA Standard Thermal/Fluid System Analyzer. *33rd Intersociety Engineering Conference on Energy Conversion*, (IECEC-98-028), 1998.
- [97] F. Jouffroy. Thermal model correlation using Genetic Algorithms. *21st European Workshop on Thermal and ECLS Software*, October 2007.
- [98] T. Beck, A. Bieler, and N. Thomas. Numerical thermal mathematical model correlation to thermal balance test using adaptive particle swarm optimization (APSO). *Applied Thermal Engineering*, 38:168–174, 2012.
- [99] O.L. de Weck. *Multivariable Isoperformance Methodology for Precision Opto-Mechanical Systems*. PhD thesis, Massachusetts Institute of Technology, 2001.
- [100] R.A. Masterson. *Dynamic Tailoring and Tuning for Space-Based Precision Optical Structures*. PhD thesis, Massachusetts Institute of Technology, 2005.

- [101] R. Romanowicz, K. J. Beven, and J. Tawn. Evaluation of predictive uncertainty in non-linear hydrological models using a Bayesian approach. *Statistics for the Environment*, 2:297–317, 1994.
- [102] P.S. Craig, M. Goldstein, A. H. Seheult, and J.A. Smith. Bayes linear strategies for matching hydrocarbon reservoir history. *Bayesian Statistics 5*, 5:69–95, 1996.
- [103] P.S. Craig, M. Goldstein, J.C. Rougier, and A.H. Seheult. Bayesian forecasting for complex systems using computer simulators. *Journal of the American Statistical Association*, 96(454):717–729, 2001.
- [104] D.D. Cox, J.S. Park, and C.E. Singer. Tuning complex computer codes to data. *Proceedings of the 23rd Symposium of the Interface of Computing Science and Statistics*, pages 266–271, 1991.
- [105] D. W. Apley, J. Liu, and W. Chen. Understanding the effects of model uncertainty in robust design with computer experiments. *Journal of Mechanical Design*, 128(4):945–958, 2006.
- [106] E.C. DeCarlo, S. Mahadevan, and B.P. Smarslok. Bayesian Calibration of Aerothermal Models for Hypersonic Air Vehicles. *54th AIAA/ASME/ASCE/AHS/ASC Structures, Structural Dynamics, and Materials Conference*, (AIAA 2013-1682), 2013.
- [107] M.J. Bayarri, J.O. Berger, M.C. Kennedy, A. Kottas, R. Paulo, J. Sacks, J.A. Cafeo, C. Lin, and J. Tu. Predicting vehicle crashworthiness: Validation of computer models for functional and hierarchical data. *Journal of the American Statistical Association*, 104(487):929–943, 2009.
- [108] M. Strong, J.E. Oaklay, and J. Chilcott. Managing structural uncertainty in health economic decision models: a discrepancy approach. *Journal of the Royal Statistical Society: Series C*, 61(1):25–45, 2012.
- [109] H.K.H. Lee, B. Sanso, W. Zhou, and D.M. Higdon. Inference for a proton accelerator using convolution models. *Journal of the American Statistical Association*, 103(482):604–613, 2008.
- [110] S. Habib, K. Heitmann, D. Higdon, C. Nakhleh, and B. Williams. Cosmic calibration: Constraints from the matter power spectrum and the cosmic microwave background. *Physical Review D*, 76(8):083503, 2007.
- [111] B. Sanso and C. Forest. Statistical calibration of climate system properties. *Journal of the Royal Statistical Society: Series C*, 58(4):485–503, 2009.
- [112] J. Rougier. Probabilistic inference for future climate using an ensemble of climate model evaluations. *Climatic Change*, 81(3-4):247–264, 2007.
- [113] D. Higdon, C. Nakhleh, J. Gattiker, and B. Williams. A Bayesian calibration approach to the thermal problem. *Computer Methods in Applied Mechanics and Engineering*, 197(29):2431–2441, 2008.

- [114] D. M. Higdon, J. Gattiker, B. Williams, and M. Rightley. Computer Model Calibration Using High-Dimensional Output. *Journal of the American Statistical Association*, 103(482):570–583, 2008.
- [115] P. Z. G. Qian and C. F. J. Wu. Bayesian Hierarchical Modeling for Integrating Low-accuracy and High-accuracy Experiments. *Technometrics*, 50(2):192–204, 2008.
- [116] M. J. Bayarri, J. O. Berger, R. Paulo, J. Sacks, J. Cafeo, J. Cavendish, C. Lin, and J. Tu. A Framework for Validation of Computer Models. *Technometrics*, 49(7):138–154, 2007.
- [117] D. M. Higdon, M. C. Kennedy, J. C. Cavendish, J. A. Cafeo, and R. D. Ryne. Combining Field Data and Computer Simulations for Calibration and Prediction. *SIAM Journal on Scientific Computing*, 26(2):448–466, 2004.
- [118] H.N. Bradshaw. Thermal Design, Test, and Lessons Learned for a Thermally-Tuned Optical Component for the ICESat-2 Mission. *43rd International Conference on Environmental Systems*, (AIAA 2013-3446), 2013.
- [119] M. DiPirroa, C. Cottinghamb, R. Boylea, S. Ollendorfa, and D. Leisawitz. The SPIRIT Thermal System. *UV/Optical/IR Space Telescopes: Innovative Technologies and Concepts III*, (SPIE No. 6687), 2007.
- [120] R.M. Amundsen, J.A. Dec, and J.F. Gasbarre. Thermal Model Correlation for Mars Reconnaissance Orbiter. *ICES*, 2007. SAE Technical Paper No. 2007-01-3243.
- [121] I.M. Sobol. On sensitivity estimation for nonlinear mathematical models. *Matematicheskoe Modelirovanie*, 2(1):112–118, 1990.
- [122] A. Saltelli, S. Tarantola, F. Campolongo, and M. Ratto. *Sensitivity Analysis in Practice*. John Wiley and Sons Ltd, West Sussex, England, 2004.
- [123] D. Allaire and K. Willcox. A variance-based sensitivity index function for factor prioritization. *Reliability Engineering and System Safety*, 107:107–114, September 2012.
- [124] J. C. Mather, D. J. Fixsen, R. A. Shafer, C. Mosier, and D. T. Wilkinson. Calibrator Design for the COBE 1 Far Infrared Absolute Spectrophotometer (FIRAS). *The Astrophysical Journal*, 512(2), 2008.
- [125] A. Saltelli and P. Annoni. How to avoid a perfunctory sensitivity analysis. *Environmental Modelling and Software*, 25(12):1508–1517, 2010.
- [126] A. Solonen, H. Haario, and M. Laine. Simulation-Based Design Using a Response Variance Criterion. *Journal of Computational and Graphical Statistics*, 21(1):234–252, 2012.
- [127] D.S. Lauretta and OSIRIS-REx Team. An overview of the OSIRIS-REx asteroid sample return mission. *43rd Lunar and Planetary Institute Science Conference*, (No. 2491), 2012.

- [128] B. Allen, J. Grindlay, J. Hong, M. Oprescu, N. Induni, K. Fogarty, R.P. Binzel, R.A. Masterson, M. Chodas, N. Inamdar, M.J. Smith, G. Sondecker, M.W. Bautz, and J. Villaseñor. The REgolith X-Ray Imaging Spectrometer (REXIS) for OSIRIS-REx: Identifying regional elemental enrichment on asteroids. *SPIE Optical Engineering Applications. International Society for Optics and Photonics*, 8840, August 2013.
- [129] M. Jones, M. Chodas, M. J. Smith, and R. A. Masterson. Engineering design of the REgolith X-ray Imaging Spectrometer (REXIS) instrument: An OSIRIS-REx student collaboration. *Proc. SPIE Astronomical Telescopes and Instrumentation*, June 2014.
- [130] D.B. Carte, N.K. Inamdar, M.P. Jones, and R.A. Masterson. Design and Test of a Deployable Radiation Cover for the REgolith X-ray Imaging Spectrometer. *42nd MEA Aerospace Mechanisms Symposium*, 9144:145–152, 2014.
- [131] J. P. Emery, Y. R. Fernandez, M. S. P. Kelley, K. T. Warden, C. Hergenrother, D. S. Lauretta, M. J. Drake, H. Campins, and J. Ziffer. Thermal Infrared Observations and Thermophysical Characterization of OSIRIS-REx Target Asteroid (101955) Bennu. *Icarus*, 234:17–35, 2014.
- [132] K.D. Stout and R. A. Masterson. Thermal design and performance of the REgolith X-ray Imaging Spectrometer (REXIS) instrument. *Proc. SPIE Astronomical Telescopes and Instrumentation*, 9150, June 2014.
- [133] N. Inamdar, R.P. Binzel, J.S. Hong, B. Allen, J. Grindlay, and R.A. Masterson. Modeling the Expected Performance of the REgolith X-ray Imaging Spectrometer (REXIS). *Optical Engineering and Applications. International Society for Optics and Photonics*, 9222, August 2014.
- [134] Thermal Environments. Technical report, TRW, Inc., 1984. In Project MILSTAR Engineering Design Standards, Section 2.2.
- [135] S. Glasgow and K. Kittredge. Performance Testing of Thermal Interface Filler Materials in a Bolted Aluminum Interface Under Thermal Vacuum Conditions. Technical report, NASA Marshall Space Flight Center, 2003. Report NASA/TM-2003-212500.
- [136] J. C. Spall. An overview of the simultaneous perturbation method for efficient optimization. *Johns Hopkins APL Technical Digest*, 19(4):482–492, 1998.
- [137] J. C. Spall. Implementation of the simultaneous perturbation algorithm for stochastic optimization. *IEEE Transactions on Aerospace and Electronic Systems*, 34(3):817–823, 1998.
- [138] J. A. Nelder and R. Mead. A simplex method for function minimization. *The Computer Journal*, 7(4):308–313, 1965.
- [139] H.J. Goldsmid. *Electronic Refrigeration*, volume 76. Pion, London, second edition, 1986.

- [140] B.J. Huang, C.J. Chin, and C.L. Duang. A design method of thermoelectric cooler. *International Journal of Refrigeration*, 23(3):208–218, 2000.
- [141] N. Metropolis, A.W. Rosenbluth, M.N Rosenbluth, A.H. Teller, and E. Teller. Equation of state calculations by fast computing machines. *The Journal of Chemical Physics*, 21(6):1087–1092, 1953.
- [142] W.K. Hastings. Monte Carlo sampling methods using Markov chains and their applications. *Biometrika*, 57(1):97–109, 1970.
- [143] Andrieu, C., De Freitas, N., Doucet, A., and Jordan, M. I. An introduction to MCMC for machine learning. 50(1-2):4–43, 2003.
- [144] R.H. Myers. *Response Surface Methodology*. Allyn and Bacon, Inc., Boston, MA, 1971.
- [145] S.D. Glasgow and K. B. Kittredge. Performance Testing of Thermal Interface Filler Materials in a Bolted Aluminum Interface Under Thermal Vacuum Conditions. Technical report, Marshall Space Flight Center, 2003. Report No. NASA-TM-2003-212500.
- [146] A. Gelman, J.B. Carlin, H.S. Stern, D.B. Dunson, A. Vehtari, and D.B. Rubin. *Bayesian Data Analysis*, volume one. CRC Press, Boca Raton, FL, third edition, 2014.
- [147] C.E. Rasmussen and H. Nickish. Gaussian Processes for Machine Learning (GPML) Toolbox. *The Journal of Machine Learning Research*, 11:3011–3015, 2010.
- [148] C.E. Rasmussen and C.K.I. Williams. *Gaussian Processes for Machine Learning*. The MIT Press, Cambridge, MA, 2006.

Appendix A

Solar X-ray Monitor (SXM) Thermal Test Plan



**REXIS Engineering Model Solar X-Ray Monitor (SXM):
Thermal Balance Test Plan**

MIT Space Systems Laboratory (SSL)
Cambridge, MA

Prepared by: Kevin D. Stout

A.1 Introduction

The REXIS Solar X-ray Monitor (SXM), shown in Figure A-1, provides context to the measurements made by the spectrometer by measuring the X-ray solar spectrum during instrument operation. The driving SXM thermal design challenge is to cool the sun-facing detector below $-30\text{ }^{\circ}\text{C}$ operationally while keeping the support electronics at warmer temperatures. The SXM is thermally coupled to the spacecraft deck via an aluminum bracket. Spacecraft MLI blankets to radiatively isolate the SXM from the flight thermal environment cover all components but the detector aperture collimator. A two-stage thermoelectric cooler (TEC) is located directly beneath the detector to provide active cooling.

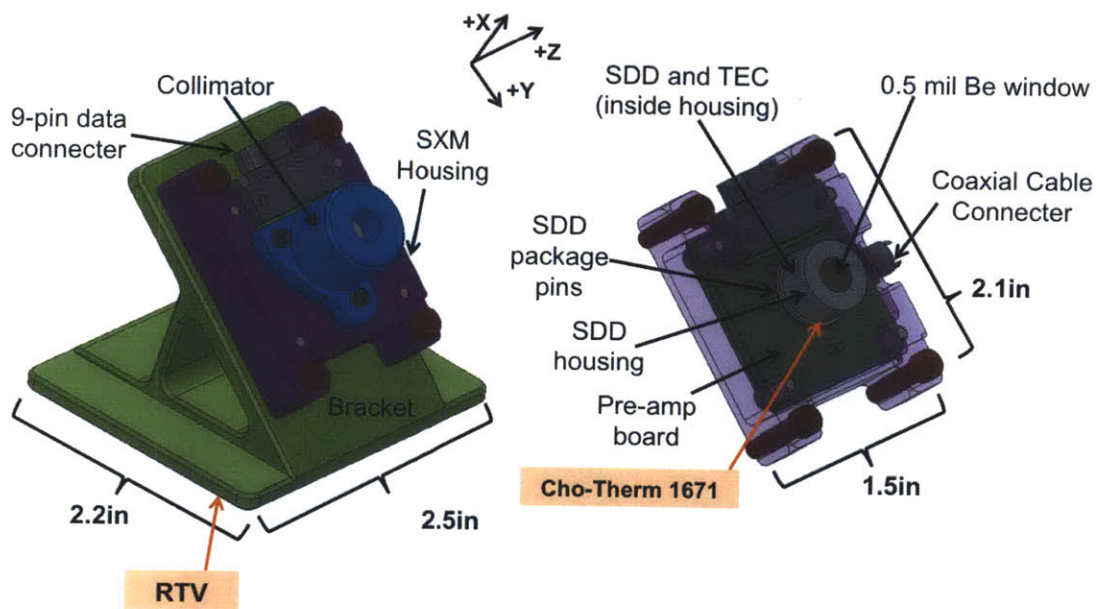


Figure A-1: SXM structure and component overview. MLI not shown.

Figure A-1 shows the SXM structure, whose bracket mechanically interfaces with the spacecraft. There are five primary components of the SXM:

- Bracket
- Collimator
- SXM housing
- SXM electronics board (SEB) (i.e., pre-amp board)

- Amptek package

The Amptek package includes the silicon drift detector (SDD), the SDD housing, the pins that are soldered to the SEB, and the mounting stud that mounts the package to the SXM housing. The primary thermal path for the SXM is from the Amptek package to the spacecraft via conduction. Thus, thermal gap filler is applied between the bracket and the spacecraft and between the Amptek package and the SXM housing to minimize thermal resistance.

A.2 Engineering Model SXM Hardware Pictures

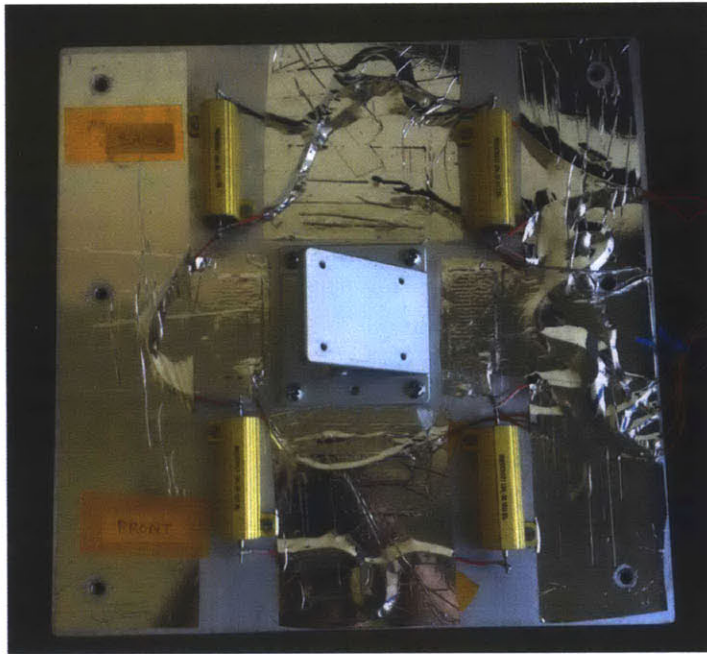


Figure A-2: Top view of interface plate with heaters and the SXM bracket. Labels on the interface plate indicate the “Front” and “Back” sides of the plate. MLI not shown.



Figure A-3: SXM structure showing resistive temperature detector on SDD housing. MLI and collimator not shown.

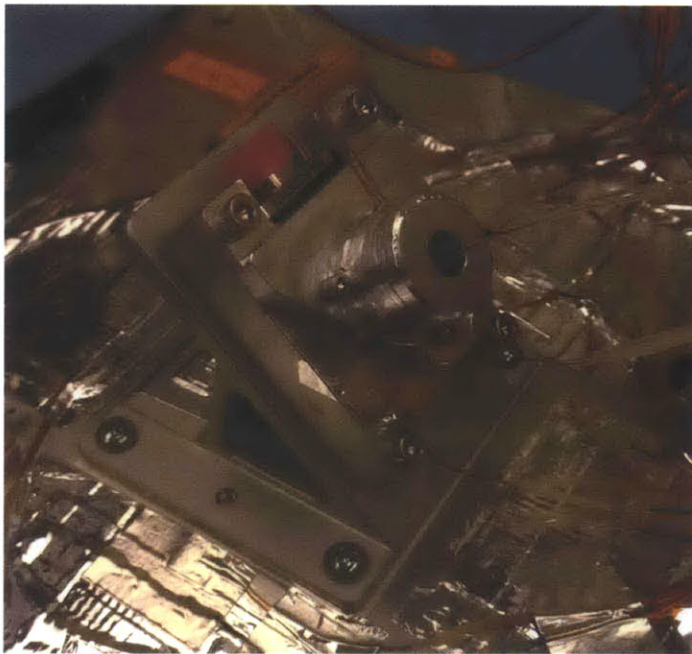


Figure A-4: SXM structure with all SXM resistive temperature detectors applied externally. MLI not shown.



Figure A-5: Final view of SXM test article with MLI blanket in SSL thermal vacuum chamber

A.3 Test Objectives and Success Criteria

Objective 1: To validate the SXM thermal model

Success Criterion: If the thermal balance test temperatures agree to within 5 °C of the predictions, correlation should be considered to have been achieved. If differences of greater than 5 °C exist, then correlation should not be considered to have been achieved until further analysis can satisfactorily explain the differences.

Objective 2: To assure that the instrument thermal design satisfies the temperature requirements of the instrument in the flight thermal environments.

Success Criterion: Satisfy all component requirements with 5 °C margin as defined in Table A.1.

Table A.1: SXM component temperature limits

Component	Survival (°C)		Operational (°C)	
	Min	Max	Min	Max
TEC (base)	-65	150	-40	100
SEB	-55	100	-40	85
SDD	–	–	-100	-30

Objective 3: Characterize the performance of the TEC over the entire domain of applied voltage and hot side temperatures expected during the mission.

Success Criterion: Obtain a functional relationship between the TEC power draw and SDD temperature given a TEC applied voltage, V_{TEC} , and hot side temperature, T_h , using calibration data on the domain $V_{TEC} \in [0,4]$ V and $T_h \in [-30,75]$ °C. Quantify the uncertainty in the calibrated estimates of TEC power draw and SDD temperature.

A.4 Personnel and Schedule

A.4.1 Personnel

Test Lead: Kevin Stout

Emergency Contacts:

- Kevin Stout
- Rebecca Masterson

Test Members:

- Kevin Stout

A.5 Test Program

A.5.1 Test Description

The thermal balance (T/B) test will be performed at a pressure of 5×10^{-5} torr or less. After the chamber is pumped down and the pressure has reached 5×10^{-5} torr, the T/B test begins. The test will consist of 45 test phases, T1 through T45, as shown in Figure A-6. The stabilization requirement is $0.25 \text{ }^\circ\text{C/hr}$ for 30 min. The test cases in Figure A-6 are a coarse grid of the entire domain of expected TEC voltages, V_{TEC} , and spacecraft interface temperatures, T_{O-REx} . Because the SXM thermal capacitance is very small, the time required to execute each test phase is expected to be <2 hr. There will be no bakeout in the SXM T/B test.

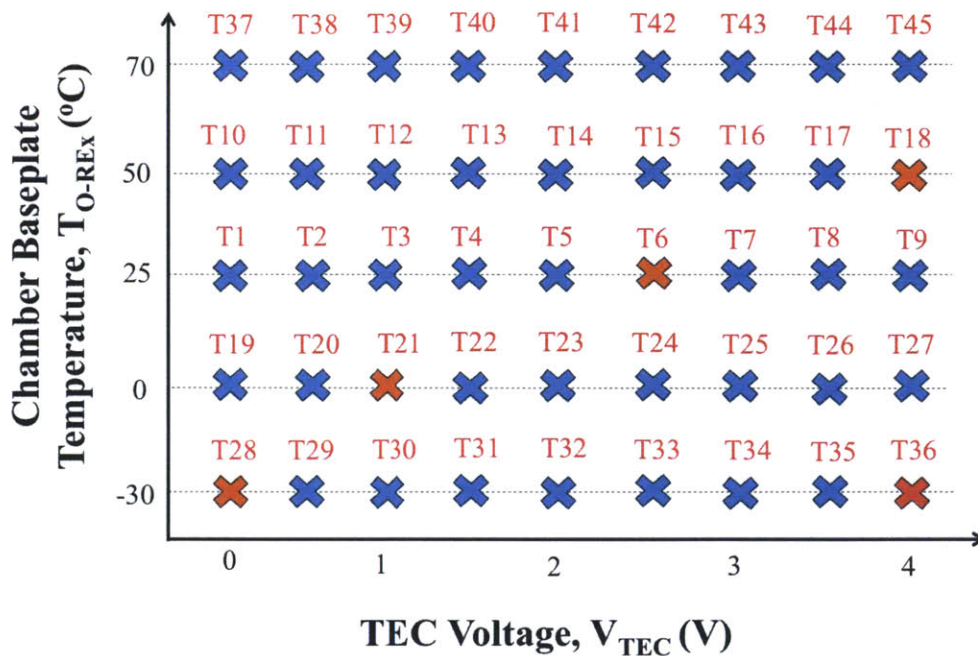


Figure A-6: SXM test grid. Blue crosses indicate test phases for *exclusively* model validation (all phases are considered as part of the model validation experiment), orange crosses indicate thermal balance test phases per a conventional thermal balance testing approach, and the red cross indicates the experimental conditions corresponding to the optimal experimental design to find the SXM conductance parameter, G_h .

In Figure A-6, there are 45 phases corresponding to three types of experiments discussed in the thesis:

- **Parameter inference experiment (BMV):** red cross (T36) in Figure A-6. The experimental conditions are selected to create data to optimally reduce uncertainties in the conductance parameter G_h .
- **Model validation experiment (BMV):** all crosses in Figure A-6. Test phases are meant to coarsely grid all possible experiments over the domain of expected V_{TEC} and T_{O-REx} during the mission.
- **Thermal balance (a conventional model validation approach):** orange crosses in Figure A-6. T18 is the hottest operational case, T21 is the coldest operational case, and T28 is the coldest survival case. T6 was selected as an additional operational data point.

A.5.2 Test Configuration

The SXM bracket will be mounted with gap filler (Cho-Therm 1671) to an interface plate to ensure good thermal conduction between the two surfaces. Good thermal conduction at the interface is similar to the flight interface because room temperature vulcanization (RTV) silicone will be used. The interface plate allows the SXM bracket to be mechanically and thermally coupled to the chamber baseplate, which is directly temperature controlled. The interface plate represents OSIRIS-REx and corresponds to T_{O-REx} in Figure A-6. Kapton heaters will be mounted to the interface plate to supplement the heating of the interface, if necessary (will be driven by external power supplies). An MLI blanket will be draped over the entire SXM with a single hole cut-out for the collimator. The MLI radiatively decouples the SXM from the chamber thermal environment, which largely is the room-temperature chamber walls.

A.5.3 Materials

Test Article

The test article includes:

- Bracket

- SXM housing
- Collimator
- Multi-layering insulation blanket
- Amptek package
- SEB

Instrumentation and Fixturing

- Resistance temperature detectors (RTDs) (11)
- Data acquisition system
- Power supplies (6)
- SXM engineering test unit (ETU) electronics
- Interface plate
- Liquid nitrogen
- Chamber baseplate controller
- Oscilloscope

A.5.4 Facility Requirements

The SSL thermal vacuum chamber, shown in Figure A-7, will be used for this test. This chamber has ambient temperature walls and a temperature-controlled baseplate. The SXM is mounted to the baseplate via an interface plate.

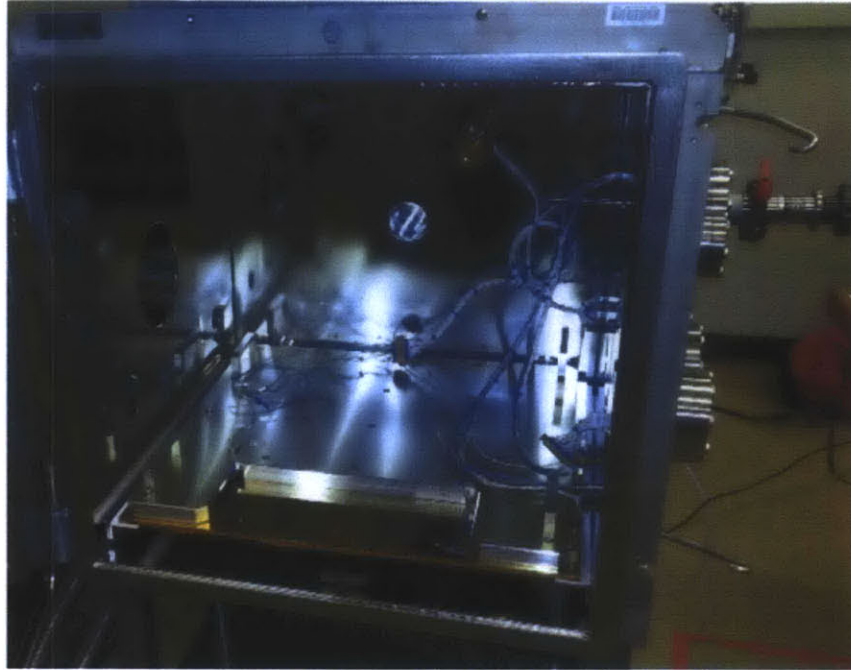


Figure A-7: SSL thermal vacuum chamber

A.5.5 Instrumentation

The instrumentation configuration for the test is shown in Figure A-8. The SXM is mechanically mounted to an interface plate, which is mechanically mounted to the chamber baseplate. The chamber baseplate has a heater and plumbing for liquid nitrogen; its temperature is regulated by a controller. Two sets of heaters on the interface plate are powered directly by power supplies outside the chamber to supplement the chamber baseplate in warming the SXM interface. Four additional power supplies are needed to control the SXM TEC and measure the SDD temperature via the ETU SXM electronics. Finally, a data acquisition (DAQ) system records the RTD readings on the SXM, interface plate, and chamber baseplate.

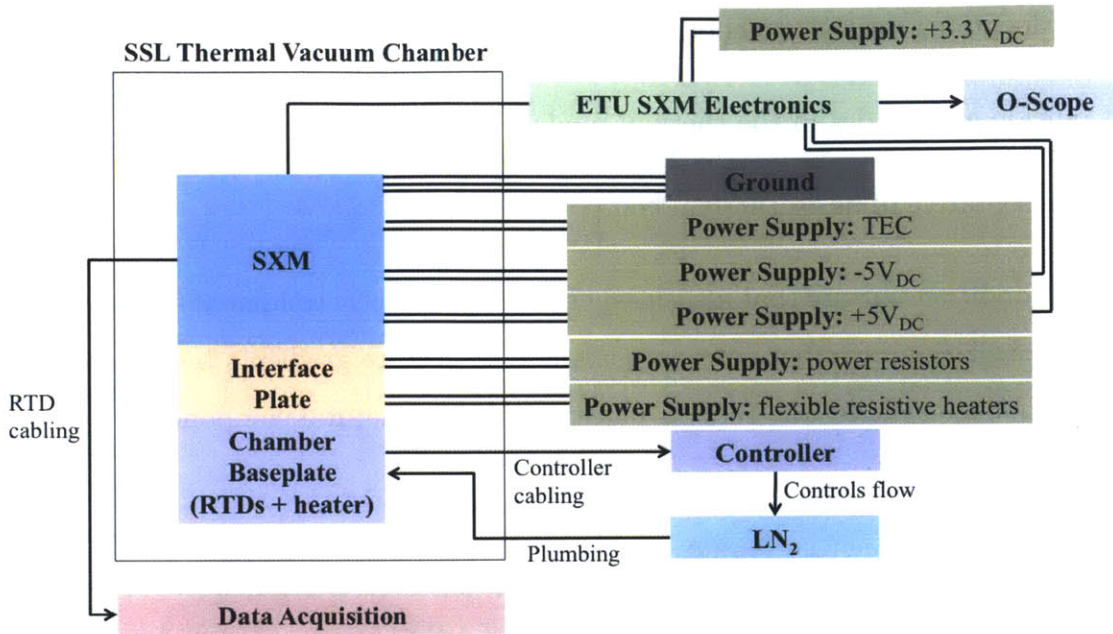


Figure A-8: Notional SXM thermal balance test electronics/control configuration

Chamber Baseplate

The chamber baseplate is temperature controllable: it is LN₂ cooled and has heaters if the baseplate must be warmer than room temperature. The SXM bracket mechanically interfaces with the interface plate, and the interface plate mechanically interfaces with the chamber baseplate. For the T/B test, the chamber baseplate is expected to operate on the interval [-30,75] °C.

Temperature Sensor Description and Placement

Temperature measurements will be made using 2-lead RTDs. RTDs are adhered to the surface of the component using aluminum tape and an additional regular Kapton overtape, if necessary.

This T/B test utilizes 11 RTDs. The RTD placement for the SXM is shown in Figure A-9. Furthermore, the locations and sensor numbers are listed in Table A.3. Two RTDs are placed on the SXM housing, one on the SDD housing, one on the collimator, and three on the bracket. Two RTDs are placed on the interface plate, and one RTD is on the chamber baseplate. One RTD is placed on the inner surface of the MLI blanket. All SXM sensor

placement locations satisfy two conditions:

- Coincide with nodes in the thermal model
- Representative of an isothermal component/region of SXM

The above conditions ensure that measurements can be directly compared to nodes within the model for correlation. Furthermore, important temperature gradients between components are captured since at least one RTD is placed on each structural component.

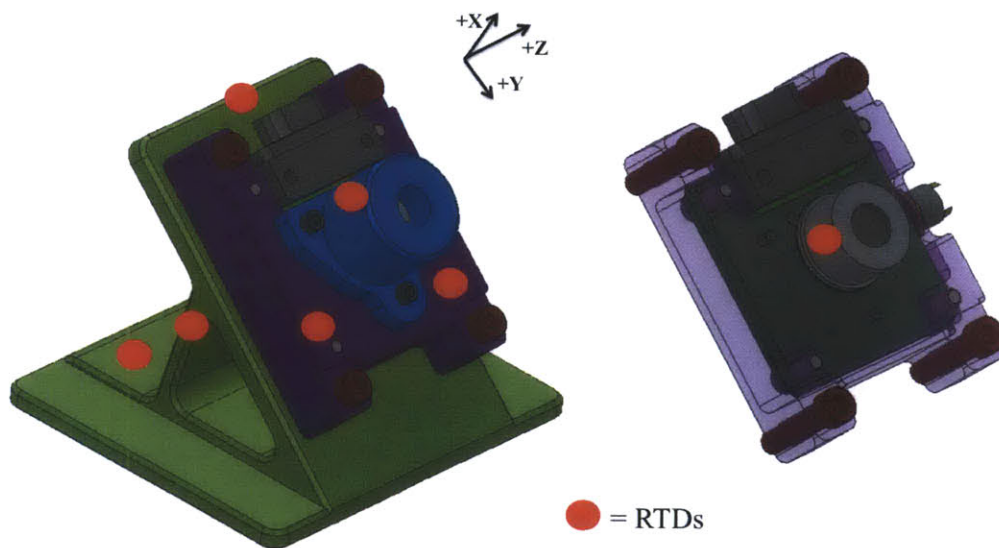


Figure A-9: SXM RTD placement

Table A.3: List of RTDs for T/B test. Sensor 10 is omitted because the RTD is not functioning properly and could not be repaired/replaced. See Figure A-2 for “Front” and “Back” designations.

Category	Component	Sensor Number
Chamber Baseplate	Bottom	Controller
Chamber Baseplate	Back	11
Interface Plate	Front	2
Interface Plate	Back	3
SXM	Bracket Base	4
SXM	Bracket Brace	5
SXM	Bracket Top	6
SXM	Housing Front	7
SXM	Housing Back	8
SXM	Collimator	9
SXM	MLI	1
SXM	SDD housing	12

Silicon Drift Detector (SDD)

During flight, the SDD temperature is measured via the SXM ETU electronics on the MEB. There is no RTD measurement of the SDD. For the thermal balance test, the temperature signal (a voltage measurement from a diode on the cold side of the TEC near the SDD) for the SDD is routed through the SEB, through the chamber wall, and into the SXM ETU electronics, as shown in Figure A-8. The temperature diode signal is measured via an oscilloscope which returns both a root-mean-squared (RMS) and a peak-to-peak voltage value.

The SDD temperature diode calibration was performed by the package manufacturer

Amptek, Inc. Equation (A.1) shows how the SDD diode voltage relates to temperature.

$$T(V_{sdd}) = -432.9V_{sdd} + 239.7 \quad (\text{A.1})$$

where V_{sdd} is the final RMS diode voltage measured via an oscilloscope and $T(V_{sdd})$ is in units of Celsius. Equation (A.1) is used to generate all SDD temperature predictions for the thermal balance test.

Thermoelectric Cooler (TEC)

The TEC is powered directly via a single power supply channel. Feedthrough cables into the chamber interface with the SEB connectors. The power signal is routed through the SEB directly to the Amptek package TEC.

Power Dissipations

Six total power supplies (6 independent channels) are needed for the SXM T/B test:

1. Interface Plate Kapton heaters (0-20 V)
2. Interface Plate power resistors (0-20 V)
3. Amptek TEC power (0-4 V)
4. +3.3 V to SXM ETU electronics to read SDD temperature
5. +5.0 V to SXM ETU electronics to read SDD temperature
6. -5.0 V to SXM ETU electronics to read SDD temperature

A.5.6 Data Requirement

Data will be collected by an Agilent data logger connected to a SSL computer. The computer uses Benchlink software to collect data every 10 s. Data shall be recorded and saved as *.csv files at the end of each test phase, T1-T45 (i.e., there will be 45 individual data files). All SDD temperature data, final RTD temperatures, and other miscellaneous test information

will be recorded on “EM SXM Thermal Balance Data Log.xlsx.” The thermal test lead is responsible for ensuring all data is stored on the REXIS SVN file repository.

A.6 Thermal Model Predictions

The Thermal Desktop model predictions for the mission Cruise Phase cold case and for test phase T28 are shown in Figure A-10. Because the SXM is off, the entire structure is isothermal and approximately -30 °C. The temperature predictions for the flight and test simulations agree well with each other.

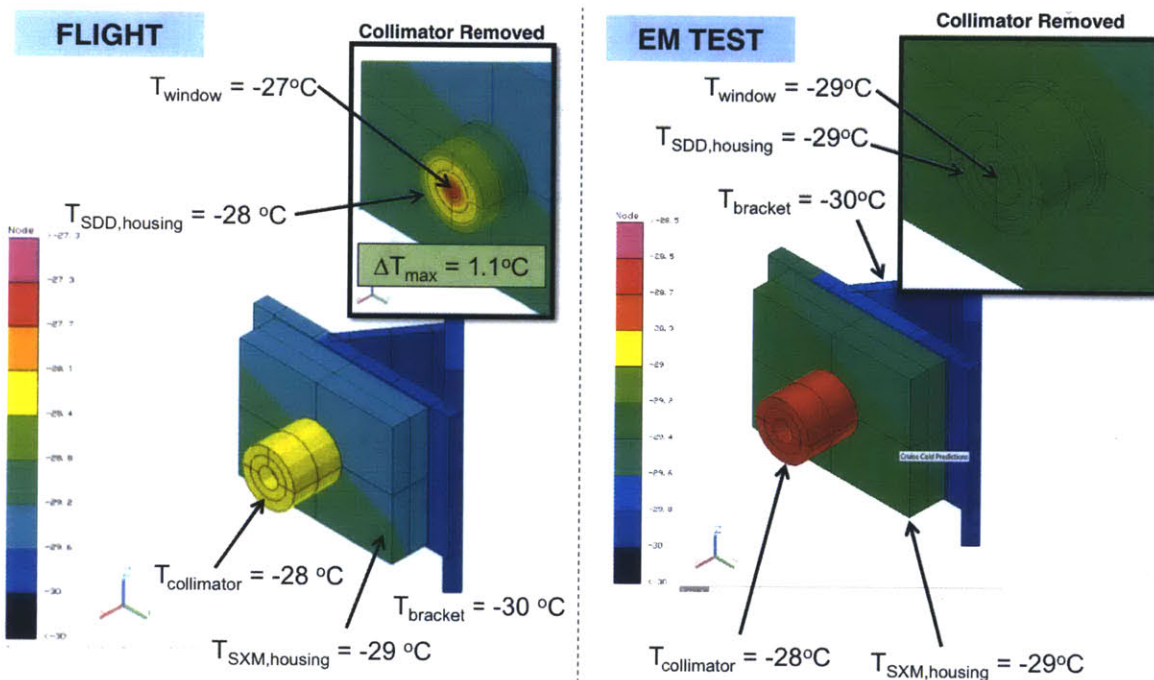


Figure A-10: Model predictions for the mission Cruise Phase cold case and for test phase T28

The Thermal Desktop model predictions for the mission operational hot case and for test phase T18 are shown in Figure A-11. The temperature difference between the SXM housing and the SDD housing is $\approx 10^{\circ}\text{C}$. The temperature predictions for the flight and test simulations agree well with each other.

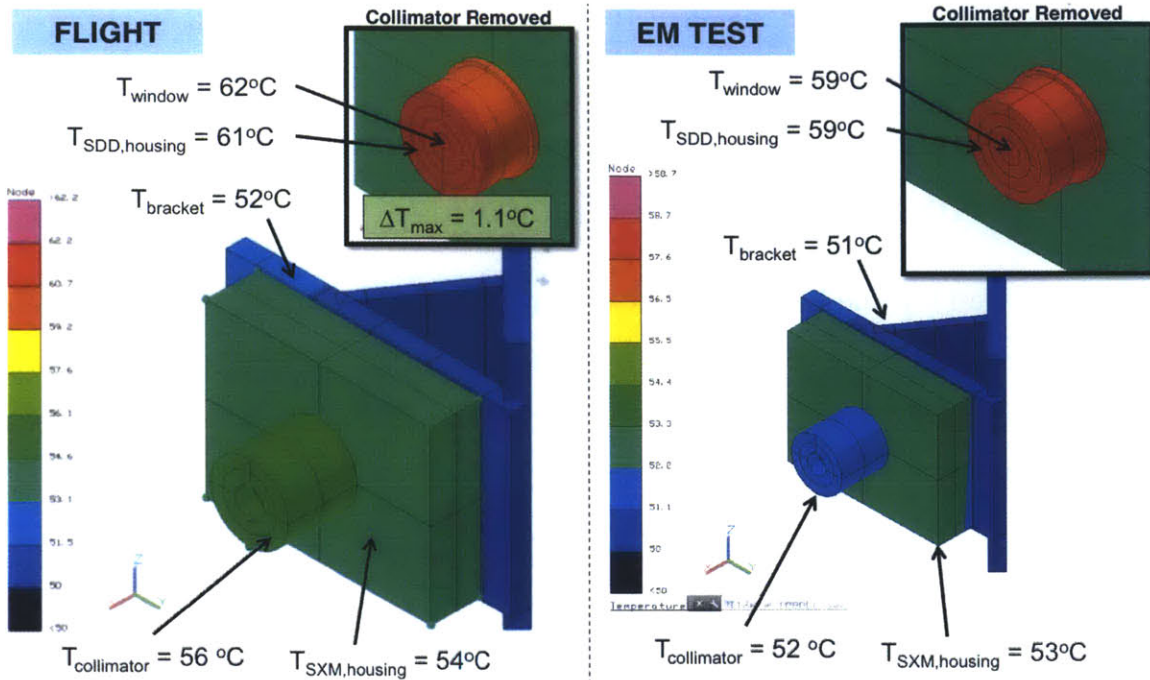


Figure A-11: Model predictions for the mission operational hot case and for test phase T18

A.7 Red/Yellow Limits

The red limits are set so that a component will never exceed its temperature limit in test. The yellow limits are set to 10 °C inside the component limits, and the red limits are set 5 °C inside the component limits. The yellow and red limits are shown for the survival and operation modes of the SXM in Table A.4 and A.5, respectively.

Note: the failure mode of the SDD in-flight at the hot limit is failure to meet spectral resolution requirement. No red limit is shown because the component will not break. The yellow limit is set to warn the monitors that the science requirement is not met at current temperature.

Table A.4: SXM survival temperature limits

Component	Yellow (°C)		Red (°C)	
	Min	Max	Min	Max
TEC	-55	140	-60	145
SEB	-45	95	-50	100

Table A.5: SXM operational temperature limits

Component	Yellow (°C)		Red (°C)	
	Min	Max	Min	Max
TEC	-30	90	-35	95
SEB	-30	75	-35	80
SDD	-60	-30	-65	–

A.8 Test Procedure

The test procedure includes phases for pre-test inspection, pump-down, the 45 thermal tests in Figure A-6, and the vent-back/pump-up procedures. Because the 45 thermal tests follow the same process, a procedure is scripted below for the i^{th} test and a log called “EM SXM Thermal Balance Data Log.xlsx” was created to table all information for each phase.

Initials	Step Number	Action
	0.1	<p>Table-top inspection: visually inspect the SXM and interface plate to ensure no damage occurred during assembly or transport. Take clear pictures of:</p> <ul style="list-style-type: none"> • Top and side view MLI • SXM and interface plate before MLI is applied • Harness/sensor locations and tie-down
	0.2	Applied Cho-Therm 1671 gap filler to chamber baseplate and secure interface plate to chamber baseplate.
	0.3	Install chamber temperature sensors and record placement of sensors with both diagram and pictures
	0.4	Install feedthrough heater cable and temperature sensor cables
	0.5	Arrange all harnesses neatly with tie-down
	0.6	Confirm that all temperature sensors are reading room temperature on the data logger to within ± 1 °C. Save 5 min of room temperature data as "RoomTemps.csv."
	0.7	Measure all resistances individually using feed-through cabling and record the resistances on "Reference" sheet of EM SXM Thermal Balance Data Log.xlsx.

	0.8	Apply heat load to each heater individually to verify operation and check neighboring temperature sensors to confirm temperature increase. Record voltage, current, and total power applied to each heater on “Reference” sheet of EM SXM Thermal Balance Data Log.xlsx.
	0.9	Perform final visual inspection of chamber identical to step 0.1. Close chamber door.
	0.10	Set all red and yellow limits in data logger for entire test.
	i.1	Record time of beginning i^{th} phase on “Time” sheet of EM SXM Thermal Balance Data Log.xlsx.
	i.2	Set chamber baseplate temperature per Figure A-6. Record final chamber baseplate temperature on “SDD” sheet of EM SXM Thermal Balance Data Log.xlsx. If necessary, apply interface plate heaters and manually tune voltages. Record interface plate heater parameters on “Reference” sheet of EM SXM Thermal Balance Data Log.xlsx once temperatures have stabilized.
	i.3	Set TEC voltage per Figure A-6. Record final voltage and current draw on “SDD” sheet of EM SXM Thermal Balance Data Log.xlsx.
	i.4	Set ETU SXM Electronics voltages to +5.0 V, -5.0 V, and +3.3 V. Record final voltage and current draw on “Reference” sheet of EM SXM Thermal Balance Data Log.xlsx.
	i.5	Stabilization has occurred when the temperatures rates for all sensors are less than 0.25 °C/hr for 30 min. Record temperatures of RTDs on “SXM Structure” sheet of EM SXM Thermal Balance Data Log.xlsx.

	i.6	Record final voltages and temperatures of SDD on “SDD” sheet of EM SXM Thermal Balance Data Log.xlsx.
	i.7	Record time of end of i^{th} test phase on “Time” sheet of EM SXM Thermal Balance Data Log.xlsx.
	i.8	Save data file to data directory as “Ti.csv”.
	35.1	Record time of beginning warm-up:
	35.2	Turn chamber baseplate off, allowing baseplate and test article to warm to ambient temperatures. Ensure liquid nitrogen is disengaged.
	36.1	Vent back chamber to ambient pressure using SSL chamber procedures once the baseplate is at ambient temperature.
	37.1	<p>Table-top inspection: visually inspect the SXM and interface plate to ensure no damage occurred during test. Take clear pictures of:</p> <ul style="list-style-type: none"> • Top and side view MLI • SXM and interface plate before MLI is applied • Harness/sensor locations and tie-down

A.9 Documentation

Storage of the documentation of the test materials, both hard/soft copies and data, is the responsibility of the test lead. All soft copies of documentation and data will be stored on the REXIS SVN. All hard copies are to be placed in the EM documentation binder.

All procedural documentation, completed by following the test plan, should be initialed and dated in the procedure section. However, the table below is also included to keep additional notes of discrepancies that arise during testing.

A.10 Safety

The test lead shall assess the test set-up and continuing performance from a safety aspect to assure that safety concerns are being considered.

A.10.1 Handling of SXM

All lifting and mounting operations of the SXM shall be performed by the thermal test lead or personnel with the permission of the thermal test lead. Where possible, all handling of the SXM should be done via the bracket. In particular, the Amptek package, SEB, RTDs, and MLI should be handled as little as possible. In transport (if applicable), the RTD wire should be supported to ensure proper adherence to the surface.

A.10.2 General Safety Practices

If any of the SXM temperatures reaches the yellow limits, the test lead (or test members) must take caution by having the thermal environment adjusted to maintain the SXM within the red limits. The yellow and red limits will be set by the test lead on the data acquisition software prior to testing.

A.10.3 Emergency Procedure

In the event of equipment failure or building evacuation, the following emergency procedures shall be followed:

- **Momentary Power Outage:** all chamber and systems will be restarted; testing resumes.
- **Extended Power Outage:** all chamber and systems will be restarted; testing resumes.
- **Building Evacuation:** the chamber will be closed and the vacuum system will be left on. The liquid nitrogen system will be turned off. Baseplate controller will be off, and the baseplate temperature will drift toward room temperature.

Appendix B

Solar X-ray Monitor (SXM) Thermal Test Data

The raw data from the SXM thermal test are provided in Table B.1 and Table B.2. The temperatures in Table B.1 are the stabilized temperatures from the 11 RTDs used in the thermal balance test. RTDs were placed on the chamber baseplate, interface plate, MLI, and SXM structure (as shown in appendix A). The temperature versus time data for each test phase was recorded through a data acquisition system and was stored on the REXIS file repository system. The data in Table B.2 are the final TEC and SDD parameters for each test phase. For each TEC voltage, both the current draw of the TEC and SDD temperature were recorded to characterize the thermal performance of the TEC.

Table B.1: Stabilized RTD readings for test phases T1 through T43 of SXM thermal balance test in Celsius.

RTD Number	11	2	3	4	5	6	7	8	9	1	12
RTD Name	Chamber Baseplate Back	Interface Plate Front	Interface Plate Back	Bracket Base	Bracket Brace	Bracket Top	Housing Front	Housing Back	Collimator	MLI	SDD Housing
T1	25.81	26.63	26.05	26.21	26.14	26.12	25.64	26.2	26.5	26.78	26.21
T2	25.74	26.57	25.99	26.16	26.1	26.1	25.64	26.24	26.52	26.81	26.21
T3	25.83	26.68	26.09	26.27	26.22	26.23	26.03	26.6	26.88	26.86	26.63
T4	25.84	26.73	26.14	26.34	26.32	26.37	26.56	27.14	27.42	26.97	27.26
T5	25.87	26.8	26.2	26.43	26.45	26.57	27.33	27.92	28.2	27.1	28.18
T6	25.89	26.9	26.31	26.56	26.65	26.85	28.39	28.99	29.25	27.29	29.44
T7	25.93	27.02	26.42	26.72	26.88	27.19	29.67	30.28	30.52	27.53	30.98
T8	25.95	27.15	26.55	26.9	27.15	27.57	31.13	31.76	31.98	27.79	32.75
T9	25.99	27.31	26.7	27.1	27.45	28	32.74	33.39	33.59	28.09	34.7
T10	50.38	51.26	50.59	50.8	50.75	50.73	49.99	50.6	50.64	50	50.5
T11	50.37	51.24	50.59	50.8	50.74	50.74	50.05	50.66	50.71	50.06	50.55
T12	50.38	51.28	50.61	50.84	50.79	50.8	50.29	50.9	50.94	50.13	50.82
T13	50.39	51.32	50.65	50.9	50.89	50.93	50.7	51.32	51.37	50.23	51.31
T14	50.43	51.4	50.74	51	51.02	51.11	51.34	51.97	52	50.37	52.08
T15	50.46	51.49	50.82	51.12	51.18	51.35	52.17	52.81	52.84	50.54	53.09
T16	50.5	51.61	50.95	51.28	51.41	51.67	53.23	53.87	53.88	50.75	54.36
T17	50.56	51.76	51.08	51.47	51.67	52.02	54.46	55.13	55.12	50.99	55.87
T18	50.62	51.91	51.24	51.66	51.95	52.44	55.84	56.53	56.5	51.25	57.55
T19	0.36	1.17	0.68	0.8	0.72	0.73	0.48	1.03	1.55	3.29	1.08
T20	0.31	1.2	0.71	0.83	0.76	0.79	0.64	1.19	1.7	3.32	1.24
T21	0.53	1.31	0.82	0.95	0.89	0.94	1	1.55	2.06	3.36	1.66
T22	0.5	1.39	0.9	1.05	1.03	1.13	1.67	2.23	2.73	3.49	2.45
T23	0.44	1.46	0.97	1.14	1.19	1.36	2.63	3.2	3.69	3.66	3.58
T24	0.64	1.6	1.1	1.32	1.42	1.68	3.84	4.41	4.89	3.89	5.03
T25	0.62	1.69	1.18	1.46	1.65	2.03	5.3	5.89	6.36	4.13	6.78
T26	0.62	1.93	1.43	1.76	2.06	2.57	7.17	7.78	8.22	4.53	8.98
T27	0.64	2.09	1.58	1.97	2.38	3.04	9.07	9.69	10.11	4.93	11.23
T28	-29.95	-29.11	-29.5	-29.45	-29.54	-29.51	-29.38	-28.88	-28.09	-23.52	-28.74
T29	-29.85	-29.09	-29.47	-29.42	-29.5	-29.47	-29.26	-28.75	-27.96	-23.74	-28.59
T30	-29.93	-29.06	-29.44	-29.37	-29.43	-29.35	-28.75	-28.24	-27.46	-23.76	-28.01
T31	-29.88	-28.96	-29.35	-29.26	-29.27	-29.13	-27.85	-27.33	-26.56	-23.65	-26.95
T32	-29.76	-28.85	-29.24	-29.1	-29.04	-28.82	-26.59	-26.06	-25.31	-23.44	-25.46
T33	-29.71	-28.67	-29.07	-28.89	-28.74	-28.41	-24.96	-24.42	23.69	-23.16	-23.53
T34	-29.75	-28.54	-28.95	-28.71	-28.45	-27.98	-23.07	-22.52	-21.81	-22.84	-21.31
T35	-29.69	-28.34	-28.75	-28.44	-28.08	-27.46	-20.85	-20.29	-19.6	-22.43	-18.71
T36	-29.6	-28.11	-28.53	-28.15	-27.67	-26.89	-18.47	-17.88	-17.22	-29.61	-15.93
T37	69.91	70.87	70.15	70.41	70.35	70.31	69.36	70.07	69.86	68.89	69.88
T38	69.91	70.87	70.16	70.42	70.37	70.32	69.43	70.14	69.93	68.92	69.94
T39	69.91	70.88	70.18	70.44	70.4	70.38	69.61	70.32	70.11	68.95	70.14
T40	69.92	70.91	70.22	70.49	70.47	70.48	69.95	70.65	70.44	69.01	70.55
T41	69.94	70.97	70.27	70.56	70.58	70.63	70.46	71.16	70.96	69.12	71.17
T42	69.98	71.06	70.35	70.66	70.74	70.84	71.15	71.85	71.66	69.26	72.01
T43	70.01	71.15	70.45	70.8	70.92	71.11	72.04	72.73	72.54	69.45	73.1

Table B.2: Temperature of chamber baseplate, final TEC parameters, and final SDD raw voltage and temperature estimates for test phases T1 through T43 of SXM thermal balance test

Test Phase	Final Baseplate Temperature (°C)	Final TEC Voltage (V)	Final TEC Power Dissipation (W)	Final TEC Current Draw (A)	Final SDD RMS Voltage (V)	SDD Temperature Estimate (°C)
T1	25	0	0	0	0.493	26.2803
T2	25	0.5	0.026	0.052	0.536	7.6656
T3	25	1	0.112	0.112	0.595	-17.8755
T4	25	1.5	0.27	0.18	0.63	-33.027
T5	25	2	0.506	0.253	0.655	-43.8495
T6	25	2.5	0.825	0.33	0.674	-52.0746
T7	25	3	1.218	0.406	0.684	-56.4036
T8	25	3.5	1.673	0.478	0.688	-58.1352
T9	25	4	2.18	0.545	0.684	-56.4036
T10	50	0	0	0	0.429	53.9859
T11	50	0.5	0.0225	0.045	0.485	29.7435
T12	50	1	0.097	0.097	0.532	9.3972
T13	50	1.5	0.2325	0.155	0.571	-7.4859
T14	50	2	0.438	0.219	0.603	-21.3387
T15	50	2.5	0.715	0.286	0.622	-29.5638
T16	50	3	1.062	0.354	0.638	-36.4902
T17	50	3.5	1.4735	0.421	0.645	-39.5205
T18	50	4	1.94	0.485	0.647	-40.3863
T19	0.2	0	0	0	0.54	5.934
T20	0	0.5	0.031	0.062	0.596	-18.3084
T21	-0.2	1	0.134	0.134	0.642	-38.2218
T22	-0.7	1.5	0.318	0.212	0.676	-52.9404
T23	-0.3	2	0.596	0.298	0.698	-62.4642
T24	-0.7	2.5	0.96	0.384	0.711	-68.0919
T25	0.5	3	1.404	0.468	0.713	-68.9577
T26	-0.4	3.5	1.9075	0.545	0.712	-68.5248
T27	-0.1	4	2.456	0.614	0.704	-65.0616
T28	-29.7	0	0	0	0.614	-26.1006
T29	-30.5	0.5	0.038	0.076	0.668	-49.4772
T30	-29.9	1	0.166	0.166	0.707	-66.3603
T31	-29.9	1.5	0.396	0.264	0.733	-77.6157
T32	-30.4	2	0.728	0.364	0.747	-83.6763
T33	-30.3	2.5	1.155	0.462	0.751	-85.4079
T34	-30.1	3	1.656	0.552	0.748	-84.1092
T35	-30.2	3.5	2.2155	0.633	0.739	-80.2131
T36	-29.9	4	2.804	0.701	0.724	-73.7196
T37	70	0	0	0	0.373	78.2283
T38	70	0.5	0.0205	0.041	0.429	53.9859
T39	70	1	0.087	0.087	0.477	33.2067
T40	70	1.5	0.2085	0.139	0.52	14.592
T41	70	2	0.392	0.196	0.553	0.3063
T42	70	2.5	0.64	0.256	0.58	-11.382
T43	70	3	0.957	0.319	0.599	-19.6071

Appendix C

Solar X-ray Monitor (SXM) Thermal Model Formulation

This appendix provides details of the SXM lumped parameter thermal model, η_{SXM} , utilized by BMV in Chapter 5. Below, the general lumped parameter formulation (including the physical relationships of conduction, radiation, and the SXM thermoelectric cooler) and model fidelity and assumptions are discussed.

C.1 Lumped Parameter Formulation

The lumped parameter modeling concept, illustrated in Figure C-1, is commonly used to model thermal systems [11, 12]. Solid, heterogeneous materials are discretized into homogeneous regions where material properties are isotropic. Each region of material is assigned a node, and temperature is assumed to be isothermal within the region. The lumped parameter approach is effective when nodes are assigned to volumes that are approximately isothermal.

The governing equation for the SXM lumped parameter model with n nodes is a differential equation of the form of Equation (C.1):

$$\frac{d\mathbf{T}}{dt} = f(\mathbf{T}, t) \quad (\text{C.1})$$

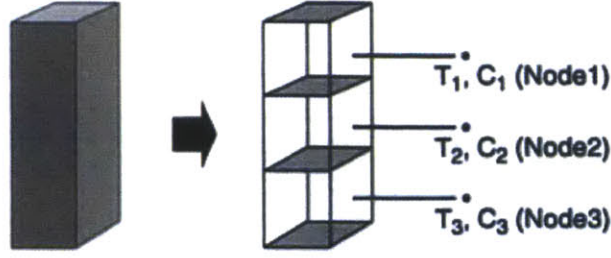


Figure C-1: Lumped parameter concept. Figure modified from [4, Fig. 15.1].

where $\mathbf{T}=[T_1 \ T_2 \ \dots \ T_n]^T$ is the vector of node temperatures. An expression for $f(\mathbf{T},t)$ can be found by reducing the heat transfer equation. Using the above assumptions a lumped parameter model, multiplying by the volume of each node, and writing for each node, the heat transfer equation in Equation 1.1 becomes:

$$\mathbf{C} \frac{d\mathbf{T}}{dt} = \mathbf{G}\mathbf{T} + \mathbf{Q}(\mathbf{T}, t) \quad (\text{C.2})$$

where \mathbf{C} is the heat capacity matrix, \mathbf{G} is the nodal matrix, and \mathbf{Q} captures the total effect of radiation and internal power dissipations. When radiation between nodes is neglected (as is the case for the SXM), \mathbf{Q} reduces to a vector, $\mathbf{Q}=[Q_1 \ Q_2 \ \dots \ Q_n]^T$, where each Q_i is the net effect of thermal radiation and internal power dissipations for the i^{th} node. \mathbf{C} and \mathbf{G} are given by:

$$\mathbf{C} = \begin{pmatrix} m_{1,1}c_{p1,1} & 0 & \cdots & 0 \\ 0 & m_{2,2}c_{p2,2} & \cdots & 0 \\ \vdots & \vdots & \ddots & \vdots \\ 0 & 0 & \cdots & m_{n,n}c_{p3,3} \end{pmatrix} \quad (\text{C.3})$$

$$\mathbf{G} = \begin{pmatrix} G_{1,1} & G_{1,2} & \cdots & G_{1,n} \\ G_{2,1} & G_{2,2} & \cdots & G_{2,n} \\ \vdots & \vdots & \ddots & \vdots \\ G_{n,1} & G_{n,2} & \cdots & G_{n,n} \end{pmatrix} \quad (\text{C.4})$$

where $m_{i,i}$ is the nodal mass, $c_{pi,i}$ is the nodal specific heat and $G_{i,j}$ is the conductance between two nodes. Thus, $f(\mathbf{T},t)$ in Equation (C.1) is given by Equation (C.5):

$$f(\mathbf{T}, t) = \mathbf{C}^{-1}[\mathbf{GT} + \mathbf{Q}(\mathbf{T}, t)] \quad (\text{C.5})$$

To solve Equation (C.1) (and thus evaluating $\eta_{SXM}(\mathbf{x})$ in Equation (5.1) for a given \mathbf{x}), a Forward Euler procedure is implemented to solve the ordinary differential equations for each node. The Forward Euler method, shown in Equation (C.6), is a simple, easy to implement method that is conditionally stable:

$$T_i(t_{k+1}) = \Delta t \left. \frac{dT}{dt} \right|_{T_i, t_k} + T_i(t_k) \quad (\text{C.6})$$

where T_i is the temperature of the i^{th} node, and t_k is the k^{th} time step. The time step increment, Δt , is constant in η_{SXM} and must be selected to be small enough so that the solver is stable and errors in the QoIs are small.

To select a suitable time step so that the solver is stable and the error in the temperature predictions is small, the time step, Δt , is incrementally increased to observe the QoI predictions for the nominal parameter values (discussed later, shown in Table 5.2). The error is very small for time steps less than $\mathcal{O}(10^0)$. At approximately $\Delta t = 6$ s, the solution is unstable and “blows up.” Consequently, a conservative time step of $\Delta t = 0.5$ s is selected. By selecting a time step value that is an order of magnitude lower than the critical time step for the nominal parameters, the solver is stable for all possible parameter sets in this case study. Furthermore, the solve time at $\Delta t = 0.5$ s is less than 0.5 s and is acceptably low.

C.2 Conduction

To develop the expression for $G_{i,j}$ in Equation (C.4), consider a 1D mesh with uniform spacing and n nodes, as shown in Figure C-2. The distance between nodes is Δx , the conductivity of the material is homogenous with value k , and the cross-sectional area is a constant area, A . Equation (C.7) shows the conservation of energy written for the i^{th} node in the x-direction:

$$Q_{i-1} + Q_{i+1} = 0 \quad (\text{C.7})$$

where Q_{i-1} and Q_{i+1} are the heat flows to the i^{th} node from the $i - 1$ and $i + 1$ nodes, respectively. For 1D conduction, the heat flows are given by Fourier's Law (analogous to Ohm's Law when discretized). For Q_{i+1} , the heat flow is given by Equation (C.8):

$$Q_{i+1} = \frac{\Delta T_{i+1}}{R_t} = \frac{T_{i+1} - T_i}{R_t} \quad (C.8)$$

where R_t is the thermal resistance equal to $\frac{\Delta x}{kA}$. By plugging Equation (C.8) into Equation (C.7):

$$0 = \frac{T_{i-1} - T_i}{R_t} + \frac{T_{i+1} - T_i}{R_t} = \frac{kA}{\Delta x}(T_{i+1} - 2T_i + T_{i-1}) = G(T_{i+1} - 2T_i + T_{i-1}) \quad (C.9)$$

The conductance, $G = R_t^{-1}$, is a scalar that is factored out. Equation (C.9) gives G for the 1D uniform mesh in Figure C-2. If written for all n nodes of the 1D mesh, Equation (C.9) will result in a linear system, $Ax = b$, where A is a tridiagonal matrix.

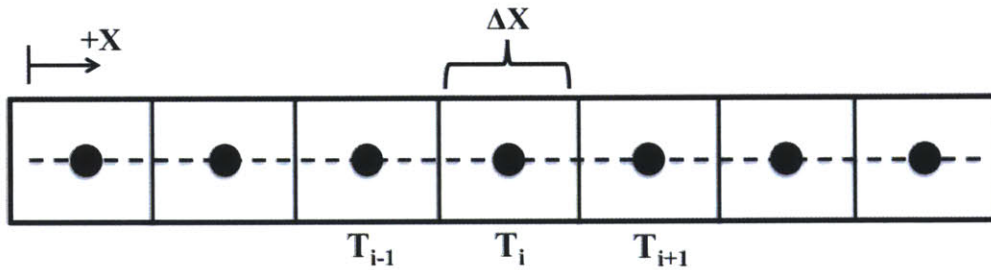


Figure C-2: 1D mesh with uniform discretization

For a general system, the mesh is not 1D, and all nodes in a system are not necessarily coupled to neighboring nodes. For the SXM, each nodal region is isothermal, but the conduction between nodes is assumed to be linear, per Equation (C.8). Thus, the form of G in Equation (C.9) holds for the conductance *between* nodes. For the \mathbf{G} matrix in Equation (C.4), each $G_{i,j}$ term is given by Equation (C.10):

$$G_{i,j} = \frac{k_{i,j}A_{i,j}}{\Delta x_{i,j}} \quad (C.10)$$

where between the i^{th} and j^{th} node: $k_{i,j}$ is the conductivity of the material, $A_{i,j}$ is the

cross-sectional area of the material, and $\Delta x_{i,j}$ is the length of the material in the direction of heat transfer. For example, consider a gap filler inserted between two components that are physically connected via fasteners: $k_{i,j}$ is the conductivity of the gap filler, $A_{i,j}$ is the contact area between the two components, and $\Delta x_{i,j}$ is the gap filler thickness. For nodes that do not conduct to each other, $G_{i,j} = 0$.

C.3 Radiation

The heat loads due to external thermal radiation are kept in the $\mathbf{Q}(\mathbf{T},t)$ term of Equation (C.5). For the SXM, external radiation consists of both direct radiation from the sun and radiation to deep space. The total heat load absorbed by a surface due to direct solar impingement is given by Equation (C.11):

$$Q_{solar} = \alpha A \phi_s \cos(\theta) \quad (C.11)$$

where α is the material absorptivity, A is the surface area, ϕ_s is the solar heat flux, and θ is the angle of incidence. If the sunlight is perpendicular to the surface, $\cos(\theta)=1$. As the surface area or absorptivity are increased, the heat load absorbed increases.

Heat transfer via radiation to deep space occurs mostly in the infrared (IR) spectrum and is modeled via the Stefan-Boltzmann Equation. Equation (C.12) gives the total heat rejected from a single surface to another surface, which acts as a thermal sink:

$$Q_{IR} = \sigma \varepsilon A (T^4 - T_{ext}^4) \quad (C.12)$$

where ε is the material emissivity, A is the surface area, T is the temperature of the surface, and T_{ext} is the temperature of the external sink. Because Equation (C.12) is nonlinear with respect to temperature, inclusion of IR radiation means that Equation (C.5) is nonlinear. Although the nonlinear form is used for η_{SXM} , the Stefan-Boltzmann Equation can be linearized [4, 9]. The $\mathbf{Q}(\mathbf{T},t)$ term in Equation (C.5) for the i^{th} node, Q_i , is the sum of internal power dissipation(s), the direct sunlight radiation component from Equation (C.11), and the IR component to deep space from Equation (C.12) for that node.

C.4 Thermoelectric Cooler (TEC)

A TEC is an active thermal control component that operates based on the Peltier effect to create a heat flux between two different materials. A two-stage TEC is used to cool the SDD for the SXM. Within the SXM thermal model, performance estimates of the TEC are used to predict the SDD temperature, T_{sdd} , based on a voltage setting and its hot side temperature. The hot side temperature is the same as the SDD housing temperature, T_h . The SDD housing manufacturer Amptek, Inc. provided estimates of the TEC's performance based on in-house analysis and testing. Figure C-3 shows T_{sdd} versus voltage, and Figure C-4 shows T_{sdd} versus current. The curves in Figure C-3 and Figure C-4 are fit to produce a direct relationship between applied TEC voltage and current, as shown in Figure C-5. The resistance of the TEC is constant with respect to voltage but increases as the TEC hot side temperature decreases.

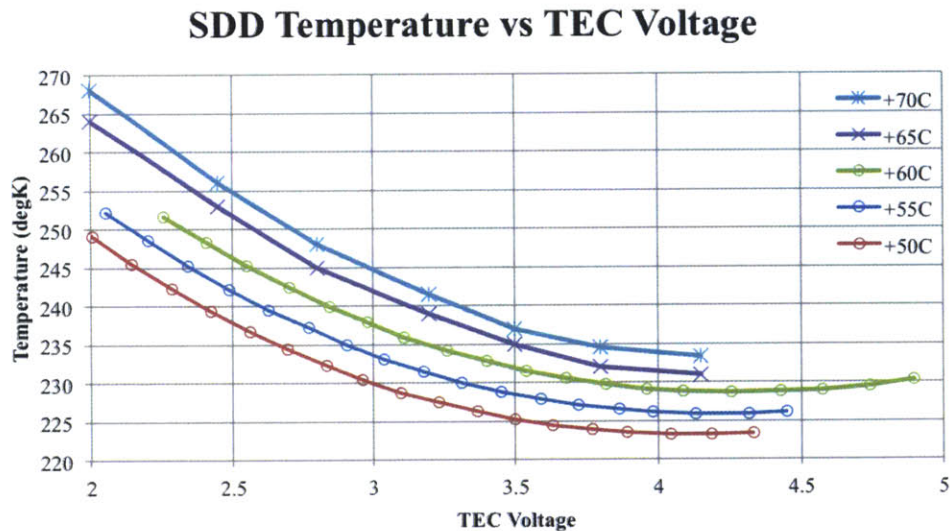


Figure C-3: SDD temperature versus voltage for SXM TEC at various hot side, T_h , values. TEC performance curves in plot provided by Amptek, Inc.

For flight, the TEC will be controlled by REXIS software to a temperature set point, T_s . Although currently the control software is not written, the *capability* of the TEC to achieve T_s is of more interest for thermal design than the *performance of the controller* because all requirements are steady state temperature limits. For simplicity, a proportional controller

SDD Temperature vs TEC Current

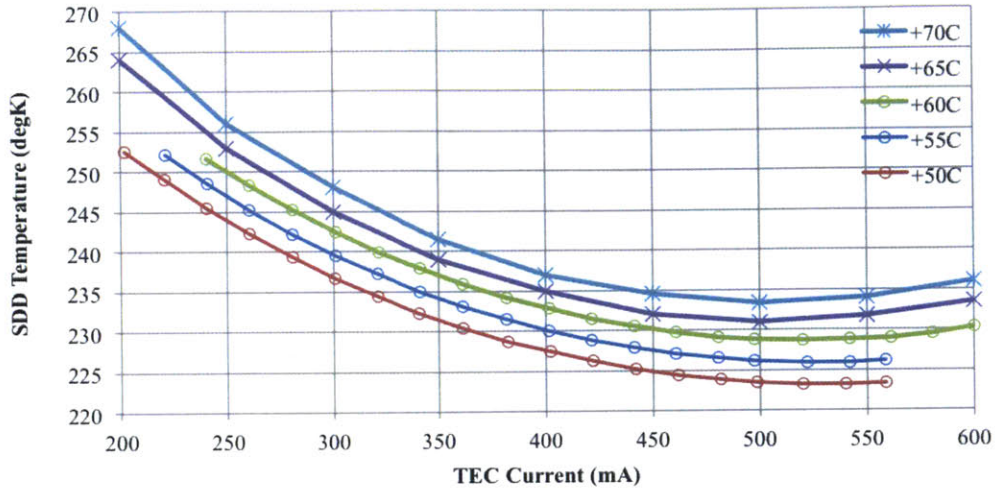


Figure C-4: SDD temperature versus current for SXM TEC at various hot side, T_h , values. TEC performance curves in plot provided by Amptek, Inc.

is used in the lumped parameter model, given by Equation (C.13):

$$V(t_{k+1}) = K_p e(t) = K_p (T_{sdd} - T_s) \quad (\text{C.13})$$

where $e(t)$ is the process error, K_p is the proportional gain in units of volts per temperature, and $V(t_{k+1})$ is the voltage at the next time step. A gain of $K_p = 0.05$ is selected via manual tuning. For each time step of the thermal model solver:

1. The voltage and TEC hot side temperature are used to predict the SDD temperature using Figure C-3
2. The voltage and the TEC hot side temperature are used in Figure C-5 to estimate the current draw, providing the TEC power dissipation
3. If it is time to update the TEC voltage (per the prescribed control frequency), Equation (C.13) is applied to correct the voltage for the next time step.

Item 1 provides the temperature prediction for the SDD, T_{sdd} , for the current time step. Item 2 estimates the current draw so that the TEC power dissipation is available for the next time step as a heat load input for the thermal system.

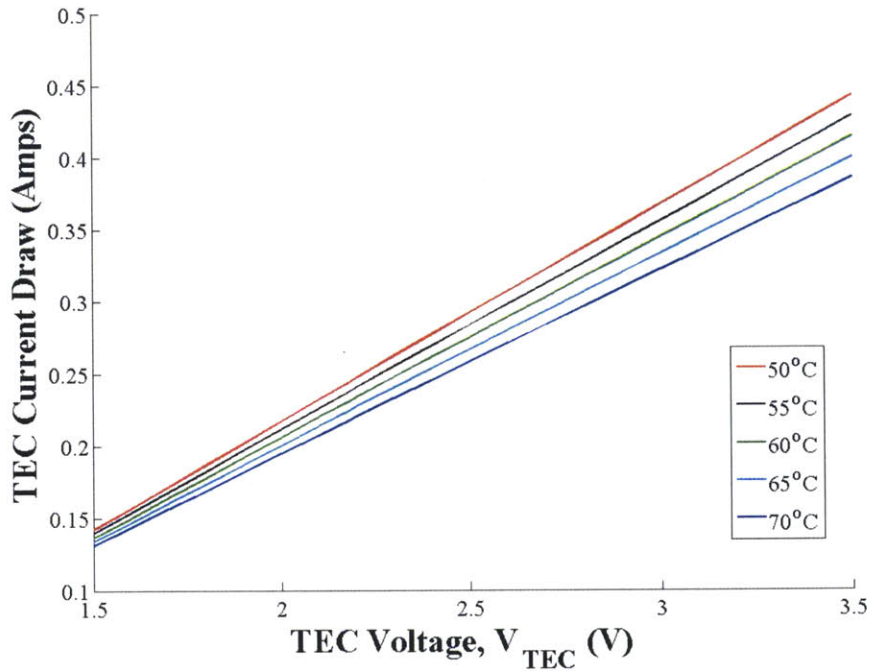


Figure C-5: Applied voltage versus current draw for SXM TEC at various TEC hot side temperatures

The curves in Figure C-3 and Figure C-4 are all that is known of the TEC's performance prior to testing. Because the range of possible TEC hot side temperatures for the mission is well outside the temperature range provided by Amptek, Inc., extrapolation of the polynomial parameters in Figure C-3 and Figure C-5 is necessary. The polynomial parameters used to estimate the TEC's performance are treated as deterministic quantities prior to testing due to the poor prior information (the only non-probabilistic SXM model parameters prior to testing).

C.5 Model Fidelity and Important Assumptions

Nodes are assigned to the SXM components within η_{SXM} that both capture the physical structure of the assembly and represent SXM material that is relatively isothermal by design. In total, there are five nodes (not including the SDD), labeled in Figure C-6, and thermally connected as shown in Figure C-7. Above the matrix diagonal in Figure C-7, heat transfers *from* the upper left *to* the lower right nodes. Below the matrix diagonal, heat transfers

from the lower right to upper left nodes. Each \mathbf{C} entry represents a conductance term, $G_{i,j}$, in Equation (C.4) of the lumped parameter model. Radiation occurs from the sun to the SDD housing and collimator because they are not covered by the MLI blankets and receive sunlight. Furthermore, the collimator is the only SXM component with a significant view factor and area exposed to deep space so IR heat rejection of the collimator is included.

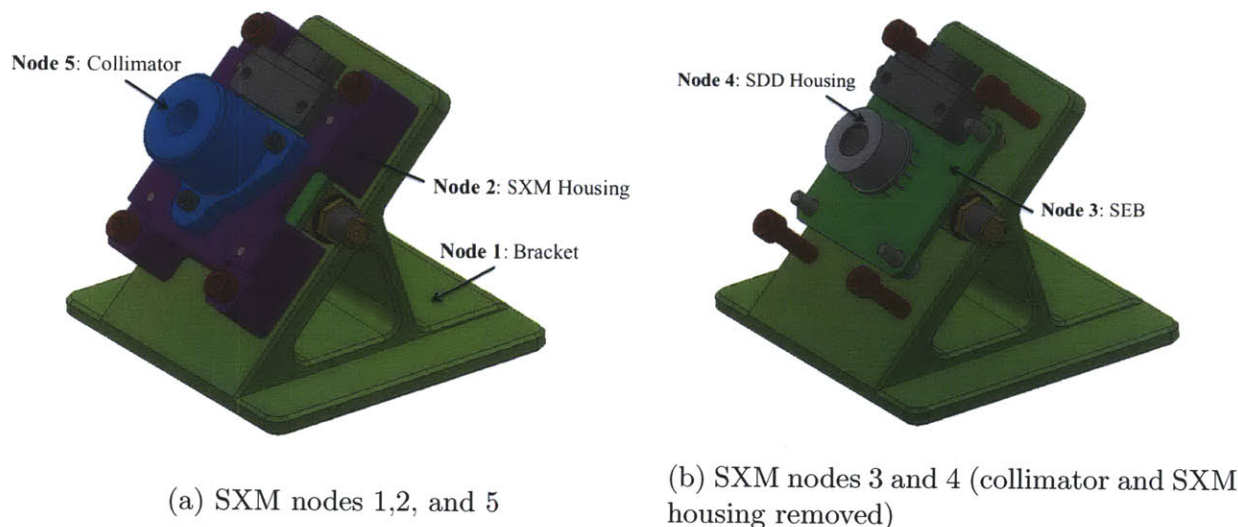


Figure C-6: SXM node assignments for the lumped parameter model

In Figure C-7, the decision not include the effects of solar radiation on the other SXM components is shown (an **X** is drawn over radiation from the sun to the bracket and SXM housing). Although the MLI greatly reduces the total absorbed heat, a sensitivity analysis is performed to justify the exclusion of solar radiation on the bracket and SXM housing. Figure C-8a notionally depicts the nominal thermal scenario during operation. The entire SXM, except the collimator and a portion of the SXM housing visible through the collimator, is beneath the MLI blanket and does not receive direct sunlight. Figure C-8b reduces the scenario in Figure C-8a to a single node representing the MLI blanket. Treating the entire blanket as a node, the heat load, Q_{MLI} , that travels through the MLI will directly affect the SXM temperatures. As long as the heat load is small, the effects of solar radiation can be neglected.

To estimate Q_{MLI} , first the outer cover temperature, T_c , is found. Once T_c is known, Q_{MLI} is approximated via the Stefan-Boltzmann equation. The first step is to sum the heat

		→ Environment					
Deep Space							
	Sun		R	R		R	R
		O-REx					
		C	1 – Bracket				
			C	2 – SXM Housing			
				C	3 – SEB		
				C	C	4 – SDD Housing	
R				C			5 – Collimator
		↳ SXM					

Figure C-7: Connectivity matrix for SXM model. Blue boxes with **C** indicate conductive heat transfer, and red boxes with **R** indicate heat transfer through radiation. Blank boxes indicate no thermal connection (e.g., $G_{i,j} = 0$). Above the matrix diagonal, heat transfers *from* the upper left *to* the lower right nodes. Below the matrix diagonal, heat transfers *from* the lower right *to* upper left nodes. An **X** is drawn over radiation from the sun to the structural components beneath MLI blankets to explicitly show the assumption to neglect solar radiation to these components.

flows in Figure C-8b according to the law of conservation of energy:

$$Q_{solar} - Q_{IR} - Q_{MLI} = 0 \quad (C.14)$$

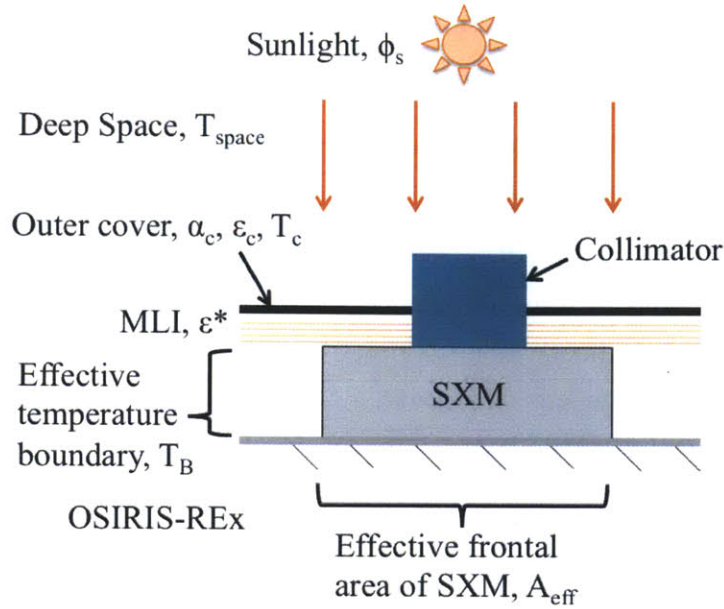
where Q_{solar} and Q_{IR} are Equations (C.11) and (C.12), respectively, rewritten in terms of the MLI sensitivity analysis variables. Q_{solar} , Q_{IR} , and Q_{MLI} are given by:

$$Q_{solar} = \alpha_c A_{eff} \phi_s \quad (C.15)$$

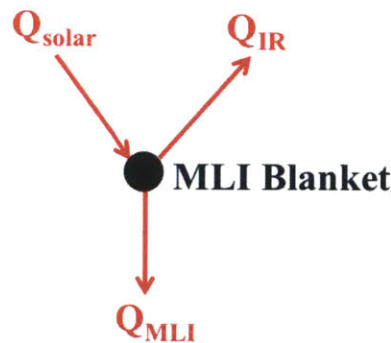
$$Q_{IR} = \sigma \varepsilon_c A_{eff} (T_c^4 - T_{space}^4) \quad (C.16)$$

$$Q_{MLI} = \sigma \varepsilon^* A_{eff} (T_c^4 - T_B^4) \quad (C.17)$$

All parameters in Equations (C.15), (C.16), and (C.17) are given in Table C.1. The



(a) Notional diagram of MLI applied to minimize the solar flux absorbed by the SXM



(b) Heat flows for MLI blanket idealized as a single node

Figure C-8: Notional SXM MLI heat flow diagrams to solve for the temperature of the MLI outer cover

boundary temperature, T_B , is the temperature of the SXM and spacecraft deck. The solar flux, ϕ_s , is based on a heliocentric radius of 1 AU, the median distance from the sun during the mission. The effective emissivity, ϵ^* , is a single parameter representing the transmission of heat through all the layers of MLI. The effective emissivity of large, 12-layer MLI blankets depends heavily on the blanket design and can range from $\epsilon^*=0.001$ to $\epsilon^*=0.03$ [4]. A conservative value of $\epsilon^*=0.03$ is chosen (a “leaky” blanket) for this sensitivity analysis to allow for the maximum possible value of Q_{MLI} . The MLI cover emissivity, ϵ_c , and absorptivity, α_c , have values associated with black Kapton [4]. Finally, the effective area, A_{eff} , is

the projected area of the SXM (i.e., the area seen by the sun if the blankets are not used, including the SXM housing and bracket).

Table C.1: Parameter values for SXM MLI sensitivity analysis

Parameter/Constant	Value	Units
Solar flux, ϕ_s	1,367	$\frac{W}{m^2}$
Stefan-Boltzmann constant, σ	5.67×10^{-8}	$\frac{W}{m^2 K^4}$
MLI effective emissivity, ε^*	0.03	–
MLI cover emissivity, ε_c	0.70	–
MLI cover absorptivity, α_c	0.80	–
Temperature of Deep Space, T_{space}	2.73	K
Effective area, A_{eff}	0.002	m^2

To find T_c , Equations (C.15), (C.16), and (C.17) are plugged into Equation (C.14). The effective area drops out, leaving Equation (C.18):

$$\phi_s \alpha_c - \sigma \varepsilon_c (T_c^4 - T_{space}^4) - \sigma \varepsilon^* (T_c^4 - T_B^4) = 0 \quad (C.18)$$

Rearranging and solving for T_c :

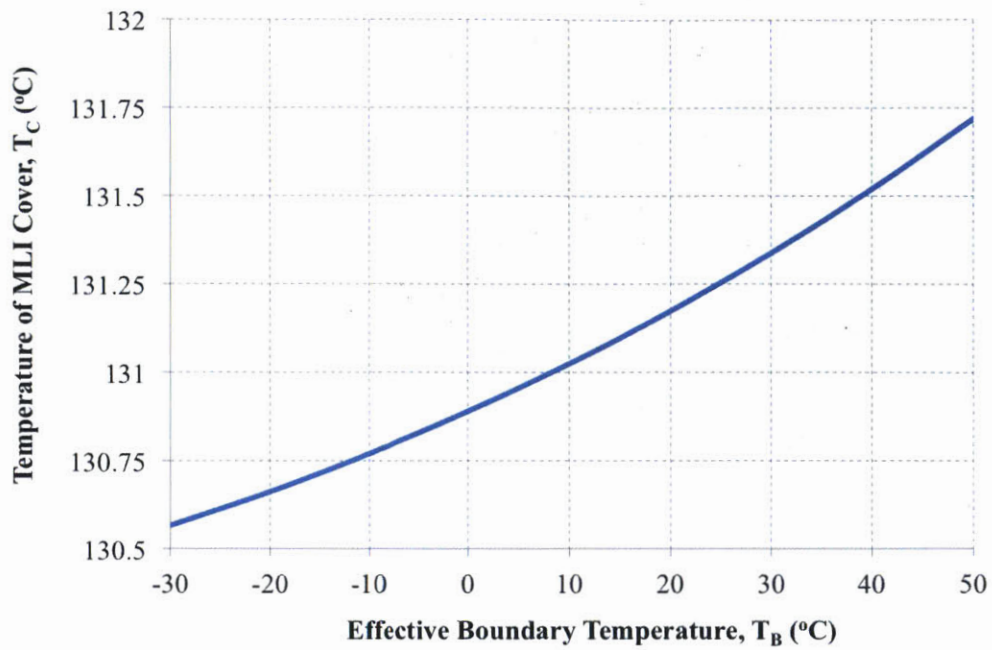
$$T_c = f(T_B) = \sqrt[4]{\frac{\phi_s \alpha_c + \sigma \varepsilon^* T_B^4 + \sigma \varepsilon_c T_{space}^4}{\sigma \varepsilon^* + \sigma \varepsilon_c}} \quad (C.19)$$

Equation (C.19) is functionally dependent on the SXM and spacecraft temperature. The SXM is designed to be as close as possible to the spacecraft deck temperature so for simplicity, the boundary temperature, T_B , is a single temperature representing the SXM/deck beneath the MLI blankets. T_B is controlled by the spacecraft and is variable throughout the mission on the interval [-30,50] °C. Thus, a range of T_c values is possible.

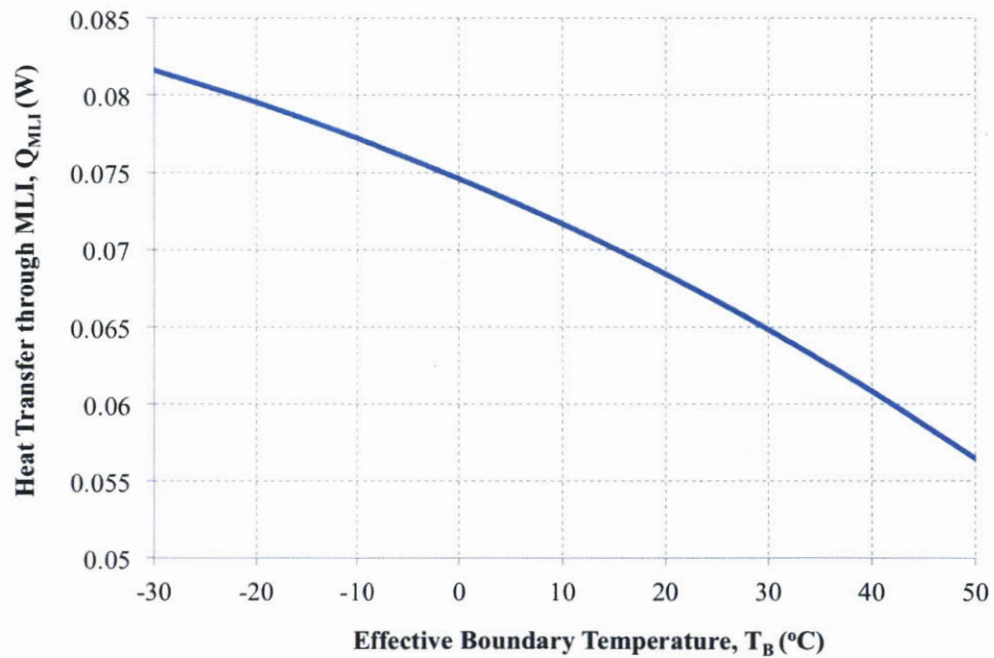
Figure C-9a shows the MLI cover temperature versus the effective boundary temperature by plotting Equation (C.19). The takeaway is that over the large range of T_B values, the MLI cover temperatures varies very little and is approximately 131 °C. Figure C-9b uses the results of Figure C-9a with Equation (C.17) to plot heat load passing through the MLI, Q_{MLI} , versus the effective boundary temperature. At the coldest possible T_B value, the maximum Q_{MLI} value occurs and is approximately 0.08 W distributed across the entire

SXM structure. Because the total, maximum expected SXM power dissipation is 2.8 W, $Q_{MLI}=0.08$ W represents only $\approx 3\%$ of the total heat load. Thus, the effect of the sun on the SXM housing and bracket is assumed to be small and is neglected from the thermal model prior to validation.

At this point in the documentation of the model, the structure is fixed: a five-node lumped parameter model is constructed with conduction and radiation between nodes according Figure C-7. For each time step, the SDD temperature is approximated *within* the lumped parameter model using performance estimates of the TEC. Based on a prescribed parameter vector, \mathbf{x} , η_{SXM} outputs temperature and heat flows versus time for all five nodes and the SDD.



(a) MLI outer cover temperature for various effective boundary temperatures



(b) Heat transfer through layers of MLI for various effective boundary temperatures

Figure C-9: Examination of the absorbed heat from the sun through the layers of MLI. The effective boundary temperature is an idealization of the radiation sink for the MLI inner cover with a projected area of the SXM structure.